REALISTIC TOOL–TISSUE INTERACTION MODELS FOR SURGICAL SIMULATION AND PLANNING

by

Sarthak Misra

A dissertation submitted to The Johns Hopkins University in conformity with the requirements for the degree of Doctor of Philosophy.

Baltimore, Maryland

June, 2009

© Sarthak Misra 2009

All rights reserved

Abstract

Surgical simulators present a safe and potentially effective method for surgical training, and can also be used in pre- and intra-operative surgical planning. Realistic modeling of medical interventions involving tool-tissue interactions has been considered to be a key requirement in the development of high-fidelity simulators and planners. The soft-tissue constitutive laws, organ geometry and boundary conditions imposed by the connective tissues surrounding the organ, and the shape of the surgical tool interacting with the organ are some of the factors that govern the accuracy of medical intervention planning.

This thesis is divided into three parts. First, we compare the accuracy of linear and nonlinear constitutive laws for tissue. An important consequence of nonlinear models is the Poynting effect, in which shearing of tissue results in normal force; this effect is not seen in a linear elastic model. The magnitude of the normal force for myocardial tissue is shown to be larger than the human contact force discrimination threshold. Further, in order to investigate and quantify the role of the Poynting effect on material discrimination, we perform a multidimensional scaling study. Second, we consider the effects of organ geometry and boundary constraints in needle path planning. Using medical images and

ABSTRACT

tissue mechanical properties, we develop a model of the prostate and surrounding organs. We show that, for needle procedures such as biopsy or brachytherapy, organ geometry and boundary constraints have more impact on target motion than tissue material parameters. Finally, we investigate the effects surgical tool shape on the accuracy of medical intervention planning. We consider the specific case of robotic needle steering, in which asymmetry of a bevel-tip needle results in the needle naturally bending when it is inserted into soft tissue. We present an analytical and finite element (FE) model for the loads developed at the bevel tip during needle-tissue interaction. The analytical model explains trends observed in the experiments. We incorporated physical parameters (rupture toughness and nonlinear material elasticity) into the FE model that included both contact and cohesive zone models to simulate tissue cleavage. The model shows that the tip forces are sensitive to the rupture toughness. In order to model the mechanics of deflection of the needle, we use an energy-based formulation that incorporates tissue-specific parameters such as rupture toughness, nonlinear material elasticity, and interaction stiffness, and needle geometric and material properties. Simulation results follow similar trends (deflection and radius of curvature) to those observed in macroscopic experimental studies of a robot-driven needle interacting with gels.

Primary Readers: Allison M. Okamura (Professor, Mechanical Engineering), K. T. Ramesh (Professor, Mechanical Engineering), Benjamin W. Schafer (Associate Professor, Civil Engineering), and Louis L. Whitcomb (Professor, Mechanical Engineering).

Acknowledgements

This thesis would not have been possible without the help of my advisors, my research collaborators, and all my teachers at the Johns Hopkins University. First and foremost, I thank my advisor Professor Allison M. Okamura for her help and support over the past four years. I thank her for accepting me into the Haptics Laboratory and providing me with the necessary resources to succeed. She encouraged the various research collaborations that made this thesis possible.

This thesis would also not have been possible without the help of Professor K. T. Ramesh, my unofficial co-advisor. I thank him for his patience and for introducing me to the beauty of continuum mechanics. His great efforts to explain things clearly and simply have been a source of inspiration for me. I have learnt great many life lessons from both Allison and KT, and I am grateful for having such excellent mentors.

The majority of the research presented in Chapter 5 of this thesis was based on discussions with Professor Benjamin W. Schafer. I thank Ben for all his help and time, and also for agreeing to be a member of my thesis committee. He was always accessible and willing to help, in spite of his many other obligations. His enthusiasm was infectious and

his motivation propelled me to drive on during tough times. Finally I also thank Professor Louis L. Whitcomb for agreeing to be a member of my thesis committee and also for being one of the best teachers I have had at Johns Hopkins.

This thesis is a result of discussions and collaborations with many people. In particular I wish to acknowledge Prof. Andrew S. Douglas, Dr. Katarzyna J. Macura (Johns Hopkins Medical Institutions), and Dr. Matthias Harders (Eidgenössische Technische Hochschule Zürich). I also thank post-doctoral fellows, graduate, and undergraduate students who have directly helped me with my research. These include Dr. Kyle B. Reed, Dr. Shailendra Joshi, Matthew Moses, Dheeraj Singaraju, Philipp Fuernstahl, and Debjoy Mallick.

My doctoral studies would not have been possible without the financial support from the following funding sources: the National Science Foundation under Grant Nos. EIA-0312551 and IIS-0347464, the Whitaker Foundation under Grant No. RG-02-911, the National Institutes of Health under Grant Nos. R01-EB002004 and R01-EB006435, the IEEE Robotics and Automation Society Technical Committee on Haptics Travel Award, the Swiss National Science Foundation (Computer Aided and Image Guided Medical Interventions), and a Link Foundation Fellowship.

I have been fortunate enough to be part of two research groups at Johns Hopkins – that of Allison Okamura (Haptics Laboratory) and that of K. T. Ramesh. I thank all the members for being so welcoming into their respective research groups. Every single member of these groups has helped and affected my work in a positive way. I am especially thankful to Lawton Verner, Tomonori Yamamoto, Panadda Marayong, Thomas Wedlick,

ACKNOWLEDGEMENTS

David Grow, Netta Gurari, Tricia Gibo, Kyle Reed, Steven Charles, Paul Griffiths, Amy Blank, Jim Gwilliam, and Ann Majewicz within the Haptics Laboratory; and Rika Wright, Emily Huskins, Jessica Meulbroek, Jamie Kimberley, Krishna Jonnalagadda, Cynthia Byer, Buyang Cao, Reuben Kraft, Nitin Daphalapurkar, Guangli Hu, Cyril Williams, and Libby Starnes within the K. T. Ramesh research group. These are the people who know the real story that went behind the making of this doctoral thesis. I am grateful for the support network they provided and for making my stay in Baltimore an enjoyable one. I believe I have found some life-long friends here.

I would like to thank Radio Paradise (www.radioparadise.com) for providing me with my continuous and awesome fix of alternative and eclectic music, and National Public Radio for accompanying me on my long drives to Montreal during the early part of my doctoral studies and on my shorter drives to New York City during the later part of my doctoral studies. In addition, I thank the Baltimore Road Runners Club for keeping my cortisol levels low and serotonin levels high. Running has become a part of my life!

I thank my parents for instilling the importance of a good education very early in life. I am grateful to my parents, my sister, and my in-laws for their constant encouragement and love. And finally I thank Marije for all that she had to put up with over the past four years. The decision to start my doctoral program at Johns Hopkins was made by both Marije and myself. I do not think I can adequately articulate my gratitude for her love, help, and support which made this thesis possible. Ik dank je vanuit het diepste van mijn hart.

Dedication

This thesis is dedicated to my dearest Marije.

Contents

CONTENTS

List of Tables

List of Figures

Chapter 1

Introduction

Realistic modeling of medical interventions involving tool-tissue interactions is considered a key requirement in the development of high-fidelity simulators and planners. Surgical simulators present an efficient, safe, realistic, and ethical method for surgical training, practice, and pre-operative planning. Computer-based surgical trainers use virtual patients. These simulators can generate realistic human anatomy, physiological responses including certain types of pathology, and in some cases also provide haptic feedback to the user. Using medical simulators, students can practice on a variety of complex cases and receive detailed feedback on their performance. Patient safety is not compromised while the student is learning. In addition to training health care professionals, surgical simulation systems are also useful for pre- and intra-operative planning of medical interventional procedures. Surgical and interventional radiology procedures often require a patient-specific plan prior to performing an operation. Thus, simulation systems which account for patient-specific

anatomical details and tissue properties may help clinicians increase accuracy of the surgical procedure and minimize patient trauma.

A fundamental, yet unanswered, research question is how much fidelity a surgical simulator needs in order to provide appropriate skill transfer to real procedures. There is some controversy over the relevance of haptic feedback and accurate tissue modeling for skill transfer, and rigorous, quantitative work needs to be done in this area [23]. In contrast, for surgical planning the required accuracy is determined by the clinical application. For example, in procedures like biopsies of the abdominal organs, breast, and lung tissue, predicting the location of the tumor as the needle penetrates the tissue is of primary importance, while reaching the target precisely in order to place radioactive seeds is paramount for procedures like prostate brachytherapy. Validation of surgical simulators is essential to motivate their application as a method for training and pre- and intra-operative planning. Validation techniques can be subjective (e.g. face and content validation) or objective (e.g. construct, concurrent, and predictive validation) [24]. If we follow the assumption that model fidelity and haptic feedback are important, then consider an approach in which we model the flow of information from the real tissue to acquired data, the model, the rendering technique, the haptic and/or visual display, and eventually the human user (Figure 1.1). We conjecture that each of these stages act as a "filter" in which information about force-motion relationships are lost or transformed. For example, the filter may be a result of the resolution of the measurement device used for gathering experimental data, the simulation model based on the constitutive law derived from experimental data, or simplification of the model required

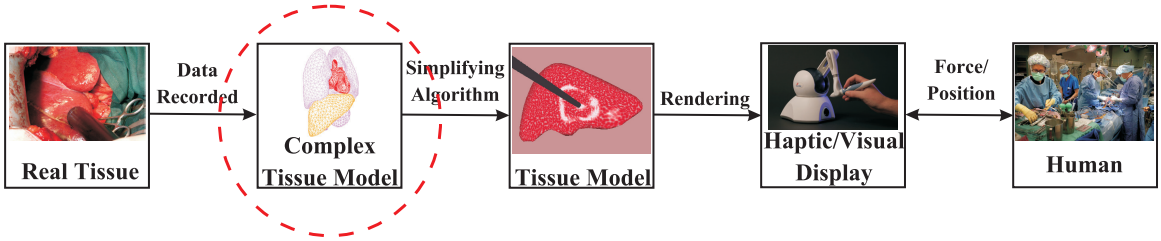

Figure 1.1: Modeling the information flow in simulator development and application. Each stage acts as a "filter" in which information about force-motion relationships is lost or transformed. This thesis specifically explores the factors important in the development of the complex tissue models (circled). *Images are obtained from [3], [4], [5], [6], and [7]. Image corresponding to [3] printed with permission from ©2007 Elsevier Ltd.*

to perform real-time haptic rendering. In addition, haptic devices have their own dynamics and are affected by control issues such as sample-and-hold and quantization. Finally, the just noticeable difference of force perception of the human plays a vital role in quantifying the necessary fidelity of the simulation.

As highlighted in Figure 1.1, the development of a high-fidelity surgical simulator involves many stages or filters. The first step is obtaining material properties of the tissues using *in vivo* experiments. This is followed by developing realistic organ models. These complex organ computational models need to be simplified such that they can be rendered in real time. This is generally done so that the models can be used to render force and/or visual information to the end user. This information is displayed to the user via haptic devices and using immersive virtual reality environments.

This thesis specifically explores the factors important in the development of the complex tissue models (circled in Figure 1.1). Some of the factors that govern the accuracy of medical intervention simulation and planning include the organ geometry, the shape and

mechanical properties of the surgical instrument interacting with the organ, the soft-tissue constitutive laws, and boundary conditions imposed by the connective tissues surrounding the organ. Understanding these factors will help researchers in making justified simplifications to complex tissue models, and as a result quantify the "filter" while going from "Complex Tissue Model" to "Tissue Model" in Figure 1.1.

This thesis is organized as follows: Chapter 2 provides an introduction to surgical simulation in the context of tool and tissue interaction models and reviews previous work done in this area. Following the literature review, the thesis focuses on the following three factors important for modeling tool and tissue interactions for surgical simulation and planning:

- The choice of soft tissue constitutive laws and comparison of linear versus nonlinear elastic tissue models for surgical simulation (Chapter 3).
- The importance of anatomical geometry and organ boundary constraints for surgical planning (Chapter 4).
- The effects of tool shape and tissue properties during path planning of invasive surgical procedures (Chapter 5).

Finally, the thesis concludes by providing directions for future research in the area of realistic modeling of tool-tissue interactions (Chapter 6).

1.1 Dissertation Contributions

The major contributions of this dissertation are:

- **Modeling and perception of linear and nonlinear elastic tissues for surgical simulation**: Primarily due to computational considerations, most previously reported surgical simulation research within the robotics and virtual reality research communities has assumed linear elastic behavior for modeling tissues, even though human soft tissues generally possess nonlinear viscoelastic properties. Hence, we quantitatively compare linear and nonlinear elasticity-based models and demonstrate the importance of appropriate selection of soft tissue constitutive laws for realistic surgical simulation where force feedback might be provided to the user. It is shown that for a nonlinear model, normal forces are developed during shearing of tissue. These forces, which are not seen in a linear elastic model, result from a phenomenon known as the Poynting effect. Using continuum mechanics, we derive analytical expressions in order to describe the Poynting effect. This is followed by experimental studies on soft tissue simulants and tissue. Psychophysical experiments were also conducted in order to quantify the role of the Poynting effect on material discrimination. This work is described in Chapter 3 and has also been published in [25–28].

- **Importance of organ geometry and boundary constraints for planning of medical interventions**: During surgical tool and tissue interactions, in addition to soft tissue constitutive laws, the shape of the organ and surrounding tissue affect the

deformation response of the organ. In this thesis, we demonstrate that, during the planning of medical interventions which are displacement-driven interventional procedures, the geometry of the organs and the surrounding boundary constraints are the most important factors influencing organ deformation. As an example, the procedure of needle insertion into the prostate is considered. Image segmentation is used to extract the anatomical details from magnetic resonance images, while object-oriented finite element analysis (OOF) software is used to generate patient-specific finite element (FE) meshes from the segmented images. Further, cohesive zone models are used simulate relative contact between the prostate and surrounding tissue. This work is described in Chapter 4 and has also been published in [29].

- **Modeling the interaction of flexible needles through soft tissue**: The shape of the surgical tool is another important factor that affects the accuracy of a medical intervention procedure, such as needle insertion. A possible method to mitigate needle targeting errors during the procedure is to robotically steer the needle to reach its intended target. In this thesis, we investigate the interaction of flexible bevel-tipped needles with soft tissue. The asymmetry of a bevel tip results in the needle naturally bending when it is inserted into soft tissue. Thus, a bevel-tipped needle can be steered by providing a series of translational and rotational inputs to reach its intended target within the body. We provide an analytical model that computes the tip loads based on the geometry of the bevel edge and tissue material properties. The analytical model explains trends observed in the experiments. We also present

a mechanics-based model that calculates the deflection of the needle embedded in an elastic medium. Confocal microscopic observations of needle-gel interactions are used to characterize the tissue cleavage process. The model design is guided by both microscopic and macroscopic observations of several needle-gel interactions. The energy-based model formulation incorporates tissue-specific parameters such as rupture toughness, nonlinear material elasticity, and interaction stiffness, and needle geometric and material properties. The tissue properties (elasticity and toughness) for both gels and soft tissue are evaluated and incorporated into the model. We also incorporate these physical parameters into an FE model that includes both contact and cohesive zone models to simulate tissue cleavage. The results of this study contribute to a mechanics-based model of robotic needle steering, extending previous work on kinematic models. This work is described in Chapter 5 and has also been published in [30–33].

Chapter 2

Literature Review: Modeling of Tool-Tissue Interactions for Computer-Based Surgical Simulation

2.1 Introduction

People have always sought ways to understand and model the structure and functions of the human body. The earliest known anatomical models used for surgical planning were recorded around 800 B.C. in India for the procedure of rhinoplasty, in which a flap of skin from the forehead is used to reconstruct a nose. These ancient Indian practitioners used leaves to represent three-dimensional (3D) flexible tissues and plan the surgical operation [34]. Before the advent of medical imaging a century ago, the only practical way to see

inside the human body was to observe an operation or by dissection. Cultural and religious beliefs, the difficulty of obtaining cadavers, and lack of refrigeration imposed restrictions on the widespread use of dissection. Frustrated by these limitations, Louis Thomas Jerôme Auzoux, a 19th century French physician, improved and popularized anatomical papier-mâché models [35]. By the early 20th century, inexpensive and realistic plastic anatomical models that could be assembled and painted became popular with training medical students. Human cadavers and animals, however, are still used for training and, in some cases, surgical planning.

In the past decade, advances in computer hardware and software, and use of high-fidelity graphics have made it possible to create simulations of medical procedures. Computer-based surgical simulation provides an efficient, safe, and ethical method for training clinicians by emphasizing the user's real-time interaction with medical instruments, surgical techniques, and realistic organ models that produce anatomically and physiologically accurate behavior. The objective is to create models that support medical practitioners by allowing them to visualize, feel, and be fully immersed in a realistic environment. This implies that the simulator must not only accurately represent the anatomical details and deformation of the organ, but also feed back realistic tool-tissue interaction forces to the user. As an example, consider the prototype hysteroscopy training simulator shown in Figure 2.1, which was developed at Eidgenössische Technische Hochschule (ETH) Zürich [8]. This surgical simulator allows real-time visualization of the surgical procedure along with force feedback to the user.

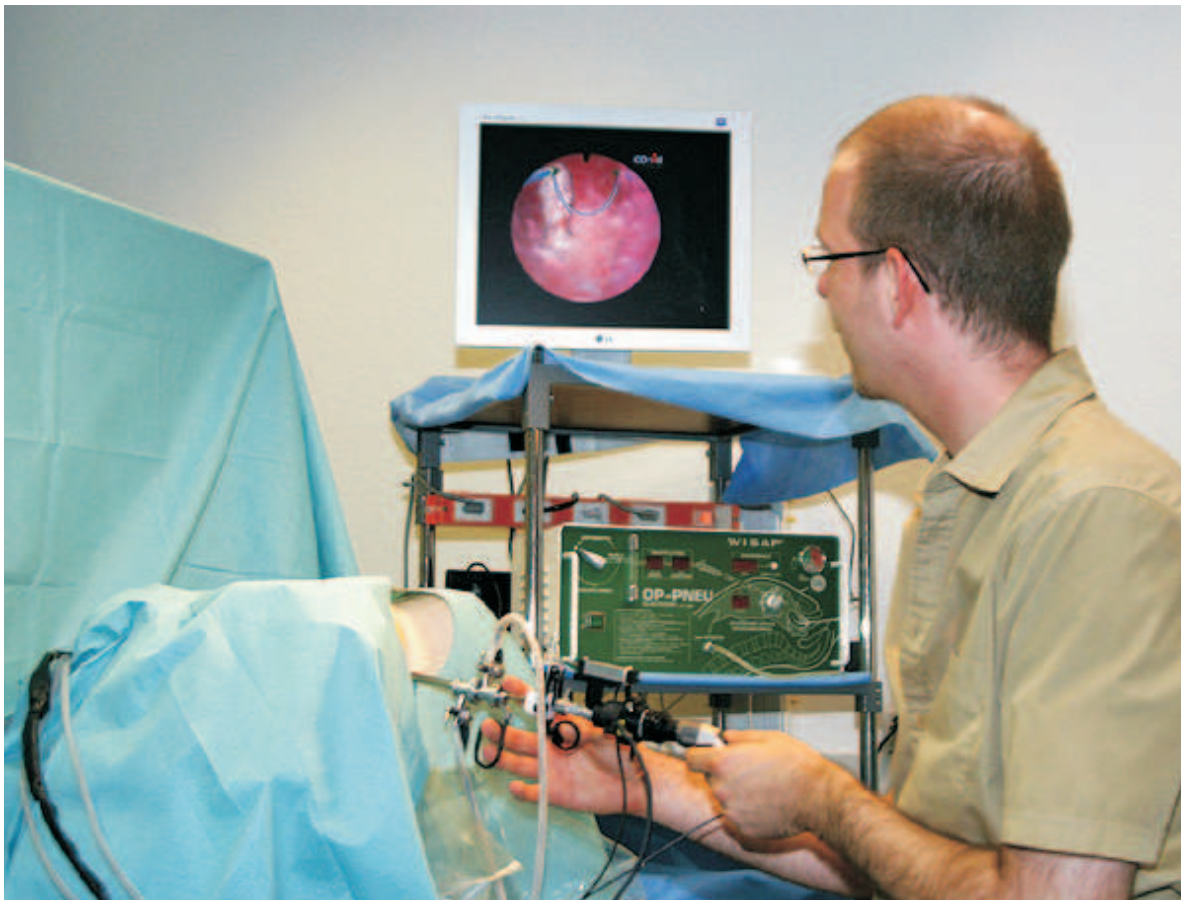

Figure 2.1: Hysteroscopy training simulation environment coupled with a haptic device [8]. *Reprinted from Studies in Health Technology and Informatics, Vol. 119, Harders et al. Highly-realistic, immersive training environment for hysteroscopy, pp. 176-181, ©(2006), with permission from IOS Press.*

The development of realistic surgical simulation systems requires accurate modeling of organs/tissues and their interactions with the surgical tools. The benefits of tissue modeling are not only useful for training, planning, and practice of surgical procedures, but also optimizing surgical tool design, creating "smart" instruments capable of assessing pathology or force-limiting novice surgeons, and understanding tissue injury mechanisms and damage thresholds. Given the complexity of human organs and the challenges of acquiring tis-

sue parameters, realistic modeling and simulation of tissue mechanics is an active research area. There is a large volume of literature on the topic of tissue modeling that is distributed across the biomechanics, robotics, and computer graphics fields. For certain topics outside the scope of this review, good references are available in the literature:

- There exists a rich literature in the biomechanics community involving the measurement of tissue properties of specific organs. In the 1970s, researchers such as Fung [10,36] and Yamada [2] applied the techniques of continuum mechanics to soft tissues and conducted extensive tests to characterize tissue properties.

- Extensive work has been done by researchers in the area of computer graphics to model and simulate deformable bodies in real time [37,38]. The present survey does not cover work in which the focus is to produce seemingly realistic visual effects while ignoring the physics underlying tissue deformation.

- Approaches for complete simulator design, specific medical applications, and training evaluation methods have also been widely studied in the last two decades [39,40].

This chapter summarizes the literature and presents a taxonomy (Table 2.1) of significant work in the field of *realistic modeling of tool-tissue interactions for simulation and robot-assisted surgery*. Since continuum mechanics provides a mathematical framework to model the deformation of biological tissues, the primary focus of this review is to compile the research done in the area of modeling and simulating surgical tool-tissue interactions in real time using the principles of continuum mechanics and FE methods, respectively. Some

Operation		**Model**			
		Linear elastic FE	Hyperelastic FE	Visco-hyperelastic FE	Other methods
Deformation (via indentation)	*Simulation only*	[41] † [46] [51] † [54] [56] [58] †	[42] [47]	[43]	LEM [44, 45] † Mass- [48–50] spring- [52, 53] damper model [55] † Walled model [57] PCMFS [59] †and PAFF [60] † BEM solution [61] † J-shaped function [62]
	Real/Phantom tissue studies	[63] † [13] [68]- viscoelastic	[64] [66] [69] [71] [73]	[14] † [70] [72] [74]	Curve-fitting [65] Green's function [67]
Rupture (via needle insertion)	*Simulation only*	[75]	[76]		Spring model [77] Volume model [78] † 3D chain mail [79] †
	Real/Phantom tissue studies	[80] [82] † [84]			Resistive- [81] † force model [83] † Curve-fitting [85] Friction model [86]
Cutting (via blade/scissors)	*Simulation only*	[87] † [89]	[16]		Hybrid model [88]
	Real/Phantom tissue studies	[90]			Fracture [91] † Haptic Scissors [92] †

Table 2.1: Survey of tool-tissue interaction models for surgical simulation and robot-assisted surgery. Within each category, authors are listed alphabetically and simulators that provide haptic feedback are designated by †.

other methods that could be used to simulate physically realistic tool-tissue interactions are also discussed.

This chapter is organized as follows. Section 2.2 summarizes the basic concepts and theories of linear and nonlinear elasticity, and Section 2.3 provides an overview of the FE modeling technique. Sections 2.4 and 2.5 classify the prior research work that has been done in modeling non-invasive and invasive surgical tool-tissue interactions, respectively. Realistic tool-tissue interaction models requires populating models with accurate material properties; Section 2.6 provides a summary of some of the methods for acquiring tissue properties. Section 2.7 lists some of the commercially available surgical simulators. This chapter concludes with Section 2.8, which describes some important directions for research in the area of realistic modeling of tool-tissue interactions.

2.2 Continuum Mechanics for Tissue Modeling

The study of deformation or motion of a continuous material under the action of forces is known as continuum mechanics. The objective of this section is to provide a brief introduction to the mechanics of soft tissues using the theories of linear and nonlinear elasticity.

The field equations of continuum mechanics are normally formulated using tensors. An overview of tensor analysis is beyond the scope of this chapter, but [93] provides a good introduction to this subject and its application to continuum mechanics. Tensor notations and manipulations consistent with the mechanics literature are used in the derivations in

this thesis, e.g., bold face characters signify tensors, matrices, and vectors, while normal face characters are scalar quantities.

2.2.1 Kinematics of Continua

Consider a body undergoing deformation so that material points initially at $\mathbf{x}$ are mapped to spatial locations, $\mathbf{y}$. Then the deformation gradient tensor, $\mathbf{F}$, is defined by

$$\mathbf{F} = \nabla \mathbf{y}, \tag{2.1}$$

where ∇ is the gradient operator with respect to $\mathbf{x}$. If the displacement is $\mathbf{u}$, then $\mathbf{y} = \mathbf{x} + \mathbf{u}$. Thus,

$$\mathbf{F} = \mathbf{I} + \nabla \mathbf{u}, \tag{2.2}$$

where $\mathbf{I}$ is the identity tensor. A useful measure of strain is the Green strain tensor, $\mathbf{E}$, defined by

$$\mathbf{E} = \frac{1}{2}\left(\mathbf{F}^T\mathbf{F} - \mathbf{I}\right). \tag{2.3}$$

Substituting (2.2) in (2.3) results in

$$\mathbf{E} = \frac{1}{2}\left(\nabla \mathbf{u} + \nabla \mathbf{u}^T + \nabla \mathbf{u}^T \nabla \mathbf{u}\right). \tag{2.4}$$

In linear elasticity theory, strains are assumed to be small ($|\nabla \mathbf{u}| \ll 1$), hence,

$$\mathbf{E} \cong \varepsilon := \frac{1}{2}\left(\nabla \mathbf{u} + \nabla \mathbf{u}^T\right), \tag{2.5}$$

where ε is the infinitesimal strain tensor. Thus, linear elasticity theory is valid only for small strains (1%-2%). One of the fundamental drawbacks of using a linear elasticity formulation to describe soft tissues is that surgically relevant strains often significantly exceed the small strain limit, invalidating the assumption of linearity. However, linear elasticity is still used in many simulation applications due to analytical simplicity and computational efficiency, and so it is described next.

2.2.2 Linear Elasticity

Linear elastic modeling of soft tissues is the most widely used approach within the robotics and haptics community. Materials exhibiting linear elasticity obey the generalized Hooke's Law, which relates the stresses, $\boldsymbol{\sigma}$, and infinitesimal strains, ε, by the fourth-order tensor of elastic moduli, $\tilde{\mathbf{C}}$, as

$$\boldsymbol{\sigma} = \tilde{\mathbf{C}} : \varepsilon. \tag{2.6}$$

where : denotes double contraction. $\boldsymbol{\sigma}$ is also known as the Cauchy stress tensor and (2.6) could be rewritten as

$$\sigma_{ij} = \sum_{m=1}^{3}\sum_{n=1}^{3} \tilde{C}_{ijmn}\varepsilon_{mn}, \tag{2.7}$$

where $\tilde{C}_{ijmn}$ are the components of the fourth-order tensor, $\tilde{\mathbf{C}}$, with 81 constants, which are specific to the material. The subscript indices represent the components of the stress and strain tensor. Symmetry of the stress and strain tensors leads to $\tilde{C}_{ijmn} = \tilde{C}_{jimn}$ and $\tilde{C}_{ijmn} = \tilde{C}_{ijnm}$, and the postulated existence of a strain energy density leads to $\tilde{C}_{ijmn} = \tilde{C}_{mnij}$. Thus, $\tilde{C}_{ijmn}$ has 21 independent constants (called moduli) for a fully anisotropic material, i.e. a material whose properties change with direction.

If the assumption is made that the material is isotropic, then the material properties can be described by just 2 independent parameters: Young's modulus, E, and Poisson's ratio, ν. The Cauchy stress tensor and the infinitesimal strain tensor given in component form, are related by

$$\varepsilon_{ij} = \frac{1+\nu}{E}\sigma_{ij} - \frac{\nu}{E}\sigma_{kk}\delta_{ij}, \tag{2.8}$$

where δ_{ij} is the Kronecker delta. Alternatively, the Cauchy stress tensor can be compactly written as

$$\sigma_{ij} = \lambda\varepsilon_{kk}\delta_{ij} + 2\tilde{G}\varepsilon_{ij} \tag{2.9}$$

where λ and $\tilde{G}$ are Lamé moduli. λ and $\tilde{G}$ and related to E and ν as follows:

$$\lambda = \frac{E\nu}{(1+\nu)(1-2\nu)}, \tag{2.10}$$

$$\tilde{G} = \frac{E}{2(1+\nu)}. \tag{2.11}$$

In the vast majority of surveyed literature (the research cited under "Linear elastic FE" in

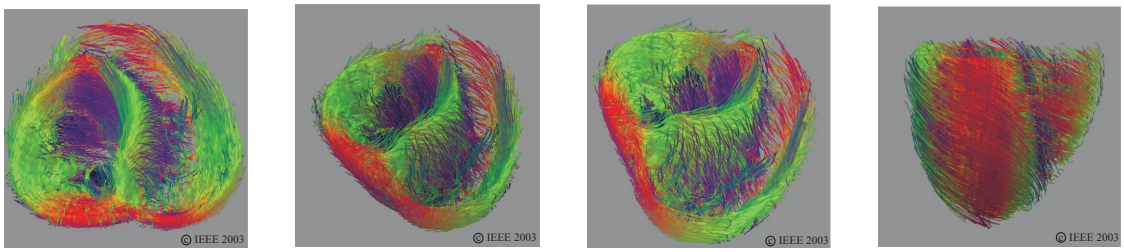

(a) (b) (c) (d)

Figure 2.2: Tissue fiber orientation of the heart on the inside surface, (a) and (b), and outside surface, (c) and (d), constructed using diffusion tensor imaging (Zhukov and Barr [9]). *Images are printed with permission from IEEE ©2003.*

Table 2.1), E and ν are the two parameters used to describe the soft tissue properties. Most biological materials are, however, intrinsically anisotropic. Figure 2.2 depicts the orientation of muscle fibers in the heart [9]. For example, a soft tissue containing fibers aligned along an axis will have different properties along and transverse to that axis. A summary of such anisotropies is presented in [94]. The nonlinear elastic behavior of myocardial tissue and its application to surgical simulation is highlighted in [25, 26].

2.2.3 Linear Viscoelasticity

Most soft tissues are inherently viscoelastic – they have a response that changes with time because of structural relaxations. Viscoelastic materials exhibit properties of both elastic solids and viscous fluids. Like linear elastic materials, linear viscoelastic materials retain the linear relationship between stress and strain, but the effective moduli depend on time. For small strains, the general linear viscoelastic constitutive equations can be derived by separating the stresses and strains into the hydrostatic (superscript H) and deviatoric

(superscript D) components:

$$\boldsymbol{\sigma} = \boldsymbol{\sigma}^H + \boldsymbol{\sigma}^D, \tag{2.12}$$

$$\varepsilon = \varepsilon^H + \varepsilon^D. \tag{2.13}$$

Hydrostatic stresses/strains act to change the volume of the material, but maintain shape, while deviatoric or shear stresses/strains are those that distort the shape, but preserve volume (in isotropic and linear elastic materials). The hydrostatic stresses and strains are related by

$$\boldsymbol{\sigma}^H = 3K\varepsilon^H. \tag{2.14}$$

For most materials, the bulk modulus, $K = \frac{E}{3(1-2\nu)}$, has little variation with time as compared to the shear modulus. Thus, K considered to be independent of time. The deviatoric stresses and strains can be related by

$$\sum_{i=0}^{N} p_i \frac{\partial^i \boldsymbol{\sigma}^D}{\partial t^i} = \sum_{j=0}^{M} q_j \frac{\partial^j \varepsilon^D}{\partial t^j}, \tag{2.15}$$

where p_i and q_j are material constants. In (2.15), the indices N and M depend on the number of material constants required to have good fit with the experimental results.

Two characteristic behaviors specific to viscoelastic materials are creep and stress relaxation. Creep occurs when a constant stress applied to the material results in increasing strain. On the other hand, stress relaxation occurs when a material is under constant strain

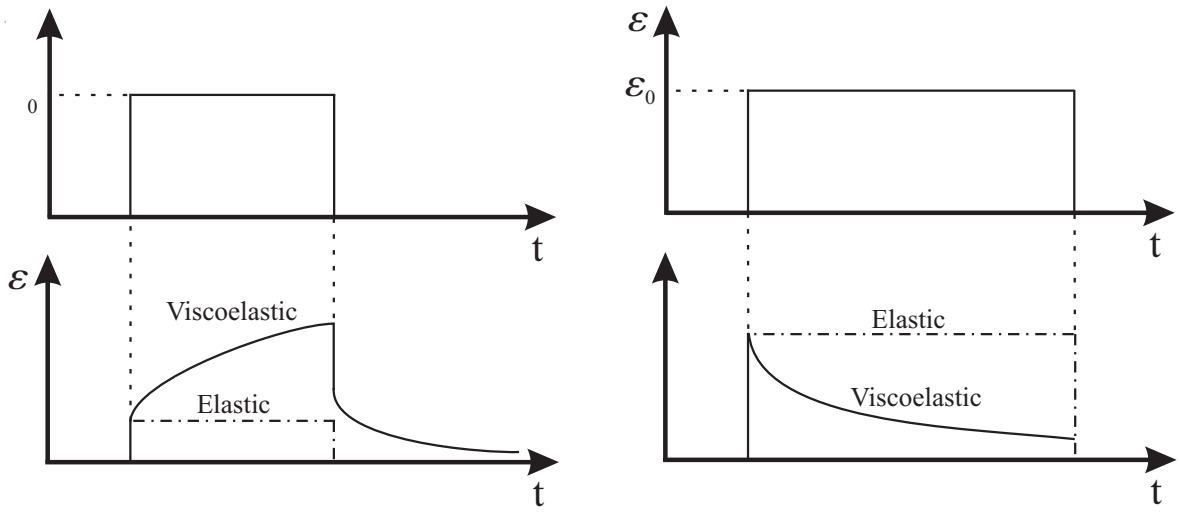

Figure 2.3: Examples of characteristic properties of viscoelastic materials: (a) Creep and creep recovery - a constant applied shear stress σ_0 results in an increase in shear strain. (b) Stress relaxation - a constant applied shear strain ε_0 results in a decrease in shear stress until it reaches a steady state value.

but the stress decreases until it reaches some steady-state value. Figures 2.3(a) and (b) depict the behaviors of creep and stress relaxation, respectively. The one-dimensional (1D) models of creep deformation and stress relaxation are

$$\varepsilon(t) = \sigma_0 J(t), \tag{2.16}$$

$$\sigma(t) = \varepsilon_0 G(t), \tag{2.17}$$

where $J(t)$ is a material property called the "creep compliance" for constant stress, σ_0, and $G(t)$ is a material property called the "stress relaxation modulus" for constant strain, ε_0. The creep compliance and relaxation modulus are empirically determined and describe the creep and stress relaxation behavior of the viscoelastic material as a function of time.

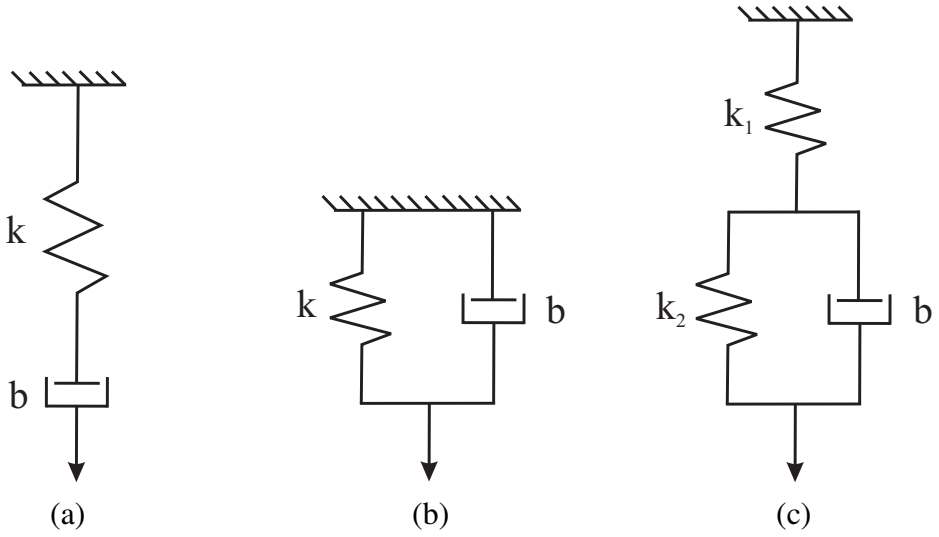

Figure 2.4: Standard viscoelastic models commonly used to represent soft tissues where k, k_1, and k_2 represent the spring stiffness, and b is the damping coefficient of the dashpot: (a) Maxwell. (b) Kelvin-Voigt (or Voigt). (c) Zener standard linear solid (or Kelvin) [10].

In many cases, viscoelastic properties of soft tissues are represented by rheological models, which are obtained by connecting springs (elastic elements) and dashpots (viscous elements) in serial or parallel combinations [10]. Three simple material models used to represent solids are the Maxwell, Kelvin-Voigt (or Voigt), and Zener standard linear solid (or Kelvin) models shown in Figures 2.4(a), (b), and (c), respectively.

The Maxwell model predicts the relaxation behavior for soft solids accurately. This model postulates that for creep conditions, the strain will increase linearly with time. But for soft solids like polymers, the strain rate is observed to be decreasing with time. The creep compliance and stress relaxation modulus for the Maxwell model are given by

$$J(t) = \frac{1}{k} + \frac{t}{b}, \tag{2.18}$$

$$G(t) = ke^{-\frac{k}{b}t}, \tag{2.19}$$

where t is time. The Voigt model provides a satisfactory first-order approximation of creep, but is an inadequate model for stress relaxation. For the Voigt model, the governing equation is that of an elastic material, so there is no relaxation of stress, hence, the creep compliance is given by

$$J(t) = \frac{1}{k}\left(1 - e^{-\frac{k}{b}t}\right). \tag{2.20}$$

The Zener standard linear solid model provides a good qualitative description of both creep and stress relaxation. The creep compliance and relaxation modulus are given by

$$J(t) = \frac{1}{k_1} + \frac{1}{k_2}\left(1 - e^{-\frac{k_2}{b}t}\right), \tag{2.21}$$

$$G(t) = \frac{k_1}{k_1 + k_2}\left(k_2 + k_1 e^{-\frac{(k_1+k_2)}{b}t}\right). \tag{2.22}$$

2.2.4 Nonlinear Elasticity

Elastic materials undergoing deformations with large strains (>1%-2%) are described by nonlinear elasticity theory. In order to model biological tissues, it is common to use hyperelasticity and visco-hyperelasticity [10]. A hyperelastic material is characterized by the existence of a strain energy density function, $W(\mathbf{F})$. The stress in the material as a result

of deformation can be obtained from

$$\mathbf{P} = \frac{\partial W(\mathbf{F})}{\partial \mathbf{F}}, \tag{2.23}$$

where $\mathbf{P}$ is the first Piola-Kirchhoff stress tensor and $\mathbf{F}$ is the previously defined deformation gradient tensor. The Cauchy stress tensor and first Piola-Kirchhoff stress tensor are related by

$$\mathbf{P}\mathbf{F}^T = J\boldsymbol{\sigma}, \tag{2.24}$$

where $J = \det(\mathbf{F})$. There are several formulations for the strain energy density function, e.g. St. Venant-Kirchhoff, Blatz-Ko, Ogden, Mooney-Rivlin, and Neo-Hookean models [93]. Ogden and Mooney-Rivlin strain energy density formulations provide a fairly accurately representation of the constitutive laws for many biological tissues [95]. In an Ogden model, the strain energy density function for an isotropic material is given in terms of the principal stretches, λ_i, as

$$W = \sum_{k=1}^{N} \frac{\mu_k}{\alpha_k} \left(\lambda_1^{\alpha_k} + \lambda_2^{\alpha_k} + \lambda_3^{\alpha_k} - 3 \right), \tag{2.25}$$

where $\lambda_1\lambda_2\lambda_3 = 1$, i.e. thermal incompressibility, and μ_k and α_k are material parameters determined from experiments. The Mooney-Rivlin model, commonly used to represent rubber-like materials, is widely used for soft tissues and is given in terms of the principal invariants, I_i, for isotropic and incompressible materials as

$$W = C_1 (I_1 - 3) + C_2 (I_2 - 3), \tag{2.26}$$

where C_1 and C_2 are material constants. The principal invariants are defined in terms of right Cauchy-Green tensor, $\mathbf{C} = \mathbf{F}^T\mathbf{F}$, as

$$I_1 = \mathbf{C} : \mathbf{I}, \tag{2.27}$$

$$I_2 = \frac{1}{2}\left((\mathbf{C} : \mathbf{I})^2 - (\mathbf{C} : \mathbf{C})\right), \tag{2.28}$$

$$I_3 = \det\ (\mathbf{C}). \tag{2.29}$$

Some researchers have used the Neo-Hookean model to represent soft tissues. The Neo-Hookean strain energy density function is a special case of the Mooney-Rivlin model and is given by

$$W = C_{10}(I_1 - 3), \tag{2.30}$$

where C_{10} is the material constant. If material parameter constants for Ogden or Mooney-Rivlin models are defined in terms of creep and stress relaxation functions, then the material can be modeled as visco-hyperelastic, which may realistically represent the behavior of many soft tissues [10].

2.3 Finite Element Modeling

The FE method is a numerical technique for solving field equations, typically partial differential equations, and has been used in the last decade to simulate soft tissue defor-

mation by solving the equations of continuum mechanics. The method originated from the need to find approximate solutions to complex problems in elasticity and vibration analysis [96]. Over the years, the FE method has spread to applications in many different areas of engineering, including structural analysis in civil and aeronautical engineering, thermal analysis, and biomechanics. Numerous FE computer programs are commercially available for general or specific applications. These include ABAQUS [97], ADINA [98], ANSYS [99], DYNA3D [100], FEMLAB [101], GT STRUDL [102], NX I-deas [103], and NASTRAN [104]. This section provides a very high-level overview of the FE method; there are numerous textbooks that deal with this subject, e.g. [96], [105], and [106].

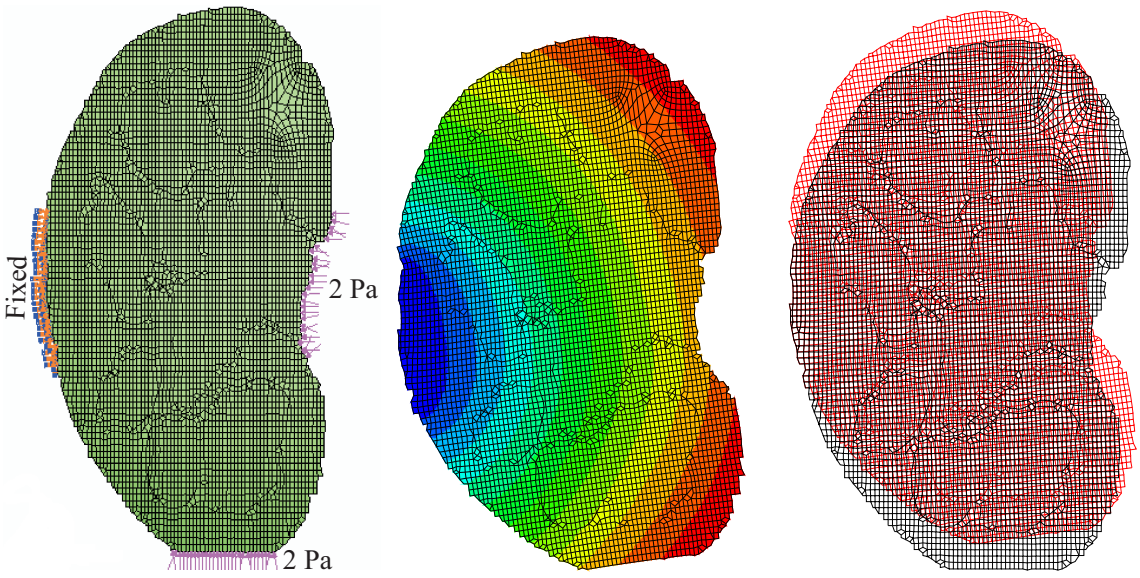

Figure 2.5: Two-dimensional ABAQUS simulation results for soft tissue deformation of the human kidney that incorporates a hyperelastic constitutive model (Mooney-Rivlin model: $C_{10} = 682.31$ Pa and $C_{01} = 700.02$ Pa [11]) and the left side boundary nodes are fixed, while loads (2 Pa) are applied at the bottom and right edge nodes. (a) Undeformed mesh. (b) Contour plot of displacements. (c) Undeformed mesh is black and deformed mesh is red.

In the FE method, the continuum is divided or meshed into a finite number of sub-regions called *elements*, such as tetrahedrons, quadrilaterals, etc. Two adjacent elements are connected via *nodes*. The elastic behavior of each element is categorized using matrices in terms of the element's material and geometric properties, and distribution of loading within the element and at the nodes of the element. Linear or quadratic *shape* or *interpolation functions* are used to approximate the behavior of the field variables at the node. The element behavior is characterized by partial differential equations governing the motion of material points of a continuum, resulting in the following discrete system of differential equations:

$$\mathbf{M}\ddot{\mathbf{u}} + \mathbf{C}\dot{\mathbf{u}} + \mathbf{K}\mathbf{u} = \mathbf{F} - \mathbf{R}, \tag{2.31}$$

where $\mathbf{M}$, $\mathbf{C}$, and $\mathbf{K}$ are the element mass, damping, and stiffness matrices, respectively. $\mathbf{u}$ is the vector of nodal displacements, and $\mathbf{F}$ and $\mathbf{R}$ are the external and internal node force vectors, respectively. All these matrices and vectors may be time dependent. One approach to solve (2.31) in a quasi-static manner is by setting $\dot{\mathbf{u}} = \ddot{\mathbf{u}} = 0$. Thus, with every simulation iteration, a large number of element-stiffness and element-force vectors are assembled, which leads to a system of algebraic equations, called the global system. The accuracy and numerical efficiency of the FE method lies largely in the development of effective pre- and post-processors, and algorithms for efficiently solving large systems of equations. On the other hand, (2.31) can be solved with a dynamic approach, using implicit or explicit integration schemes. For explicit integration methods, the state at a given instant is a function of the previous states, while for the implicit scheme, the state

at a certain instant cannot be explicitly expressed as a function of the state at the previous time step. The implicit scheme involves inversion of the stiffness matrix at each time step, typically a computationally expensive process. The explicit scheme can be easily implemented, avoiding the matrix inversion process, but potentially requires very small time steps to provide a suitably accurate and stable solution. Properly designed implicit methods can be numerically stable over a wide range of integration time step values. Hence, they are preferable for simulation of systems described with stiff and nonlinear differential equations.

In recent years, FE methods have been applied to simulate the responses of tissues and organs (Figure 2.5). Biological tissues are anisotropic, inhomogeneous, undergo large strains, and have nonlinear constitutive laws; FE techniques present an attractive method to numerically solve such complex problems. However, most commercial FE codes are optimized for linear elastic problems. The number of nonlinear elastic material models available in most codes is quite limited and are sensitive to small variations in material properties. In general, the finer the mesh in an FE model, the more accurate the simulation. But a greater number of elements leads to larger computational time, which hampers the ability of surgical simulators to run in real time. The speed of the simulation may depend on the constitutive law used, the material parameters chosen, and the scale of the deformation. Further, it is difficult to obtain the material properties of an inhomogeneous and anisotropic organ, which limits the accuracy of results obtained from an FE model. Finally, organs have anatomically complex geometries and boundary conditions which are difficult to model.

Despite these limitations and challenges, the FE technique remains the most widely used numerical method for realistic modeling of surgical tool-tissue interactions.

2.4 Non-Invasive Tool-Tissue Interaction Modeling

Having described the fundamental mechanics and simulation techniques required for realistic soft tissue modeling, we now begin the literature survey. We classify surgical tasks that do not involve tissue rupture as non-invasive tasks. Several modeling methods have been considered in the literature for modeling local and global tool-tissue interactions. Some studies have also investigated the effect of the tool geometry on interaction forces. Figures 2.6(a), (b), (c), and (d) provide some examples of the tools used to measure tool-material interaction forces [12]. It was observed that changes in tool geometry caused variations in the force-deflection responses only for large localized deformations of the material.

Most of the research presented in this section considered either distributed uniaxial compressive loads or loads exerted by indentors, without focusing on the tool geometry. For the purpose of building models for surgical simulators, this section categorizes the various non-invasive tissue modeling techniques as linear elasticity-based and nonlinear (hyperelastic) elasticity-based FE methods, and other methods which do not fall into the

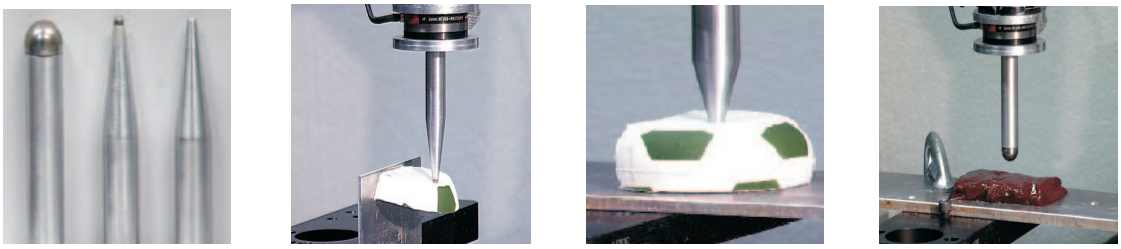

(a) (b) (c) (d)

Figure 2.6: (a) Tools tested and measuring tool-material interaction forces during (b) and (c) deformation of rubber (d) deformation of bovine liver (Mahvash et al. [12]). *Images printed with permission from publisher (EuroHaptics 2002).*

realm of continuum mechanics and/or do not use FE methods for simulation.

2.4.1 Linear Elastic Finite Element Models

Linear elasticity-based FE models are probably the most widely used techniques to model tissue deformation in surgical simulators. Motivating factors include simplicity of implementation and computational efficiency, which enables real-time haptic rendering, since only two material constants are needed to describe isotropic and homogenous materials. This section describes the modeling of tool-tissue interactions using linear elasticity-based FE methods.

In general, due to the steps involved in setting-up and running a FE calculation, linear or nonlinear elasticity-based FE models cannot be simulated in real time. Hence, some researchers have focused their efforts on optimizing FE-based computational techniques to be applicable to surgical simulators. Bro-Nielsen [46] was one of the first researchers to apply the condensation method to an FE model for real-time surgical simulations. This method

is based on the idea that only displacement of nodes that are in the vicinity of the tool need to be rendered. It was shown that nodal displacements resulting from this method are similar to those obtained from conventional linear FE analysis. Comparison studies were performed on an FE model of the human leg having 700 nodes. Tensile and compressive loads were applied to 3 nodes on the calf area of the leg while one edge of the leg was fixed. Cotin et al. [51] created real-time heptatic (liver) surgery simulations using a modified FE method wherein the bulk of the computations were performed during the pre-processing stage of the FE calculation. Using data from computed tomography (CT) scans, they also built a 3D anatomical model of the liver and used linear elasticity-based modeling to simulate its deformation. Basdogan et al. [41] and Kühnapfel et al. [58], used linear elastic theory to develop simulators for laparoscopic cholecystectomy (gallbladder removal) and endoscopic surgical training, respectively. In order to enable real-time visual and haptic simulation, [41] only considered the significant vibration modes to compute tissue deformation, while [58] implemented the condensation method. An example of a non-real-time surgical simulation system using linear FE modeling is that of Gladilin et al. [56], who used a conventional linear FE model to simulate tissue deformations for craniofacial surgery.

The models discussed above typically used assumed material properties, and were not validated by comparing them with experimental results. Some researchers, however, have attempted to develop their linear elastic FE models based on experimental studies conducted on phantom or real tissue. Since non-invasive tool-tissue interaction modeling is a subset of the invasive surgical procedures, researchers such as DiMaio and Salcud-

ean [15], and a few others presented in Table 2.1 (under invasive surgical procedures) first performed indentation or other non-invasive measurements to characterize the tissue properties. Gosline et al. [63] developed a FE simulation model and coupled it to the haptic device used by DiMaio and Salcudean [107]. In [63], the authors used a linear elasticity-based FE model to simulate organs filled with fluid. Simulations were compared with experimental studies done on phantom tissue with a fluid pocket. The phantom tissue was deformed with a known load, while the fluid pocket was imaged using ultrasound and the surface of the tissue was tracked using a digitizing pen. Kerdok et al. [13] devised a method to measure the accuracy of soft tissue models, by comparing experimental studies against FE models. They built the "Truth Cube" (Figure 2.7(a)), which was a silicone cube embedded with fiducials having Young's modulus of 15 kPa. They found good agreement between the experimental and simulation results for small strains (1%-2%), where linear elasticity theory is valid. As expected, the linear elasticity-based FE method did not compare well against the experimental results for large strains. Figure 2.7(b) depicts the CT image for a large strain indentation case. The results from the imaging studies were compared to the FE model, shown in Figure 2.7(c). Sedef et al. [68] used a linear viscoelastic model where the material properties, time constants for the relaxation function, and normalized values of shear moduli were derived from indentation experiments performed *in vivo* on porcine liver.

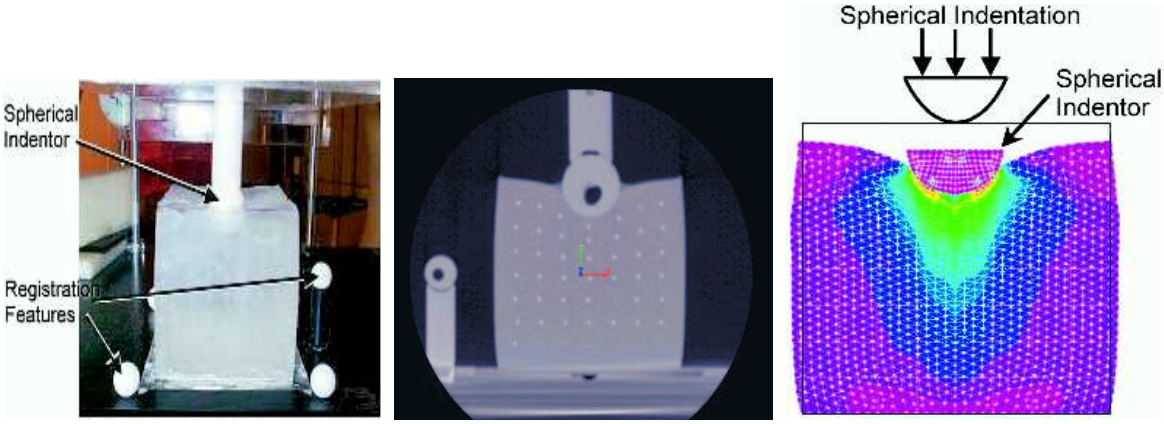

(a) (b) (c)

Figure 2.7: Indentation test on the "Truth Cube" embedded with fiducials (Kerdok et al. [13]). (a) Experimental test setup. (b) CT of center vertical slice under 22% strain. (c) FE model under 22% strain. *Images printed with permission from Elsevier B.V. ©2003.*

2.4.2 Hyperelastic Finite Element Models

Soft tissues undergo large deformations during surgical procedures. The study of non-linear solid mechanics, specifically hyperelasticity, provides a framework for analyzing such problems. The key to studying large deformation problems is the identification of an appropriate strain energy function. Once the strain energy function is known, the constitutive stress-strain relationships can be derived. A vast majority of the strain energy functions used for biological soft tissues are adapted from those used to model polymers and rubber-like materials. The Arruda-Boyce model [108], which is based on statistical mechanics and is normally used to model rubber, has been used to simulate palpation of breast tissues in [42]. Wu et al. [47] implemented the widely used Mooney-Rivlin model to simulate tissue deformation in the training simulator developed by Tendick et al. [109]. They introduced the concept of dynamic progressive meshing to enable real-time compu-

tation of deformation.

In order to develop the best possible constitutive model and add greater realism to the tissue model, several researchers have used experimental data and elaborate setups to populate the coefficients of the strain energy function. Carter et al. [64] conducted several indentation tests on sheep and pig liver, pig spleen *ex vivo*, and human liver *in vivo* for the intended development of a laparoscopic surgical simulator. An exponential relationship that relates the stress to the stretch ratio, developed by [36], was used to fit the experimental data. Davies et al. [69] conducted large and small probe indentation experiments on unperfused and perfused pig spleen for potential use in surgical simulators. The experimental data were fitted with hyperelastic models of Neo-Hookean, Mooney-Rivlin, and exponential forms. The goal of their study was to underscore the fact that experimental studies are required to build realistic tool-tissue interaction models, and the hyperelastic model of exponential form is suitable for modeling pig spleen. Both Hu and Desai [71] and Chui et al. [66] based their model on results obtained from pig liver. In [71], the authors compared results obtained from Mooney-Rivlin and Ogden models, while [66] considered several strain energy functions that were combinations of polynomial, exponential, and logarithmic forms. Chui et al. [66] concluded that both the Mooney-Rivlin model with nine material constants and the combined strain energy of polynomial and logarithmic form with three material constants were able to fit the experimental data. The lowest root mean square error of 29.78 ± 17.67 Pa was observed between analytical and experimental results for the tension experiments where the maximum stresses were in the order of 3.5 kPa.

Molinari et al. [73] present a model of the scalp skin to be used by plastic surgeons for pre-operative planning. The authors assumed a strain energy function of polynomial form with four parameters dependent on the skin tissue. The maximum nodal displacement between the simulated and experimental results was observed to be 0.45 mm for load cases ranging from 5 N to 50 N.

2.4.3 Visco-Hyperelastic Finite Element Models

Real soft tissues exhibit both viscoelastic and nonlinear elastic properties. Thus, the coupling of viscoelastic and hyperelastic modeling techniques results in a more realistic representation of soft tissues. Puso and Weiss [43] were the first to implement an anisotropic visco-hyperelastic FE model for soft tissue simulations and applied this technique to model the femur-medial collateral ligament-tibia complex. In order to model the quasi-linear viscoelastic behavior, the authors used an exponential relaxation function. This was coupled with the Mooney-Rivlin model to represent hyperelasticity of the tissue. Though simulation data were not compared with real tissue data and this work does not represent a surgical tool-tissue interaction model, it provides an elegant FE modeling framework for modeling soft tissues.

An endoscopic surgical simulator developed at ETH Zürich is one of the few complete systems that incorporates continuum mechanics-based tool-tissue interaction modeling techniques, and provides realistic visualization and haptic feedback in real time [14]. This simulator is the culmination of many years of work and taps into the expertise of sev-

eral engineering disciplines [14, 17, 110]. Székely et al. [14] built a very detailed anatomical model of the uterus to be simulated, followed by the development of a 3D homogenous isotropic FE model of the organ and populated it with real tissue material properties. Further, they designed parallel computing capability for the simulator to function in real time and integrated a custom-built force feedback device that would enable simulation of hysteroscopy. The authors used a novel tissue aspiration method to capture the force-displacement relationship of the uterine tissue *in vivo*. The authors considered a hyperelastic model [14] with five material constants and a visco-hyperelastic model [17] with two material constants and two constants due to the stress relaxation function. Nava et al. [72] used the tissue aspiration method of [17] on bovine liver and focused on modeling the preconditioning phase of soft tissue. The authors believe that the preconditioning phase provides information on the capabilities of the tissue to adapt to load and to recover its original configuration when unloaded during surgical tool and tissue interactions. A reduced polynomial form of the strain energy function was used to model hyperelasticity. Thirteen material constants relating to the visco-hyperelastic model were deemed sufficient to match the experimental data. Figures 2.8(a) and (b) depict the FE model and tool-tissue interaction presented in [14], respectively.

A few other researchers have also used visco-hyperelastic models to simulate soft tissue behavior, though their studies are not as detailed as the work presented in [14]. Work in accurate fitting of hyper-viscoelastic constitutive models to real tissue data is presented below. Both Kim et al. [74] and Kim and Srinivasan [11] used data from indentation experiments

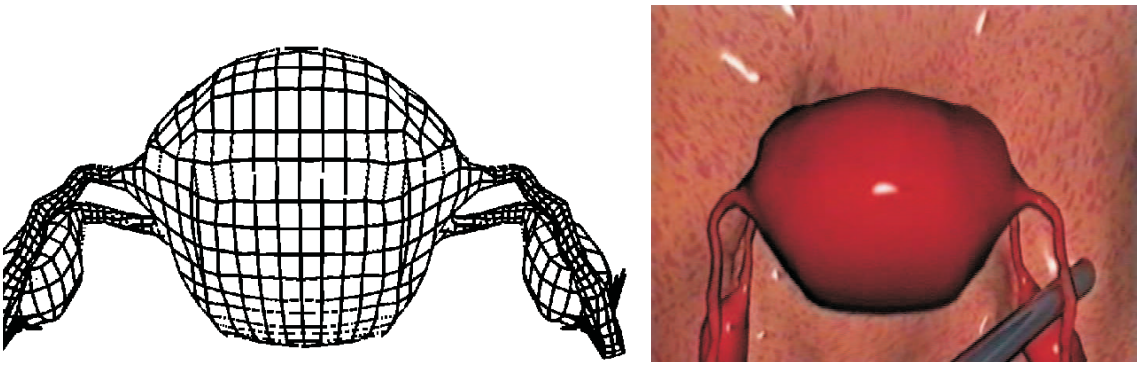

(a) (b)

Figure 2.8: Formulation and results of the endoscopic simulator: (a) FE model of the human uterus containing 2000 elements. (b) Tool-tissue interaction model used in the surgical simulator (Székely et al. [14]). *Images printed with permission from MIT Press Journals ©2000 by the Massachusetts Institute of Technology.*

on porcine esophagus, liver, and kidney. They fit a Blatz-Ko form strain energy function to force-displacement data obtained from quasi-static experiments, while both linear (Kelvin) and nonlinear viscoelastic models were used to fit force-time data from dynamic experiments [74]. A Mooney-Rivlin model was used in [11]. The nonlinear viscoelastic model consisted of several nonlinear springs and dampers in parallel, and was able to match the stress relaxation curves derived from dynamic experiments. Miller [70] and Miller and Chinzei [111] presented a visco-hyperelastic model to simulate the tissue response of pig brain to external loads. In [70], biphasic (a mixture of a solid deformable porous matrix and a penetrating fluid) and single phase models were evaluated, and the single phase model showed good correlation with the experimental data for up to $\sim$30% strains. The visco-hyperelastic models considered were in terms of strain invariants and fractional powers of principal stretches in [70] and [111], respectively. Both models had two independent material parameters and one parameter relating to the stress relaxation function. In [70],

theoretical results were also compared with published *in vivo* stress-strain data for Rhesus monkey liver and kidney. Real-time implementation of the simulation models has not been shown.

2.4.4 Other Modeling Methods

The primary motivation for choosing a tissue modeling technique that is not based on linear elasticity or hyperelasticity-based FE methods is to generate a computationally efficient simulation model. These specialized models are designed for straightforward implementation and could be used for static and dynamic computation, as described in Section 2.3. The realism of tissue deformation can be compromised as a result of such modeling simplicities since it is difficult to relate fundamental tissue properties to these models.

Mass-spring-damper models are the most common non-continuum mechanics-based technique used for modeling soft tissues. Organs have been modeled by combining the spring-damper models, described in Section 2.2.3, in series or parallel combination. In this case, a set of points are linked by springs and dampers, and the masses are lumped at the nodal points. [48], [49], [50], [52], and [53] are some of the studies that have used mass-spring-damper models to simulate tissue deformation, but they do not provide any information on the tissue properties required for the simulation. On the other hand, [55] used a sophisticated apparatus for data acquisition to enable virtual ultrasound display of the human thigh while providing force feedback to the user. The model for the human

thigh was composed of a mass-spring system whose physical parameters were based on an earlier study conducted by authors [112]. The two-layer model was composed of a mesh of masses and linear springs, and a set of nonlinear springs orthogonal to the surface mesh to model volumetric effects. The novelty of this research was that in order to provide real-time haptic feedback to the user, the authors incorporated a buffer model between the physical model and haptic device. This computationally simple model locally simulates the physical model and can estimate contact forces at haptic update rates. The buffer model was defined by a set of parameters and was continuously adapted in order to fit the values provided by the physical model.

In addition to continuum mechanics and FE methods, other innovative approaches have been developed to achieve real-time performance. In order to ease the computation burden caused by using FE-based modeling techniques, without resorting to non-physical methods such as mass-spring-damper models, researchers have tried to implement models with two-dimensional (2D) distributed elements filled with an incompressible fluid. Such models are known as Long Element Models (LEM) and the advantage of this method is that the number of the elements is one order of magnitude less than in a FE method based on tetrahedral or cubic elements. Balaniuk and Salisbury [44] presented the concept of LEM to simulate deformable bodies. Their approach implements a static solution for linear elastic global deformation of objects based on Pascal's principle and volume conservation. Using this method, it is possible to incorporate physically-based simulation of complex deformable bodes, multi-modal interactivity, stable haptic interface, changes in topology, and increased

graphic rendering, all done in real time. The use of static equations instead of partial differential equations avoids problems concerning numerical integration, ensuring stability during simulation. Sundaraj et al. [45] used the concept of LEM to simulate palpation of the human thigh with a probe, where the average linear elastic material constant was derived from experimental studies. Sagar et al. [62] presented a detailed and complete training system for ophthalmological applications. Their micro-surgical training system included a teleoperated device for the user to interact with the virtual model eye, a high-fidelity 3D anatomical model of the eye, and a FE model of the cornea. Modeling of the collagen fibers in the cornea was done using nonlinear elastic J-shaped uniaxial constitutive laws. Simulation tests concluded that the virtual environment was able to provide graphics in real time. Similar to all the studies mentioned in this section, no comparisons have been made between simulation results and actual tissue deformations during micro-surgery in the eye. In essence, [62] used a FE technique for simulation, but the soft tissues were not modeled using linear or hyperelastic models, and hence this work fits in this section.

FE modeling methods can be extremely sensitive to mesh resolution, and so in the last decade technologies have been developed to avoid using meshes altogether. Such meshless, particle, or finite point methods share the characteristic that there is no need to explicitly provide the connectivity information between the nodes. De et al. [59] described a meshless technique for modeling tool-tissue interactions during minimally invasive surgery. They call this method the Point Collocation-based Method of Finite Spheres (PCMFS), wherein computational particles are scattered on a domain which are linked to a node. Approxima-

tion functions are defined on each particle and are used to solve the differential equations based on linear elasticity. The PCFMS proved to be computationally superior than commercially available FE packages, and performed simulations in real time. The authors are currently extending PCFMS to include nonlinear elastic properties of tissues and future work would enable users to simulate tissue cutting. The work presented in [59] is based on continuum mechanics but does not use FE techniques for simulation; hence, it is included in this section. In [60], the authors extended the concept of PCMFS to Point-Associated Finite Field Approach (PAFF), where points are used as computational primitives and are connected by elastic force fields. PAFF also assumes linear elasticity for modeling soft tissues. De and Srinivasan [57] presented an innovative method to model soft tissue by modeling organs as thin-walled membranes structures filled with fluid. Using this technique, it was possible to model experimental data obtained *in vivo*, though the authors did not provide information on the simulation input parameters.

In order to add realism to their simulation models, some researchers have performed experimental studies to populate their models with material parameters. Hu and Desai [65] described a hybrid viscoelastic model to fit the experimental results obtained during indentation experiments on pig liver. The hybrid model uses linear and quadratic expressions to relate the measured force-displacement values, which are valid for small strains (up to 16% compression) and large strains (from 16% - 50% compression), respectively. The model used by the authors represents the local surface deformation of liver. James and Pai [61] have achieved real-time interaction by using boundary element models. If the

geometry, homogeneous material properties, and boundary conditions of the model are known, then reasonable graphical update rates are achievable by precomputing the discrete Green's functions of the boundary value problem. A force interpolation scheme was used to approximate forces in between time steps which allowed for a higher haptic update rate than the visual update rate. Inhomogeneous materials cannot be supported by the boundary element analysis technique, which is a disadvantage in applications for surgical simulation. Lang et al. [67] used the Green's functions matrix for linear elastic deformation. The estimation of the Green's function matrix was based on local deformations while probing an anatomical soft-wrist model and plush toy. The global deformations were based on the range-flow on the object's surface. Simulation and experimental results have not been compared.

2.5 Invasive Tool-Tissue Interaction Modeling

Almost all surgical procedures involve tissue rupture and damage, usually by cutting with scissors, a blade, or procedures such as electro-cautery, and during operations involving needle insertion. Hence, realistic modeling and simulation of cutting and needle insertion is probably the most important requirement for a surgical simulator. Further, complex but common procedures such as suturing could be extrapolated from the techniques developed for modeling cutting and needle insertion. Modeling and simulation of invasive procedures involves constantly changing boundary constraints and accurate modeling of

friction, which are difficult to measure. Accurate models of friction become especially important when simulating minimally invasive surgical procedures, in which the surgeon has no direct contact with the tissue, but manipulates the tissue via laparoscopic instruments. In this case, not only must sliding friction between the instruments and the organs be accounted for, but friction in the trocar and hinges must be modeled. Organs are connected to bones, muscles, and/or other organs via connective tissue. Hence, modeling of these connective tissues is also essential to simulate accurate response of the organ for both non-invasive and invasive procedures. Similar to modeling of non-invasive surgical procedures, linear elasticity-based FE models have been the most prevalent technique for simulating invasive operations. Very few studies have invoked nonlinear elasticity-based FE methods. Some modeling techniques that are not based on continuum mechanics are also described in this section.

2.5.1 Finite Element Methods for Invasive Surgical Simulation

As mentioned earlier, the ability to model the response of soft tissue during needle insertion and/or cutting is of primary importance in the development of realistic surgical simulators. Modeling and simulation of invasive tissue deformation in a FE framework is significantly more challenging than non-invasive modeling primarily due to two factors. First, it is difficult to measure the fracture toughness of inhomogeneous soft tissues to

accurately model the rupture process. Second, invasive surgical simulation involves breaking and remeshing of nodes, which is computationally expensive for reliable simulation. Nonetheless, simulation of needle insertion through soft tissue is an active research area because of applications in minimally invasive percutaneous procedures like biopsies and brachytherapy. Research in needle insertion has examined the following topics: modeling and simulation of needle-tissue interaction forces, tissue deformation, deflection of the needle during insertion, path-planning of needle trajectories based on tissue deformation, and devising experimental setups for robot-assisted needle insertion. Also, modeling of surgical cutting has focused on using single blade scalpels or surgical scissors to model the resulting soft tissue deformation. In this section we focus on recent studies of modeling tool-tissue interaction forces and tissue response during invasive procedures using FE methods, while in Section 2.5.2 we highlight methods not based on continuum mechanics.

2.5.1.1 Linear Elastic Simulations

Tissue and needle interactions have been studied by the robotics community primarily for path planning of surgical procedures. DiMaio and Salcudean [82] were the first to develop an interactive linear elastic FE simulation model for needle insertions in a planar environment. The simulated needle forces matched experimental data using a phantom tissue of known material properties and achieved real-time haptic refresh rates by using the condensation technique [46] during pre-processing. Tissue modeling techniques have also been implemented in steering of needles by Alterovitz et al. [75, 113] and DiMaio

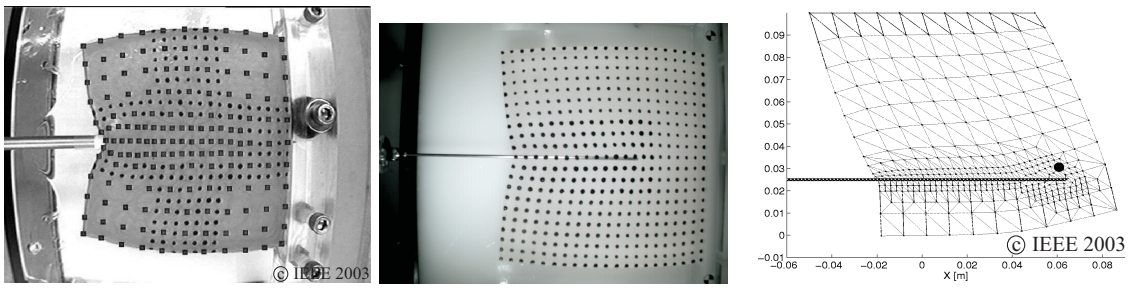

(a) (b) (c)

Figure 2.9: Needle insertion and simulation modeling: (a) Probing for estimation of material properties of phantom tissue. (b) 17 gauge epidural needle inserted into phantom tissue while motion of markers and insertion forces are recorded. (c) FE simulation of needle insertion with small target embedded within elastic tissue (DiMaio and Salcudean [15]). *Images printed with permission from ©IEEE 2003.*

and Salcudean [114]. Further, Goksel et al. [115] extended the work done by DiMaio and Salcudean [15] to integrate needle insertion simulations in 3D models. Figures 2.9(a), (b), and (c), depict the experimental and simulation work done in [15].

A 2D linear FE model for needle insertion during prostate brachytherapy is presented in [75]. The authors fine-tuned the simulation parameters to prostate deformation results obtained from a surgical procedure, but did not independently compare their model to data obtained by needle insertion with real or phantom tissues. Their results indicate that seed placement error depends on parameters such as needle friction, sharpness, and velocity, rather than patient specific parameters (tissue stiffness and compressibility). Crouch et al. [80] used experiments and FE modeling to show that a linear elastic tissue model in conjunction with a dynamic force function could accurately model interaction forces and tissue deformation during needle insertion. They used a phantom tissue model with known material properties and concluded that the accuracy of the model diminished during the

relaxation phase, because soft tissue is viscoelastic. Hing et al. [84] captured the different phases of interaction between needle and pig liver. Using experimental data, the authors estimated the linear effective modulus of the tissue sample during puncture at various speeds.

Cutting is the most common invasive surgical procedure, and this operation has been modeled by some researchers using linear elastic FE models [87, 89]. Picinbono et al. [87] discussed the software for a prototype laparoscopic surgical simulator which used linear extrapolation over time and position of the interaction forces to render haptic feedback to the user. Wu and Heng [89] presented a hybrid condensed FE model, which consisted of operational and non-operational regions. The authors assumed that topological changes only occur in the operational part. The algorithm proved to be computationally efficient, but for both studies [87, 89], no comparison between simulated and experimental results were presented. Chanthasopeephan et al. [90] computed the local effective Young's modulus of pig liver during cutting experiments. Different values of the effective modulus were obtained for plane strain, plane stress, and quasi-static models, and there was a decrease in liver resistance as the cutting speed increased.

2.5.1.2 Hyperelastic Simulations

Due to the computational burden of using FE methods for modeling invasive surgical procedures coupled with the difficulty in characterizing the nonlinear behavior of real tissues during rupture, very few studies have implemented hyperelastic models. Nienhuys and van der Stappen [76] used a compressible Neo-Hookean material model for simulating

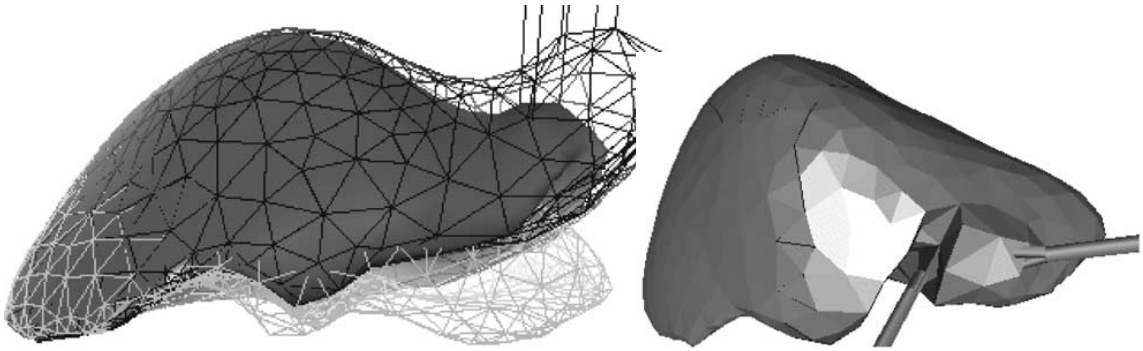

(a) (b)

Figure 2.10: Results from work presented by Picinbono et al. [16]: (a) Comparison between linear (wireframe) versus nonlinear (solid) elasticity-based models for same force applied to right lobe of the liver; the linear model undergoes large unrealistic deformation. (b) Simulating hepatic resection using a nonlinear anisotropic model. *Images printed with permission from Elsevier Science (USA) ©2003.*

needle insertion in a 3D organ model. The study was purely based on simulations, and no comparisons between real and simulation data were provided. To date, only one study by Picinbono et al. [16] has implemented a nonlinear anisotropic model to simulate cutting of liver (hepatic resection). The anisotropic framework is similar to the study done in [87], and this work was extended to include hyperelasticty based on the St. Venant-Kirchhoff model. Figure 2.10(a) depicts the difference in deformation between the linear and nonlinear elasticity-based models, while Figure 2.10(b) provides a screenshot simulating electro-cautery of the liver. No validation or comparison of the simulation model was presented.

2.5.2 Other Methods

As discussed earlier, modeling and simulation of invasive procedures requires modification of organ topology with time. Using FE methods is generally computationally expensive, hence, several studies have looked at alternative modeling methods. These are presented in this section. The objective of Glozman and Shoham [77] was to formulate path planning algorithms for flexible needles. Virtual springs were placed orthogonal to the needle insertion axis in order to model the needle-tissue interaction force. They did not mention the stiffness of the springs used in the simulations, but the authors claim they can be determined experimentally or from pre-operative images. In order to compute soft tissue deformations while simulating prostate brachytherapy, Wang and Fenster [79] used a restricted 3D ChainMail method. In the ChainMail formulation, each volume element is linked to its six nearest neighboring elements in the front, back, top, bottom, left, and right. When any of the elements is displaced beyond its defined limit (constraint zone), the neighboring element absorbs the movement due to the flexibility of the structure. The authors proposed a restricted ChainMail method by constraining the angular component of the shear constraint. The 3D prostate image was segmented based on the restricted ChainMail method. Since soft tissue deformation was not based on actual deflection data of the prostate, although the simulations could be performed in real time and were visually pleasing, one cannot be certain of the realism of the simulated tissue deformation. Kyung et al. [78] developed a simulator for spine needle biopsy using a voxel-based haptic rendering scheme. A 3D human anatomical model was generated by segmenting images derived from

CT scans or magnetic resonance imaging (MRI). The organs modeled in the region of the lumbar vertebra were bones, lung, esophagus, arteries, skin, muscle, kidney, fat, and veins. The soft tissues were modeled as a series of springs, which is not realistic. The spring stiffness was determined using needle force and insertion depth obtained from experimental results in a previously conducted study [116]. The skin deformation and puncture forces were modeled as a nonlinear viscoelatic model. The simulated forces were calculated from interactions between volume image data and the pose of the needle.

In addition to developing efficient algorithms to simulate tissue rupture, the research presented below also included experimental studies to populate the models with realistic tissue data. Brett et al. [81] described the design of a surgical needle resistance force simulator for the purpose of training and improving skills required for epidural procedures. The tissue model was composed of a Voigt mass-spring-damper model. The skin, muscular and ligmental tissues, connective tissue and fascia, and fat were modeled as nonlinear viscoelatic solid, elastic membrane, and viscous solid, respectively. The material parameters were based by fine tuning the results obtained from porcine samples and cadavers. A similar modeling technique was used by Brett et al. [83], in combination with an elaborate laser-based spectroscopy technique for determining tissue type and measuring tissue deformation. Brouwer et al. [85] fitted an exponential relationship between the applied force and the stretch ratio, which were derived from experimental data on various porcine abdominal organs. Measurements were performed both *in vivo* and *ex vivo* during needle insertion and cutting tasks in order to develop a web database of tool-tissue interaction models. The

objective of the work done by Okamura et al. [86] was to model the forces during needle insertion into soft tissue. Experimental studies were conducted *ex vivo* on bovine liver, with intended applications for liver biopsy or ablation. They divided the forces during needle insertion into forces during initial puncture, due to friction, and during cutting. The forces during initial puncture were modeled as a nonlinear spring. The spring constants were obtained by curve fitting the experimental data and wide variation in data was observed for these constants. A Karnopp friction model that includes both the static and dynamic friction coefficients was used to model the friction during needle insertion. Finally, the cutting forces were obtained by subtracting the puncture and friction force from the total measured force.

A clever modeling technique would incorporate realistic tool-tissue interactions from FE models and computational efficiency from mass-spring models. Such a hybrid model was presented by Cotin et al. [88] to simulate soft tissue deformation and cutting. The quasi-static linear elastic FE model introduced by the authors was computationally efficient but did not allow topological changes to the model. On the other hand, the mass-spring model could simulate tearing and cutting in real time, but was not visually appealing. So the authors combined the above models, such that the small region of tool-tissue interaction was composed of a mass-spring model, while the major part of the organ underwent deformation based on the linear elastic FE model. Simulation results showed that this hybrid method was computationally efficient. However, it is very difficult to relate mass-spring parameters to actual material parameters.

All the previously mentioned models in this section have focused on global deformation of tissue during interaction with a surgical tool, while the local tool-tissue interaction is simulated as a remeshing problem ignoring the energetics of cutting. In the studies presented below, the researchers investigated and modeled local tissue damage. Mahvash and Hayward [91] attempted to model cutting of soft tissues using the fracture mechanics approach. The process of cutting was divided into three subtasks: deformation, cutting, and rupture, where energy exchange occurs. In the formulation, [91] used fracture toughness to describe the material property. Experimental tests were conducted on potato sample and bovine liver. In order to match experimental results with software simulation results, the authors manually adjusted the material parameters to get the best match. Further, for the experimental studies on liver, the authors were unable to predict the different phases of fracture. Okamura et al. [92] presented the "Haptic Scissors", a two-degree of freedom device that provides the sensation of cutting in virtual environments by providing force feedback. In this study, they discussed an analytical framework to model tissue cutting, and showed via experimental studies that the users could not differentiate between the analytical model and haptic recordings created earlier. The analytical model was a combination of friction, assumed material properties, and user motion to determine cutting forces. This simplified model did not take into account the material variations in biological tissues. The forces felt by the user at the handle were assumed to be a summation of forces from friction at the scissor pivot and scissor blades, and the cutting force. The data from the analytical model did not match experimental data because the user grip force, inhomogeneous tissue

properties, and elastic forces in the tissue were not modeled. Mahvash and Okamura [117] and Mahvash et al. [118] applied the framework developed in [91] to the "Haptic Scissors". A physically valid model will require a hyperelastic model to describe the global surgical tool-tissue interactions, while local interactions will be governed by fracture mechanics.

2.6 Methods for Model Acquisition

The importance of having accurate tissue models has been recognized as a key requirement for realistic and practical surgical simulators. This section presents of some of the current experimental techniques for extracting tissue properties both *in vivo* and *ex vivo*, and using invasive and non-invasive methods. Broadly, there exist two approaches to acquire tissue properties for building surgical simulators: global and local measurement. The choice of measurement is dictated by the intended surgical simulation procedure and in turn results in the type of experimental setup developed. The design of the apparatus used is based on the organ's structure and composition, boundary conditions, and how the organ is to be loaded in order to extract force-displacement readings.

The most prevalent form of measuring local material properties of tissues involves indentation, uniaxial compression/tension, and/or shear experiments performed *ex vivo* on a tissue sample. The applied force and tissue displacement are recorded and a constitutive law or force-displacement relation that best fits the experimental results is determined. Most of this research uses phantom or *ex vivo* tissues, although *in vivo* tissues may have

significantly different dynamics due to variations in temperature, surrounding and internal blood circulation, and complex boundary constraints, which are almost impossible to replicate during *ex vivo* testing. Hence, some researchers have used elaborate schemes to perfuse the organ *ex vivo*, so as to not compromise the tissue properties that are observed *in vivo* [119]. On the other hand, some researchers have developed novel devices to measure tissue properties *in vivo* [17, 120]. Brown et al. [120] presented the "modified surgical graspers", while Vuskovic et al. [17] proposed the "tissue aspiration technique", as shown in Figure 2.11(a). Brouwer et al. [85] described instrumentation to measure the soft tissue-tool forces and tissue deflection, both *in vivo* and *ex vivo*. The following tests were performed in a pig's abdominal cavity: grasping the pig intestine wall in the longitudinal and transverse directions, indentation, needle insertion during suturing, and cutting using scissors. Further, Ottensmeyer [18] described the TeMPeST 1-D (1-axis Tissue Material Property Sampling Tool), as shown in Figure 2.11(b), which can be used to measure linear viscoelastic properties of soft tissue *in vivo*. TeMPeST 1-D is inserted laproscopically into the pig, and a waveform is commanded to the instrument. Data sampling takes approximately 20 seconds. Such localized measurement of tissue properties only provides information about a specific region of the organ, and for the purposes of modeling, local properties are usually assumed to describe the behavior of the complete organ. But as mentioned earlier, human organs are anisotropic and inhomogeneous, and in some cases tissue properties vary significantly from one location to another for the same organ. Further, with localized measurement and modeling techniques, it is not possible to account for the organ

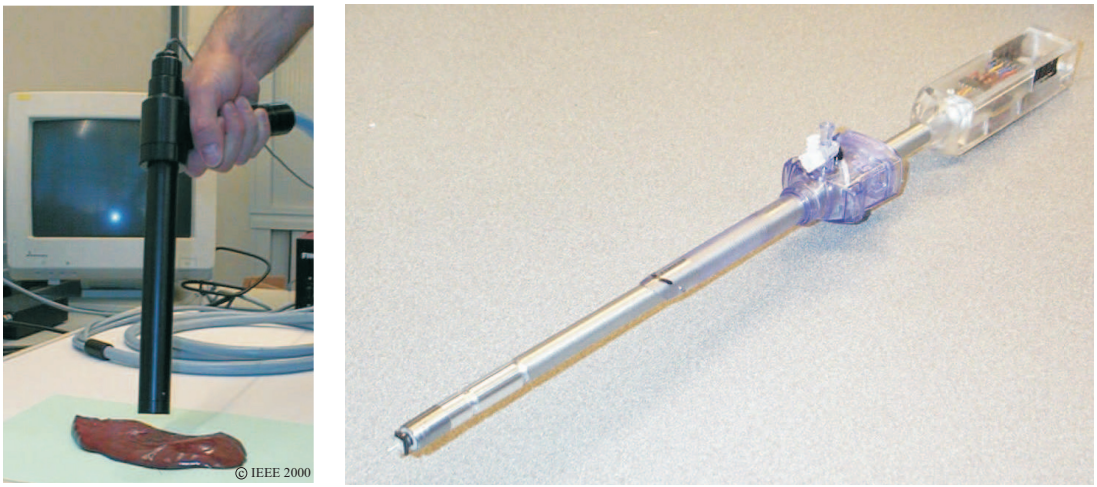

(a) (b)

Figure 2.11: Devices used to measure tissue properties *in vivo*: (a) Tissue aspiration technique (Vuskovic et al. [17]). *Image printed with permission from ©IEEE 2000.* (b) TeMPeST 1-D with 12 mm surgical port (Ottensmeyer [18]). *Image printed with permission from Wiley-Blackwell Publishing Ltd.*

geometry and complex boundary conditions.

In light of the shortcomings mentioned above, some researchers have focused on assessing the global deformation of tissues to applied loads. These techniques have typically involved placing fiducial markers on the top of the tissue sample [15] or embedding markers [13, 80, 84] within the tissue sample. As shown in Figures 2.9(a) and (b), DiMaio and Salcudean [15] first performed indentation, followed by needle insertion experiments on the phantom tissue, and captured global tissue deformation using cameras. The displacements of the markers were tracked using computer vision algorithms. A CT scanner and dual C-arm fluoroscopes were used to calculate the dislocation of the fiducial markers in [13] and [84], respectively. The main limitation of this technique is that, placing markers on

organs (either *in vivo* or *ex vivo*) is not practical. This is because use of markers in live organs might change the organ material properties and could possibly damage the organ. As opposed to using markers, Lau et al. [121] implemented an algorithm to compute the surface geometry of beating pig heart in real time using the image intensity data. Other novel techniques that do not use markers to visualize the dynamic response of organs *in vivo* include attaching an ultrasound probe to the end of a robotically controlled laparoscopic tool [122] and using an air pressure and strobe system to provide an image of the deformed tissue in real time [123]. Leven et al. [122] tested their system on liver, while [123] had designed their device to detect tumors in lungs. The technologies presented in [121], [122], and [123] could be extended to measure tissue properties of organs *in vivo*.

As an alternative to the aforementioned global measurement techniques, elastography or elasticity imaging is a quantitative technique to map internal tissue elasticity. This is extremely useful in the interpretation of image data for physical modeling process. Several elastography techniques have been developed using imaging modalities such as ultrasound, CT, MRI, and optics, employing different tissue excitations, and extracting various parameters that provide a measure of tissue displacement [124]. Depending on the method of tissue deformation and parameters that are imaged, different terms are used to describe the images obtained, including strain, stress, velocity, amplitude, phase, vibration, compression, quasistatic, and functional images [125]. The underlying method for estimation of tissue properties is that the organ or tissue is loaded with an indentor and then, using imaging, it is possible to visualize the internal strain in the tissues [126, 127]. One of

the fundamental deficiencies in using elastography for modeling tissues is that it is currently only possible to obtain Young's modulus and Poisson's ratio for the tissue, which are characteristics of linear elasticity. Turgay et al. [128] presented two methods to extract homogenous and inhomogeneous tissue properties while vibrating the tissue at a spectrum of frequencies and using an ultrasound probe to capture the tissue motion. They proposed two methods: modeling the tissues as a mass-spring-damper model and determining the transfer function from the tissue motion at two separate locations. The methods were able to determine the tissue properties for the homogenous tissue sample and only the middle layer of a inhomogeneous (layered) tissue sample.

As a result of the difficulties in measuring tissue properties *in vivo* with previously described methods, recent studies have also investigated methods for online estimation of local tissue properties during teleoperated surgical procedures. Most of the research done in this area is a subset of the work in environment property estimation during telemanipulation. Duchemin et al. [129] used a hybrid force/position controller for robotic telesurgery in skin harvesting procedures. With appropriate choice of gains, their controller estimated skin stiffness, friction, and thickness. Alternatively, De Gersem et al. [130] used a Kalman filtering technique to estimate the stiffness of soft materials during telemanipulation. Misra and Okamura [131] proposed an indirect adaptive estimation algorithm for estimating tissue properties while palpating the tissue, while Yamamoto et al. [132] presented a recursive least squares technique. Details of the work developed in [131] are given in Appendix A. With all these online estimation methods, the challenges associated with local and global

measurement of tissue properties still exist.

2.7 Commercial Surgical Simulators

In addition to the published research on modeling tool-tissue interactions summarized in Table 2.1, there exist numerous commercial surgical simulators designed for the purpose of training clinicians. The methods employed by the companies for tissue modeling is not readily available, and there is extensive emphasis on producing models that are visually appealing. Further, in most commercially available simulators, tissue material parameters are tweaked based on qualitative evaluation performed by a few surgeons, rather than actual material testing.

Surgical simulators with force feedback provide an immersive environment for training, and many commercially available simulators provide haptic feedback to the user. Reachin Technologies AB [133] markets a simulator to train for cholecystectomy performed via laparoscopic surgery. In order to train surgeons for endoscopic, endourological, percutaneous access, and laparoscopic surgery, and for interventional endovascular procedures, Simbionix USA Corp. [134] sells GI Mentor II^{TM}, URO Mentor^{TM}, PERC Mentor^{TM}, LAP Mentor^{TM}, and ANGIO Mentor^{TM}, respectively. Immersion Medical [135] has developed numerous surgical simulation systems. The training simulators include, CathSim® AccuTouch® (for vascular access and phlebotomy), Endoscopy AccuTouch® (for bronchoscopy and gastro-intestinal procedures), Endovascu-

lar AccuTouch® (for percutaneous transluminal angioplasty and stenting procedures), Hysteroscopy AccuTouch® (for myomectomy and basic hysteroscopy skills), and Laparoscopy AccuTouch® (for laparoscopic abdominal procedures). Surgical Science Ltd. [136] developed the LapSim system to train for abdominal keyhole surgery. ProMIS^{TM}, developed by Haptica Inc. [137], is used to train for minimally invasive surgery techniques, while Mimic Technologies Inc. [138] provides custom devices and software for the surgical simulation industry. Mentice AB [139] has the Procedicus VIST^{TM} (Vascular Intervention System Trainer), Procedicus VA^{TM} (Virtual Arthroscopy), and Procedicus MIST^{TM} (Minimally Invasive System Trainer), which are used for training in procedures, such as, cardiac catheterisation, shoulder and knee surgery, and laparoscopic cholecystectomy, respectively. Of these, only the Procedicus VA^{TM} and Procedicus MIST^{TM} do not provide force feedback to the user.

There exist several other commercially available surgical simulators that do not provide haptic feedback, but instead focus on training basic surgical skills (SurgicalSIM) or provide superior visualization capabilities (EYESI®). SurgicalSIM, developed by Medical Educational Technologies Inc. [140], is used to train for general surgical tasks on anatomically accurate models based on patient's gender, size, and age. EYESI®, developed by VRmagic GmbH [141], is an ophthalmosurgical simulator that simulates stereo vision through the surgical microscope and allow tracking of tool motion. In addition to commercially available surgical simulators, research centers such as the Stanford University Medical Media and Information Technology [142] develop simulators for hospitals, and the Center for

Integration of Medicine and Innovative Technology [143] and the National Capital Area Medical Simulation Center [144] develop simulation technologies, primarily for defense-related medical treatments.

2.8 Discussion

This review chapter provides an introduction to soft tissue modeling, with emphasis on the relevant continuum mechanics fundamentals and research to model surgical tool and tissue interactions for the purpose of building surgical simulators. We broadly split surgical tasks into non-invasive and invasive categories, and further divided the modeling techniques based on linear elasticity theory, nonlinear elasticity theory, and other methods. We also emphasized the use of accurate organ models by presenting some of the current methods to acquire realistic tissue properties via experiments. Our emphasis was on modeling methods that employed principles of continuum mechanics and used FE methods for simulation. A synopsis of the surveyed literature is provided in Table 2.1, and some of the commercially available surgical simulators are described in Section 2.7.

Based on our literature search, we observed that many researchers have done work in the area of modeling tool-tissue interactions using linear elasticity-based FE methods. However, few studies have been published using the more realistic nonlinear elasticity methods to model invasive tool-tissue interactions. Significant contributions have also been made using other non-standard modeling approaches. Such methods are primarily

employed to enable simulations to run in real time, and in many cases accurate physics behind tissue deformation is not deemed a priority. It is still an open research question whether continuum mechanics-based FE approaches, meshless techniques, non-physics-based methods, or some combination of these is the best method for simulating surgical tool and tissue interactions in real time. The constant challenge is to develop models that can appropriately and accurately describe the behavior of organs, yet are computationally efficient. Further, as seen in Table 2.1, physics-based modeling of invasive surgical procedures is still an open research area. Limited work has been done to understand and model the interaction of surgical tools as tissue ruptures.

On the basis of our literature survey, this thesis investigates the following three aspects related to the modeling of tool and soft tissue interactions with applications to surgical simulators and planners:

1. Quantitatively demonstrate the differences between linear and nonlinear elasticity-based models (Chapter 3).

2. Highlight the importance of using patient-specific organ geometry and boundary conditions for surgical planning (Chapter 4).

3. Investigate and model the invasive surgical procedure of needle insertion into soft tissue. We looked at the specific case of robotically steered flexible bevel-tipped needles as they interact with soft tissue and studied the effect of needle shape on surgical planning (Chapter 5).

CHAPTER 2. LITERATURE REVIEW

We begin by quantitatively comparing linear and nonlinear elasticity-based soft tissue constitutive laws, and their application to surgical simulation systems.

Chapter 3

Modeling and Perception of Linear and Nonlinear Elastic Tissues for Surgical Simulation

3.1 Introduction

Surgical simulation systems are an attractive option for surgical training, practice, and both pre- and intra-operative planning. In addition, such simulators help in optimizing surgical tool design and understanding tissue injury mechanisms and damage thresholds. These systems allow real-time visualization of a surgical procedure and, in some cases, provide force feedback to the user. As an example, Figure 3.1 shows a hysteroscopy training

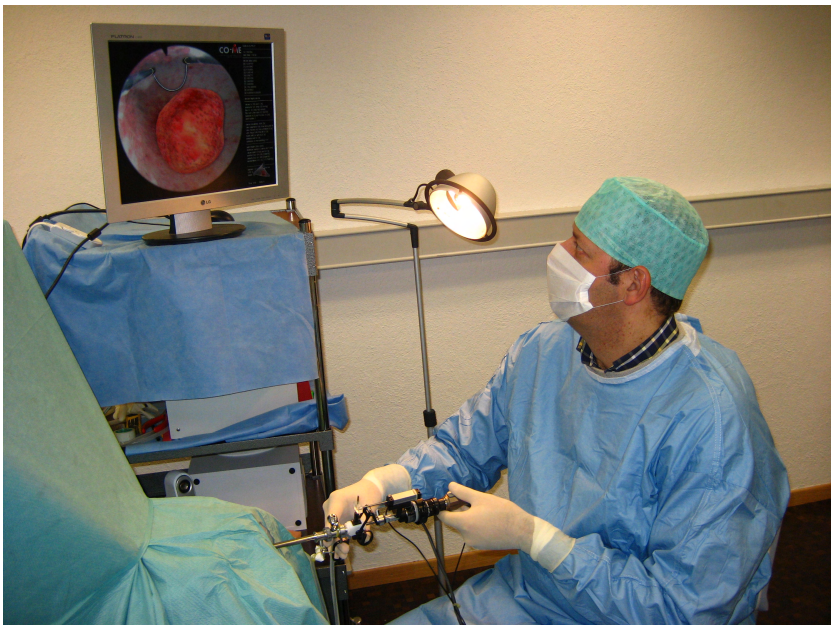

Figure 3.1: Hysteroscopy training simulation environment coupled with a haptic device [19].

simulator that was developed at ETH Zürich and includes haptic feedback [19].

The development of realistic simulation systems that provide appropriate haptic feedback requires accurate modeling of soft tissues and their interaction with surgical tools. Human organs in general are inhomogeneous and anisotropic, and exhibit nonlinear viscoelastic properties [10]. Due to limits in computation speed and memory, simplified models such as mass-spring-damper or linear elastic models [37] are frequently used to describe tissues for simulating surgical procedures. Such models are only accurate for materials undergoing small strains, while most surgical procedures involve organs being subjected to large strains. The theory of nonlinear elasticity (hyperelastic models) better describes many human tissues undergoing large strains.

In this chapter, we examine the role of the Poynting effect in modeling tissue deforma-

tion, especially in haptic rendering. The Poynting effect describes the interaction of both shear (tangential) and normal forces during tissue shearing. This chapter consists of three parts: first, theoretical analysis of nonlinear elastic tissue models in order to highlight the Poynting effect; second, experimental studies to demonstrate the presence of the Poynting effect; and third, quantification of the role of the Poynting effect in material discrimination using psychophysical experiments. The Poynting effect is relevant to nonlinear elastic tissue models, but not to linear models. Our work provides a quantitative measure of how tissue modeling techniques relate to human perception of surgical simulators [25–27].

The experimental parameter identification and analysis of nonlinear elastic models were accomplished by considering palpation of bovine myocardial tissue and Sylgard gel samples, which are often used as models for human heart and brain tissue, respectively. In order to highlight the Poynting effect, nonlinear constitutive laws were derived based on the Mooney-Rivlin, Ogden, and exponential forms of the strain energy function. The Ogden form was used for Sylgard gel, while the anisotropic behavior of myocardial tissue was captured using the exponential form of the strain energy function. We quantified the impact of shear and normal forces resulting from the Poynting effect on user perception with a multidimensional scaling (MDS) study. MDS is a family of algorithms that take proximities between pairs of objects as inputs and evaluate the coordinates of the objects embedded in a multidimensional space [145]. In the MDS experiment, different combinations of shear and normal forces are presented to users. In order to select the reference forces for the experiment, a force discrimination pre-study was also performed.

3.1.1 Related Work

Given the complexity of human organs and challenges in acquisition of tissue parameters, realistic modeling and simulation of tissue deformation is an ongoing research area. Extensive work has been done by researchers in the area of computer graphics to model deformable bodies [37]. In such studies, the focus has been to produce seemingly realistic visualization, while ignoring the physics underlying tissue deformation. The focus of the literature in the domain of biomechanics is understanding the fundamental properties of various tissues, e.g. [2, 10]. Chapter 2 provides an overview of both physical and non-physical organ modeling methods applied to surgical simulation [146].

In this study, we demonstrate that there is a significant difference between the forces applied to the user for linear and nonlinear elastic tissue models. While this is not a new concept, our work provides a concrete example of how modeling techniques relate to human perception of surgical simulators. In addition to the work presented in this chapter and [25–27], Dehghan and Salcudean [147] have compared the effects of linear and nonlinear finite element models on mesh displacement during needle insertion. Dehghan and Salcudean concluded that, in the presence of asymmetric boundary conditions, there are noticeable differences between linear and nonlinear models. Other work has focused on both qualitatively and quantitatively characterizing the efficiency, accuracy, and realism of haptic virtual environments, e.g. [148–150].

Extensive research has also studied how materials are perceived by humans, e.g. [151–153]. Recently, MDS has been used as a quantitative means of understanding hu-

man perception. Pasquero et al. [154] provide a review of MDS analysis techniques, and they applied them to perceptual data collection of a prototype mobile tactile handheld device. Yoshida [155, 156] was one of the first to use MDS techniques for quantifying metallic and fibrous tactile perceptions. Performing MDS analysis on tactile stimuli data, two dimensions (smooth/rough and hard/soft) were identified [157]. Bergmann Tiest and Kapper [158] investigated roughness and compressibility via MDS studies. MacLean and Enriquez [159] used MDS for mapping haptic perception for the design of haptic icons. Leskovsky et al. [160] evaluated the haptic perception of real and virtual deformable objects using MDS techniques. Their analysis showed a clear perceptual distinction between real and virtual objects only when low-fidelity rendering was used in the virtual environment. Also, MDS analysis showed that objects become more distinguishable as their stiffness increases.

The remainder of the chapter is organized as follows: The derivations for the constitutive law of a body undergoing shear and the Poynting effect are presented in Section 3.2. Experimental studies to populate our model and demonstration of the Poynting effect in Sylgard gel and myocardial tissue are described in Section 3.3. Details of the psychophysical experiment and MDS results are given in Section 3.4. Finally, we conclude by summarizing the results of our study.

3.2 The Poynting Effect

In order to elucidate the differences between linear and nonlinear elasticity-based tissue models and demonstrate the role of the Poynting effect, this section presents the theoretical relationships for the stresses and strains for a body undergoing simple shear, as shown in Figure 3.2. Shear is considered because it is common practice for clinicians to palpate and perform a shearing motion on the organ either by hand or with an instrument.

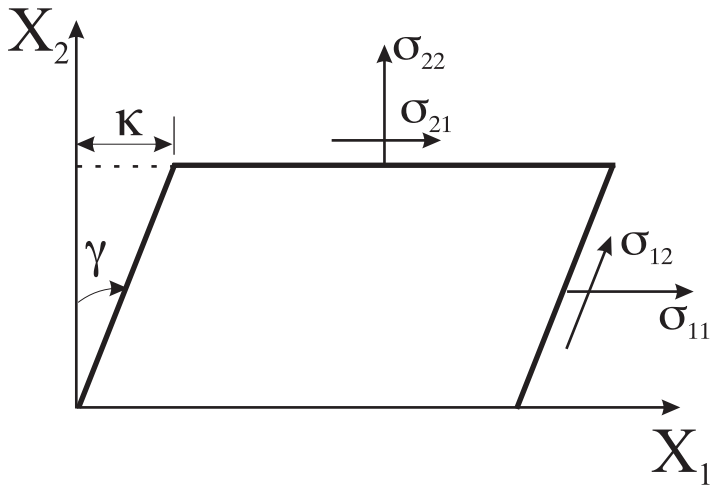

Figure 3.2: Body undergoing simple shear; the shear strain is κ in the X_1 direction.

The formulation presented here highlights only the important relationships and does not cover the fundamentals of continuum mechanics. For details, we refer the reader to [161]. The body is assumed to be sheared by an amount κ, and γ is the angle the sheared line makes with its original orientation. The shear strain is given by $\kappa = \tan(\gamma)$. If $\mathbf{y}$ represents the position after deformation of a material particle initially located at $\mathbf{X}$, we can describe

the simple shear motion by

$$\mathbf{y} = (X_1 + \kappa X_2)\,\mathbf{e}_1 + X_2\mathbf{e}_2 + X_3\mathbf{e}_3, \tag{3.1}$$

where $\{\mathbf{e}_1, \mathbf{e}_2, \mathbf{e}_3\}$ are the Cartesian base vectors. The above expression implies that shear displacement is being applied to the body, while preventing displacement in the normal direction. From (3.1), the matrix of the deformation gradient tensor, $\mathbf{F}$, is computed as

$$\mathbf{F} = \frac{\partial \mathbf{y}}{\partial \mathbf{X}} = \begin{bmatrix} 1 & \kappa & 0 \\ 0 & 1 & 0 \\ 0 & 0 & 1 \end{bmatrix}. \tag{3.2}$$

The left Cauchy-Green tensor, $\mathbf{B}$, is given in terms of the deformation gradient tensor as

$$\mathbf{B} = \mathbf{F}\mathbf{F}^T = \begin{bmatrix} 1+\kappa^2 & \kappa & 0 \\ \kappa & 1 & 0 \\ 0 & 0 & 1 \end{bmatrix}. \tag{3.3}$$

Further, the principal invariants, I_1, I_2, and I_3, are defined as

$$I_1 = \mathbf{B} : \mathbf{I},\; I_2 = \frac{1}{2}\left((\mathbf{B} : \mathbf{I})^2 - (\mathbf{B} : \mathbf{B})\right), \text{ and } I_3 = \det \mathbf{B}, \tag{3.4}$$

where $\mathbf{I}$ is the identity tensor. Thus, for a body undergoing simple shear, we derive expres-

sions for the principal invariants, in terms of the stretch ratios, λ_i $(i = 1,2,3)$, as

$$I_1 = \lambda_1^2 + \lambda_2^2 + \lambda_3^2 = \kappa^2 + 3, \tag{3.5}$$

$$I_2 = \lambda_1^2\lambda_2^2 + \lambda_2^2\lambda_3^2 + \lambda_3^2\lambda_1^2 = \kappa^2 + 3, \text{ and} \tag{3.6}$$

$$I_3 = \lambda_1^2\lambda_2^2\lambda_3^2 = 1. \tag{3.7}$$

The deformation of most biological materials under large strains (>1%-2%) can be described by the theory of nonlinear elasticity, and hyperelastic models are commonly used. For a hyperelastic material, the Cauchy stress tensor, $\boldsymbol{\sigma}$, can be derived from a strain energy density function, W. There are various formulations for the strain energy density function depending on the material, e.g. Neo-Hookean, Mooney-Rivlin, St. Venant-Kirchhoff, Blatz-Ko, Ogden, polynomial or exponential form. Depending on the choice of W, the Cauchy stress tensor for homogenous hyperelastic materials can be derived as [161]

$$\boldsymbol{\sigma} = -p\mathbf{I} + 2\left\{\left(\frac{\partial W}{\partial I_1} + I_1\frac{\partial W}{\partial I_2}\right)\mathbf{B} - \frac{\partial W}{\partial I_2}\mathbf{B}^2\right\}, \tag{3.8}$$

$$\text{or } \sigma_{ij} = -p\delta_{ij} + \lambda_i\frac{\partial W}{\partial \lambda_j}, \tag{3.9}$$

where p is the Lagrange multiplier (essentially a pressure), δ_{ij} is the Kronecker delta λ_i $(i = 1,2,3)$ and λ_j $(j = 1,2,3)$ are the stretch ratios, and $J = \det \mathbf{F}$.

In this section, using the kinematic relations for a body undergoing simple shear and

applying the boundary condition ($\sigma_{33} = 0$), we derive the stresses developed in the body for three different types of strain energy functions (Mooney-Rivlin, Ogden, and exponential form). These constitutive relations are useful to highlight the differences between linear and nonlinear elastic models, and are also relevant for the experimental and human-subject studies described later. It should be noted that the Mooney-Rivlin and Ogden strain energy functions were originally designed to model rubber-like materials, but are sufficient for the purposes of this study to highlight the differences between linear and nonlinear elastic models.

The Mooney-Rivlin strain energy density function in terms of material parameters, C_1 and C_2, is given by

$$W = C_1 (I_1 - 3) + C_2 (I_2 - 3). \tag{3.10}$$

As an example, we go through the steps to derive the constitutive relations for body under simple shear with the Mooney-Rivlin model. For the Mooney-Rivlin model given in (3.10)

$$\frac{\partial W}{\partial I_1} = C_1, \tag{3.11}$$

$$\frac{\partial W}{\partial I_2} = C_2. \tag{3.12}$$

From (3.3), we can compute $\mathbf{B}^2$, and using results from (3.5), (3.6), (3.11), and (3.12), and evaluating (3.8), we obtain the following expressions for the stress in terms of the shear, κ:

$$\sigma_{11} = 2C_1 + 4C_2 + 2 (C_1 + C_2) \kappa^2 - p. \tag{3.13}$$

$$\sigma_{22} = 2C_1 + 4C_2 - p. \tag{3.14}$$

$$\sigma_{33} = 2C_1 + 2C_2\left(2 + \kappa^2\right) - p. \tag{3.15}$$

$$\sigma_{12} = 2\left(C_1 + C_2\right)\kappa. \tag{3.16}$$

$$\sigma_{13} = 0. \tag{3.17}$$

$$\sigma_{23} = 0. \tag{3.18}$$

The Lagrange multiplier, p, can be evaluated from the boundary condition. For example, the plane stress case gives

$$\sigma_{33} = 0 \Rightarrow p = 2\left(C_1 + 2C_2 + C_2\kappa^2\right) \tag{3.19}$$

Thus, substituting (3.19) in (3.13) and (3.14), we derive the stresses in terms of shear, κ, as

$$\sigma_{11} = 2C_1\kappa^2, \tag{3.20}$$

$$\sigma_{22} = -2C_2\kappa^2. \tag{3.21}$$

The Ogden strain energy density function in terms of material parameters, μ and α, is of the form

$$W = \frac{2\mu}{\alpha^2}\left(\lambda_1^\alpha + \lambda_2^\alpha + \lambda_3^\alpha - 3\right). \tag{3.22}$$

We derived the stresses using (3.9) as

$$\sigma_{11} = \frac{2\mu}{\alpha}\left(\lambda_1^{\alpha} - 1\right), \tag{3.23}$$

$$\sigma_{12} = \frac{2\mu}{\alpha\kappa}\left(\lambda_1^{\alpha} - \lambda_1^{-\alpha}\right), \tag{3.24}$$

$$\sigma_{22} = \frac{2\mu}{\alpha}\left(\lambda_1^{-\alpha} - 1\right), \tag{3.25}$$

where $\lambda_1 = \frac{1}{2}\left(\kappa + \sqrt{4+\kappa^2}\right)$.

The exponential strain energy function that accounts for tissue anisotropy and is a function of the Green strain tensor components, E_{ij}, is

$$W = \frac{c}{2}\left(e^{Q} - 1\right), \tag{3.26}$$

where

$$Q = A_1E_{11}^2 + A_2E_{22}^2 + 2A_3E_{11}E_{22} + A_4E_{12}^2 + 2A_5E_{11}E_{12} + 2A_6E_{22}E_{12}. \tag{3.27}$$

In (3.27), c, A_1, A_2, A_3, A_4, A_5, and A_6 are material parameters. From (3.26), we can derive the second Piola-Kirchhoff stress tensor, $\mathbf{S}$, as [161]

$$S_{ij} = \frac{\partial W}{\partial E_{ij}}. \tag{3.28}$$

The Cauchy stress tensor in terms of **S** is given by

$$\boldsymbol{\sigma} = \frac{1}{J}\mathbf{F}\mathbf{S}\mathbf{F}^T. \tag{3.29}$$

For the exponential strain energy function, we derived the stresses developed due to simple shear using (3.26) and (3.29) as

$$\sigma_{11} = c\kappa\left(\frac{A_5}{2} + \kappa\left(\frac{A_3}{2} + A_4 + \frac{3A_6\kappa}{2} + \frac{A_2\kappa^2}{2}\right)\right)e^{\beta}, \tag{3.30}$$

$$\sigma_{12} = c\kappa\left(\frac{A_4}{2} + \kappa\left(A_6 + \frac{A_2\kappa}{2}\right)\right)e^{\beta}, \tag{3.31}$$

$$\sigma_{22} = c\kappa\left(\frac{A_6}{2} + \frac{A_2\kappa}{2}\right)e^{\beta}, \tag{3.32}$$

where $\beta = \kappa^2\left(\frac{A_4}{4} + \kappa\left(\frac{A_6}{2} + \frac{A_2\kappa}{4}\right)\right)$. As seen in (3.21), (3.25), and (3.32) for the Mooney-Rivlin, Ogden, and exponential strain energy functions, respectively, σ_{22} is non-zero. The presence of normal stress, σ_{22}, and the inequality $\sigma_{11} \neq \sigma_{22}$, is a manifestation of the *Poynting effect*, and is a result of the material nonlinearity.

The generalized Hooke's law for isotropic materials that relates the Cauchy stress tensor and the infinitesimal strain tensor given in (2.9) and restated below is

$$\sigma_{ij} = \lambda\varepsilon_{kk}\delta_{ij} + 2\tilde{G}\varepsilon_{ij}, \tag{3.33}$$

where ε_{ij} is the infinitesimal strain, δ_{ij} is the Kronecker delta, and λ and $\tilde{G}$ are the Lamé

moduli. For a linear elastic body undergoing simple shear, ε_{12} and ε_{21} are the only non-zero infinitesimal strains. Thus, in contrast to the nonlinear elastic case, for a homogenous and isotropic body undergoing simple shear, the stress based on linear elasticity using (3.33) is derived as

$$\sigma_{12} = \sigma_{21} = 2\tilde{G}\varepsilon_{12}, \tag{3.34}$$

and all other components of the stress tensor are zero. For the simple shear case, $\kappa = 2\varepsilon_{12}$, hence, (3.34) could be rewritten as

$$\sigma_{12} = \tilde{G}\kappa, \tag{3.35}$$

where $\tilde{G}$ is the shear modulus. The constitutive law given in (3.35) presents a computationally simple and easy to implement formulation, but such models do not exhibit the Poynting effect.

3.3 Role of the Poynting Effect in Soft Tissues

The theoretical framework for the Poynting effect was described in the previous section. In this section, we provide experimental evidence of the Poynting effect during palpation of Sylgard gel and myocardial tissue using both experiments and simulations. Further experiments were conducted to populate our analytical model with material properties.

3.3.1 Experiments to Measure Gel/Tissue Properties

We performed uniaxial compression and shear experiments on Dow Corning Sylgard 527 A & B silicone dielectric gel. These tests were done using the Rheometrics Solids Analyzer (RSA) II. Details pertaining to the individual components and various test modes can be found in the RSA II owner's manual [162]. Note that the experiments described in Chapter 5 (Section 5.5) were also performed using the RSA II. Sylgard gel is commonly used to simulate human brain tissue.

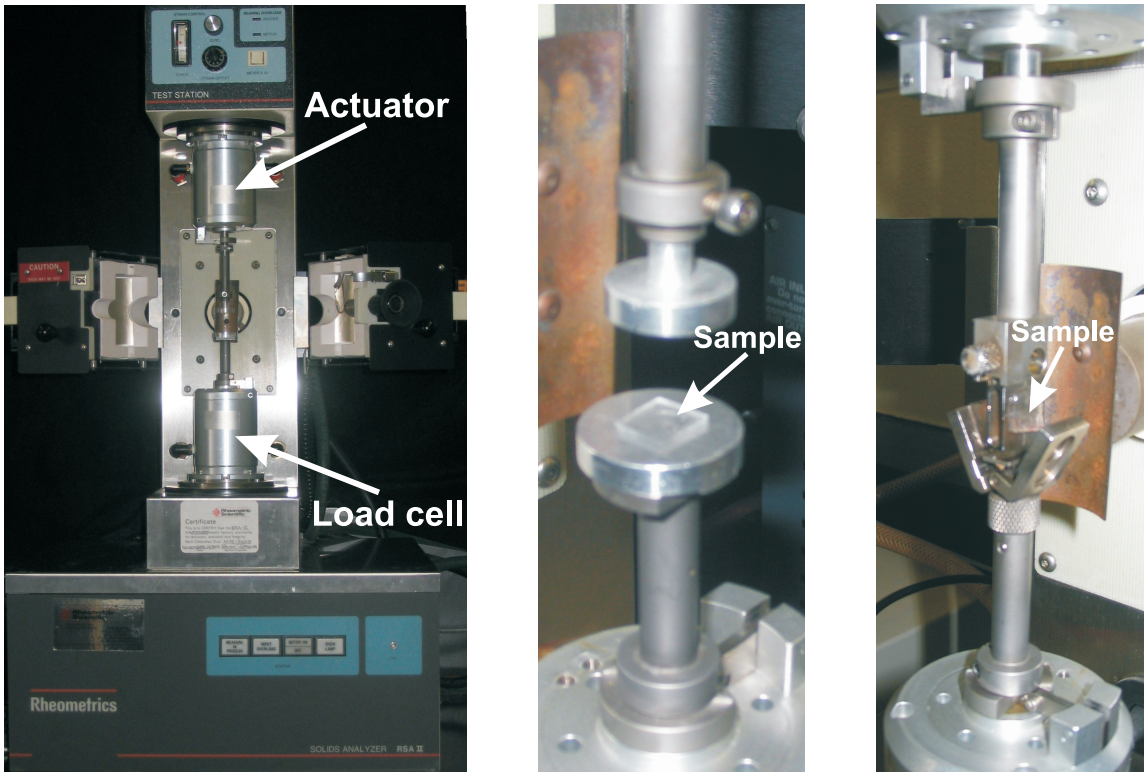

(a) (b) (c)

Figure 3.3: (a) The RSA II test station. Sylgard gel sample in the RSA II under (b) uniaxial compression and (c) shear.

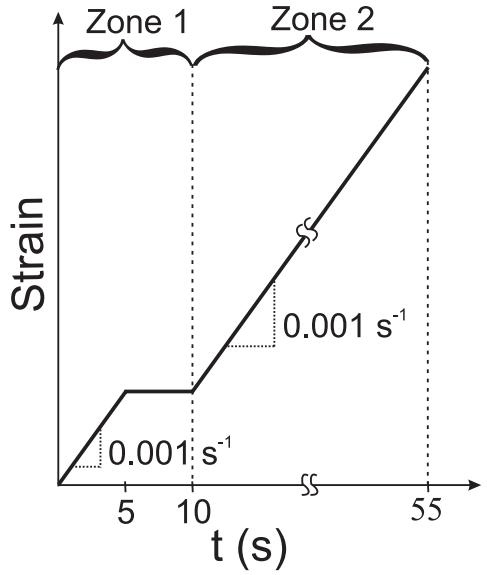

Figure 3.4: Strain rate sweep mode used for compression and shear experiments on the RSA II.

The Sylgard gel sample was placed between the actuator and load cell, which are located on the RSA II test station, as shown in Figure 3.3. The position sensor mounted onto the actuator shaft outputs a DC voltage that is proportional to the actuator displacement. The resolution of the actuator is $\pm$ 0.05 μm. The load cell is operated by using a linear variable differential transducer (LVDT) in order to maintain constant axial position during testing. Following the application of force to the load cell shaft, the LVDT outputs a DC voltage that is proportional to shaft displacement from zero position. The resolution of the load cell is $\pm$ 0.00981 N.

We prepared and tested 20 Sylgard gel samples of dimensions 10 mm $\times$ 10 mm, and thickness of 1 mm. The experiments used the RSA II in *strain rate sweep* mode. In this mode, the user commands a compressive or shear strain rate and a period for which the

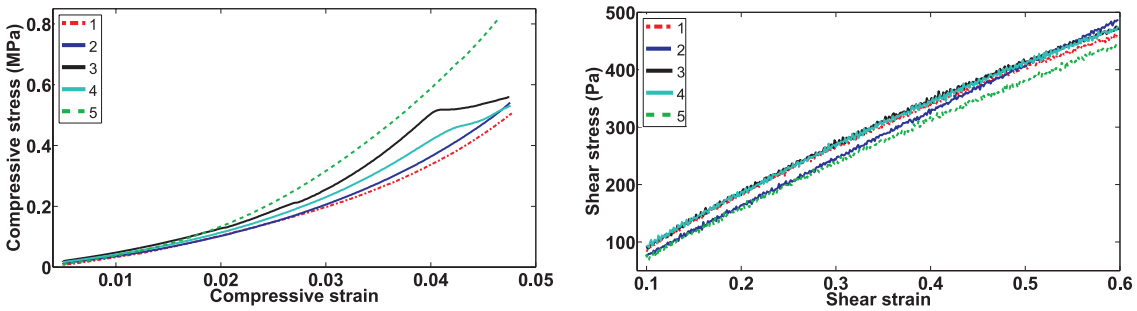

(a) (b)

Figure 3.5: RSA II stress versus strain data for Sylgard gel samples: (a) uniaxial compression and (b) shear.

strain is to be applied. In our experiments, we applied the strain histories shown in Figure 3.4. During Zone 1, the initial compressive or shear strain was applied for 5 seconds and then the sample was allowed to settle for 5 seconds. In Zone 2, the compressive or shear strain was applied for a period of 45 seconds. Zone 1 ensures that the sample is appropriately preconditioned so that reliable stress and strain data are acquired. Zone 2 provides the data for our subsequent analysis. In both zones, the strain rate was set to 0.001 $\sec^{-1}$. The stress versus strain plots for the compression and shear studies for 5 representative cases are given in Figures 3.5(a) and (b), respectively.

In order to obtain the material properties corresponding to the Ogden strain energy density function in (3.22), we derive the constitutive law for uniaxial compression and shear. The constitutive relations based on the Ogden strain energy density function were fit to the experimental data for Sylgard gel. The stress versus strain relation for a body undergoing simple shear for the Ogden strain energy function is given in (3.24). Using (3.9), in terms of the stretch ratio, λ_2 (X_2 being the direction of compression), and the

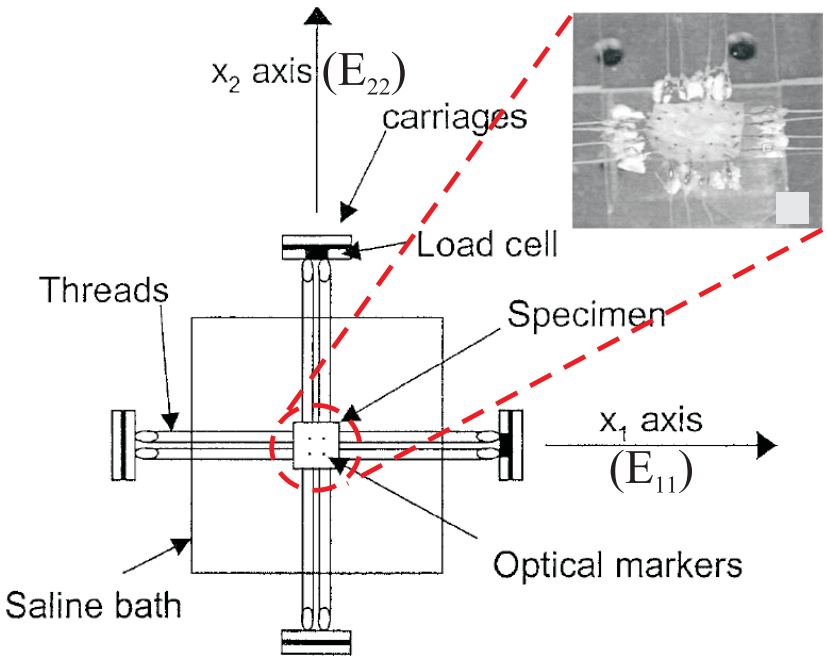

Figure 3.6: Sketch of the biaxial experimental setup as designed by Sacks [20]. *Inset*: Myocardial tissue sample. *Images are printed with kind permission of Springer Science and Business Media.*

material parameters, we derive the compressive stress to be

$$\sigma_{22} = \frac{2\mu\lambda_2^{-\frac{\alpha}{2}}}{\alpha}\left(\lambda_2^{\frac{3\alpha}{2}} - 1\right). \tag{3.36}$$

The above relation is derived using the fact that for a body under uniaxial compression, $\lambda_1 = \lambda_3 = \frac{1}{\sqrt{\lambda_2}}$. Also, the strain, ε, in terms of the stretch ratio is

$$\varepsilon = 1 - \lambda_2. \tag{3.37}$$

Using (3.24) and (3.36), the mean Ogden material parameters, μ and α, for the 5 repre-

sentative test cases are 836.3 kPa and -0.15, respectively. These material properties were evaluated by simultaneously fitting the experimental data to both the shear and uniaxial compression constitutive relations.

The material properties for myocardial tissue were obtained using biaxial test data acquired by Sacks in [20]. Sacks's experimental setup is shown in Figure 3.6. Five bovine pericardium tissue of good structural consistency and size 25 mm $\times$ 25 mm were tested on the biaxial testing device. The test samples were cut such that the myocardial tissue fibers were aligned at 45° with respect to the biaxial device's testing axes. A detailed description of the testing device and the experimental protocol is presented in [20]. Two loops of nylon suture were attached to each side of the specimens with surgical staples. Pulleys were symmetrically placed on all sides of the sample to conduct both tension and in-plane shear experiments on the same sample. Stress and strain measurements were made using two (one along each axis) force transducers and tracking the displacement of graphite markers on the sample, respectively. The digitized tension and in-plane shear data are given in Figure 3.7(a) and (b), respectively.

The material properties for myocardial tissue based on biaxial tests and using the exponential strain energy function given in (3.26) and (3.27), were computed to be 2.640 kPa, 0.977, 11.201, 7.540, -12.191, -22.406, -4.978 for material parameters c, A_1, A_2, A_3, A_4, A_5, and A_6, respectively [20].

This section presented the material properties for both Sylgard gel and myocardial tissue. These material parameters are used in the analytical models described in Section 3.2

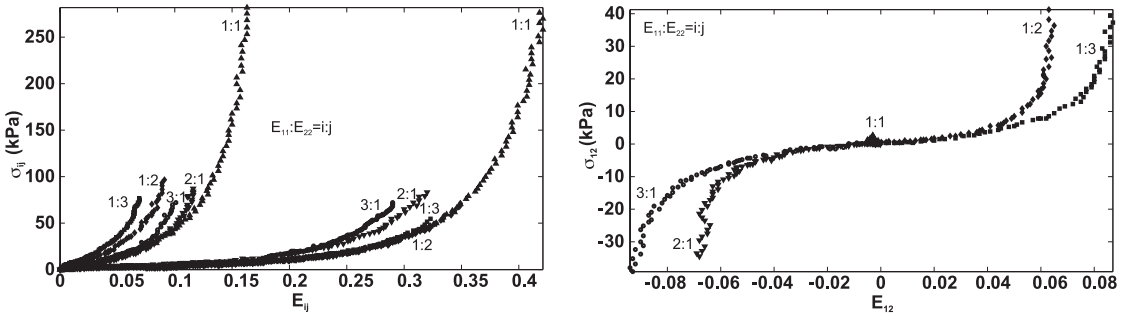

(a) (b)

Figure 3.7: Biaxial test data for myocardial tissue for (a) normal and (b) in-plane shear. This data was digitized from results published in [20].

in order to obtain the stress state of a body undergoing simple shear.

3.3.2 Observing the Poynting Effect

In addition to the acquisition of material parameters of Sylgard gel (using RSA II), large gel samples that are representative of actual organ sizes, of dimensions 100 mm $\times$ 50 mm, and thickness of 5 mm, 7.5 mm and 10 mm were sheared (30%, 50%, and 80% strains) using a robot (Figure 3.8). The experimental setup was designed to palpate Sylgard gel. The normal force versus displacement plots generated during shear of two samples are shown in Figure 3.9. Also, using the Ogden material parameters and analytical expressions for stresses developed during simple shear given in (3.24) and (3.25), forces were calculated during shear of samples of dimensions similar to the experiments. The dotted line in Figure 3.9 corresponds to the analytically calculated force value. As observed, the normal forces were 0.09 N and 0.07 N for the 5 mm (80% shear) and 10 mm (30% shear)

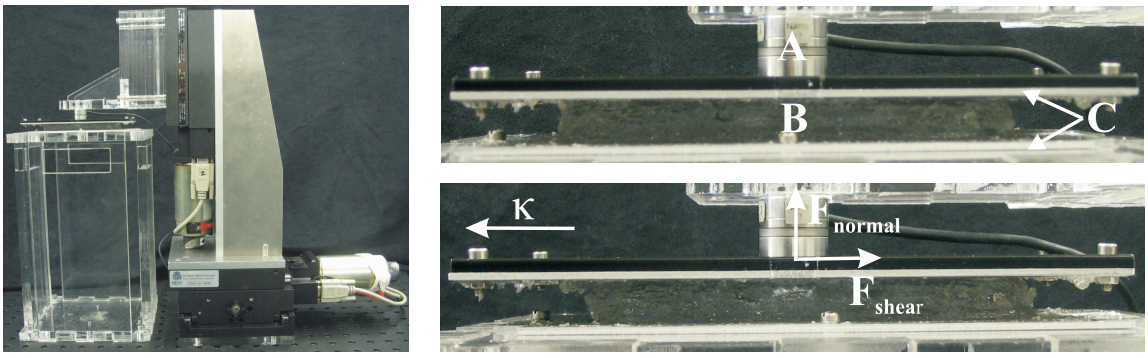

(a) (b)

Figure 3.8: Experimental setup used to perform shear tests on large Sylgard gel samples. (a) Robot with gel. (b) Robot shearing the Sylgard gel samples, where A, B, and C are the Nano17 force sensor, gel sample, and metal plates used for shearing, respectively. *Top*: Unsheared sample. *Bottom*: Sheared sample.

samples, respectively. Figure 3.10(a) shows both the shear and normal forces developed on the Sylgard gel sample of thickness 10 mm (30% shear). In all experimental cases, the normal forces generated during palpation of Sylgard gel were less than the absolute human perception threshold for force discrimination, determined from psychophysical experiments [163].

The shear and normal forces predicted to be generated during palpation of myocardial tissue are given in Figure 3.10. These forces were generated using the material properties derived from biaxial tests described previously and presented in [20], and analytical expressions derived for the simple shear task given in (3.31) and (3.32). Simple shear experiments were not conducted with myocardial tissue due to unavailability of large tissue samples. Further, such large scale simple shear studies with biological tissue would require redesigning the current experimental setup (Figure 3.8(a)). As seen, a normal force

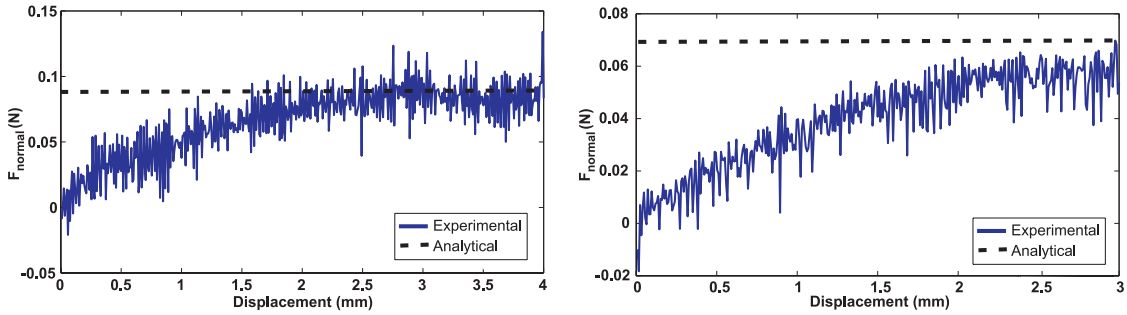

(a) (b)

Figure 3.9: Normal forces generated during the shear of large Sylgard gel samples. (a) 5 mm thick sample sheared at 80% strain. (b) 10 mm thick sample sheared at 30% strain.

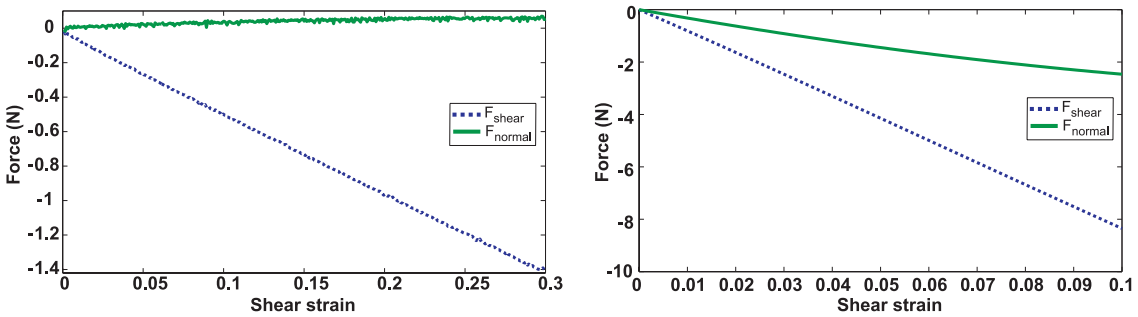

(a) (b)

Figure 3.10: (a) Shear and normal forces developed during palpation (30% shear) of the Sylgard gel sample of dimensions 100 mm $\times$ 50 mm $\times$ 10 mm (thick). (b) Analytically derived shear and normal forces developed on the shear plane of area 100 mm $\times$ 50 mm, during palpation (10% shear) of bovine myocardial tissue.

of 2.46 N would be generated by a 10% shear of bovine myocardial tissue, which is significantly larger than the absolute human perception threshold for force discrimination. In contrast, the only stress developed for the commonly implemented linear elastic tissue model is $\sigma_{12} = G\kappa$, and no normal forces are computed because of the linear elasticity assumption. Thus, depending on the type of tissue (e.g. myocardial tissue versus Sylgard gel) being sheared, the normal forces generated could significantly affect tissue deformation, as

well as the magnitude of force feedback provided during surgical simulation.

In addition to the presence of the Poynting effect, we also observe that accurate characterization of tissues may require at least two independent sets of loading condition, e.g. compression and shear or biaxial tests. The analysis and experimental results imply that, with a nonlinear elastic tissue model in a surgical simulator, the user might perceive noticeably different haptic feedback while interacting with the organ model. A caveat to this statement is that palpation of only some soft tissues will result in significantly large normal forces due to the Poynting effect. Hence, this work emphasizes careful examination of relevant simulator design parameters (e.g. soft tissue constitutive laws) that relate to final simulator behaviors.

3.4 Quantifying the Poynting Effect Using Multidimensional Scaling

As described in the previous section, the Poynting effect is significant for some organs like myocardial tissue in the heart, but may not be for others. This motivates the study of humans interacting with nonlinear virtual tissue models with varying values of shear and normal forces, in order to understand the impact of the Poynting effect on surgical simulators. Thus, we performed human subject experiments in order to determine the effects of shear and normal forces on user perception [27]. These experiments were performed at the Computer Vision Laboratory, ETH Zürich. In order to conduct this study, appropriate

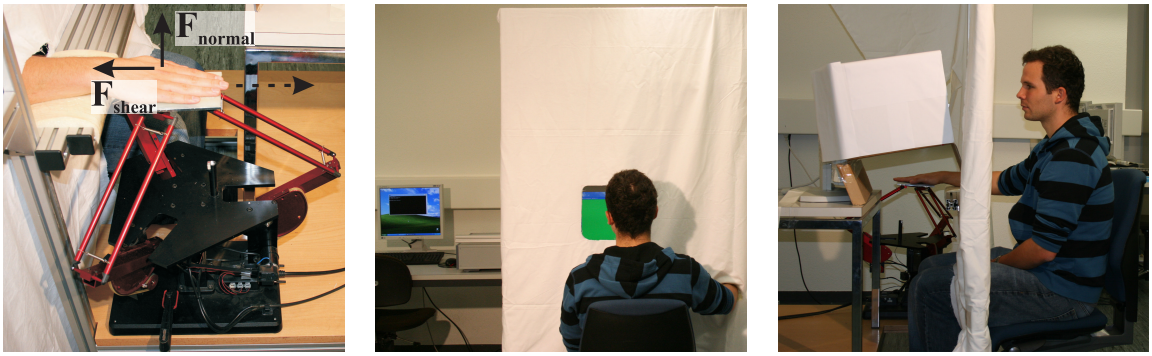

(a) (b) (c)

Figure 3.11: Experimental setup used for psychophysical experiments. (a) The Delta haptic device. As the user interacts with the nonlinear elastic virtual model and moves the device, normal (F_{normal}) and shear (F_{shear}) forces are generated. F_{normal} is due to the Poynting effect. (b) Front view. (c) Side view.

approvals were acquired from both the Johns Hopkins University Homewood Institutional Review Board and the Ethics Committee of ETH Zürich.

In order to study the effects of shear and normal forces, a two degree-of-freedom haptic stimulus is needed. We used the three-degree-of-freedom version of the Delta haptic device (Force Dimension, Inc.) [164] because it is designed to provide high-fidelity force-feedback over a large range of forces and also has a large workspace. As shown in Figure 3.11(a), the end-effector of the Delta haptic device was replaced by a custom-built flat plate covered with silicone rubber, representing the surface of the deformable virtual sample. The complete experimental setup is shown in Figure 3.11. Participants did not have direct visual access to the device, in order to prevent visual cues that might alter force perception.

Research participants were comfortably seated in front of the setup with their right forearm resting on a support. Participants were asked to place their palm on the flat plate

and move the device slowly forward (direction of shear is shown in Figure 3.11(a)). Special care was taken that all subjects touched the plate in a similar fashion; participants were not allowed to grasp the plate. After moving the plate forward by 12 cm, the computer display changed from green to red. Participants were told that this visual signal marked the end of their active movement. Following the forward shearing motion, haptic feedback was provided to guide a participant back to the initial starting position. This was done to ensure that all participants started the shearing task at the same position and sheared the virtual model by the same amount. As participants performed the shearing motion, either shear or a combination of shear and normal forces were displayed to them.

The main goal of this study was the MDS analysis. However, in order to select the force samples to be presented in this main part, a pre-study focusing on force discrimination was also performed. The details of both experiments are provided in the following sections.

3.4.1 Force Discrimination Pre-Study

The objective of this experiment was to guide the selection of combinations of material parameters to be used in the MDS study. The pre-study was essentially a force discrimination test following a two-alternative, forced-choice (2AFC) design. Participants were instructed to shear the flat plate in the forward direction twice. They were informed that, in addition to a shearing force, a normal force would be rendered during one of the two tasks. The participants were asked to identify which trial included the normal force.

In the experiment, 4 male and 3 female participants took part, with a mean age of 26.4

	Category I: $C_1 = 100$ Pa		Category II: $C_1 = 200$ Pa		Category III: $C_1 = 400$ Pa	
Model	$\frac{C_2}{C_1}$	C_2 (Pa)	$\frac{C_2}{C_1}$	C_2 (Pa)	$\frac{C_2}{C_1}$	C_2 (Pa)
a	0.005	0.5	0.05	10.0	0.05	20.0
b	0.01	1.0	0.1	20.0	0.15	60.0
c	0.05	5.0	0.15	30.0	0.25	100.0
d	0.1	10.0	0.2	40.0	0.35	140.0
e	0.2	20.0	0.3	60.0	0.45	180.0
f	0.3	30.0	0.4	80.0	0.55	220.0
g	0.4	40.0	0.5	100.0	0.65	260.0
h	0.5	50.0	0.6	120.0	0.75	300.0
i	0.6	60.0	0.8	160.0	1.0	400.0
j	0.75	75.0	0.9	180.0	1.25	500.0

Table 3.1: Parameters of virtual models used for force discrimination study. Shaded rows represent models that were used for the similarity rating study.

years. None of the participants had any prior experience interacting with a haptic device similar to the Delta. All participants were given about 15 minutes of practice time to familiarize themselves with the experiment. The duration of the session, including instructions and breaks, was three hours. Each participant was compensated with 40 CHF for taking part in the study. After the experiment, users provided additional feedback via a questionnaire.

The rendered shear and normal forces were generated based on the stress equations of the Mooney-Rivlin model given in (3.16) and (3.21), respectively. Three different model categories with C_1 values of 100 Pa, 200 Pa, and 400 Pa, and 10 different ratios of $\frac{C_2}{C_1}$ were chosen to yield 30 distinct virtual models. Table 3.1 provides an overview of the model parameters. Lower values of C_2 result in smaller normal forces. The material properties used in the pre-study are representative of liver and kidney soft tissues, as reported in [11].

For each of the trials, two forces were generated. One contained shear and normal

forces according to a unique ratio of $\frac{C_2}{C_1}$, while in the other, only the shear force was produced by setting $C_2 = 0$. Each of the reference virtual models was repeatedly shown 15 times in the pairwise comparisons, which resulted in a total to 450 trials per participant. The 2AFC data of the experiment were used to generate psychometric functions using the number of times participants were able to correctly identify the model with the normal forces. Curves were fit using psignifit version 2.5.6 (http://bootstrap-software.org/psignifit/), a software package that implements the maximum-likelihood method [165].

For each participant, three psychometric functions were generated separately for each of the three model categories. Figure 3.12 depicts an example curve for Category I ($C_1 = 100$ Pa). The *stimulus* is given by the ratio $\frac{C_2}{C_1}$, while the *performance* denotes the normalized ratio of correct detection of models containing normal forces.

Point of subjective equality (PSEs) for the ratios $\frac{C_2}{C_1}$ were determined for all curves. The observed variation in the PSEs was found to be considerably large. Means and standard deviations were 0.27 ($\sigma = 0.23$) for Category I, 0.13 ($\sigma = 0.05$) for Category II, and 0.46 ($\sigma = 0.47$) for Category III. Large standard deviations indicate that participants found the task difficult. Especially for virtual models requiring display of large forces (mainly in Category III), the psychometric functions were distorted. In these cases, participants were not able to reliably identify models with normal forces.

These difficulties also became apparent in the written feedback given by the participants via the questionnaires. For larger forces, 4 out of 7 participants reported problems in making their judgments. Participants also indicated that they experienced discontinu-

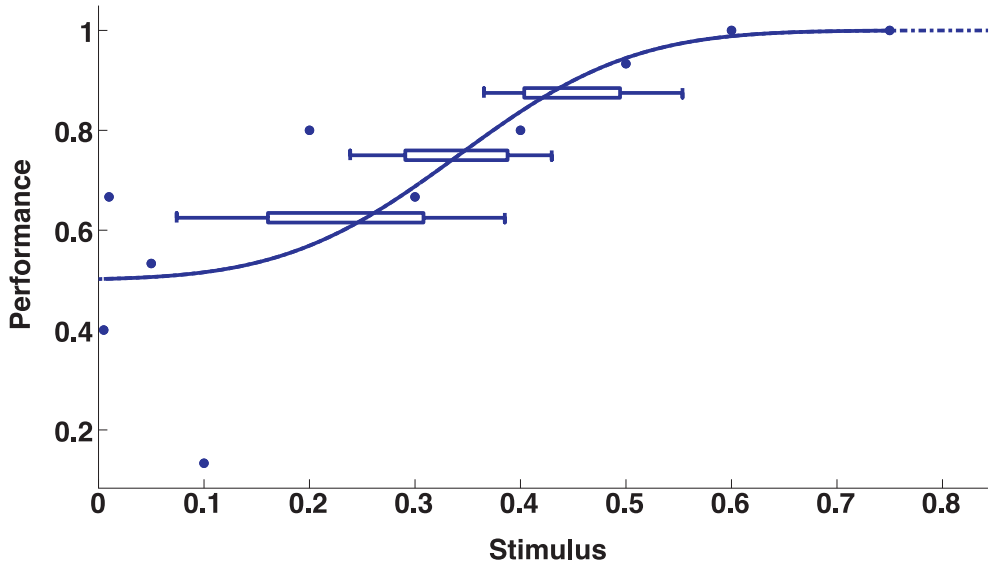

Figure 3.12: Psychometric curve for a research participant interacting with a Model I ($C_1 = 100$ Pa). *Stimulus* is the ratio $\frac{C_2}{C_1}$, while the *performance* denotes the normalized ratio of correct detection of models containing normal forces.

ities, which was later determined to be due to the unstable rendering of large forces. Some participants also reported a low comfort level with using the setup.

The intended purpose of the pre-study was to support the selection of a subset of models that would be used in the similarity rating study. Models were chosen in such a way as to cover stimulus ranges where participants had low, intermediate, and high performance values of correct discrimination of the normal forces. However, due to the reported problems in the study, our choice was finally guided only by a subset of participants who performed better in the pre-study. These models are highlighted in grey in Table 3.1.

Model #	C_1 (Pa)	C_2 (Pa)	$\frac{C_2}{C_1}$	PSE
1	100	0.5	0.005	
2	100	20	0.2	0.27
3	100	75	0.75	
4	200	10	0.05	
5	200	60	0.3	0.13
6	200	180	0.9	
7	400	20	0.05	
8	400	180	0.45	0.46
9	400	500	1.25	

Table 3.2: Models used for the similarity rating study with mean PSE values obtained from force discrimination pre-study.

3.4.2 Multidimensional Scaling Study

MDS is an statistical analysis technique that provides information about relationships between a set of stimuli via similarity or dissimilarity ratings. As in the pre-study, participants were asked to perform trials consisting of shearing two virtual deformable models with the device. The similarity between the forces felt should then be rated by the participants on a scale of 1 to 7, with 1 being most dissimilar and 7 most similar.

Shear and normal forces were presented according to the previously selected combinations of the parameters C_1 and C_2, representing 9 different virtual tissue samples. Table 3.2 lists the parameter sets used. Each possible combination of models was presented 8 times, which resulted in a total of 360 unique pairwise comparisons.

The study had 8 participants, with equal numbers of males and females. The mean age of the participants was 28.1 years. The duration of one session, including instructions and

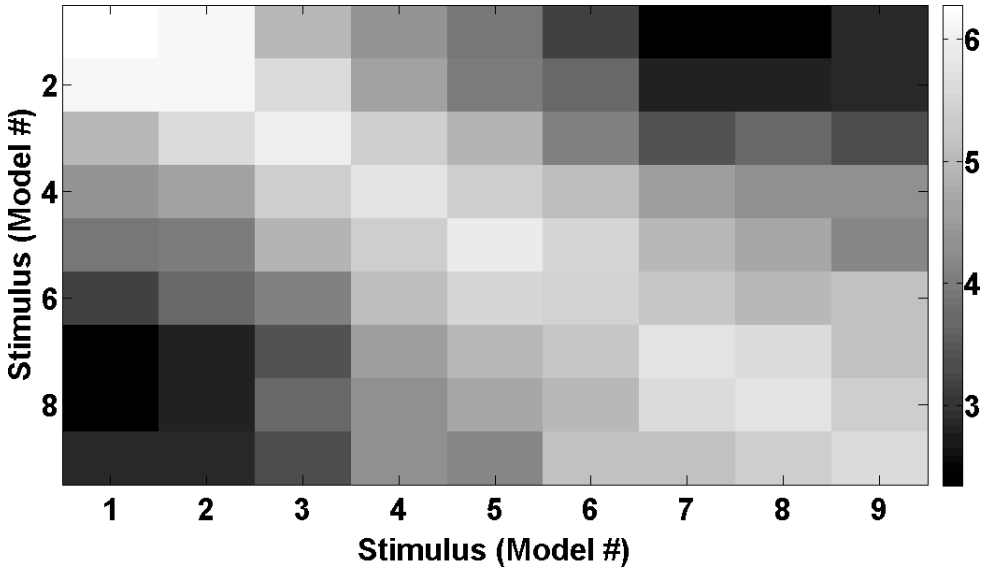

Figure 3.13: Visual representation of similarity rating matrix for all participants. The values correspond to mean rating values of all participants.

breaks, was three-and-a-half hours; each participant was compensated with 40 CHF. The participants in this study were not the same as in the pre-study, in order to avoid learning effects. Again, questionnaires were provided to the participants at the end of the study. In these, the participants were asked to describe the virtual models and explain the cues they used to perform the similarity rating.

3.4.2.1 Results

The inputs to the MDS analysis were the similarity ratings of the pairs of rendered forces; the output was a map of these renderings in a psychological space that helps us interpret the similarity data. Figure 3.13 provides a visual representation of the mean similarity ratings of all participants. The lighter color signifies that participants perceived the

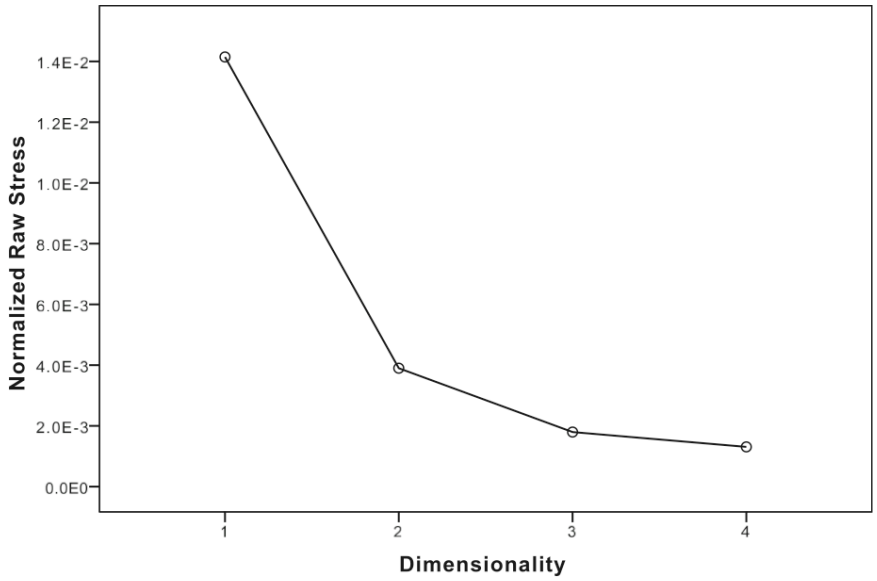

Figure 3.14: Scree plot of MDS analysis showing goodness of fit for various dimensions.

two models as being similar, and dark color represents dissimilarity between two models. Based on this proximity map, an MDS analysis was performed using proximity scaling (PROXSCAL) as implemented in the Statistical Package for the Social Sciences (SPSS Inc.) [166].

The first question to be addressed was the appropriate dimensionality of the output configuration. This can be determined by inspection of the elbow in the scree plot obtained from the analysis. In MDS, objects are represented as points in a dimensional space, such that the distances between the points match the observed dissimilarities as closely as possible. The overall measure of how the distances in the configuration fit the data is called "raw stress". Detailed derivations used to calculate the stress are provided in [167]. The raw stress divided by the sum of squared dissimilarities is called the normalized raw stress.

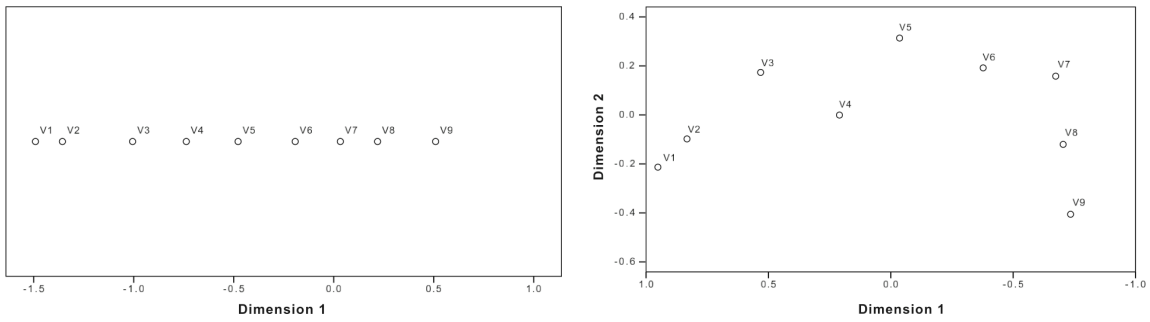

(a) (b)

Figure 3.15: Dimensional configurations obtained from MDS analysis. Configuration with (a) one dimension and (b) two dimensions. "V" denotes the variables (model #) used in the analysis.

The amount of stress is used for judging the goodness of fit of an MDS solution (stress function): a small stress value indicates a good fitting solution, whereas a high value indicates a bad fit. Figure 3.14 shows the scree plot for MDS solutions with increasing dimensionality. We can, use the elbow in the scree plot as a guide to the dimensionality of the solution. As indicated by the elbow in the curve, two perceptual dimensions provide a better fit of the data than a single dimension.

MDS analysis does not provide labels for the dimensions of the output configurations. These must be obtained by visual inspection of the output configuration and interpretation of the feedback given by the participants. Therefore, in the next step we examine the output configurations of the 1D and 2D solutions.

Figure 3.15 shows the configurations obtained both for one and two dimensions in perceptual space. Closer inspection of the 1D configuration (Figure 3.15(a)) indicates an ordering of the nonlinear models according to the corresponding shear force of each model.

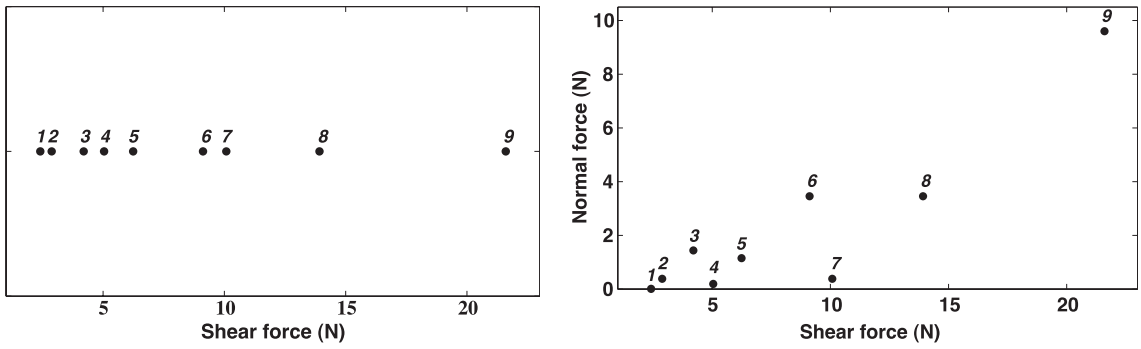

(a) (b)

Figure 3.16: (a) 1D arrangement of samples according to their shear force. (b) Normal versus shear forces for the various models used in the MDS study.

For comparison, the shear forces rendered with the samples are depicted in one dimension in Figure 3.16(a). As observed, the MDS appears to be successful in recovering the ordering of the samples according to the shear force magnitude. However, the distances between the samples were not appropriately reproduced. Nevertheless, the first dimension recovered from the similarity data likely represents the shear force of the samples.

In the 2D configuration (Figure 3.15(b)), the interpretation of the dimensions is less straight-forward. However, following the discussion in the case of one dimension, it makes sense to consider for the 2D configuration the normal forces in addition to the shear forces rendered for the samples. Therefore, the corresponding forces are plotted for all virtual models in Figure 3.16(b).

The resulting MDS arrangement in 2D perceptual space has similarities in the first five samples of the force plot. For samples with larger forces, distortions skew the 2D configuration. Thus, similar to the pre-study, participants seemed to have problems perceiving

normal components for renderings with high force magnitudes. Similar findings were again obtained from the questionnaires which are discussed below. According to the questionnaire, participants assumed on average that eight different virtual models were presented, which is close to the actual number of nine examined samples. The models were generally likened to “play-doh”, “rubber”, “cake”, “jelly”, or “sponge”. Materials of varying stiffness generate different forces when palpated. Further, participants would probably have not expected to feel any normal forces when palpating objects like “jelly”, “sponge”, etc., and the perceived reaction along the shearing direction could have been interpreted as overall object stiffness. Thus, the labeling in Figures 3.15(a) and (b) supports the interpretation of the first dimension of the MDS configuration to be related to shear forces.

Some participants generally reported difficulties in judging the similarities between the models. Also, 5 out of 8 participants reported problems in their ratings when forces became large. It was also stated that in the case of large forces, moving the device felt discontinuous and awkward. This was due to device instabilities during rendering of large forces. This could be an explanation for the deviation of the higher force samples in the perceptual space. The instabilities only appeared to occur for certain hand impedances.

For both the force discrimination pre-study and the MDS study, participants had difficulty perceiving normal components for rendering with high force magnitudes (models 6 through 9). These problems were associated with limitations in rendering large forces by the device and normal forces being masked when shear components were large. To test large forces, the experimental setup should be redesigned in the future. This could

be accomplished by using a real-time operating system coupled to the Delta haptic device and also increasing the sampling frequency to speed up force rendering. The addition of virtual or mechanical damping might also mitigate some of the observed instabilities. The study design could also be changed so that participants perform smaller shearing motions, which in turn would prevent larger forces from being rendered. Also, instead of using a virtual model, the participants could interact with physical biological and artificial tissue samples. This would produce realistic shear and normal forces but difficulty in ensuring experimental repeatability is one of the disadvantages of this approach.

3.5 Summary

The presence of normal forces during shearing of tissue is a consequence of the non-linearity of the material, which is not observed in linear elastic or typical non-physical models. For isotropic materials, this phenomenon is known as the Poynting effect. Though linear elastic models are computationally simple and easy to implement, such models do not exhibit the Poynting effect. Depending on the type of tissue (e.g. myocardial tissue and Sylgard gel) being palpated, the normal forces generated could be signifiant. We showed a significant Poynting effect is to be expected for myocardial tissue but not for Sylgard gel, based on the absolute human perception threshold for contact force discrimination thresholds published in the psychophysics literature. Further, tissue models solely based on one set of experiments, e.g. compression or indentation tests, are not sufficient to describe non-

linear tissue deformation characteristics accurately. Combinations of tension/compression and shear/torsion or biaxial tests are essential for accurate tissue characterization and identification of material properties.

An MDS study was performed to investigate the influence of the Poynting effect on user perception. Participants interacted with virtual nonlinear elastic tissue models via the Delta haptic device. The selection of the material parameters of the samples was based on a 2AFC force discrimination pre-study. Following the pre-study, MDS was performed on similarity ratings obtained by comparing nine different virtual models. Two dimensions provided an appropriate fit to the perceptual space. The first and second dimensions recovered from the similarity data represented the shear and normal forces, respectively. The MDS arrangement in 2D perceptual space was valid for small resultant forces. The MDS analysis demonstrated that for nonlinear elastic tissue models exhibiting the Poynting effect, both shear and normal forces affected user perception.

This study provides a concrete example of how tissue modeling techniques relate to user perception of forces (haptic feedback) in surgical simulation systems. Other modeling factors that affect the deformation response of the organs include anatomical details and the shape of the surgical tools interacting with the organs. In the next chapter, we investigate the importance of organ geometry and surrounding boundary constraints for surgical planning systems.

Chapter 4

The Importance of Organ Geometry and Boundary Constraints for Planning of Medical Interventions

4.1 Introduction

The development of realistic surgical simulation systems requires accurate modeling of organs and their interactions with the surrounding organs and tissues, as well as the instrumentation tools. Tool-tissue interaction modeling is useful for training, planning, and practice of surgical and medical interventional procedures. Further, modeling such interactions helps in optimizing surgical tool design, creating "smart" instruments capable of assessing pathology, and understanding tissue injury mechanisms and damage thresholds.

Chapter 2 highlighted tool-tissue interaction models, complete simulator design approaches, specific medical applications, and training evaluation methods have been widely studied in the last two decades [39, 40, 146]. However, developing accurate models for surgical simulation is challenging. Biological tissues are generally inhomogeneous, anisotropic, and viscoelastic, and require complex experimental techniques to measure accurate force versus displacement characteristics in a laboratory. Further, development of organ models requires measurement of tissue properties *in vivo*, since organs have significantly different dynamics due to variations in temperature and blood circulation, which are difficult to precisely replicate during *ex vivo* experiments. Moreover, the task of choosing an appropriate constitutive law that describes the stress-strain response of the tissue under various loading conditions is not straightforward. On the other hand, current medical imaging modalities such as x-ray, ultrasound, computed tomography (CT) scans, and magnetic resonance (MR) images, can be used to determine organ geometry with a high level of accuracy. Complex boundary constraints and connective tissues that support the organs can also be observed, but with less accuracy.

Many surgical and interventional procedures require generating a plan prior to performing the task, which is typically performed with the aid of one or more of the imaging techniques listed above. The development of a patient-specific plan is critical in many surgical and interventional radiology procedures for drug delivery and biopsies, brachytherapies, and tumor ablations, during which needles must reach specific deep locations inside the organ. Prostate brachytherapy is one example of a procedure that requires target-specific

needle insertion, so that radioactive seeds can be permanently implanted in the prostate for cancer destruction. Transrectal ultrasound (TRUS) imaging or MR imaging with an endorectal coil are imaging modalities used clinically to guide the needle to its intended target. The success of the brachytherapy depends on the accuracy of placement of seeds, whose locations are determined during the planning stage of the procedure. Deformations caused during the pre-rupture phase, and also during needle insertion and retraction, can result in the needle missing its intended target. Thus, a method to predict the deformation of the organ prior to needle insertion would help clinicians in planning the path of the needle through tissue.

Patient-specific organ models useful for planning surgical or other interventional procedures and predicting tissue deformation require knowledge of the organ anatomy and its surrounding tissues, as well as information about the properties of all tissues involved in the surgical procedure. In this study, we hypothesize that organ geometry and boundary constraints play the most important role in determining the deformation of the organ during planning of procedures such as needle insertion. As highlighted in Chapter 2, several researchers have studied interactions between needles and soft tissues for surgical simulation and planning using continuum mechanics-based formulation techniques [15, 46, 75, 76, 80, 84, 115, 168]. Among these studies, [75, 84, 115] specifically investigated needle insertion during prostate brachytherapy. All these studies presented methods to model the needle-tissue interaction forces and computational techniques required to enhance the simulation environment for real-time applications such as visual display

of realistic organ deformations, haptic feedback, or surgical path planning, and did not consider detailed anatomical structures surrounding the organ. For example, Mohamed et al. [169] studied deformations of the prostate by considering a simple geometry (the prostate was an egg-shaped structure while the rectum was a cylinder) and limited boundary conditions (sacrum and pubic arch) along with a nonlinear elasticity-based model. By considering some anatomical details, a nonlinear constitutive law, and statistical modeling techniques, their goal was to predict deformations of the prostate. In another example, Dehghan and Salcudean [147] compared the effects of linear and nonlinear FE models on the mesh displacement during needle insertion and concluded that in the presence of asymmetric boundary conditions, noticeable differences result. All of the studies mentioned above emphasized the importance of realistic tissue properties in their work and few studies have also incorporated anatomical details in their models. However, no prior work has quantified the effects of both material properties and realistic anatomical details on accurate simulation of invasive procedures, such as needle insertion.

In this chapter we show that when an organ is subjected to displacements during needle insertion, the geometry and boundary constraints surrounding the organ rather than the constitutive model dominate its deformation response. For this work, we considered the clinical application of needle insertion into the prostate (e.g. for biopsy or brachytherapy). We extracted pertinent anatomical structures from an MR image and generated a FE mesh in order to study the deformation of the prostate. In order to simulate the relative contact between the prostate and its surrounding tissue, we employed cohesive zone models. Fi-

nally, we conducted sensitivity studies to show the effects of including of these boundary constraints in the model.

This chapter is organized as follows: Section 4.2 presents representative cases that highlight the importance of geometry and boundary constraints for path planning surgical procedures. Section 4.3 applies these approaches specifically to needle insertion into the prostate and describes a method to generate FE meshes from MR images, while Section 4.4 presents the results of the sensitivity studies. Section 4.5 concludes by summarizing the results of this chapter.

4.2 Study of Model Systems

The deformation of organs when interacting with interventional tools is fundamentally governed by the following factors: (1) organ geometry, (2) soft tissue properties, and (3) boundary constraints due to surrounding structures that support the organ. In surgical and other interventional procedures such as needle insertion, the clinician intends to reach a designated target. This implies that the input to the system is a displacement that results

Geometry	Square (*S*)	Circle (*C*)
Boundary condition	Fixed edge (*F*)	Partially constrained (*P*)
Material behavior	Linear elastic (*L*)	Hyperelastic (*H*)

Table 4.1: Study of some of the factors affecting deformation of organs viz. geometry, boundary condition, and material behavior; combinations of the various factors result in 8 simulation cases with the following nomenclature: *SFL*, *SFH*, *SPL*, *SPH*, *CFL*, *CFH*, *CPL*, and *CPH*.

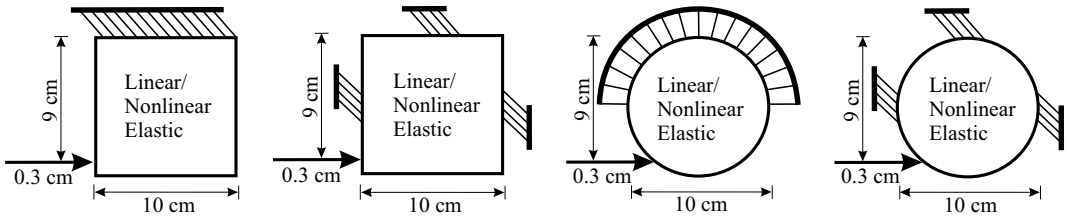

(a) *SFL*, *SFH* (b) *SPL*, *SPH* (c) *CFL*, *CFH* (d) *CPL*, *CPH*

Figure 4.1: Simulation scenarios where the top edge was completely fixed and partially constrained edges, for objects with square and circular geometries. These represent a total of 8 simulation cases, in which the constitutive laws of the objects are described by linear elastic or hyperelastic models.

in deformation of the organ. In order to understand and quantify the significance of each of the items, we performed a set of simulation studies of model systems, in which two sets of geometries (square and circle), linear and nonlinear elasticity-based material properties, and different boundary conditions were compared. Table 4.1 provides the range of variables considered. The simulation cases with the boundary conditions and applied displacements are depicted in Figure 4.1.

4.2.1 Constitutive Models

Most simulators today use a linear elastic assumption. For homogenous and isotropic models, the Cauchy stress tensor, σ, and the infinitesimal strain tensor, ε, given in component form, are related by

$$\varepsilon_{ij} = \frac{1+\nu}{E}\sigma_{ij} - \frac{\nu}{E}\sigma_{kk}\delta_{ij}, \tag{4.1}$$

where E and ν are the Young's modulus and Poisson's ratio of the material, respectively, and δ_{ij} is the Kronecker delta.

However, since biological organs undergo large strains, hyperelastic models are better suited to describe the constitutive behavior of soft tissues. Hyperelastic models are defined by a strain energy density function, W, associated with the material. The Mooney-Rivlin model is commonly used to approximate the response of rubber-like materials and some biological tissues [10], and was chosen for our analysis. For incompressible and isotropic materials, the Mooney-Rivlin model is of the form

$$W = C_1 (I_1 - 3) + C_2 (I_2 - 3), \tag{4.2}$$

where I_1 and I_2 are the invariants of the right Cauchy-Green deformation tensor, $\mathbf{C} = \mathbf{F}^T \mathbf{F}$, and $\mathbf{F}$ is the deformation gradient tensor. C_1 and C_2 are material properties. The first Piola-Kirchhoff stress in the material as a result of deformation can be obtained from

$$\mathbf{P} = \frac{\partial W(\mathbf{F})}{\partial \mathbf{F}}, \tag{4.3}$$

The Cauchy stress tensor, $\boldsymbol{\sigma}$, and first Piola-Kirchhoff stress tensor, $\mathbf{P}$, are related by

$$\mathbf{P}\mathbf{F}^T = J\boldsymbol{\sigma}, \tag{4.4}$$

with $J = \det(\mathbf{F})$. The invariants of $\mathbf{C}$ are

$$I_1 = \mathbf{C} : \mathbf{I}, \tag{4.5}$$

$$I_2 = \frac{1}{2}\Big((\mathbf{C} : \mathbf{I})^2 - (\mathbf{C} : \mathbf{C})\Big), \tag{4.6}$$

$$\text{with } I_3 = \det \mathbf{C} = 1 \text{ for incompressible materials,} \tag{4.7}$$

where $\mathbf{I}$ is the indentity tensor.

4.2.2 Modeling Methods

The simple square- and circular-shaped objects with distinctly different boundary constraints and elastic behavior provide example models that allow us to assess the importance of factors affecting the object's deformation under applied displacement conditions. We performed 2D FE simulations to quantify the relevance of these factors, namely object geometry, boundary condition, and material behavior. FE simulations of the 8 cases, as highlighted in Table 4.1 and Figure 4.1, were performed using the ABAQUS/Standard [97] simulation environment. The elements consisted of 8-node biquadratic plane strain quadrilaterals (ABAQUS element *CPE*8*H*) with nodes placed 1 mm apart for the square- and circular-shaped geometric objects. Plane strain FE models assume that the object is infinitely thick, so out-of-plane strains are not considered. This assumption is applicable for both models considered in this section and for the 2D simulation models presented in the

following sections. Mesh resolution sensitivity studies were also performed to ensure that nodes placed 1 mm apart resulted in convergence of solution. Figure 4.3(a) provides as an example, a mesh of coarser resolution used for the square object with partially fixed boundary constraints and shows the location of applied displacement. Also shown in the figure is the location of one representative node whose displacements were scrutinized in detail.

ABAQUS provides the capability to input both linear and nonlinear constitutive laws, along with user-defined boundary conditions and input displacements. For the linear elastic case, the Young's modulus, E, and the Poisson's ratio, ν, were set to 15 kPa and 0.49, respectively. These were reported in [170] as a linear elastic approximation to liver. For the nonlinear case, we choose the Mooney-Rivlin model described in (4.2), and the material parameters C_1 and C_2 were assigned to be 3.46 kPa and 2.78 kPa, respectively. These were obtained via *in vivo* indentation studies on porcine liver [170].

4.2.3 Simulation Results for Model Systems

Contour plots depicting the resultant magnitude of the computed nodal displacements for the square- and circular-shaped geometries are shown in Figure 4.2. For both the square and circular geometric objects, the differences in boundary constraints result in varying displacement contour plots. Thus, the displacement fields are insensitive to material properties. However, the maximum increase in the von Mises stress, for a given geometry and boundary constraint, was observed to be 188.6%. This increase was between the *CPL* and

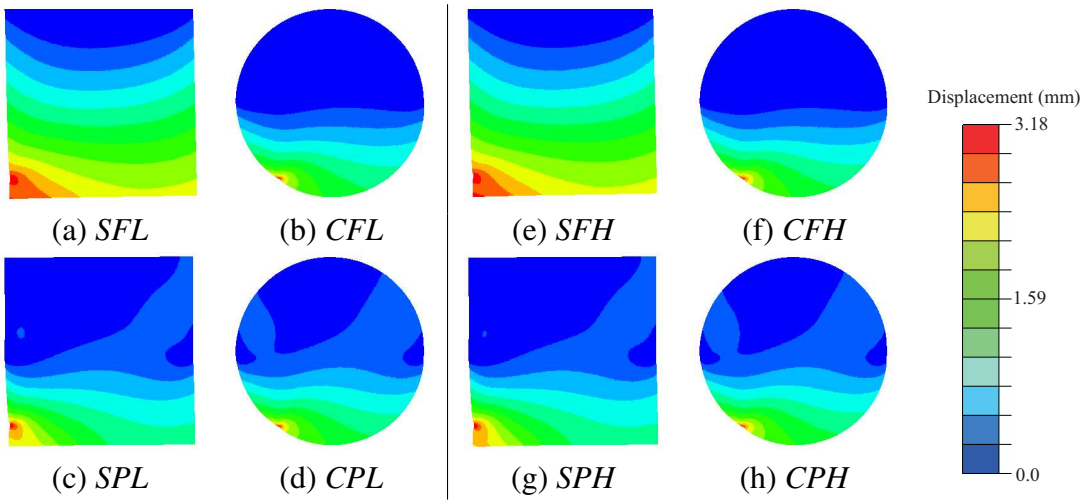

Figure 4.2: Contour plots depicting the magnitude of the nodal displacements for the 8 simulation cases. The nomenclature for the 8 simulation cases are: *S*: Square, *C*: Circle, *F*: Fixed edge, *P*: Partially constrained, *L*: Linear elastic, and *H*: Hyperelastic.

CPH cases. Figure 4.3(a) depicts a representative node used to compare nodal displacements for the 4 simulation cases for the square object, while Figure 4.3(b) provides the magnitude of the displacements at the node. The maximum increase in nodal displacement between the *SPL* (or *SPH*) and *SFL* (or *SFH*) cases was observed to be 55.1% at the representative node.

Needle insertion procedures are primarily displacement-driven problems, and our results indicate that the deformation response of the object is sensitive to boundary conditions surrounding it and not to its material properties. The *SFL* and *SPL* results are quantitatively different, as are *SFL* and *CFL*. When the input to the system is displacement, the deformation of the object is relatively insensitive to the constitutive law. On the other hand, the stresses induced in the material are very different for the linear and nonlinear elastic mod-

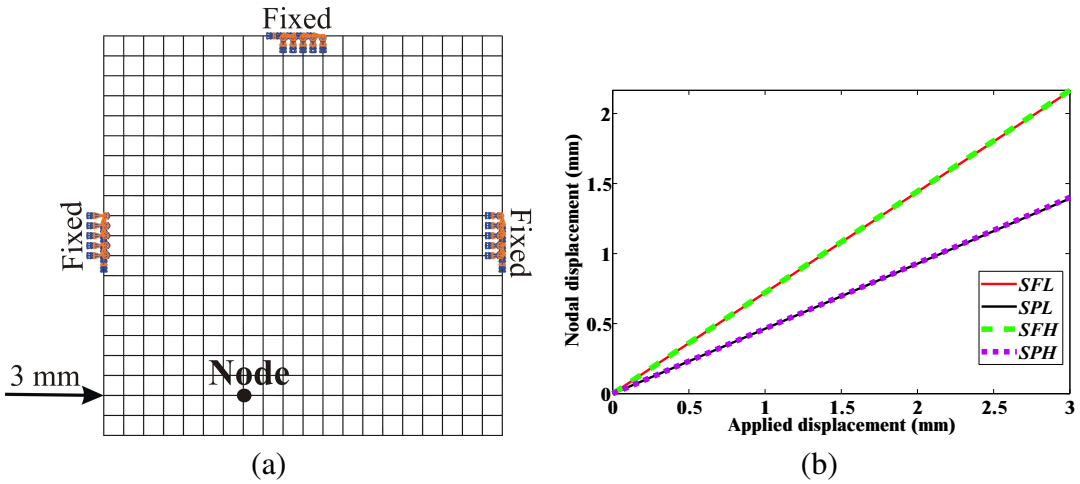

Figure 4.3: Simulation conditions for the square object: (a) Example mesh where nodes are placed 5 mm apart for clarity, with partially constrained boundary conditions, applied displacement of 3 mm, and representative node. (b) Magnitude of nodal displacement for the 4 simulation cases (*SFL*, *SPL*, *SFH*, and *SPH*) at the representative node.

els, since displacements are related to the stresses via the material properties, as shown in (4.1) and (4.4) for linear and nonlinear elastic models, respectively. This implies that, for needle insertion procedures in which linear approximations of the tissue properties are available and needle bending is not of concern, greater emphasis must be placed on accurately modeling the organ geometry and tissues surrounding the organ.

4.3 Prostate Model

In the previous section, we compared square and circular geometric objects with simplified boundary constraints, which do not represent specific human organs. In this section, we apply the results obtained from the previous section to invasive procedures involving needle insertion, examples of which are biopsies, brachytherapies, and tumor ablations.

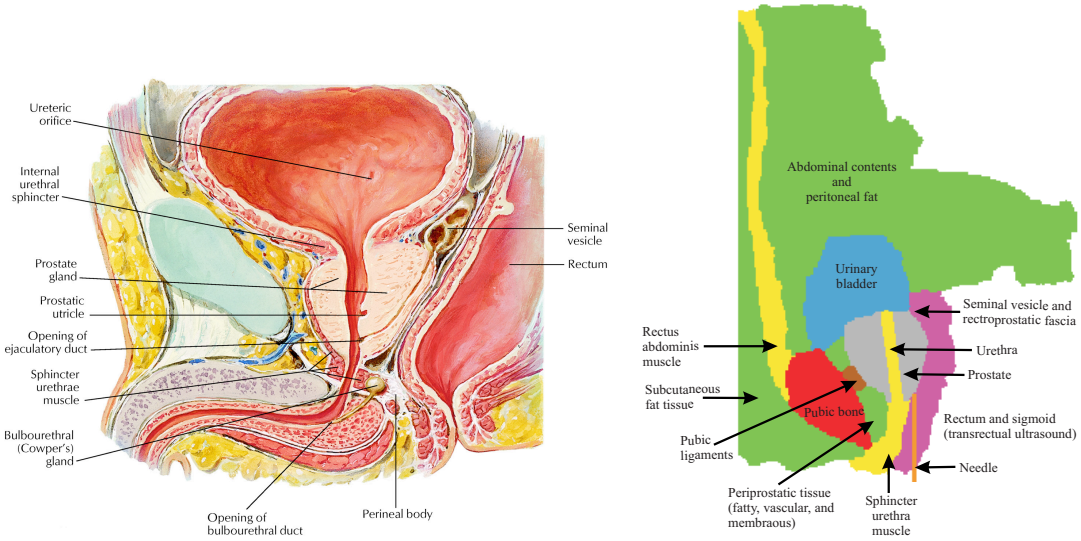

Figure 4.4: Boundary constraints surrounding the prostate gland: (a) A close-up view of an anatomically accurate drawing of the male human pelvis [21]. (Reprinted from Netter Anatomy Illustration Collection, ©Elsevier Inc. All Rights Reserved.) (b) Sagittal schematic (based on an MR image) identifying the various tissues and organs. The urethra passes through the prostate and connects the urinary bladder to the sphincter urethra muscle, and the pubic ligaments connect the prostate to the pubic bone.

In order to determine the importance of organ geometry and boundary constraints during a clinically relevant interventional procedure, we will examine needle insertion into the prostate for the purpose of brachytherapy. Prostate cancer is one of the most common malignancies among men and prostate brachytherapy represents one of the treatments options. This procedure consists of permanently placing radioactive seeds, most often ^{125}I, inside the prostate via needles passing through the perineum, relying intensively on imaging guidance using TRUS [171] or MR imaging [172].

In order to model the boundary constraints of the prostate accurately, we need to identify the various anatomical structures, that surround the prostate and connect it to other

organs. Figure 4.4(a) shows an anatomically accurate drawing of the male human pelvis in the sagittal plane, while Figure 4.4(b) provides a sagittal schematic of the various fatty tissue, ligaments, muscle, and bone surrounding the prostate based on an MR image (Figure 4.5). The urethra passes through the prostate and there are pubic ligaments attached to the prostate and the pubic bone. Also, Figure 4.4(b) shows the probable needle insertion location and applied displacement during insertion. In addition to identifying the boundary constraints of the prostate gland, it is necessary to model the geometry of the prostate as well as its surrounding tissue. In order to accomplish this, we extracted the geometric information from a sagittal view of an MR image. As opposed to other imaging modalities, MR images have larger field of view and produce the highest resolution of detail for pelvic soft tissues including prostate and surrounding structures, which in turn results in better segmentation of organ geometry. The MR image was acquired in a 3D T2-weighted sequence of the male pelvis at 3.0 T magnetic field strength (TR: 1600 ms, TE: 115 ms, field of view: 35 cm, slice thickness: 1 mm with no gap) and was reconstructed in the sagittal plane. The various anatomical parts, identified in Figure 4.4(b) and extracted from the MR image in Figure 4.5(b), were segmented using the random walker algorithm presented in [22]. Figure 4.5(c) shows the final segmented image generated from the input MR image, with the prostate in black. The random walker algorithm uses image intensities to segment an image without any prior model for the segmentation target. Therefore, it is difficult to categorize the accuracy of segmentation since the algorithm is a general purpose segmentation tool as opposed to being application specific. However, note that the random

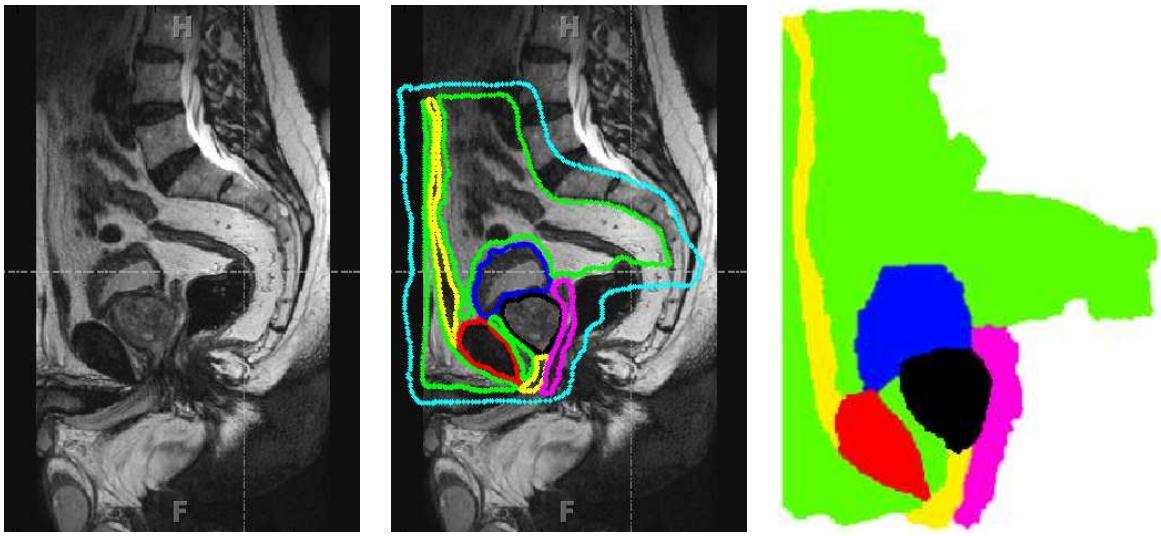

(a) (b) (c)

Figure 4.5: Segmentation of an MR image using the random walker algorithm [22]. (a) Sagittal view of the male pelvis. (b) Approximate location of the prostate and surrounding tissue identified, where the cyan color indicates the anatomy not of interest. (c) Segmented image, where the colors red, magenta, green, yellow, black, and blue signify bone, fascia, fat, muscle, prostate, and urinary bladder, respectively and also entered in Figure 4.4.

walker algorithm is an interactive technique and one can easily correct any errors in the segmentation results obtained in the first attempt. In particular, if the user is not satisfied with the required result, additional scribbles (points) can be added to improve the segmentation. Due to the lack of ground truth segmentation, we performed a qualitative evaluation of our segmentation. More specifically, an experienced radiologist confirmed that the estimated segmentation (shown in Figure 4.5(c)) is of high level of accuracy. Moreover, there has been a comparison of the random walker algorithm with state of the art segmentation schemes and it has been shown that the algorithm's performance is robust to changes in placement of the scribbles [173]. In this study, segmentation is an intermediate step in the process of developing FE meshes. The random walker algorithm was able to segment the

Tissue	E (kPa)	ν
Bone	1.80×10^6	0.3
Fascia	4249.78	0.45
Fat	3.25	0.45
Ligament	489.71	0.45
Muscle	29.85	0.45
Prostate	60.0	0.45
Urinary bladder	1.32×10^4	0.499

Table 4.2: Material properties of prostate and surrounding tissue were obtained from [1] and [2], respectively. These model constitutive parameters were derived from *ex vivo* tests. The properties of the urinary bladder were assumed to be that of water, with a bulk modulus, $K = 2.2$ GPa i.e. $E = 3K(1-2\nu)$.

MR image with desired accuracy levels.

Software for conversion from segmented images to FE meshes exist, examples of which are [174, 175]. Bharatha et al. [176] used the FE mesh generation algorithm described in [174] in order to generate a mesh while Crouch et al. [177] generated a FE mesh after image segmentation using the m-rep technique, which are a multiscale medial means for modeling 3D solid objects. Both studies only segmented the prostate gland. On the other hand, Sullivan et al. [175] developed a system to generate 3D elements and applied their technique to the abdominal region of a human body model and meshed the following regions: air, water, fat, bone, kidney, rectum, stomach, appendix, muscle, liver, bladder, prostate, and intestines. For our study, the FE mesh was generated from the segmented MR image using the open source object-oriented finite element analysis (OOF) [178] software developed by the US National Institute of Standards and Technology (NIST). OOF was designed to help materials scientists calculate macroscopic properties of materials from

images of microstructures. The FE mesh generated consisted of 8090 4-node bilinear plane strain quadrilateral elements (ABAQUS element *CPE*4) as shown in Figure 4.6. Further, mesh resolution sensitivity studies were done to ensure that 8090 elements resulted in convergence of solution. The material properties assigned to the prostate and surrounding tissue are given in Table 4.2. It is difficult to acquire and test tissue samples of the prostate gland and surrounding organs. Further, most soft tissue constitutive model parameters are based on data acquired *ex vivo* (rather than *in vivo*) and there exists limited published data [2, 10].

As the needle indents, punctures, and travels through the prostate, the gland slides and shears with respect to its surrounding tissue. In order to simulate this interaction between the prostate and its surrounding structure, we employ cohesive zone (also known as relative slip) models (Figure 4.7). Cohesive zone modeling techniques are commonly used to simulate interface failure in composite structures [179]. The cohesive zone is a mathematical approach to modeling the fact that work must be done to separate the two surfaces at an interface. This work is described in terms of a prescribed relationship between the forces required to separate the surfaces and the relative displacements of those surfaces. Cohesive zone elements are placed between bulk elements, as shown in Figure 4.7. A detailed explanation of the numerical implementation of cohesive zone models is presented in [180]. Alternatively, modeling the relative slip between the prostate and its surrounding tissue could be simulated as a contact problem. This method is computationally challenging since the interaction forces and displacements between elements are computed on the

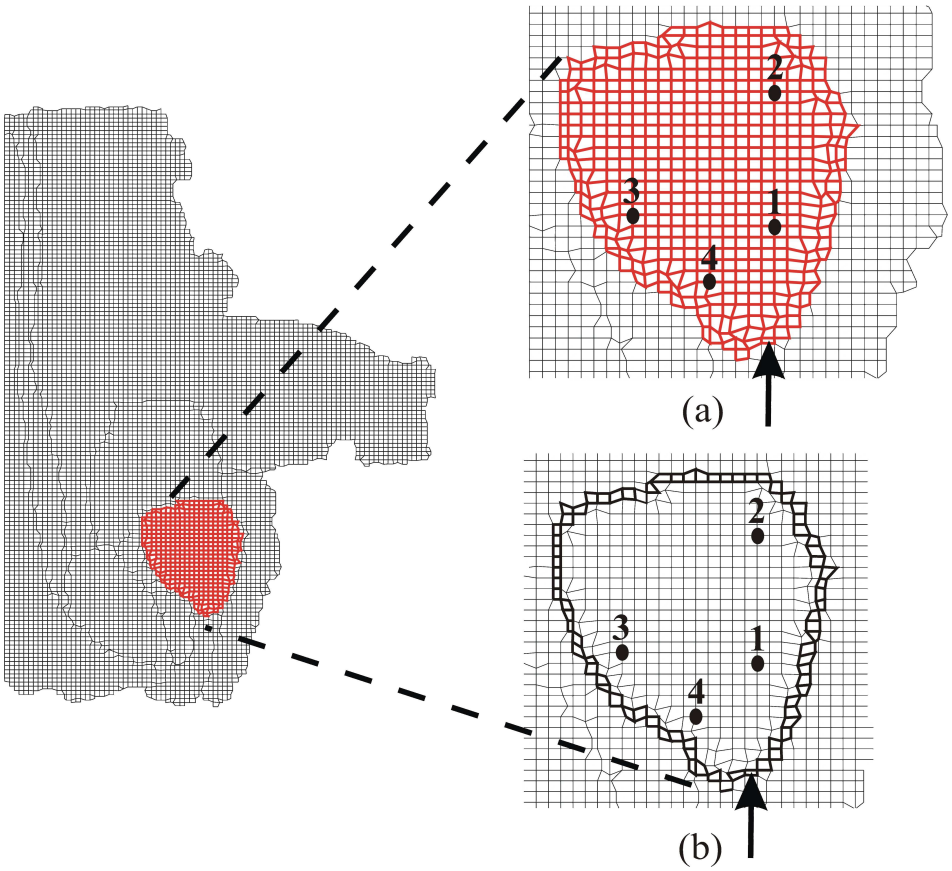

Figure 4.6: FE mesh of the prostate with its surrounding tissue generated from the segmented MR image used for simulation studies. (a) Close-up view of the simulation case where no cohesive elements surround the prostate (*NoCoh*). (b) Close-up view of the simulation case where prostate gland is surrounded by cohesive elements (in bold black) (*Coh*). Also shown are the data points at which nodal displacement were measured and the point of applied displacement used to simulate needle insertion.

basis of the inter-penetration distance between elements. Cohesive zone models are not plagued by such numerical instabilities and present an efficient solution to simulate interaction between elements.

The cohesive zone elements were defined around the prostate and are placed between continuum (bulk) elements, as shown in Figure 4.7(a). In our FE models, the cohesive zone

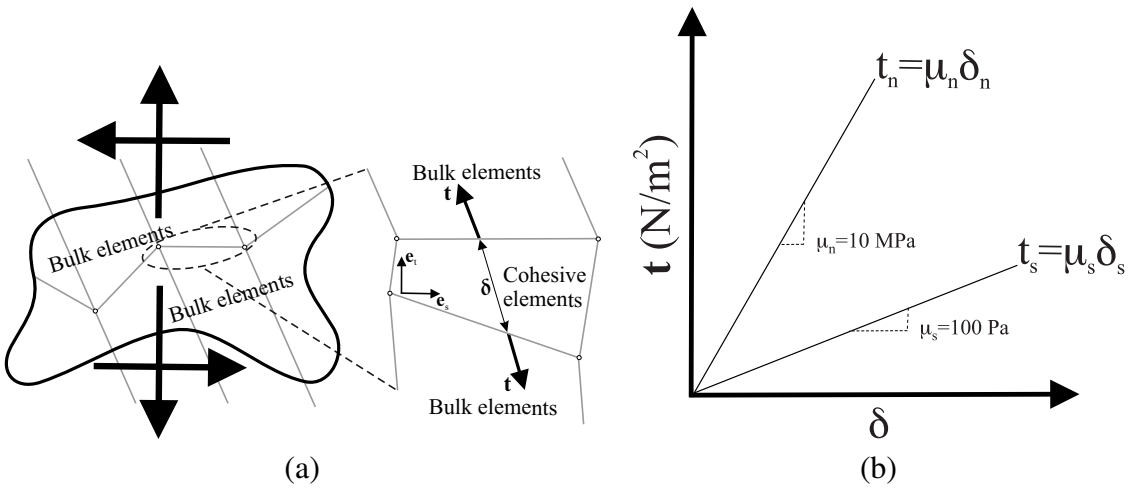

Figure 4.7: The cohesive zone model. (a) A sketch depicting application of cohesive zone elements along the bulk element boundaries; tensile/compressive (normal) and shear displacements result in deformation of the cohesive elements. (b) Linear traction-strain laws with 10 MPa and 100 Pa normal elastic and shear elastic moduli, respectively.

was implemented using 4-node elements (ABAQUS element *COH2D4*). The applied displacement primarily results in sliding of the prostate with respect to its surrounding tissue, and cohesive zone elements open up and deform in order to simulate this behavior. All of the cohesive elements use a traction-strain law (Figure 4.7(b)), which defines the relationship between the vectorial tractions (force density vectors), $\mathbf{t}$, and strains, $\boldsymbol{\delta}$, across the element. For unit original constitutive thickness of the cohesive element, which is different from the geometric thickness (which is typically close or equal to zero), the separation displacement is equal to the strain of the cohesive element. Thus, the tractions and strains are

given by

$$\begin{aligned} \mathbf{t} &= t_n \mathbf{e}_n + t_s \mathbf{e}_s, \\ &= \mu_n \delta_n \mathbf{e}_n + \mu_s \delta_s \mathbf{e}_s, \end{aligned} \tag{4.8}$$

where

$$\boldsymbol{\delta} = \delta_n \mathbf{e}_n + \delta_s \mathbf{e}_s, \tag{4.9}$$

and t_s, t_n and δ_s, δ_n are tractions and strains in the shear and normal directions, respectively. The description of the deformation and the traction evolution in these elements is governed by a linear traction law, as shown in Figure 4.7(b). Given that the relative tangential sliding is expected to be easier than normal separation or inter-penetration, we arbitrarily choose a tensile/compressive (normal) elastic modulus, μ_n, of 10 MPa and shear elastic modulus, μ_s, of 100 Pa. Changing the individual elastic moduli values by an order of magnitude did not produce significant variations in results. Experimentally-derived values for these moduli could be obtained from force-displacement measurements of the prostate interacting with its surrounding tissue, but are not currently available.

4.4 Sensitivity Studies for the Prostate Model

The deformation of the prostate gland during needle insertion can be classified into the following three distinct phases [86, 91]:

- First, the prostate undergoes elastic deformation as the tip of the needle indents the outer surface of the gland prior to puncturing the gland's capsule. The prostatic capsule is a fibromuscular membrane encasing the prostate.

- Second, the user-defined needle displacement induces a load on the prostate. When this load reaches a critical threshold the gland ruptures. The rupture process is characterized by a sharp and recognizable peak in the local organ deformation and load.

- Third, following rupture, the needle penetrates the tissue by cutting its surface. The fracture toughness of the material is the energy necessary to increase the area of fracture by an incremental amount and governs the propagation of rupture through tissue.

Consultations with clinicians and observations of needle insertion procedures indicated that maximum organ deformation occurs during the pre-rupture (first phase) stage of the prostate and the simulation of this phase is described in the chapter. In order to simulate this process, a displacement boundary condition of 3.25 mm was applied to nodes on the outer periphery of the prostate as shown in Figure 4.6. The external boundary of the FE model (Figure 4.6) was fixed since this represents regions that are outside the human body or far away from the prostate gland, so they do not affect the prostate's deformation. Further, the region marked as rectum and sigmoid in Figure 4.4(b) contains the transrectal probe or endorectal coil (depending on the imaging modality used for guiding the needle). These devices are relatively stiff and so are simulated as a fixed boundary condition. It should

be noted that the MR image (Figure 4.5(a)), from which the FE models were generated, does not contain a transrectal probe. But an image with a transrectal probe could be segmented and meshed using the procedure described earlier. As highlighted in the anatomical drawing and sketch in Figures 4.4(a) and (b), respectively, the urethra is embedded in the prostate tissue and pubic ligaments are not visible in an MR image, but (because of their relative stiffnesses) they should be accounted for in the simulation model. Figures 4.8(a) and (b) depict the elements assigned to be urethra muscle and pubic ligaments, respectively, and the cohesive zone has been modified to account for the urethra and pubic ligaments. The material properties for these tissues are given in Table 4.2.

In order to understand and compare the various modeling techniques we performed simulation studies with the following scenarios:

1. *NoCoh*: No cohesive zone or relative slip model employed (Figure 4.6(a)).

2. *Coh*: Cohesive zone model between the prostate and surrounding organs (Figure 4.6(b)).

3. *CohUr*: Cohesive zone model around the prostate and urethra passing through the prostate (Figure 4.8(a)).

4. *CohLig*: Cohesive zone model around the prostate and pubic ligaments attached to the prostate (Figure 4.8(b)).

5. *Crop*: A simpler model that is a cropped version of our original mesh wherein the

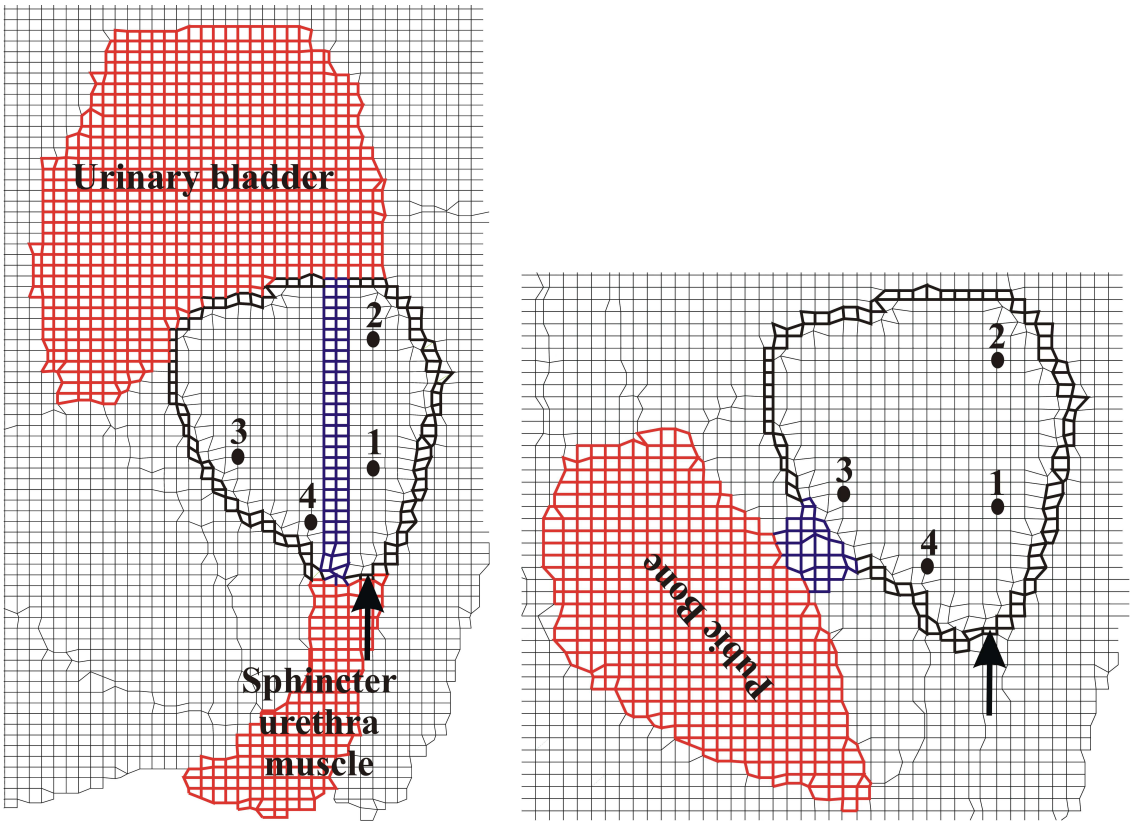

(a) (b)

Figure 4.8: Close-up views of FE meshes used for sensitivity studies. (a) Inclusion of the urethra (in blue) passing through the prostate (*CohUr*). (b) Pubic ligaments (in blue) connecting the prostate to the pubic bone (*CohLig*). The elements corresponding to the urethra and pubic ligaments have material properties associated with muscle and ligaments as provided in Table 4.2, respectively. The figure also shows the modified cohesive zone (in bold black) surrounding the prostate, location of applied displacement, and representative nodes.

surrounding tissue properties had been assigned a single value of 30 kPa and the boundary mesh had been fixed only in the region to the right of the prostate, to signify the presence of the transrectal probe or endorectal coil (Figure 4.9). This simulation case represents a 2D approximation to traditionally performed modeling scenario for

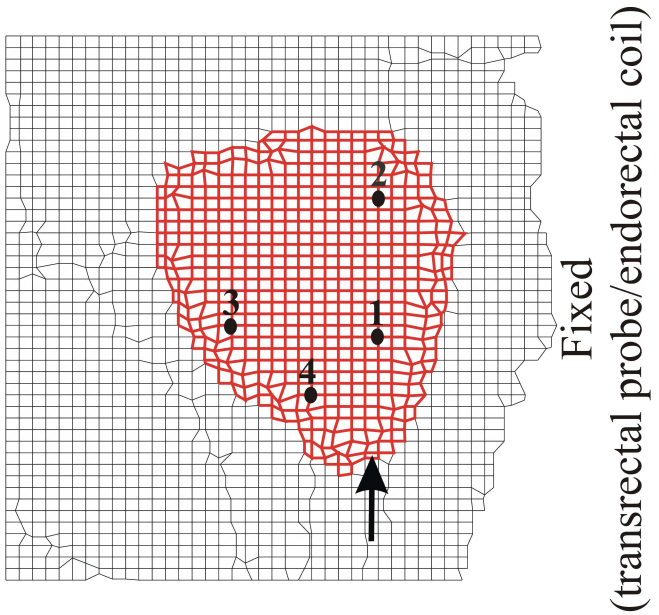

Figure 4.9: Simplified mesh generated by cropping the original mesh with only the right-hand side fixed (*Crop*). Location of representative nodes are also shown.

prostate brachytherapy where detailed organ geometry and boundary conditions are not considered [75, 79, 115].

In order to quantify the deformation of the prostate mesh for the five simulation cases, we observed the nodal displacement at the same 4 nodes specified in Figures 4.6, 4.8, and 4.9. Figure 4.10 shows the nodal displacements for the 5 simulation cases. In Figure 4.10(a), we provide the nodal displacement for simulation cases *NoCoh* and *Crop*, model with detailed anatomy and cropped up mesh, respectively. The maximum nodal displacement at node 3 for *Crop* was 14 times larger than that observed for *NoCoh*. Figure 4.11 depicts the magnitude of prostate nodal displacement for both *NoCoh* and *Crop* simulation cases. The deformation of the nodes is similar for both cases close to the location of the

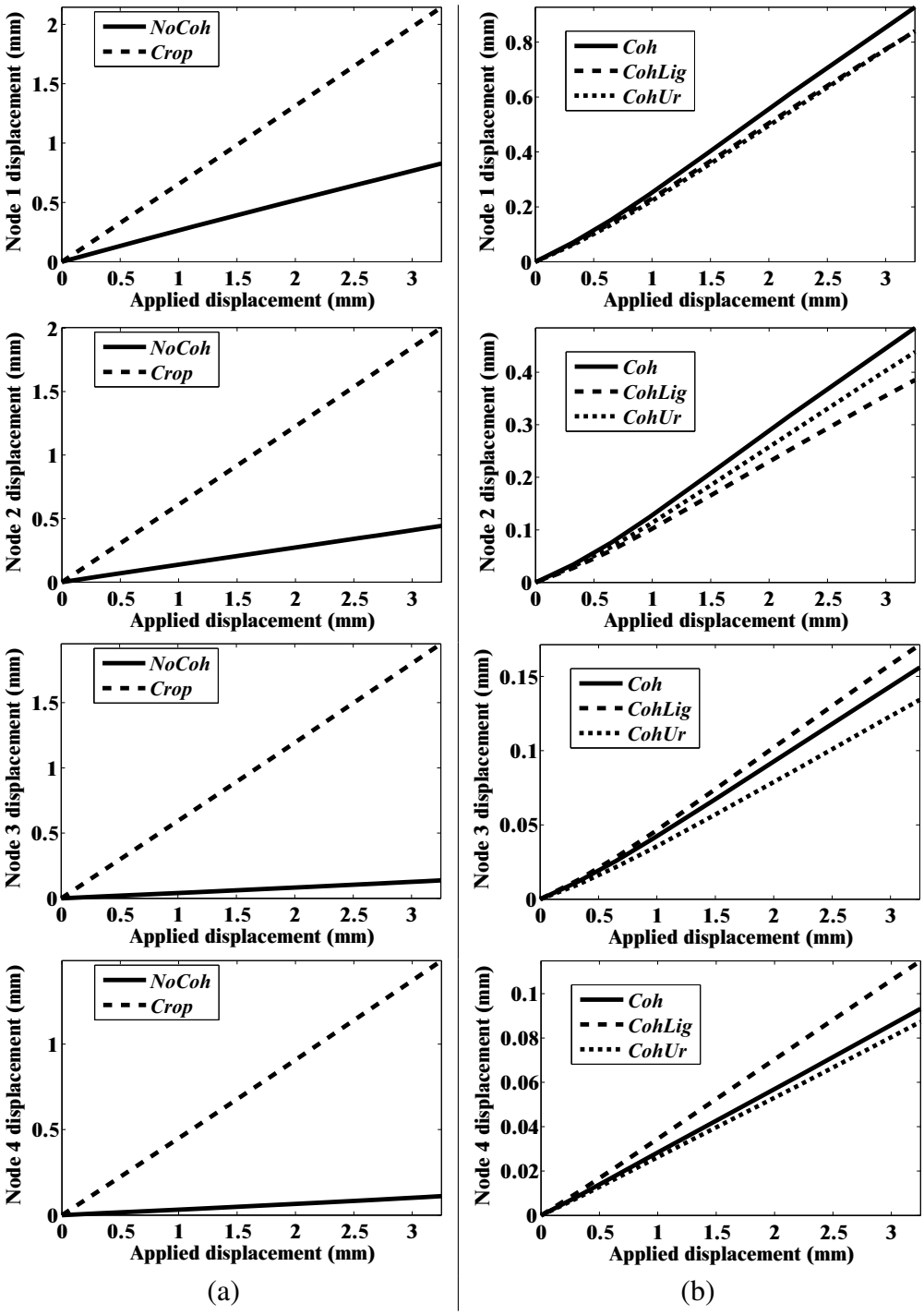

Figure 4.10: Nodal displacement for the 5 simulation cases: (a) *NoCoh* and *Crop* (b) *Coh*, *CohUr*, and *CohLig*

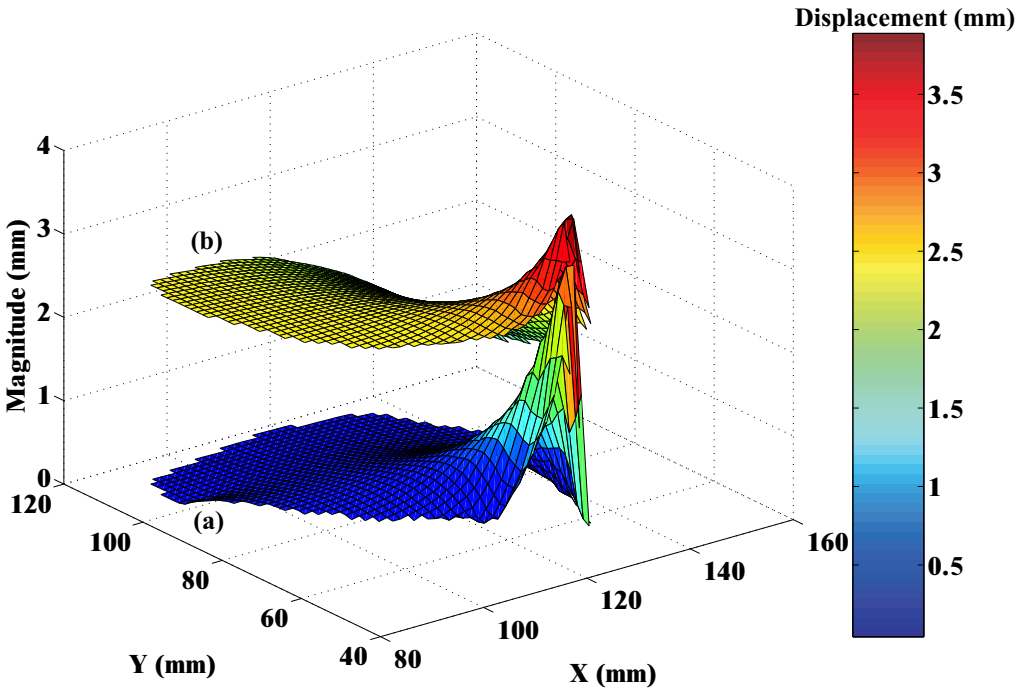

Figure 4.11: Surface plots depicting the magnitude of nodal displacements for the prostate, where X and Y axes represent the nodal co-ordinates of the prostate in the FE model. (a) Simulation with complex anatomy and boundary conditions (*NoCoh*) and (b) simulation with simple organ geometry and boundary conditions (*Crop*). For both simulation cases relative motion between the prostate and surrounding tissue is not modeled.

input displacement, but further away the magnitudes of displacement are highly dissimilar. In Figure 4.10(b) we compare nodal displacements for the simulation cases *Coh*, *CohUr*, and *CohLig*. In addition to having complex geometry and boundary conditions, these simulation cases also include cohesive zones, the urethra passing through the prostate, and pubic ligaments connecting the prostate to the pubic bone, respectively. A 9.5% (at node 1) and 20.4% (at node 2) increase in maximum nodal displacement was observed for the *CohUr* and *CohLig* cases, respectively, when compared to *Coh*. Thus, in the 2D simulation cases, the inclusion of the urethra and pubic ligaments did not cause large differences in the

nodal displacement. However, significant differences in nodal displacement are observed between the anatomically accurate and simpler models.

4.5 Summary

Biopsies, brachytherapies, and other needle insertion procedures are primarily displacement-driven interventional operations. This means that the clinician applies an input displacement to the needle in order to reach the target, and this applied displacement results in deformation of the organ. For one such task, our results show that the organ geometry and boundary constraints surrounding the organ (rather than the constitutive behavior of the tissue) dominate its deformation. We apply this approach to the clinical procedure of needle insertion into the prostate by identifying boundary constraints and tissue surrounding the prostate gland, and simulated the pre-rupture deformation of tissue. We compare our results to a case where the anatomy surrounding the prostate was not accurately defined, and our results show that the use of more detailed geometry results in significantly smaller displacements (by a factor of 14 at one representative point). It should be noted that this study does not attempt to equate greater or lesser nodal displacements to better performance of the model. Rather, it presents sensitivity studies in which simulation models of varying fidelity (in terms of realistic organ geometry and surrounding boundary constraints) are compared. We believe our study is the first to consider this level of sophistication in simulation by incorporating anatomical details and using the concept of cohesive

zone models to account for relative slip between the prostate and surrounding tissue.

The previous chapter investigated the importance of soft tissue constitutive laws in the context of surgical simulation. The current chapter quantitatively demonstrated that anatomically valid organ geometry models and appropriate boundary constraints are essential for accurate simulation of organ deformation during planning of invasive surgical procedures. In the following chapter, we investigate the importance of the shape of the surgical tool and tissue properties in the context of surgical planning. We specifically examine the interaction of robotically steered flexible bevel-tip needles with soft tissues.

Chapter 5

Effects of Tool Geometry and Tissue Properties for Medical Intervention Planning

5.1 Introduction

Percutaneous needle insertion is one of the most common minimally invasive clinical procedures. It is used for diagnosis, localized therapeutic drug delivery, and sample removal from tissues deep within the body. Inaccurate needle placement may result in malignancies not being detected during biopsy, radioactive seeds not being placed in the correct location to destroy cancerous lesions during brachytherapy, and traumatic or even

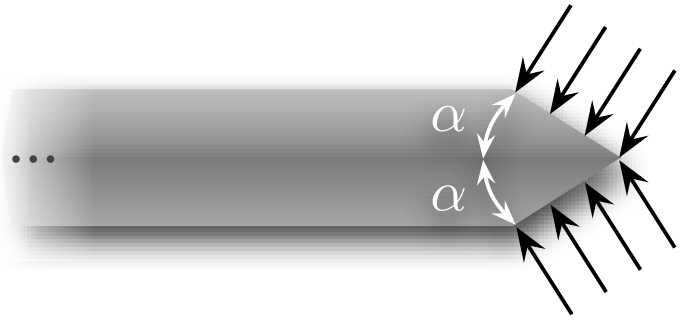

(a) Symmetric needle tip.

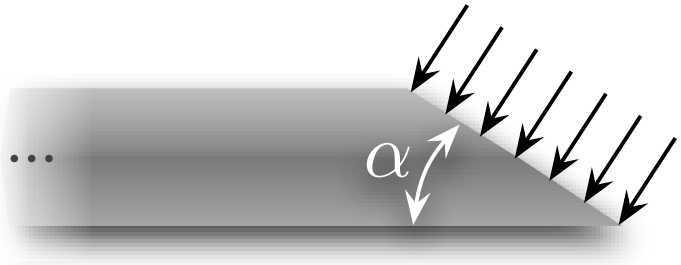

(b) Asymmetric (bevel) needle tip.

Figure 5.1: Asymmetry of the bevel tip produces a resultant transverse load which causes the flexible needle to naturally bend when it interacts with a soft medium. This phenomenon is not observed in needles with symmetric tips.

fatal effects during administration of anesthesia. Thus, for effective medical diagnoses and treatments, the needle must reach its intended target. However, a variety of issues (e.g. tissue inhomogeneity and anisotropy, organ deformation, anatomy obstructing the needle path, and physiological processes, such as respiration, flow of fluids, and edema) cause the needle to deviate from its intended path. A possible method to mitigate needle targeting errors is to use a needle that can be robotically steered inside the body to reach the intended target. Such needle insertion systems promise to enhance physicians' abilities to accurately reach targets and maneuver inside the human body while minimizing patient trauma. An

understanding and model of the needle and soft tissue interaction is required to plan such robotic medical interventions.

Several groups have examined the use of robotically steered flexible needles through tissue [82, 168, 181–185]. Abolhassani et al. [186] provide a review of recent research being conducted in the area of robotic needle insertion in soft tissue. One of the methods to steer needles through the body uses flexible needles with standard bevel tips that naturally cause the needle to bend when interacting with soft tissue [185]. This phenomenon is attributed to the asymmetry of the bevel edge, which results in bending forces at the needle tip (Figure 5.1). Ideally, a mechanics-based model of the tip force would be used to predict needle behavior based on information about geometry and material properties.

Several research groups have developed physics-based needle and soft tissue interaction models that are not specific to bevel-tipped needles [15, 75, 76, 80, 84, 187]. A general survey of surgical tool and tissue interaction models, which describes both physics- and non-physics-based interaction models, is provided in Chapter 2 and [146]. In all these studies, the objective of the researchers was to develop models to render simulation of needle-tissue interaction for real-time applications without specifically focusing on the interaction forces at the needle tip. However, experimental work has identified forces (due to puncture, cutting, and friction) that develop during needle insertion through tissue [86]. Further, Shergold and Fleck [188] provided a fracture mechanics-based model for flat-bottomed and sharp-tipped cylindrical punches as the tip interacted with soft solids (although their model does not consider the interaction of the punch shaft with the surrounding medium). Web-

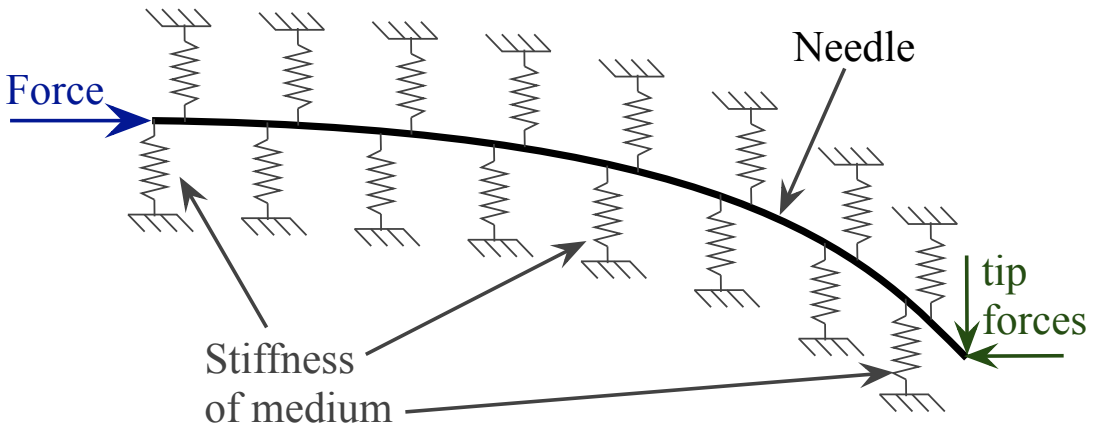

Figure 5.2: Diagram showing our 2D nonlinear model incorporating tip forces generated by rupture at the bevel edge of the needle, a continuous set of springs to model the needle-tissue interaction, and an input force.

ster et al. [185] presented a nonholonomic model for steering flexible needles with bevel tips. The parameters for their kinematic model were fit using experimental data, but this model did not consider the interaction of the needle with an elastic medium. None of these studies focused on relating the tip forces to the amount of needle deflection based on the fundamental principles of continuum and fracture mechanics.

In this chapter, we present experimental results and an analytical model to study the effect of tissue material and needle tip geometric parameters on tip forces. Also, using FE simulations we show the relationship between the bevel angle and the forces generated at the needle tip. The FE model includes contact between the needle tip and tissue, and also incorporates a cohesive zone model to simulate the tissue cleavage process. In addition, we present a 2D model for a bevel-tip needle embedded in an elastic medium (shown in Figure 5.2). Our mechanics-based model is based on both macroscopic observations of a

robotically steered needle inserted through soft gels and microscopic observations of the needle tip interacting with soft gels. The model accounts for the needle's geometric and material properties, and also the medium's nonlinear material properties. Uniaxial compression and toughness tests were performed to extract medium-specific material properties. We incorporate these physical values into our FE simulation and mechanics-based analytical model. In addition to capturing needle tip effects, our analytical model attempts to provide a physics-based understanding of the effect of the needle-tissue interaction (both along needle shaft and at the bevel tip) on the evolving shape of the needle with applications to surgical planning.

This chapter is organized as follows: Section 5.2 presents microscopic and macroscopic observations of needle-gel interactions. Section 5.3 highlights the importance of both tissue elasticity and toughness for needle bending calculations, while Sections 5.4 and 5.5 present the mathematical preliminaries and experiments required to obtain the tissue elasticity and toughness values for several gels and soft tissue, respectively. Section 5.6 describes the FE simulations and sensitivity studies done to evaluate forces at the bevel tip using the derived material properties. Section 5.7 provides an energy-based formulation for a needle inserted in an elastic medium. Section 5.8 compares the results from the experimental needle-gel interaction studies to those obtained from the energy-based model. Finally, this chapter concludes with a summary of these efforts.

5.2 Observations of Needle-Tissue Interactions

In order to guide the development of models for a needle embedded in an elastic medium, we conducted microscopic and macroscopic experiments. Nitinol wires (Nitinol Devices and Components, Fremont, CA, USA) of varying diameter were used as flexible "needles". These needles were solid rather than hollow. Each needle had a bevel tip. A smooth and sharp bevel was obtained by fixing the needles at an angle in Crystalbond^{TM} (Aremco Products, Inc., Valley Cottage, NY, USA) mounting adhesive, which is a thermo-plastic, and then polishing the edges (Figure 5.3). Crystalbond^{TM} holds the needles at a fixed angle while they are polished. After the needle tips have been polished, the needles are removed by breaking the Crystalbond^{TM} mounting adhesive. Finally, the needle tips are cleaned with Acetone solution. The Plastisol (M-F Manufacturing Co., Inc., Ft. Worth, TX, USA) gels were used in the experiments; the ratio of plastic and softener was varied to change the stiffness of the gel.

5.2.1 Global Observations

We used the experimental setup shown in Figure 5.4 to measure the radius of curvature for three needles inserted into two phantom tissues. This setup was developed by Webster et al. [189], and revised by Reed et al. [190] and John Swensen (Locomotion in Mechanical and Biological Systems Laboratory, Johns Hopkins University). The device can rotate and

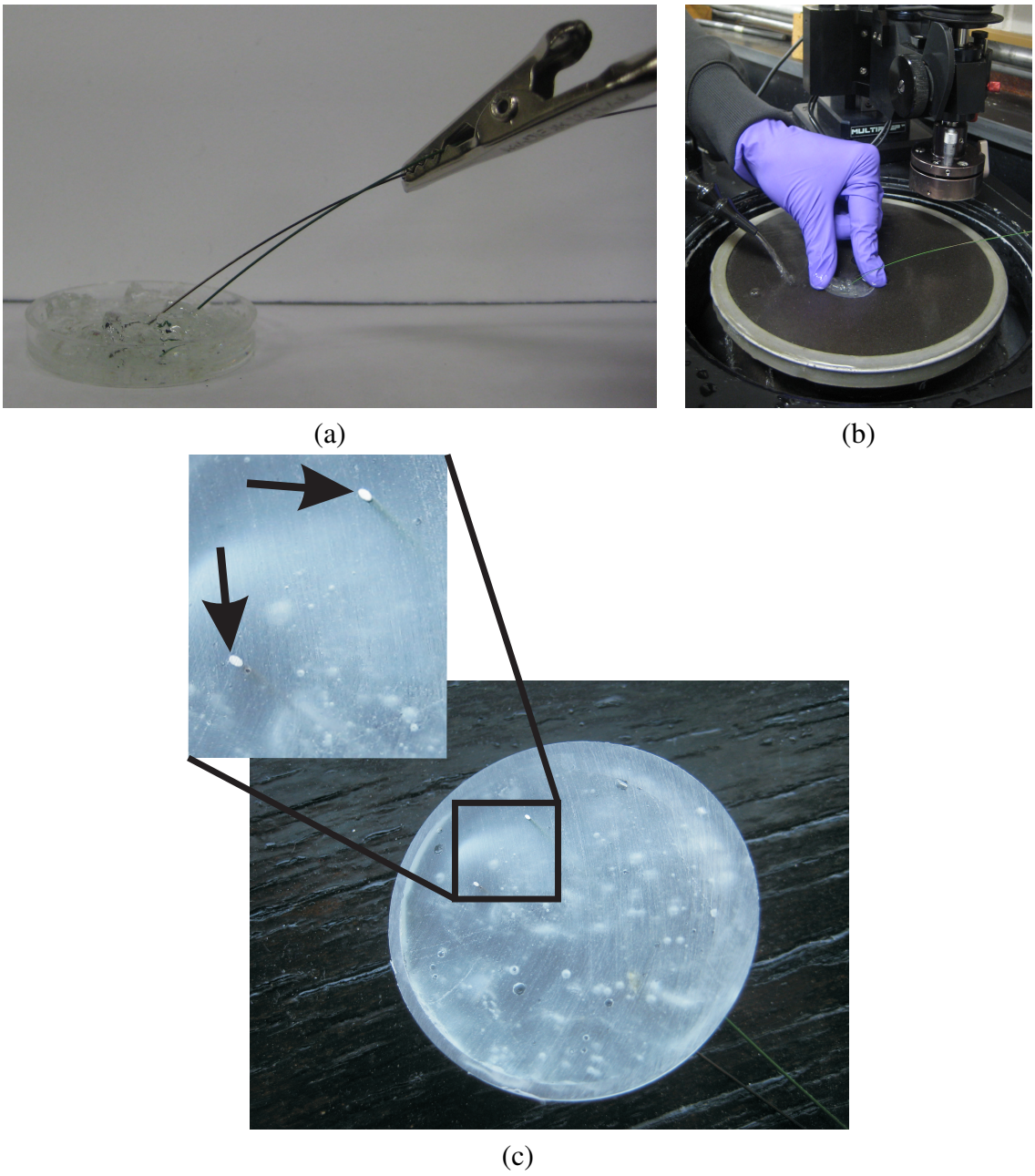

Figure 5.3: Preparation of needles with bevel edges. (a) Two needles fixed at an angle in Crystalbond^{TM} mounting adhesive in a plastic petri dish. (b) The needles tips being polished using a rotating disc polisher (Allied High Tech Products Inc., Rancho Dominguez, CA, USA) to get a smooth edge. (c) Needles with polished bevel edges.

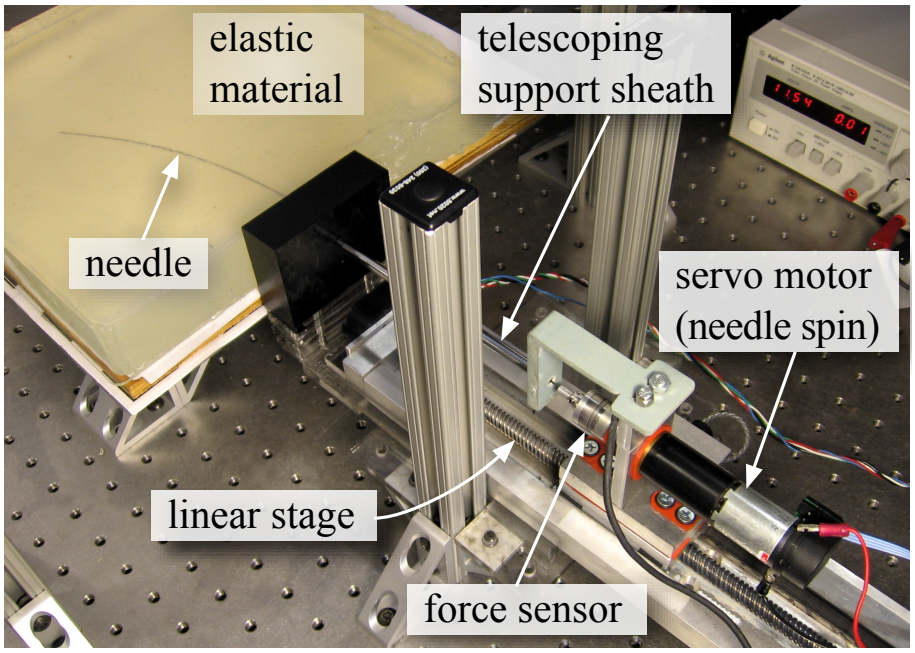

Figure 5.4: Experimental setup used to robotically steer a flexible needle though soft elastic materials.

insert a needle into tissues using two DC motors. A 6-axis sensor (ATI Nano 17) measures the force and torque at the base of the needle. Motion control and measurements run at 1 kHz. Nitinol wires with diameters of 0.40 mm ($\alpha = 38.0°$), 0.71 mm ($\alpha = 38.7°$), and 0.90 mm ($\alpha = 30.9°$) were used. Two transparent Plastisol gels were used, with a plastic to softener ratio of 4:1 (gel #1) and 32:9 (gel #2). Tracking of the needle tip was performed at 7 Hz by triangulating images from a pair of XCD-X710 firewire cameras (Sony Corporation, Tokyo, Japan) mounted above the phantom tissue. A telescoping support sheath prevents the needle from buckling during insertion. The device is further described in [189].

For each experiment, we inserted the needle 20 cm into the gel at a constant velocity of 0.25 cm/sec. To determine the radius of curvature throughout the insertion, we segmented the needle tip position every 5 cm and calculated the radius of curvature over three regions.

gel, Ø(mm)	5-10cm (mm)	10-15cm (mm)	5-20cm (mm)	mean ρ (mm)	max % deviation
#1, 0.40	165.1	161.0	168.5	179.4	6.5%
#1, 0.71	201.0	176.8	191.5	196.6	5.9%
#1, 0.90	299.4	191.3	259.9	289.1	15.2%
#2, 0.40	278.1	264.2	272.8	276.0	2.0%
#2, 0.71	368.9	314.8	337.0	327.3	9.5%
#2, 0.90	541.7	340.2	428.7	404.1	26.4%

Table 5.1: Radius of curvature for needle path segments where Ø is the diameter of needle and ρ is the radius of curvature.

Data from the first 5 cm were not used in the radius of curvature calculation because the pre-puncture deformation, the interaction of the support sheath, and the gel surface contaminate the initial needle deflection data. Figure 5.5 shows the needle tip positions for three needles inserted into both materials. The figures show planar data. The depth direction varied by a maximum of 15 mm. The needle tip deviates from the horizontal plane since the initial rotation angle of the bevel varies slightly from trial to trial. The radius of curvature for each insertion was determined using a 3D least squares fitting algorithm. Table 5.1 shows the radii calculated over each section of the needle. We found that a needle length segment of 5 cm was sufficiently small to fit a circle while highlighting the low variation in the radius of curvature across different segments. The radius of curvature varies by an average of 10.7% for these six insertions, with most of this deviation found in the Ø 0.90 mm needle. The other two needles have an average deviation of only 5.7%. Given this low variation, we assume a constant radius of curvature throughout the insertion, which corresponds to the kinematic model of [185].

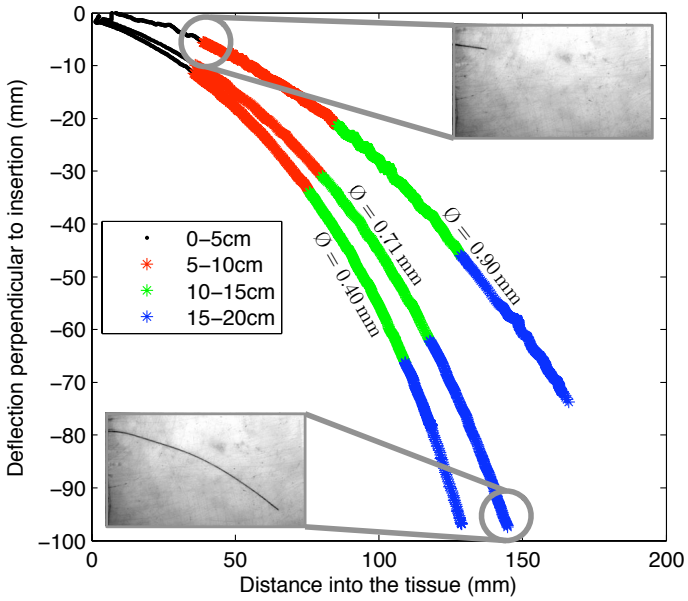

(a)

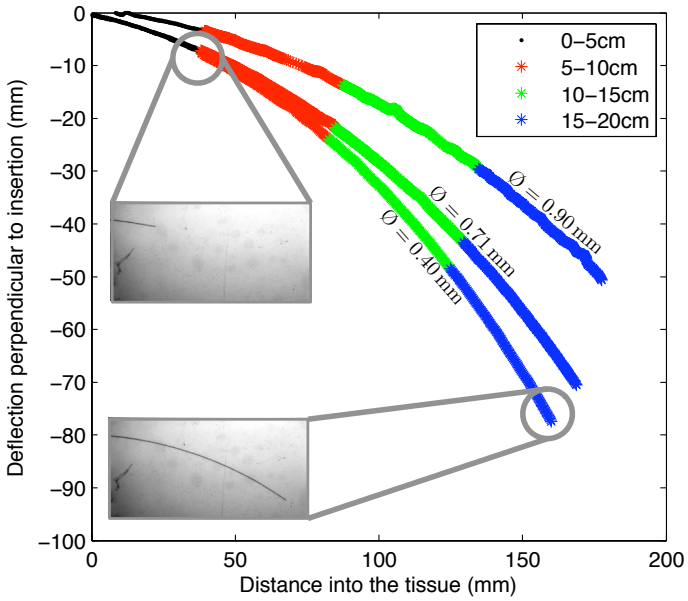

(b)

Figure 5.5: Needle tip position: During each 20 cm insertion, the tip position is measured. The radius of curvature remains relatively constant throughout the insertion. (a) Gel #1 (stiffest). (b) Gel #2 (less stiff).

5.2.2 Local Macroscopic Tip Observations

In order to understand the tissue cleavage process as the needle tip interacts with the medium, we performed experiments in which we physically magnified the bevel tip by machining needles of diameter Ø 1.5 cm. These needles had bevel angles ranging from 10° to 60°. Figure 5.6 shows the needles with five bevel angles used in the experiments.

Three different types of Plastisol gel were used as the soft medium for these studies. The ratio of plastic to softener for the Plastisol was set to 3:1 (gel A), 8:1 (gel B), and 4:1 (gel C). These experiments were performed using the experimental setup described in Section 5.2.1 and shown in Figure 5.7.

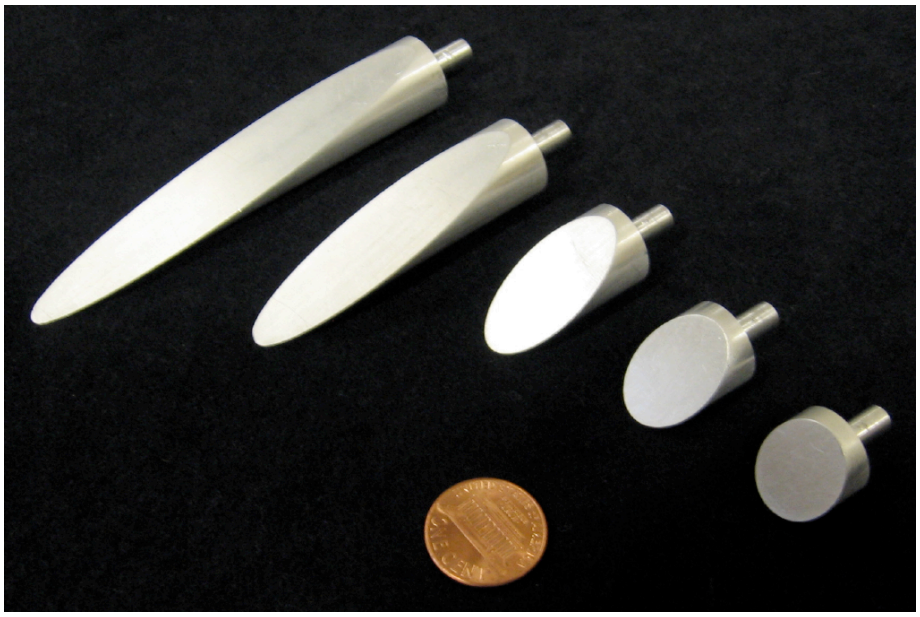

Figure 5.6: Scaled needles of Ø 1.5 cm used to understand the interaction between the needle tip and medium. Needles of various bevel angles (10°, 15°, 30°, 45°, and 60°) were used in the study.

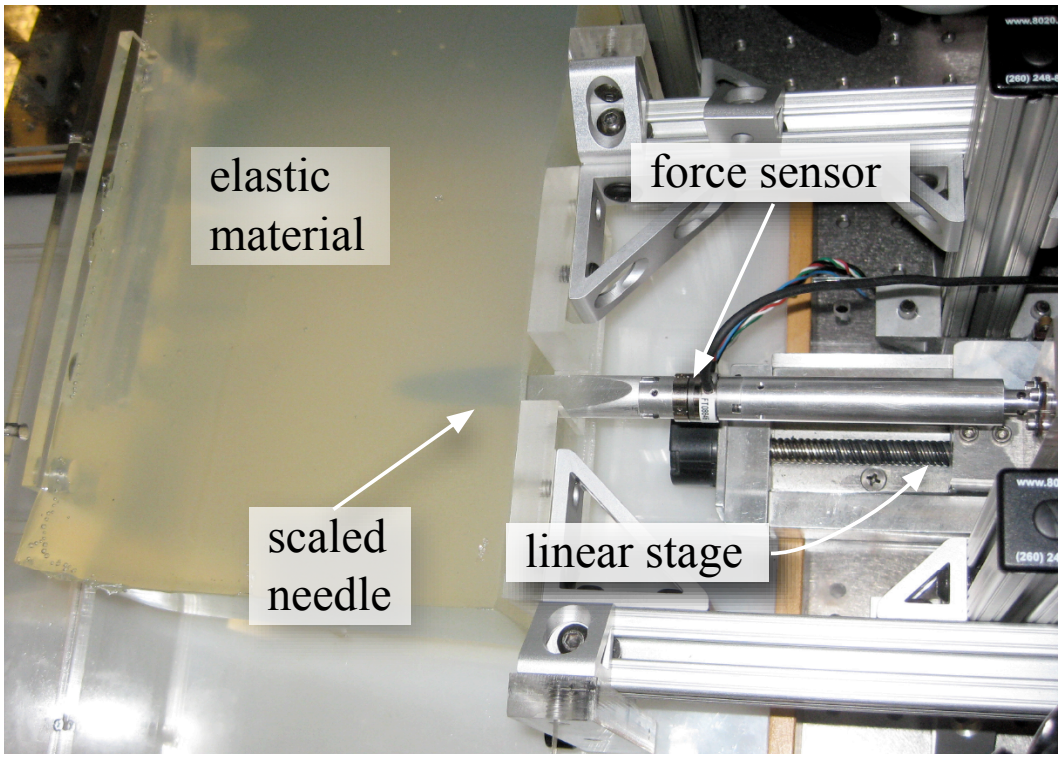

Figure 5.7: Experimental setup used to insert a scaled needle with 10° bevel angle and Ø 1.5 cm into gel A (3:1 Plastisol gel).

As the needle tip cuts through the soft solid, it moves material out of the way. We assume that the needle tip cuts the elastic medium along the dotted line, as shown in Figure 5.8(a). The angle by which the needle tip cuts and displaces material is given by γ. The resulting material displacements along the dotted line (cut path) in order to accommodate the needle tip are δ_1 and δ_2 (Figure 5.8(a)). This material displacement as the needle tip interacts with medium and moves forward results in a distributed load along the bevel and bottom edges of the needle tip.

The load distribution along the edges of the needle tip is hypothesized to be triangular

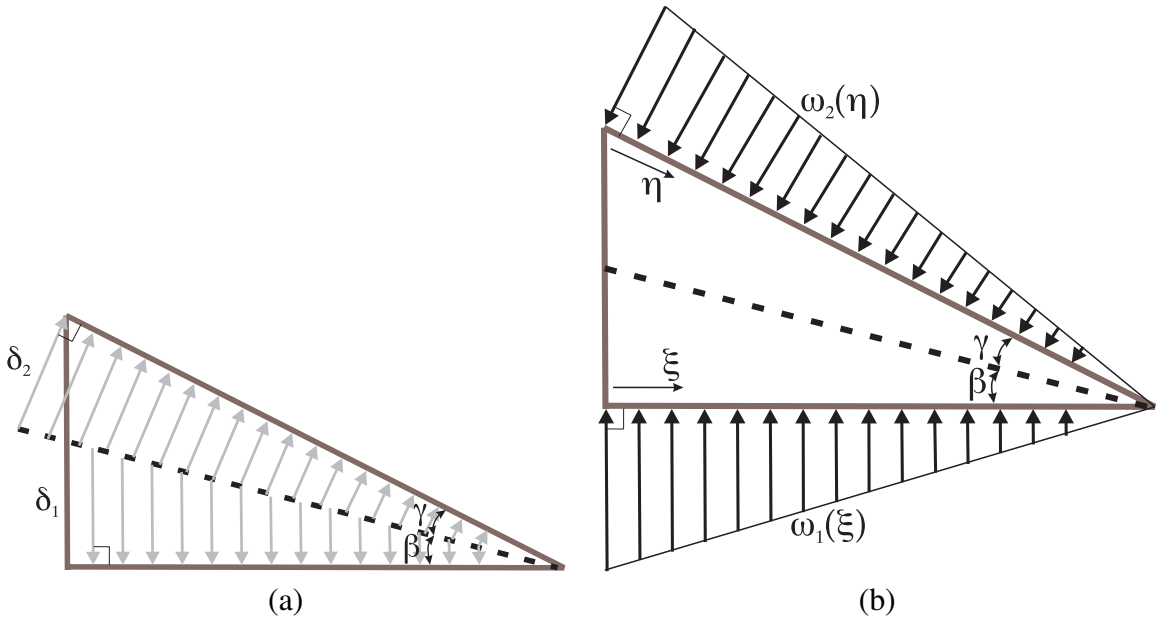

Figure 5.8: (a) Displacement of material as the needle tip interacts with a soft solid. (b) As material is moved out of the way to accommodate the needle tip, this results in a load distribution along the edges of the needle tip. ξ and η are defined as the positive directions for the triangular load distributions on the bottom and bevel edges of the needle tip, respectively.

(Figure 5.8(b)). We define ξ and η as the positive directions for the triangular load distributions on the bottom and bevel edges of the needle tip, respectively. Characterization of the frictional forces along the edges of the needle tip needs to be performed in order to choose an appropriate friction model. This has not been performed at the current state of our analysis. Hence, the effects of friction along the edges of the needle tip have not been considered in this calculation. However, when needles interact with soft biological tissues during clinical procedures, the fluids within the organ lubricate the needle's surface and reduce friction. Thus, we believe that friction will not play a major role in the needle-tissue interaction forces.

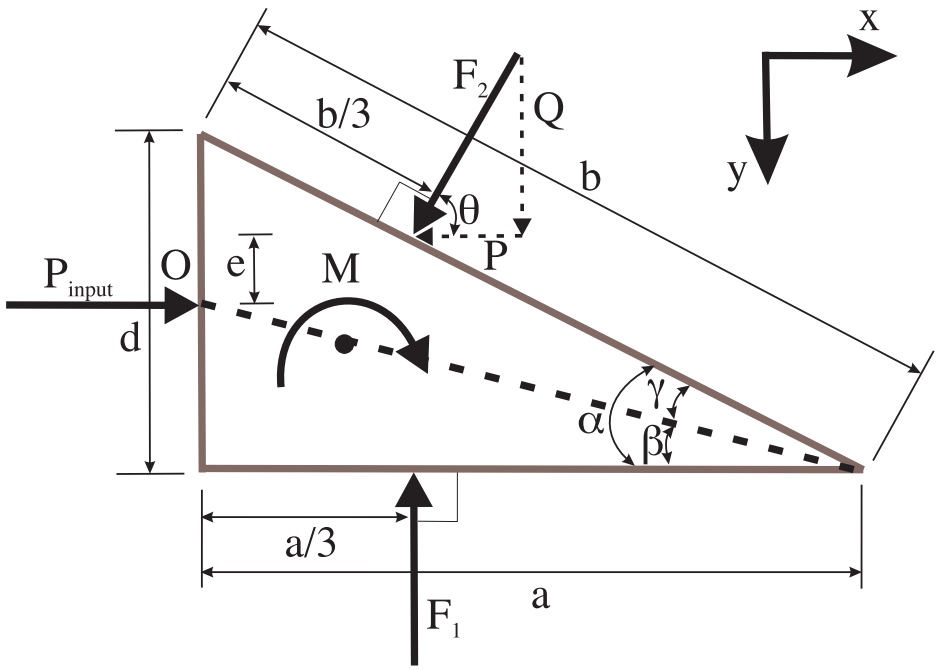

Figure 5.9: Free-body diagram of the forces acting on the needle tip as it interacts with the medium.

The resultant forces and moments acting on the needle tip due to deformation of the medium and inclusion of the bevel tip are shown in Figure 5.9. Using d and α, the diameter of the needle and the bevel angle, respectively, we define other variables representing various dimensions in Figure 5.9 as follows:

$$\alpha = \gamma + \beta. \tag{5.1}$$

$$a = \frac{d}{\tan\alpha}. \tag{5.2}$$

$$b = \frac{d}{\sin\alpha}. \tag{5.3}$$

$$e = d - a\sin\beta - \frac{b}{3}\sin\alpha. \tag{5.4}$$

$$\theta = 90^\circ - \alpha. \tag{5.5}$$

Our objective is to derive expressions for the forces and moments developed at the bevel tip. In particular, we are interested in the transverse load, Q, that results from the tip asymmetry and causes the needle to bend. We define K_T as the needle-tissue interaction stiffness per unit length. The triangular load distribution along the bottom edge of the needle, $\omega_1(\xi)$, has the following constraints:

$$\omega_1(0) = K_T \delta_1(0) = K_T a \tan\beta, \tag{5.6}$$

$$\omega_1(a) = 0, \tag{5.7}$$

where $\delta_1(0) = a\tan\beta$. Similarly, the triangular load distribution along the bevel edge of the needle, $\omega_2(\eta)$, has the following constraints:

$$\omega_2(0) = K_T \delta_2(0) = K_T b \tan\gamma, \tag{5.8}$$

$$\omega_2(b) = 0, \tag{5.9}$$

where $\delta_2(0) = b\tan\gamma$. With this triangular load distribution assumption, we derive the following total forces along the bottom and bevel edges of the needle:

$$F_1 = \int_0^a \omega_1(\xi)\, d\xi = \frac{K_T a^2}{2}\tan\beta, \tag{5.10}$$

$$F_2 = \int_0^b \omega_2(\eta)\, d\eta = \frac{K_T b^2}{2} \tan\gamma. \tag{5.11}$$

These resultant forces act at the bevel edge of the needle tip. Let us define P_{input} as the input force used to drive the needle into the medium, then using (5.10) and (5.11), the forces along the x and y directions are as follows:

$$\Sigma F_x = -P = P_{\text{input}} - F_2 \cos\theta. \tag{5.12}$$

Thus,

$$P = -P_{\text{input}} + \frac{K_T b^2}{2} \tan\gamma \sin\alpha. \tag{5.13}$$

$$\Sigma F_y = Q = -F_1 + F_2 \sin\theta. \tag{5.14}$$

Thus,

$$Q = \frac{K_T b^2}{2} \tan\gamma \cos\alpha - \frac{K_T a^2}{2} \left(\frac{\tan\alpha - \tan\gamma}{1 + \tan\alpha \tan\gamma} \right). \tag{5.15}$$

Similarly, we derive the resultant moment, M, acting on the needle tip by resolving the moments about point O (Figure 5.9)

$$\Sigma M_o = M = \frac{F_1 a}{3} - \frac{F_2 b}{3} \sin\theta \cos\alpha + F_2 e \cos\theta. \tag{5.16}$$

Thus,

$$M = \frac{K_T a^3}{6} \left(\frac{\tan\alpha - \tan\gamma}{1 + \tan\alpha \tan\gamma} \right) - \frac{K_T b^3}{6} \tan\gamma \cos^2\alpha + \frac{K_T b^2 e}{2} \tan\gamma \sin\alpha. \tag{5.17}$$

We observe in (5.15) and (5.17) that the transverse tip force and the resultant tip moment are independent of the input force, respectively. Also, we have provided an expression for tip loads that is function of the elastic medium (K_T) and the needle tip geometry. Both (5.15) and (5.17) are linear in K_T.

The inputs to the model are K_T and γ. K_T is a material property of the elastic medium, while γ depends both on the medium and the bevel angle. The material property of the medium, K_T, is 4.83 kN/m^2, 9.21 kN/m^2, and 12.61 kN/m^2, for the gels A, B, and C, respectively. These values were measured using uniaxial compression tests, described in greater detail in Sections 5.4.1 and 5.5. The optimized values for γ/α were obtained by minimizing the error between the experimentally derived normal force to the analytically derived Q, given in (5.15). For our model, γ/α were calculated to be 0.97, 0.79, and 0.74, for gels A, B, and C, respectively. We compared the transverse tip force, Q, derived in (5.15) to the experimental results. Figure 5.10(a) provides the maximum experimentally observed transverse force and analytically derived tip force for all bevel angles. The analytically derived transverse tip forces qualitatively match the experimental values. In Figure 5.10(b), when the ratio γ/α is fixed to be 0.83, the transverse tip force also follows a trend similar to that of the experimental results. The ideas resulting from this analysis could be applicable not just to bevel-tipped needles, but to any wedge embedded in an elastic medium.

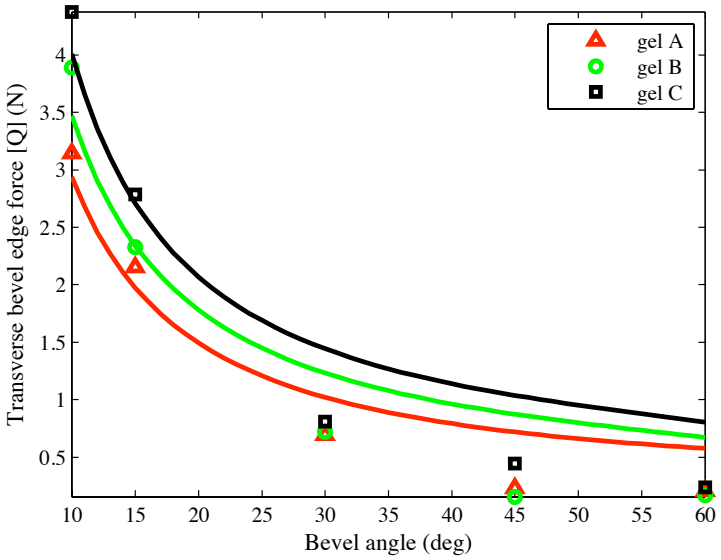

(a)

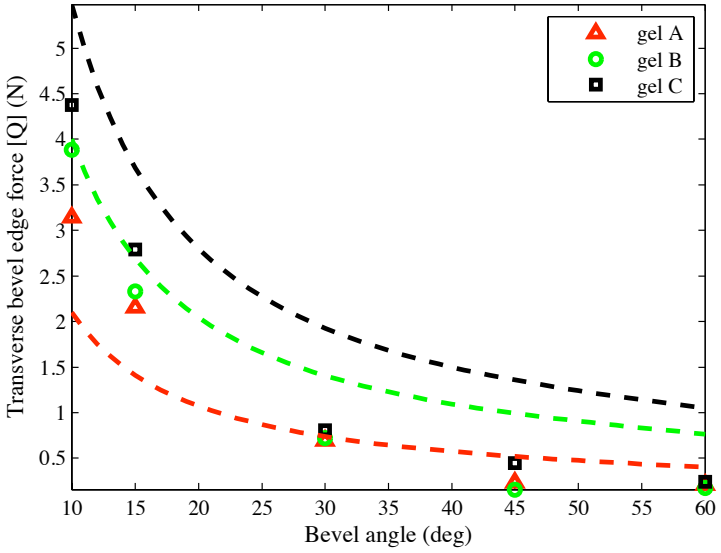

(b)

Figure 5.10: Transverse tip load (Q) based on the analytical model and experiments. (a) The solid curves represent the analytical results where the ratio γ/α is varied for each material. (b) The dashed curves represent the analytical results where the ratio $\gamma/\alpha = 0.83$ for all the materials.

5.2.3 Local Microscopic Tip Observations

Microscopic observations of needle and elastic medium interactions have been reported previously (e.g. [191]), but most of the published literature focuses on observing the damage to the gel or tissue surface after the needle has punctured the medium. Sections of the gel have also been observed, but again only after the needle has penetrated the medium. In

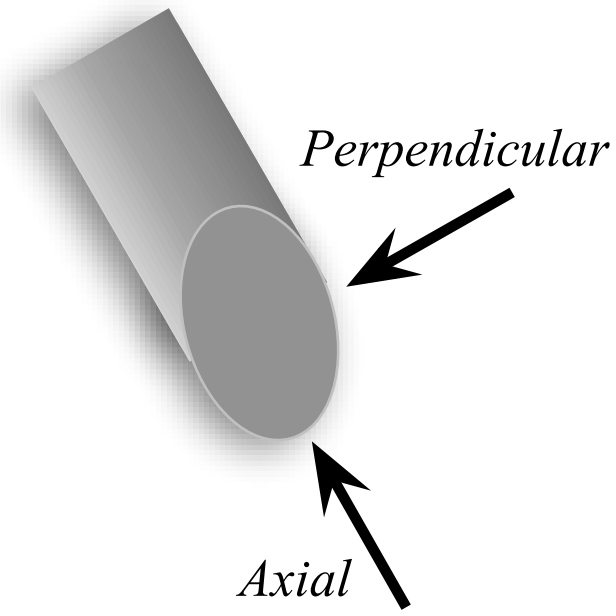

Figure 5.11: Microscopic observations of needle-tissue interactions were made in two configurations: *axial* and *perpendicular*. The arrows indicate the direction of the laser light relative to the bevel tip of the needle.

order to observe the needle-tissue interaction within the gel as the needle is embedded in the medium, we used a Zeiss LSM 510 Meta laser scanning confocal microscope. The needle and gel were visualized with differential interference contrast (DIC), epifluorescence,

and reflected light using the 488 nm line of an argon/ion laser and 0.3 NA Plan-Neofluar 10x objective lenses (Carl Zeiss Inc., Maple Grove, MN, USA) with pin hole diameter set at 9.33 Airy units.

The ratio of plastic to softener for Plastisol gel was 4:1. The Plastisol gel (400 cm^3) was doped with 20 μl of 10 mg/ml rhodamine green solution (Invitrogen, Carlsbad, CA, USA). This dye was added to facilitate epifluorescent confocal imaging of Plastisol gel. Since a very small amount of dye was used, we assume that it does not significantly change the material properties of the gel. Cubes of 0.5 cm^3 were prepared and needles were manually inserted into the gel and viewed under the microscope. Observations were made in two configurations (*axial* and *perpendicular*), for needles of 4 different diameters and bevel angles (Figure 5.11). In the *axial* configuration, the laser light was along the needle axis, while in the *perpendicular* configuration the laser light was perpendicular to the needle axis. DIC and epifluorescent images were obtained for each configuration, as shown in Figure 5.12.

In classical fracture mechanics, a Mode-I crack is characterized by opening and a Mode-II crack by sliding, as shown in Figure 5.13. Shergold and Fleck [188] model the interaction of symmetric sharp-tipped and flat-bottomed punches with a soft medium as Mode-I and Mode-II cracks, respectively. As a bevel-tipped needle interacts with a soft elastic medium, we hypothesize that a combination of Mode I and II cracks are developed. Figure 5.14 shows the hypothesized interaction and corresponding rupture of the soft medium. The

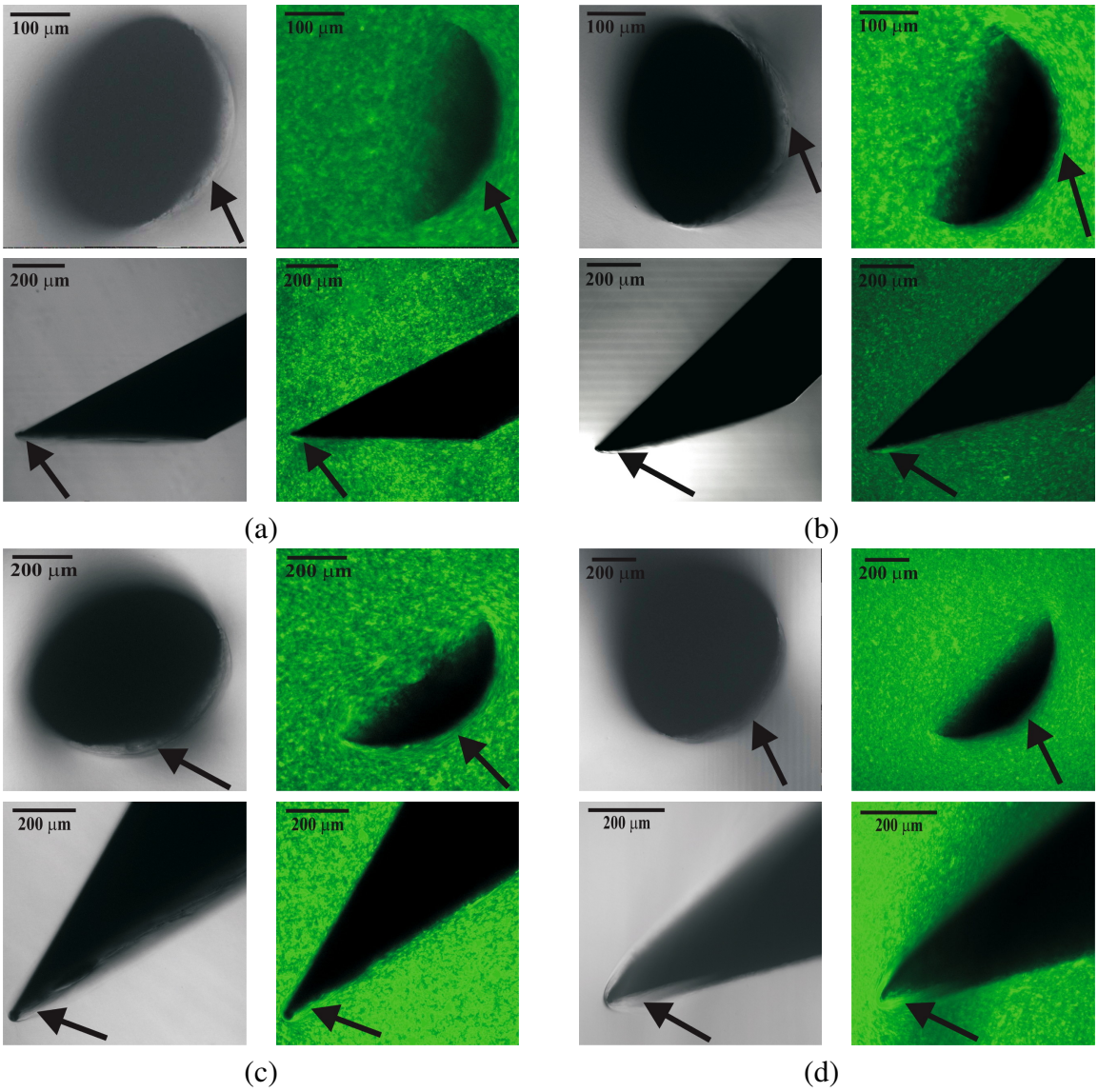

Figure 5.12: DIC (first and third columns) and epifluorescent (second and fourth columns) images taken using a confocal microscope where the first and third rows are in the *axial* configuration, while the second and fourth rows pertain to the *perpendicular* configuration. The needle geometric properties were: (a) Ø 0.38 mm, $\alpha = 26.4°$ (b) Ø 0.40 mm, $\alpha = 33.9°$ (c) Ø 0.71 mm, $\alpha = 28.2°$ (d) Ø 0.90 mm, $\alpha = 26.6°$. Arrows in the DIC and epifluorescent images in the *axial* configuration indicate the occurrence of a Mode-I crack (opening), while in the *perpendicular* configuration a Mode-II crack (rupture) is observed.

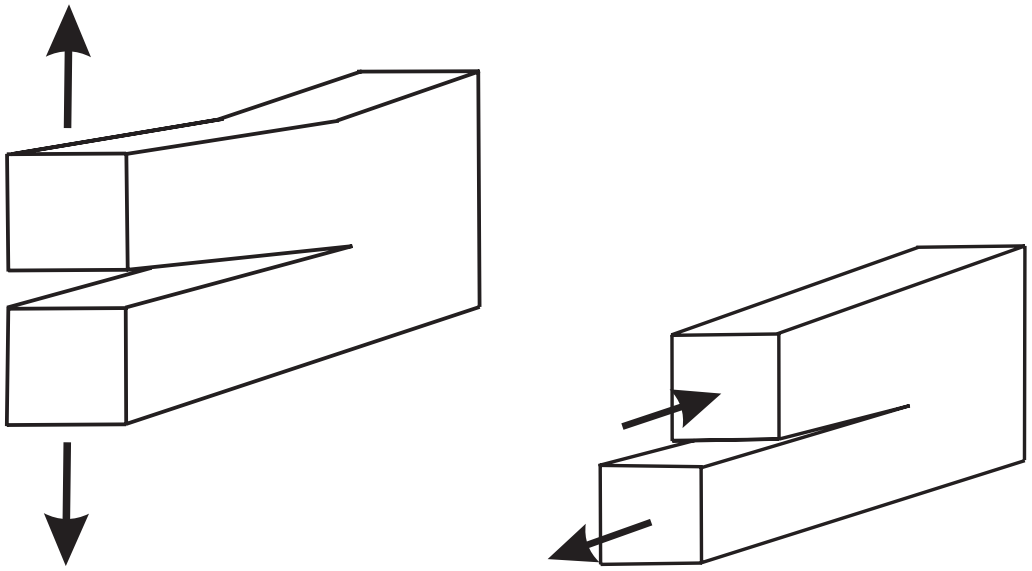

(a) (b)

Figure 5.13: Modes of fracture. (a) Mode-I (Tension, Opening). (b) Mode-II (In-Plane Shear, Sliding). Arrows indicate the direction of applied load.

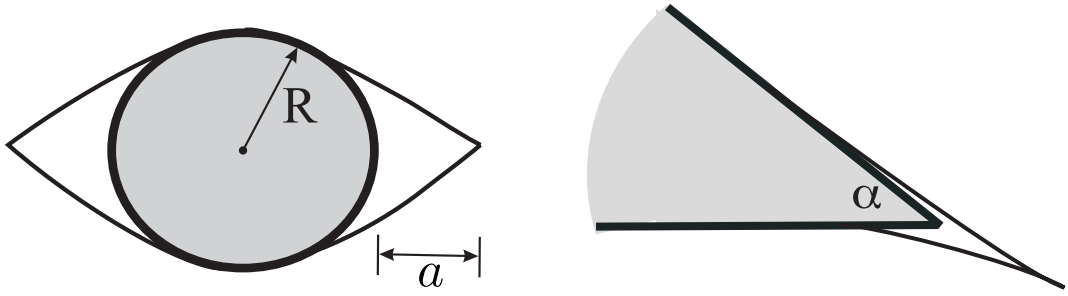

(a) (b)

Figure 5.14: Bevel-tipped needle interacting with a soft elastic medium. (a) Mode-I crack or opening (*axial* configuration) where R and a are the needle radius and crack length, respectively. (b) Mode-II crack or rupture (*perpendicular* configuration) where α is the bevel angle.

size of the cracks has been exaggerated to highlight the modes. Figure 5.14(a) is a form of Mode-I crack while Figure 5.14(b) represents a Mode-II crack (a "rupture"). We believe that these modes of fracture are visible in the microscopic images.

For all the needles, rupture and opening are observed at the bevel edge. In the *axial* configuration, the needle cross-section appears crescent-shaped because of the bevel edge. As pointed out in Figure 5.12, arrows in both the DIC and epifluorescent images in the *axial* configuration indicate regions where Mode-I crack (opening) of the gel is visible. In the *perpendicular* configuration, arrows point to the occurrence of Mode-II crack (rupture) near the bevel edge of needle. In the epifluorescent images, the speckle pattern is uniform except in regions near the bevel face of the tip. In these regions, the gel appears to trace along the edges of the needle tip. This is an indication of Mode-I crack (*axial*) and Mode-II crack (*perpendicular*) in the gel. Unlike brittle materials, crack propagation (classical unstable Mode-I fracture) is not seen during the interaction of sharp needles and soft gels.

5.3 Dimensional Analysis

Our objective is to develop a mechanics-based needle-tissue interaction model that relates the radius of curvature of the needle to tissue and needle material and geometric properties. The radius of curvature of a bevel-tipped needle is a function of several parameters (shown in Figure 5.15):

- The needle's Young's modulus $(E, \text{units: Pa})$, second moment of inertia $\left(I, \text{units: } \text{m}^4\right)$, and tip bevel angle (α).
- The tissue's nonlinear (hyperelastic) material property $(C_{10}, \text{units: Pa})$, rupture toughness $(G_c, \text{units: N/m})$, and coefficient of friction (μ).

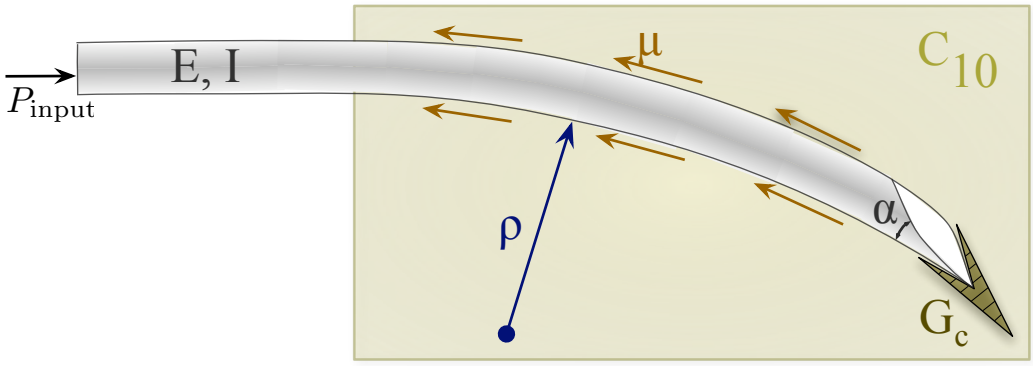

Figure 5.15: Schematic of a bevel-tip needle interacting with a soft elastic medium.

- The input insertion force from the robot controller $\left(P_{\text{input}}, \text{units: N}\right)$.

Thus, the radius of curvature of the needle $(\rho, \text{units: } m)$ can be written as a function, f, of these parameters

$$\rho = f\left(\underbrace{E, I, \alpha}_{\text{needle}}, \underbrace{C_{10}, G_c, \mu}_{\text{tissue}}, \underbrace{P_{\text{input}}}_{\text{input force}}\right). \tag{5.18}$$

Dimensional analysis provides an organized method to group dimensionally similar variables. The Buckingham Π theorem is commonly used to perform dimensional analysis [192]. This theorem describes how a physically meaningful equation involving n variables can be equivalently rewritten as an equation of $n - m$ dimensionless parameters, where m is the number of fundamental dimensions used. Dimensional analysis involves scaling quantities by characteristic units of a system or natural units of nature (e.g. mass, length, and time). This gives insight into the fundamental properties of the system.

Performing dimensional analysis and invoking Buckingham's Π theorem on this system (5.18) results in the following Π-groups, for primary variables E, I, C_{10}, and G_c: $\Pi_1 = \frac{\rho E C_{10} \sqrt[4]{I}}{G_c^2}$, $\Pi_2 = \frac{P_{\text{input}} E C_{10} \sqrt[4]{I}}{G_c^3}$, $\Pi_3 = \frac{\alpha E C_{10} \sqrt{I}}{G_c^2}$ and $\Pi_4 = \frac{\mu E C_{10} \sqrt{I}}{G_c^2}$. Thus, the non-dimensional form of (5.18), is given by

$$\frac{\rho}{\rho_0} = \frac{\rho E C_{10} \sqrt[4]{I}}{G_c^2} = g\left(\frac{P_{\text{input}} E C_{10} \sqrt[4]{I}}{G_c^3}, \frac{\alpha E C_{10} \sqrt{I}}{G_c^2}, \frac{\mu E C_{10} \sqrt{I}}{G_c^2}\right), \tag{5.19}$$

where ρ_0 is the length scale of the system given by

$$\rho_0 = \frac{G_c^2}{E C_{10} \sqrt[4]{I}}. \tag{5.20}$$

We observe that with increase of the medium toughness, the length scale increases, while increasing the medium or needle stiffness results in reduction of ρ_0, and vice versa. From (5.19), irrespective of the choice of the primary variables, it is observed that the radius of curvature is dimensionally scaled by both the tissue elasticity (global parameter) and also the tissue rupture toughness (local parameter), which tells us that in addition to α and μ, the effect of both of these parameters (C_{10} and G_c) needs to be investigated.

5.4 Tissue Elasticity and Toughness

In order to understand and characterize the needle-tissue interaction, medium-specific material parameters need to be evaluated and incorporated into the model. In this section,

we present the mathematical formulation and data acquisition techniques used to evaluate the tissue elasticity and rupture toughness.

5.4.1 Tissue Elasticity

The deformation of materials under strains greater than 1%-2% is described by the theory of nonlinear elasticity, and hyperelastic models are commonly used. As highlighted previously in this thesis in Chapter 2 (Section 2.2.4), Chapter 3 (Section 3.2), and Chapter 4 (Section 4.2.1), for a hyperelastic material, the Cauchy stress tensor, $\boldsymbol{\sigma}$, can be derived from a strain energy density function, W. There are various formulations for the strain energy density function depending on the material. The material parameters associated with the hyperelastic model are experimentally derived using tensile, compression, shear, or biaxial tests. In this study, only uniaxial compression experimental data was used and it fit the Neo-Hookean model well.

In order to fit the experimental data to a nonlinear elastic constitutive relation, we proceed to derive the stress-strain relationship. For a body under uniaxial compression (Figure 5.16), if $\mathbf{y}$ represents the position after deformation of a material reference initially located at $\mathbf{X}$, we can describe compression by

$$\mathbf{y} = \lambda_1 X_1 \mathbf{e}_1 + \lambda_2 X_2 \mathbf{e}_2 + \lambda_3 X_3 \mathbf{e}_3, \tag{5.21}$$

where $\mathbf{e}_i$ and λ_i, for $i = 1$ to 3, are the Cartesian base vectors and stretch ratios, respec-

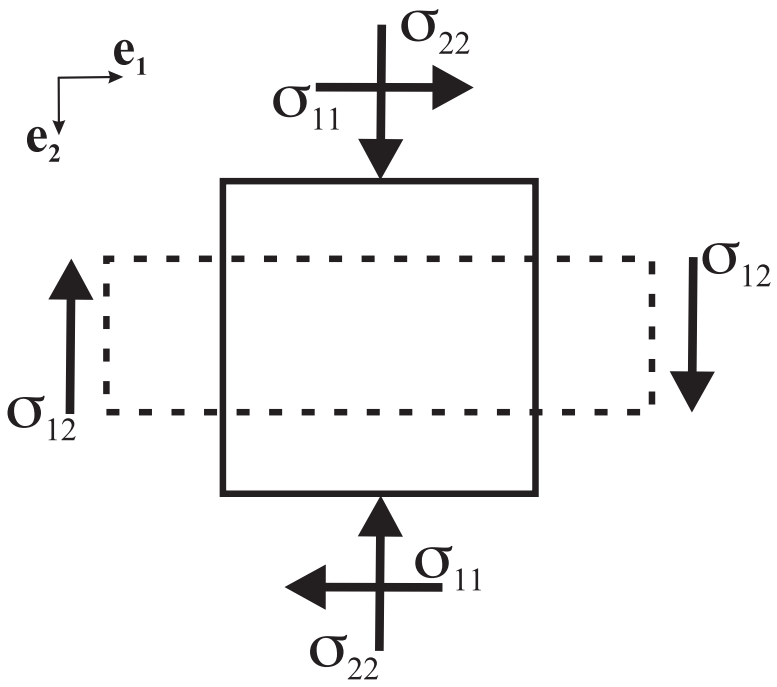

Figure 5.16: Stresses acting on body under plane stress, where the solid and dashed lines represent the body before and after compression, respectively.

tively. From (5.21), the matrix of the deformation gradient tensor, $\mathbf{F}$, for axisymmetric ($\lambda_1 = \lambda_3$ and $\lambda = \lambda_2$) and incompressible $\left(\lambda_1 = \lambda_3 = \frac{1}{\sqrt{\lambda}}\right)$ materials is computed as

$$\mathbf{F} = \frac{\partial \mathbf{y}}{\partial \mathbf{X}} = \begin{bmatrix} \frac{1}{\sqrt{\lambda}} & 0 & 0 \\ 0 & \lambda & 0 \\ 0 & 0 & \frac{1}{\sqrt{\lambda}} \end{bmatrix}. \tag{5.22}$$

$\boldsymbol{\sigma}$ for an isotropic, homogenous, and incompressible hyperelastic material can be derived as [161]

$$\boldsymbol{\sigma} = -p\mathbf{I} + 2\left\{\left(\frac{\partial W}{\partial I_1} + I_1\frac{\partial W}{\partial I_2}\right)\mathbf{B} - \frac{\partial W}{\partial I_2}\mathbf{B}^2\right\}, \tag{5.23}$$

where I_1 and I_2 are the principal invariants, $\mathbf{B}$ is the left Cauchy-Green tensor, and p is the Lagrange multiplier (essentially a pressure). The Neo-Hookean strain energy density function is given by

$$W = C_{10}(I_1 - 3), \tag{5.24}$$

where C_{10} is a material parameter specific to the tissue. In (5.24), the principal invariant, I_1, can be evaluated from $\mathbf{B} = \mathbf{F}\mathbf{F}^T$ as

$$I_1 = \mathbf{B} : \mathbf{I} = \frac{2 + \lambda^3}{\lambda}. \tag{5.25}$$

The Lagrange multiplier, p, in (5.23) can be evaluated from the boundary condition

$$\sigma_{11} = \sigma_{12} = 0 \Rightarrow p = \frac{2C_{10}}{\lambda}. \tag{5.26}$$

From (5.22) and (5.24) we can compute $\mathbf{B}^2$ and $\frac{\partial W}{\partial I_1}$, respectively, and using (5.23) and (5.26), the compressive stress, σ_{22}, is computed as

$$\sigma_{22} = \frac{2C_{10}}{\lambda}\left(\lambda^3 - 1\right), \tag{5.27}$$

where the stretch ratio is $\lambda = 1 - \text{strain}$. (5.27) is used to fit experimental stress-strain data to obtain C_{10}. In Section 5.5 we describe the uniaxial compression tests performed on the RSA II to evaluate C_{10}.

We now redefine K_T as the needle-tissue interaction stiffness of the medium per unit

length (N/m^2). K_T is calculated from the stress-strain uniaxial compression data of a tested sample (height: $\tilde{h}$, width: $\tilde{w}$, and cross-sectional area: $\tilde{a}$) of the elastic medium. For a linear elastic medium

$$K_T = E_T \frac{\tilde{a}}{\tilde{h}\tilde{w}}, \tag{5.28}$$

where E_T is the Young's modulus of the material. For cylindrical samples,

$$K_T = E_T \frac{\tilde{a}}{\tilde{h}\tilde{c}}, \tag{5.29}$$

where $\tilde{c}$ is the sample circumference. In both (5.28) and (5.29), we assume that $\tilde{a}/\left(\tilde{h}\tilde{w}\right)$ and $\tilde{a}/\left(\tilde{h}\tilde{c}\right)$ are of the same order of magnitude as the ratio of the medium displaced perpendicular to the insertion direction to the out-of-plane displacement of the medium during the needle-tissue interaction. Alternatively, evaluating the slope, $\frac{\partial \sigma_{22}}{\partial \lambda}$, for unit uniaxial stretch ratio, $\lambda = 1$, results in

$$E_T = 6C_{10}. \tag{5.30}$$

Thus, using (5.28), (5.29), and (5.30) results in

$$K_T = 6C_{10} \frac{\tilde{a}}{\tilde{h}\tilde{w}}, \tag{5.31}$$

$$K_T = 6C_{10} \frac{\tilde{a}}{\tilde{h}\tilde{c}}. \tag{5.32}$$

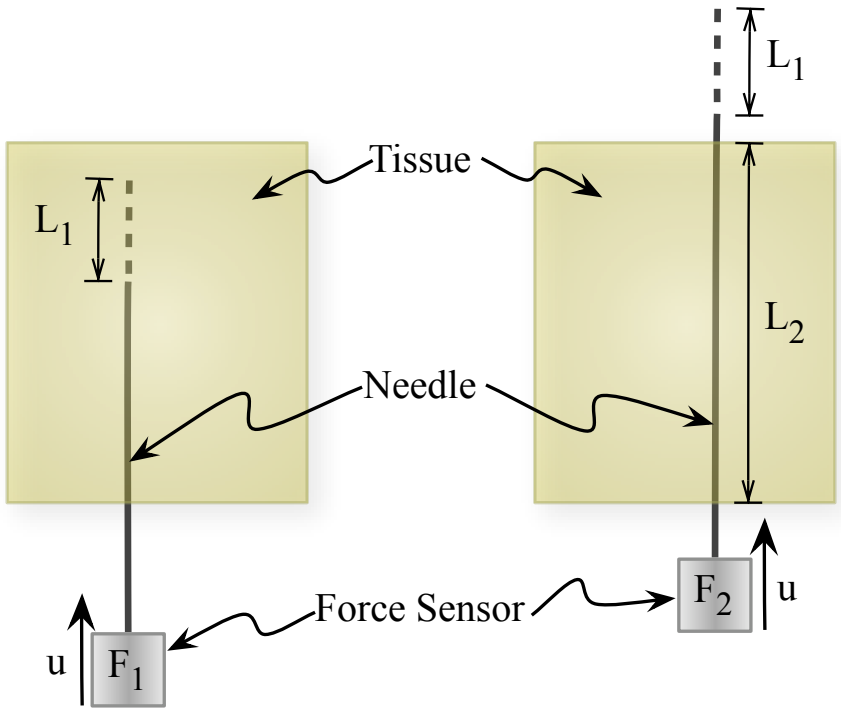

Figure 5.17: Schematic describing the procedure to calculate the rupture toughness of an elastic material during needle insertion.

5.4.2 Tissue Toughness

As the needle penetrates through material, the total insertion force during this phase includes the forces needed to cut through tissue, overcome friction, and slide through tissue. Figure 5.17 provides a schematic representation of the method we use to extract the toughness. F_1 is the insertion force recorded when the needle travels some distance L_1. The work done to overcome friction and slide, and to cut through tissue is G_{ftc}, and is given by

$$G_{ftc} = \int_0^{L_1} F_1 dL. \tag{5.33}$$

Once the needle tip has completely passed through the material, there is no cutting force. The force recorded during this phase, for a distance L_1 travelled by the needle, is given by F_2. F_2 includes the frictional force along the needle shaft and is given by

$$F_2 = \underbrace{\mu\left(\sigma_n \pi \tilde{d}\right)}_{\tilde{k}} L_2 = \tilde{k} L_2 \Rightarrow \tilde{k} = \frac{F_2}{L_2}. \tag{5.34}$$

where μ, σ_n, and $\tilde{d}$ are the co-efficient of friction between the needle and the tissue, stress along the needle shaft normal to the direction of insertion, and diameter of the needle, respectively. In order to account for the differences in frictional force along the needle shaft when the needle tip has completely passed through the material versus the case when the needle tip is interacting with the elastic medium let

$$F_2^{'} = \tilde{k} L_1. \tag{5.35}$$

Substituting (5.34) in (5.35)

$$F_2^{'} = F_2 \frac{L_1}{L_2}. \tag{5.36}$$

Thus, the work done to overcome friction and slide a distance L_1, when the needle tip has completely passed through the material is G_{ft}, and is given by

$$G_{ft} = \int_0^{L_1} F_2^{'} dL. \tag{5.37}$$

In both (5.33) and (5.37), dL is the variable of integration that represents the incremental increase in needle length. Hence, the work done per unit needle cross-section area, A, to rupture and cut through tissue, is the rupture toughness (effective) of the tissue, G_c, and is given by

$$G_c = \frac{1}{A}\left(G_{ftc} - G_{ft}\right), \tag{5.38}$$

where G_{ftc} and G_{ft} are calculated for various materials using needle insertion experiments. In the following section we describe experimental studies done to evaluate G_c for several gels and tissues.

5.5 Tissue Parameter Acquisition

Experimental studies on soft tissue simulants (gels) and chicken tissue were performed in order to obtain both tissue elasticity and toughness parameters. Specifically, we found the Neo-Hookean model material parameter C_{10} given in (5.27) and the rupture toughness derived in (5.38).

In Section 5.5.1 we describe the experiments conducted to evaluate elasticity properties (C_{10}) of Plastisol gels, which were used in the analysis presented in Section 5.2.2. In Section 5.5.2 we present experiments used to calculate both elasticity (C_{10}) and toughness (G_c) properties for Plastisol and porcine gels, and chicken tissue. The Plastisol gel samples described in Sections 5.5.1 and 5.5.2 were prepared several months apart, hence the material parameter acquisition tests had to be repeated.

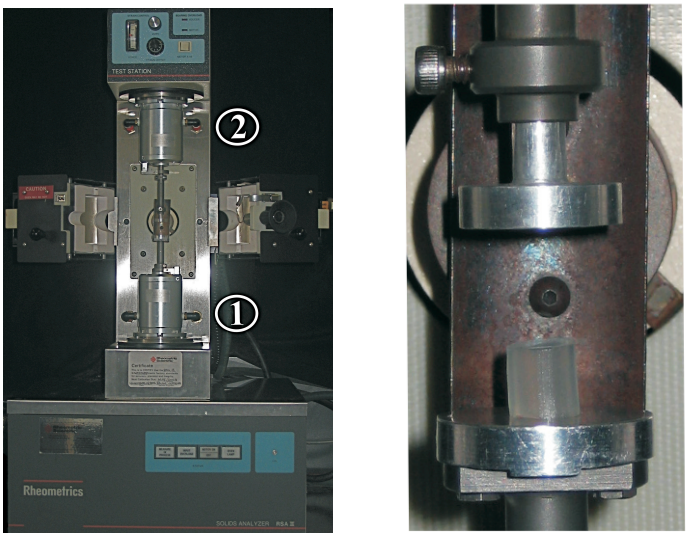

(a) The RSA II test station (b) Gel C (4 : 1 Plastisol gel)

Figure 5.18: Tissue elasticity measurement performed on several materials via uniaxial compression tests using the RSA II, where ① and ② are the actuator and load cell, respectively.

5.5.1 Elasticity Properites of Plastisol Gel

In this section, we describe the experiments conducted to evaluate C_{10} for three variants of Plastisol gel (similar to the gels used in Section 5.2.2). In order to obtain values for C_{10}, uniaxial compression tests were performed on the soft materials using the RSA II shown in Figure 5.18. Seven samples of each material were prepared and tested. The mean diameter of the samples was Ø 6.34 mm (gel A), Ø 6.51 mm (gel B), and Ø 7.03 mm (gel C). The mean height of the tested samples was 7.31 mm (gel A), 6.78 mm (gel B), and 6.31 mm (gel C). The compression tests were performed at a strain rate of 0.001 s^{-1}. Representative stress versus strain curves for various materials are shown in Figure 5.19.

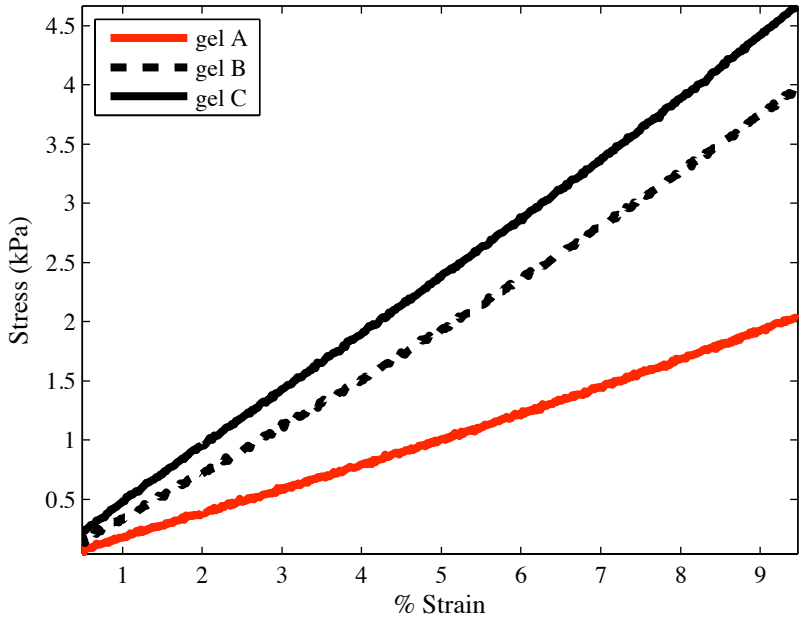

Figure 5.19: Representative compressive stress versus strain curves for Plastisol recorded using the RSA II.

The experimental data were fit to the constitutive equation given in (5.27) to obtain C_{10}, and Table 5.2 provides the mean values of tissue elasticity for various materials. Linear elastic models were also fit to the experimental data. Table 5.2 gives the mean values of the Young's modulus, E_{T}, and stiffness per unit length, K_T (5.28), for the various materials.

Material	C_{10} (kPa)	E_{T} (kPa)	K_T (kN/m^2)
gel A	3.68	22.29	4.83
gel B	6.52	38.38	9.21
gel C	7.57	45.24	12.61

Table 5.2: Measured material elasticity and rupture toughness properties for various Plastisol gels.

5.5.2 Elasticity and Toughness Properties for Gels and Tissue

In this section we describe tests conducted to evaluate material elasticity (C_{10}) and the rupture toughness (G_c) for two variants of Plastisol gel (soft and hard versions), porcine gel, and chicken breast tissue. The measured material parameters are used in the analysis presented in Section 5.6. All tests were performed at room temperature and the chicken samples were thawed prior to the experiments.

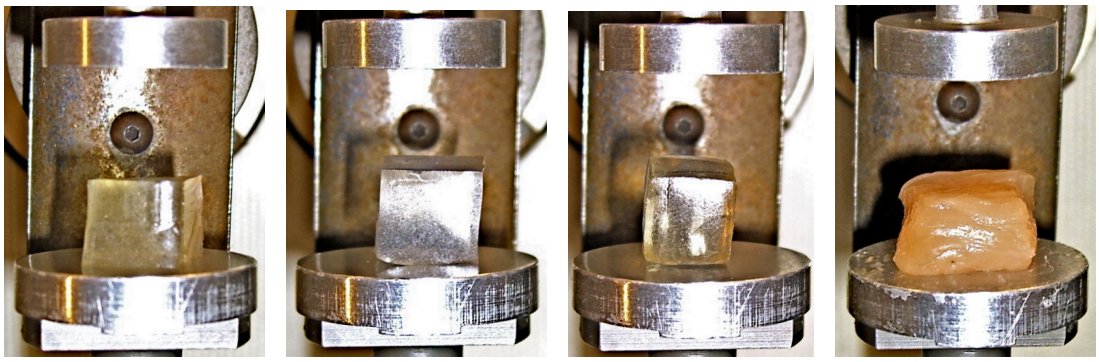

(a) Plastisol (soft) gel (b) Plastisol (hard) gel (c) Porcine gel (d) Chicken breast tissue

Figure 5.20: Tissue elasticity measurement performed on several materials via uniaxial compression tests using the RSA II.

In order to obtain values for C_{10}, uniaxial compression tests were performed on the soft materials using the RSA II, as shown in Figure 5.20. Three 1 cm^3 cube samples of each material were prepared and tested. The compression tests were performed at a strain rate of 0.001 s^{-1}. Representative stress versus strain curves for various materials are shown

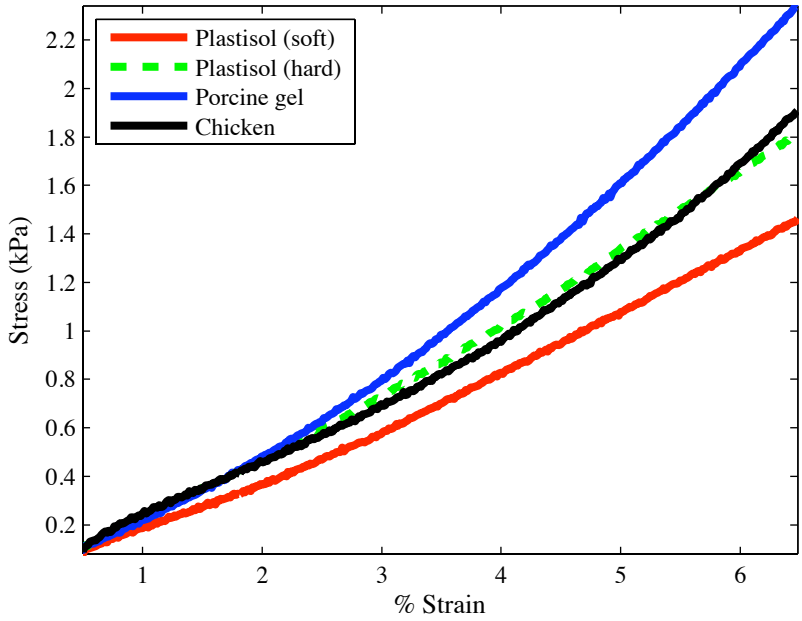

Figure 5.21: Representative compressive stress versus strain curves for various materials recorded using the RSA II.

Material	C_{10} (kPa)	E_{T} (kPa)	G_c (N/m)	t_c (kPa)
Plastisol (soft)	3.6	21.5	39.3	110.6
Plastisol (hard)	4.0	24.2	46.8	131.8
Porcine	4.9	29.6	114.4	322.2
Chicken	3.7	22.1	24.2	68.2

Table 5.3: Measured material elasticity and rupture toughness properties for gels and tissue. Note: $E_T = K_n = K_s$.

in Figure 5.21. The experimental data were fit to the constitutive equation given in (5.27) to obtain C_{10}, and Table 5.3 provides the mean values of the tissue elasticity for various materials. Linear elastic models were also fit to the experimental data and Table 5.3 gives the mean values of the Young's modulus, E_{T}, for the various materials.

In addition to tissue elasticity, the rupture toughness of several materials were evaluated

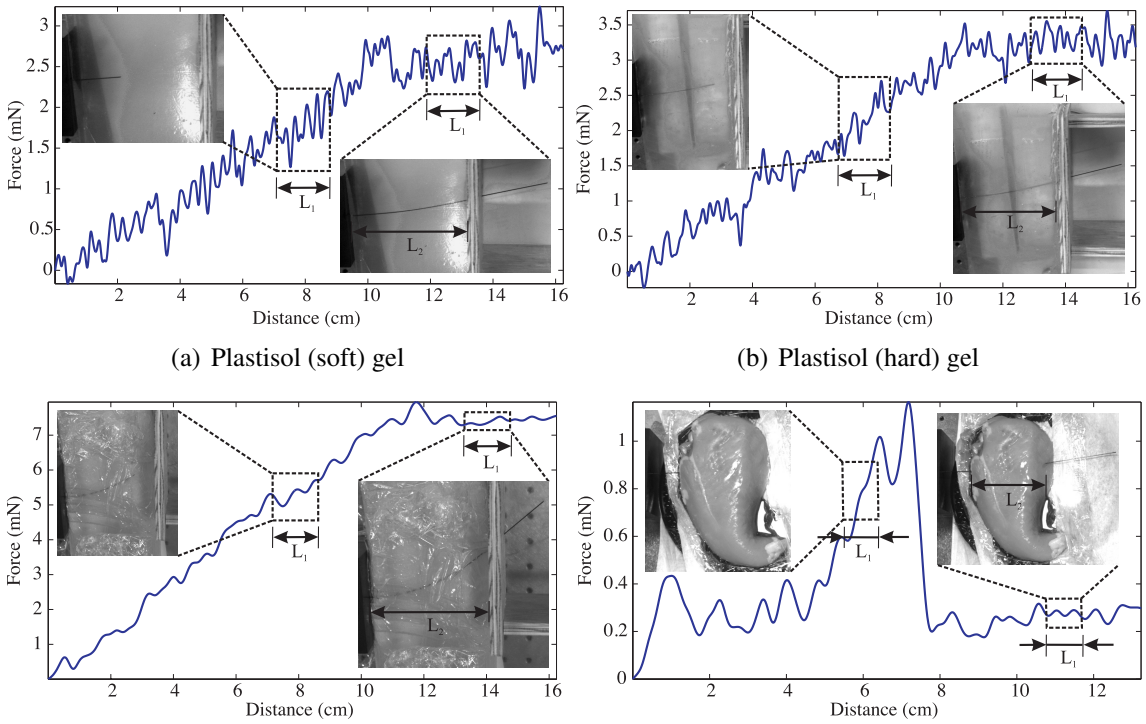

(a) Plastisol (soft) gel

(b) Plastisol (hard) gel

(c) Porcine gel

(d) Chicken breast tissue

Figure 5.22: Insertion force versus distance travelled by needle used for rupture toughness measurement. The representative snapshots show the needle tip interacting and outside the tissue samples. Data collected in the windows during which the needle tip travelled L_1 are used to calculate G_{ftc} and G_{ft}. The choice of L_1 is arbitrary, as long as the force data collected within this window is rich and the same L_1 is used for both the G_{ftc} and G_{ft} calculations.

using the needle steering robot shown in Figure 5.4. The nitinol needle had a diameter of 0.71 mm and a tip bevel angle of 55°. As the needle penetrated through the material, the insertion force was recorded using an ATI Nano 17 force sensor. The material toughness was calculated for soft and hard versions of plastisol gel, porcine gel, and chicken breast tissue using the expression given in (5.38).

Figure 5.22 shows the insertion force recorded as the needle travels through different

materials. The needle was driven at a constant insertion velocity of 0.125 cm/sec and the length, L_2, for all gels was 10.2 cm, for the chicken tissue it was 7.5 cm. Also shown in Figure 5.22 are representative snapshots during which the toughness measurements were made. The length of the window when the needle tip is interacting and outside the tissue is given by L_1. During the phase when the needle tip is outside the tissue and only the needle shaft interacts with tissue, the insertion force is fairly constant. The rupture toughness for the various materials are provided in Table 5.3.

5.6 Bevel Tip and Tissue Interaction Forces - Sensitivity Studies

This section presents a FE-based method to calculate the forces acting at the needle tip. The inputs to the simulation model are the tissue elasticity and toughness parameters determined as described in the previous section. The FE model includes both contact and cohesive zone models to simulate tissue cleavage. We investigated the sensitivity of the tip forces to tissue rupture toughness, linear and nonlinear tissue elasticity, and needle tip bevel angle.

The material parameters obtained from the experiments in the previous section were incorporated into FE simulations using ABAQUS [97] in order to evaluate the forces at the needle tip. Figure 5.23 shows the various forces acting on the needle interacting with

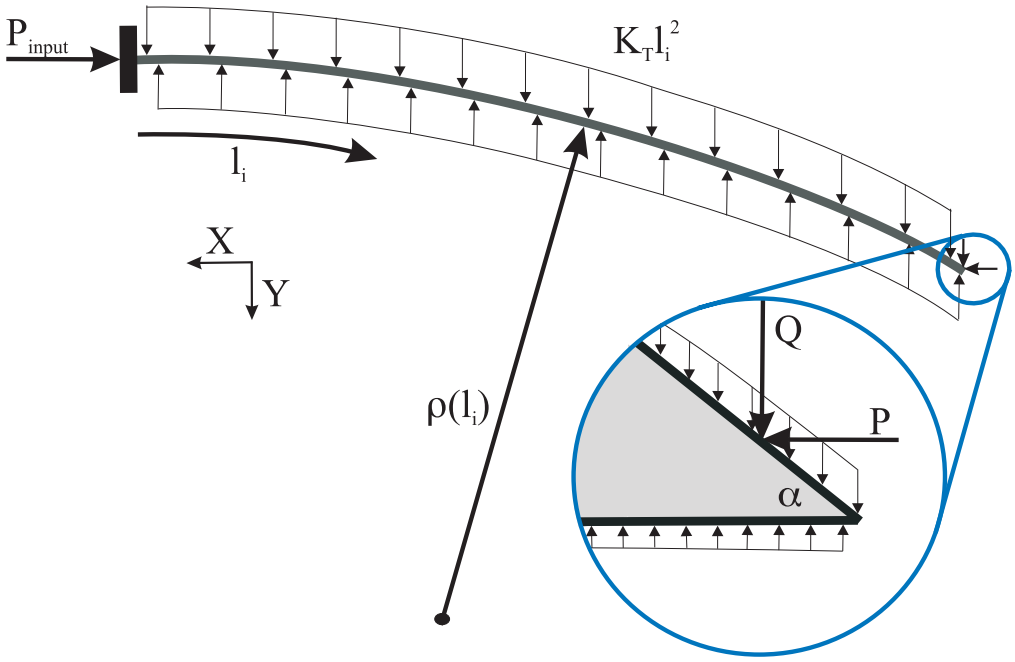

Figure 5.23: Distributed load acting on a needle shaft as it interacts with an elastic medium. *Inset*: Forces acting on the bevel tip, where P and Q are the resultant forces along the bevel edge. K_T is the stiffness of the elastic medium per unit length, while P_{input} is the insertion force.

an elastic medium. The needle is subjected to compressive and frictional forces along its needle shaft, and forces due to tip asymmetry. In this section, we investigate the effect of rupture toughness, bevel angle, and tissue elasticity on the forces at the bevel tip.

5.6.1 Sensitivity to Tissue Rupture Toughness

In order to simulate the interaction of the needle tip deforming and rupturing tissue as it travels, we employ a cohesive zone model (Figure 5.24). Cohesive zone modeling techniques are commonly used to simulate interface failure in composite structures. The cohesive zone is a mathematical approach to modeling, using the fact that work must be

done to separate the two surfaces at an interface. This work is described in terms of a prescribed relationship between the tractions, $\mathbf{t}$, required to separate the surfaces and the relative strains, $\boldsymbol{\delta}$, of those surfaces. A detailed explanation of the numerical implementation of cohesive zone models is presented in [180]. Cohesive zone elements are placed between bulk elements, as shown in Figure 5.24(a).

The cohesive zone elements are placed between continuum (bulk) elements and are defined in a small region (1 mm long and 0.072 mm wide) near the needle tip, as shown in Figure 5.25(a). In our FE simulation models, the cohesive zone is implemented using quadrilateral elements (ABAQUS element $COH2D4$), while the bulk elements are a mixture of quadrilaterals (ABAQUS element $CPE4H$) and triangular elements (ABAQUS element $CPE3H$). The bulk elements are assigned the nonlinear material properties (C_{10}) given in Table 5.3, in addition to having geometric nonlinearity. As the needle tip deforms the tissue and the cleavage process is initiated, the cohesive zone elements open up in order to simulate this behavior. All of the cohesive elements use a traction-separation law (Figure 5.24(b)), which defines the relationship between the vectorial tractions (force density vectors), $\mathbf{t}$, and strains, $\boldsymbol{\delta}$, across the element. The tractions and strains are given by

$$\mathbf{t}_c = K_n \delta_n \mathbf{e}_n + K_s \delta_s \mathbf{e}_s, \tag{5.39}$$

where K_s, K_n and δ_s, δ_n are stiffnesses and strains in the shear and normal directions, respectively. The description of the deformation and the traction evolution in these elements

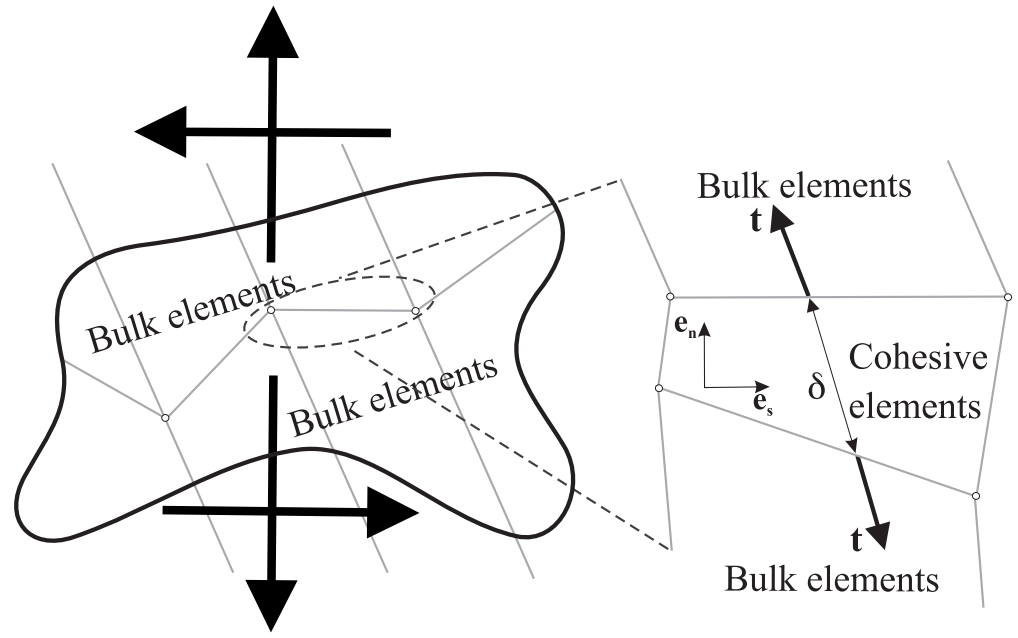

(a)

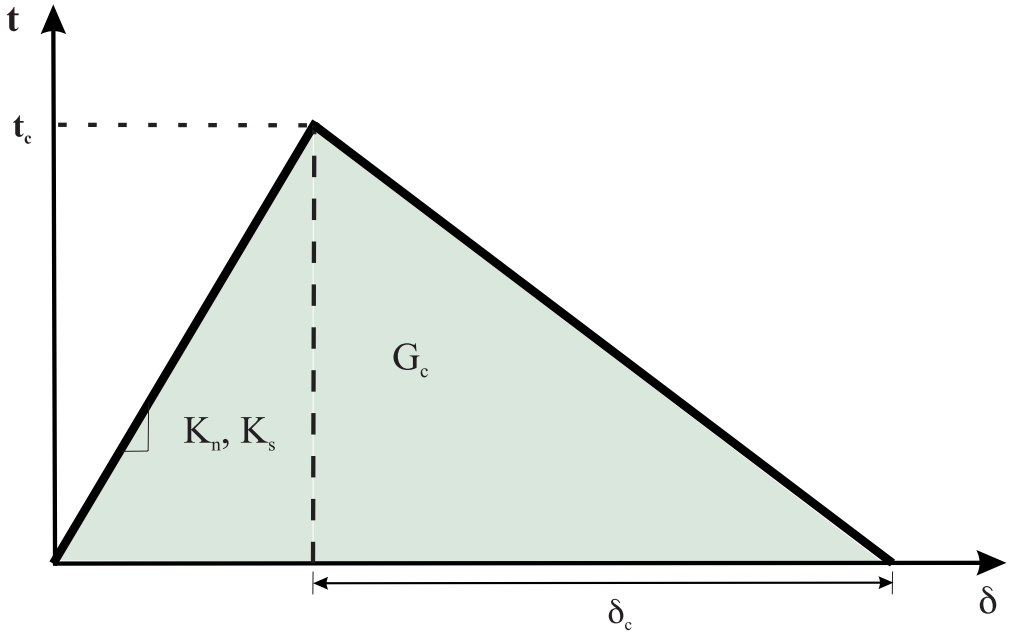

(b)

Figure 5.24: The cohesive zone model used to simulate tissue cleavage process. (a) A sketch depicting application of cohesive zone elements along the bulk element boundaries, where tensile/compressive (normal) and shear strains result in deformation and rupture of the cohesive elements. (b) Linear traction-separation laws where values for K_n, K_s, G_c, and t_c are obtained from experiments and given in Table 5.3.

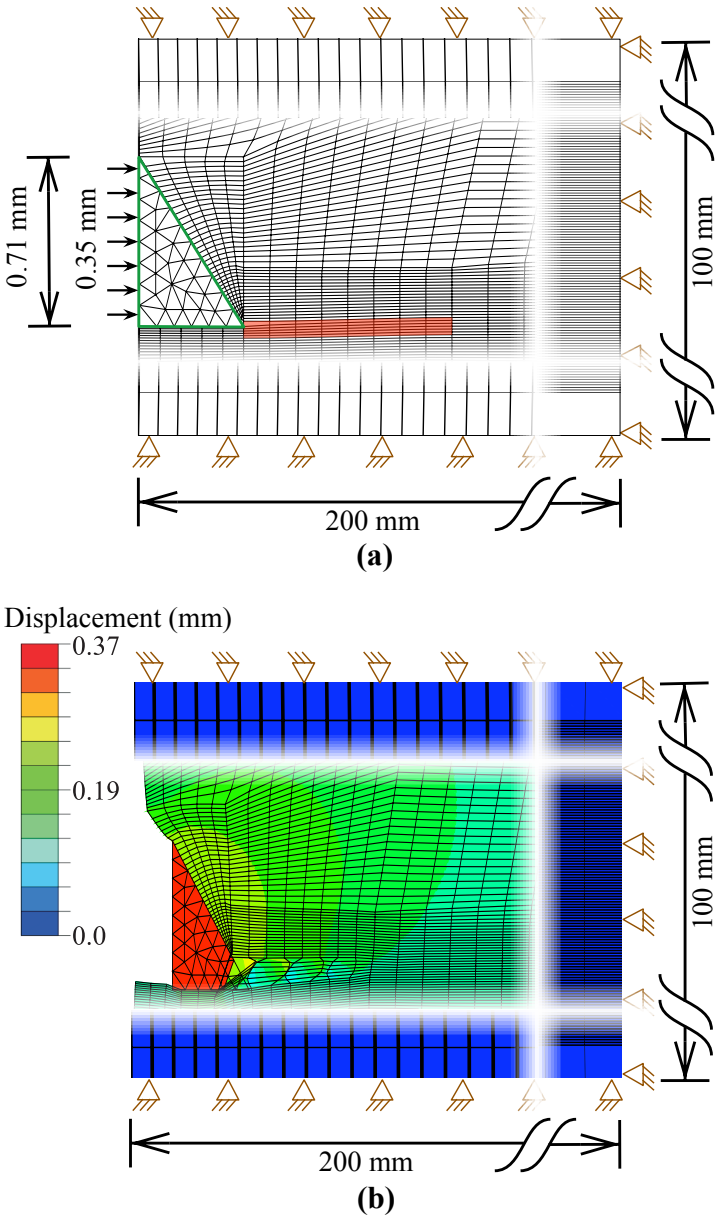

Figure 5.25: FE simulation setup used to model needle and tissue interaction for a needle with 55° bevel angle and 0.71 mm diameter. The needle tip was made of nitinol ($E = 50$ GPa, $\nu = 0.3$). (a) The green border used to signify contact surfaces and the elements in red are assigned to be the cohesive zone. (b) Magnitude of nodal displacement contour plot for the needle tip penetrating the tissue. The elements where the needle appears to penetrate the medium have reached the critical traction (t_c) value and are deleted from the simulation. The visualization of element deletion does not work in ABAQUS and is a software bug.

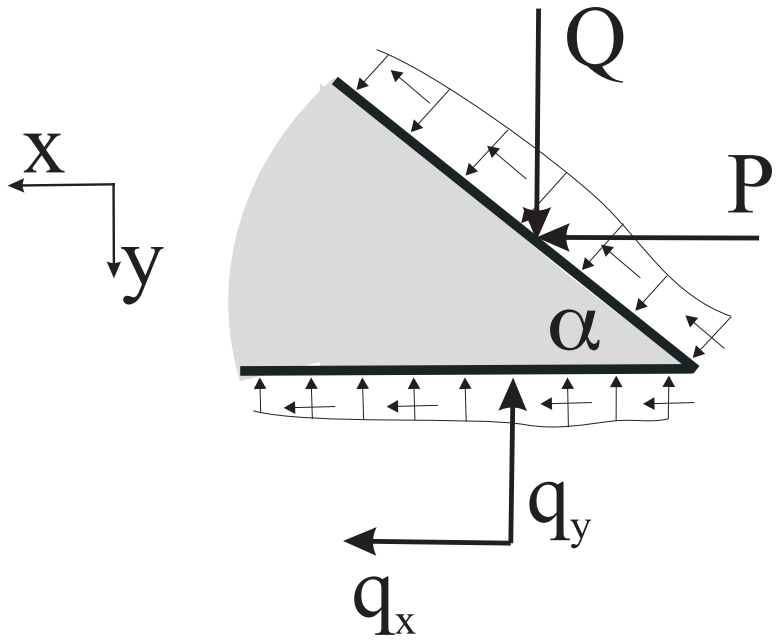

Figure 5.26: Forces acting on the bevel tip, where $F_x = q_x + P$ and $F_y = q_y + Q$.

is governed by a linear traction-separation law, as shown in Figure 5.24(b). The damage evolution and subsequent cleavage of the tissue is given by the rupture toughness, G_c. In order to define the traction-separation law, inputs to the FE simulation model are: K_n, K_s, t_c, and G_c. We assume the cohesive stiffnesses in the normal and shear directions are the same and given by the elastic modulus of the tissue, as provided in Table 5.3, i.e. $K_n = K_s = E_{\mathrm{T}}$. G_c values are also provided in Table 5.3. For unit original constitutive thickness of the cohesive element, δ_c is taken to be the same order of magnitude as the diameter of the needle (i.e. $\delta_c = 0.71$ mm) and t_c is calculated for G_c being the area of the shaded region (Figure 5.24(b)). The frictionless contact surfaces and the cohesive zone are highlighted in Figure 5.25(a) with an applied displacement of 0.35 mm.

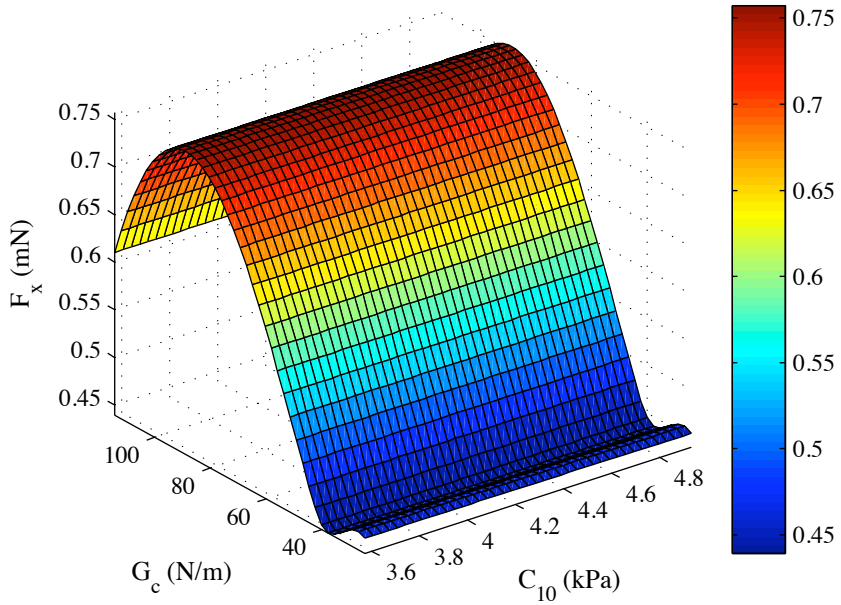

(a) Forces in the axial (x) direction.

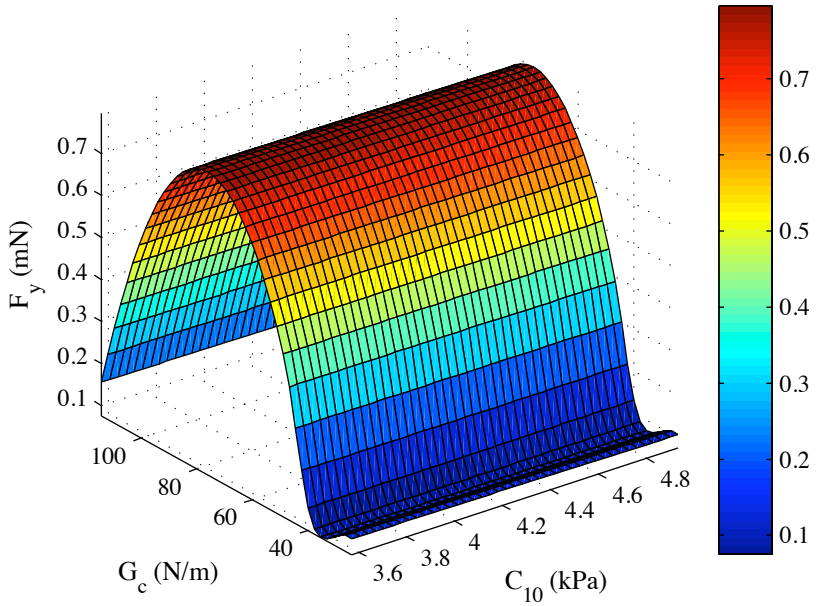

(b) Forces in the transverse (y) direction.

Figure 5.27: FE simulation results for needle tip forces with variation in nonlinear material elasticity and rupture toughness. Note: The slight increase in force values for $G_c < 40$ N/m is believed to be an artifact of the interpolation performed in order to generate the mesh plots.

Figure 5.25(b) shows the contour of the magnitude of nodal displacement in the vicinity of the needle tip and cohesive zone. Also shown is the needle tip penetrating through the tissue elements and the initiation of cleavage. The tissue rupture process is simulated as the cohesive zone elements open up, which in turn is governed by the traction-separation law. The resultant tip forces in the axial and transverse directions are given by $F_x = q_x + P$ and $F_y = q_y + Q$, respectively (Figure 5.26). Figure 5.27 shows the variation in F_x and F_y as the rupture toughness, G_c, and the material elasticity, C_{10}, changes for the different tested materials. G_c and C_{10} varied from 24.22 N/m to 114.4 N/m i.e. 372.3% change, and 3.57 kPa to 4.93 kPa, i.e. 38% change, respectively. This resulted in a 38% (0.44 N to 0.61 N) and 260.2% (0.11 N to 0.39 N) variation in F_x and F_y, respectively. Also, as seen in Figure 5.27, changes in tip forces are dominated by the variations in G_c, and not C_{10}. The overall bending of the needle is due to a combination of forces along the needle shaft and at the tip. The results of this study indicate that the tip forces are primarily governed by the rupture toughness. However, in order to predict the path the needle will follow, the structural stiffness of the needle shaft needs to be included in the model.

5.6.2 Sensitivity to Needle Tip Bevel Angle and Tissue Elasticity

FE simulations were performed to assess the effect of bevel angle and tissue elasticity. Figure 5.28 shows the simulation setup with boundary conditions and input displacement.

Also shown is an example FE mesh used for the study. The elements used in this study are a combination of quadrilateral (ABAQUS element *CPE*8) and triangular (ABAQUS element *CPE*6 and *CPE*6*M*) elements. Unlike the study presented in Section 5.6.1, in which contact was simulated between the needle tip and the elastic medium, here we model the tissue and needle tip as one body but assign different material properties to signify the needle and tissue.

To study the effect of bevel angle, α was varied from 10° to 80°, while the tissue Young's modulus and Poisson's ratio were kept constant at $E_\mathrm{T} = 25$ kPa and $\nu_\mathrm{T} = 0.45$, respectively. In order to study the sensitivity of tip forces to tissue elasticity, E_T was varied from 10 kPa to 35 kPa with $\nu_\mathrm{T} = 0.45$ and $\alpha = 45^\circ$. It should be noted that a variation in bevel angle entails changing the geometry of the model, and requries re-meshing the model, unlike the cases in which the elastic property of the tissue is changed. For all studies, needle tip Young's modulus and Poisson's ratio were set to $E = 2 \times 10^{11}$ Pa and $\nu = 0.3$, and the needle diameter was 2 mm with applied displacement of 0.5 mm. Also, though the constitutive behavior of the elements is linear, geometric nonlinearity of the elements has been incorporated.

Figure 5.29(a) provides the variation of the needle tip forces in the axial (P, q_x) and transverse (Q, q_y) directions as bevel angle is changed. q_x decreases in a nonlinear manner with increase in bevel angle, while P decreases to a minimum value at approximately 35° and then begins to rise for increase in bevel angle. It is seen that Q monotonically decreases

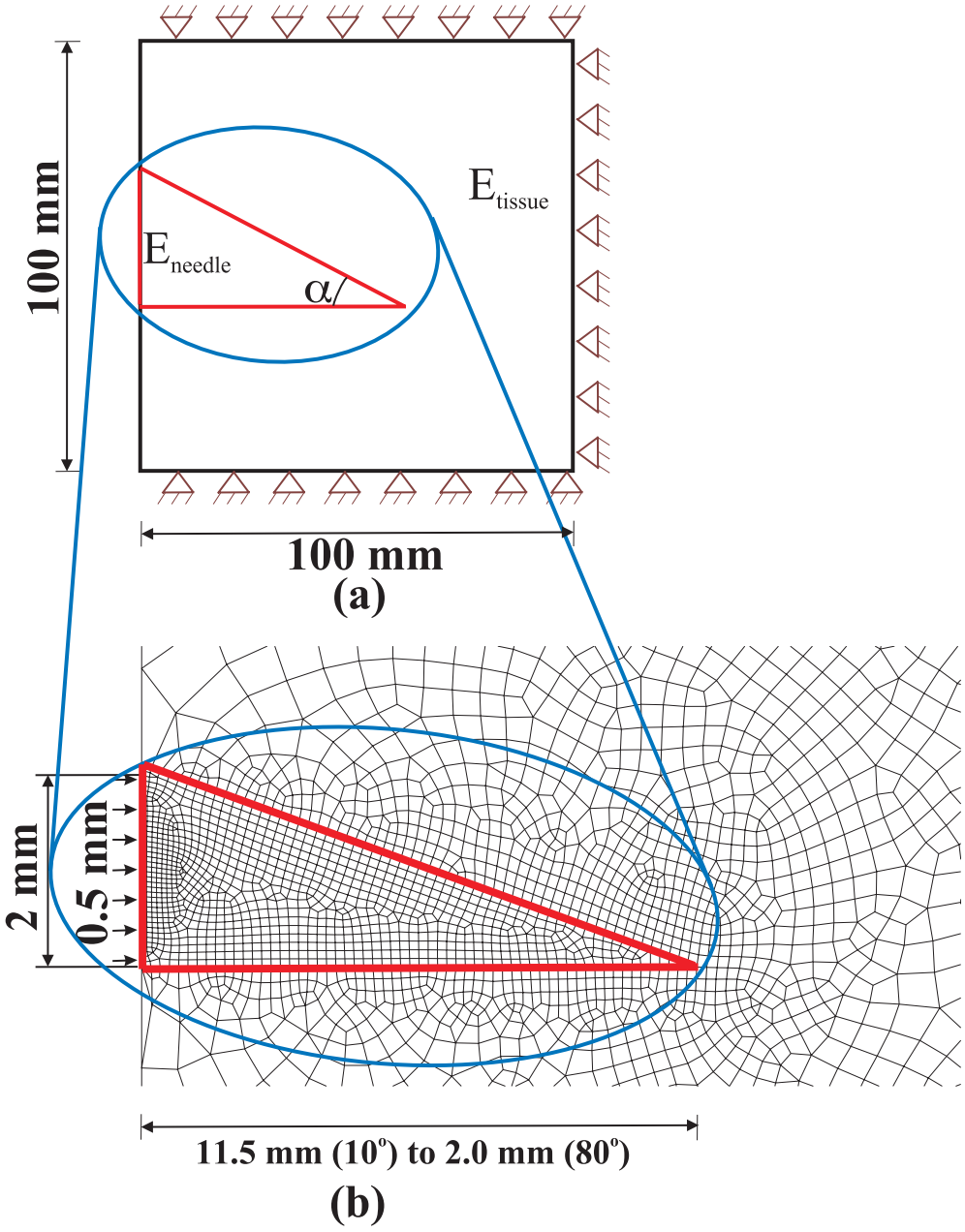

Figure 5.28: (a) FE simulation model for performing tip force versus bevel angle and tissue elasticity sensitivity studies. (b) Example FE mesh for a 20° bevel angle where the elements within the red border have been assigned needle material properties.

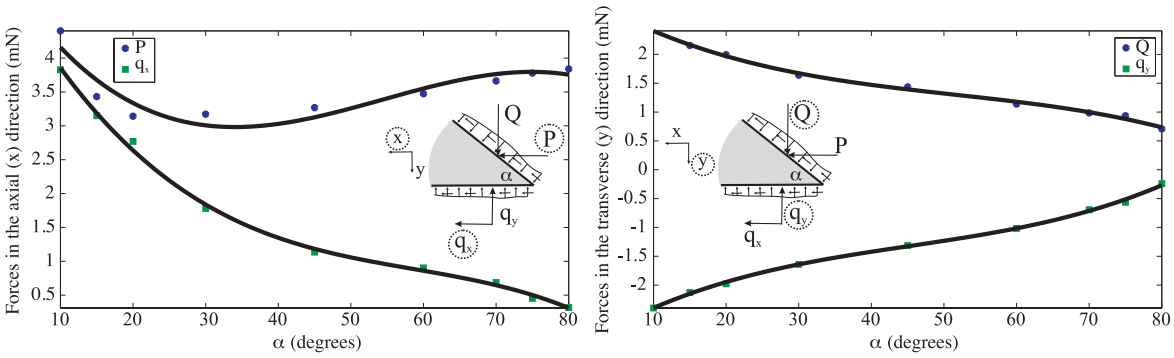

(a) Forces in the axial (x) and transverse (y) directions change with bevel angle.

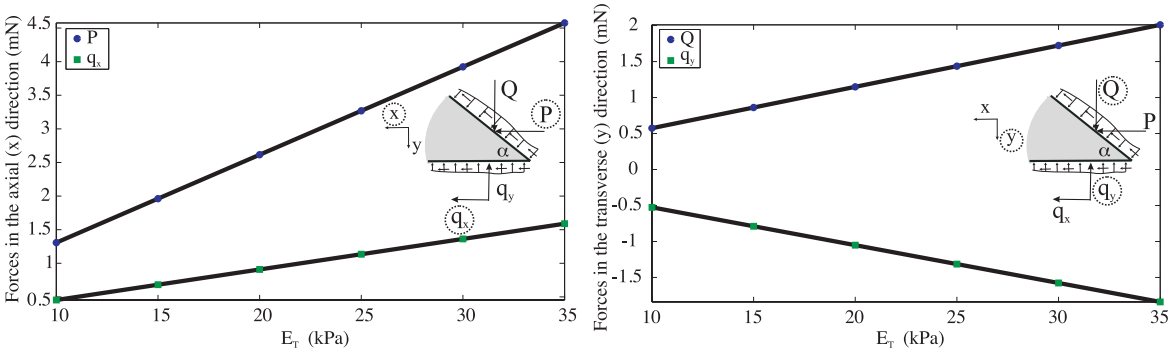

(b) Forces in the axial (x) and transverse (y) directions change with tissue elasticity.

Figure 5.29: FE simulation results depicting the sensitivity of tip forces to changes in bevel angle and tissue elasticity, where the solid lines show the trend in the tip forces.

with increase in bevel angle, while q_y monotonically increases (decreases in the opposite direction) with increase in bevel angle. The trends observed for q_x, q_y, and Q could be explained as follows: With the increase in bevel angle, for constant needle diameter, the length of the bevel and bottom edges decrease and hence the sum of the nodal forces along these edges also decrease. In Figure 5.29(b), Q and q_y linearly increase and decrease (increases in the negative direction) with increase in tissue elasticity, respectively. Further, Q follows a similar trend as the analytical model for transverse tip force (Figure 5.10), although the numerical values of the forces for both cases are different. This is due, at the

minimum, to differences in elastic medium and needle geometric parameters. Also, P and q_x increase linearly with increase in tissue elasticity. The trend followed by the tip forces could be explained as follows: With the increase in Young's modulus (linear elasticity), the tissue resistance increases and thus, the tip forces linearly increase for the same input displacement.

5.7 Models for Needle-Tissue Interaction

We now present a mechanics-based model that incorporates the observations from microscopic and macroscopic experiments described in Sections 5.2.1 and 5.2.3.

5.7.1 Energy Approach

We derive expressions that describe the deflection of a bevel-tip needle embedded in an elastic medium. The analysis assumes a 2D model with the needle undergoing a single bend. The derived expression incorporates the needle material and geometric properties, as well as the local and global elastic properties of the medium. Further, given the deflection, the radius of curvature of the needle can be readily evaluated. In the derivation presented below, the needle trajectory is discretized into a series of steps, i, where the length of the needle is l_i and the deflection is y_i. Figure 5.23 depicts the load distribution of a needle of length l_i surrounded by an elastic medium, where P_{input} is the applied needle insertion force, P and Q are the tip loads at the bevel edge, and K_T is defined as the stiffness per unit

length of the elastic medium. The functional form for the deflection of the needle in an elastic medium is initially assumed and the Rayleigh-Ritz approach is used to evaluate the coefficients of the deflection equation. The Rayleigh-Ritz method is a variational method in which the minimum of a potential defined by the sum of the total energy and work done by the system are calculated.

The system potential, Λ, of a needle of length, l_i, interacting with an elastic medium, is given by

$$\Lambda = \underbrace{(N_E + S_E)}_{\text{energy}} + \underbrace{(-W_Q - W_P - W_R)}_{\text{work}} + \underbrace{P_{\text{input}} l_i}_{\text{input work}}, \tag{5.40}$$

where N_E and S_E are the energies associated with needle bending and needle-tissue interaction, respectively, W_Q and W_P are the work due to transverse and axial bevel tip loads, respectively, and W_R is the work done to rupture the tissue. We now derive explicit expressions for each of the terms in (5.40).

5.7.1.1 Needle Bending

N_E is the sum of energy due to pure needle bending, U_B, and bending due to axial load, U_P, i.e. $N_E = U_B + U_P$. The expression for curvature is

$$\frac{1}{\rho} = \left(\frac{d^2 y_i / dx^2}{\left(1 + (dy_i/dx)^2\right)^{3/2}} \right) \approx \frac{d^2 y_i}{dx^2}. \tag{5.41}$$

Thus, for needle segments of length l_i, N_E is reported in [193] as

$$U_B = \frac{EI}{2}\int_0^{l_i}\frac{1}{\rho^2}\,dx = \frac{EI}{2}\int_0^{l_i}\left(\frac{d^2y_i}{dx^2}\right)^2 dx. \tag{5.42}$$

The bending due to axial load, P, is evaluated by considering a segment, dl_i (Figure 5.30), along the needle. The axial strain due to P is $\frac{dl_i}{dx}$. Thus, $E\frac{dl_i}{dx} = \frac{P}{A}$, where A is the needle cross-sectional area. Hence, using change of variable such that $ds = dl_i$

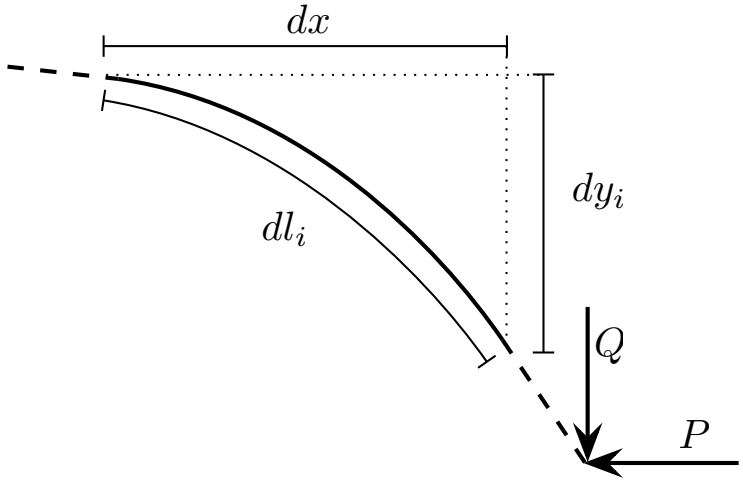

Figure 5.30: Needle of segment dl_i and with needle tip loads P and Q.

$$U_P = \frac{1}{2}\int_0^{l_i} P\,ds = \frac{1}{2AE}\int_0^{l_i} P^2\,dx. \tag{5.43}$$

Substituting (5.42) and (5.43) into the expression for N_E gives

$$N_E = \underbrace{\frac{EI}{2}\int_0^{l_i}\left(\frac{d^2y_i}{dx^2}\right)^2 dx}_{U_B} + \underbrace{\frac{1}{2AE}\int_0^{l_i} P^2\,dx}_{U_P}. \tag{5.44}$$

5.7.1.2 Needle-Tissue Interaction

In (5.40), S_E is a combination of energy stored in the system due to compression of the elastic medium due to the needle, U_C, and interaction of the elastic medium along the needle shaft, U_T. Thus,

$$S_E = U_C + U_T. \tag{5.45}$$

The compression of the gel due to the bevel-tipped needle occurs along the needle shaft. Pressure is applied by the needle to the elastic medium and ΔV is the resulting change in volume of the medium. Thus, U_C is

$$U_C = \text{Pressure} \times \Delta V = K\frac{(\Delta V)^2}{V}, \tag{5.46}$$

where K is the bulk modulus of the elastic medium and the change in volume of the medium is $\Delta V = Al_i$. For linear elastic materials $K = \frac{E_T}{3(1-2\nu_T)}$, where E_T and ν_T are the Young's Modulus and Poisson's ratio of the medium, respectively. Thus,

$$U_C = \frac{E_T\,(Al_i)^2}{3V\,(1-2\nu_T)}. \tag{5.47}$$

For compressible hyperelastic strain energy functions, using (5.30), we can also express U_C in terms of hyperelastic material parameters.

As mentioned earlier, the needle trajectory is discretized into a series of steps and U_T is calculated at each step. In the absence of an elastic medium surrounding the needle,

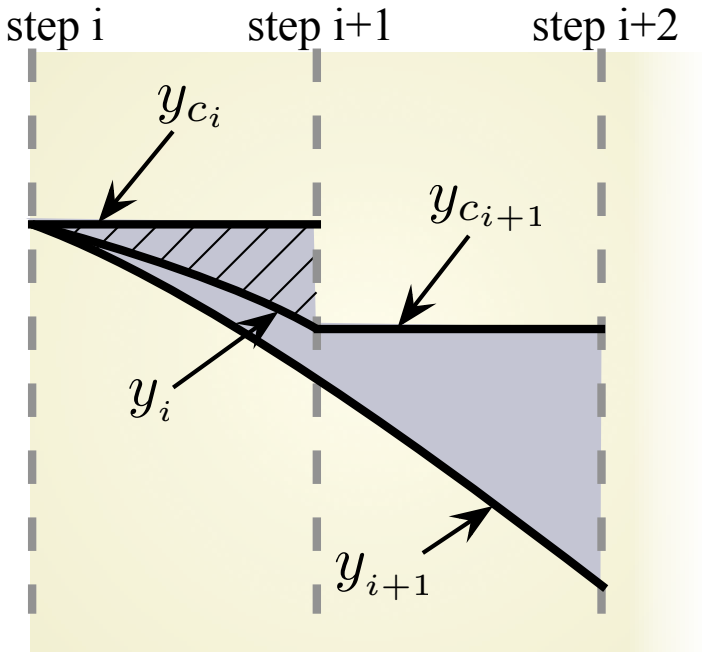

Figure 5.31: Schematic for calculation of U_T, energy due to the interaction between the needle shaft and elastic medium.

no tip forces would be generated and the needle would not bend. This corresponds to the stress-free path of the needle and the deflection in this case is denoted by y_{c_i}. The key idea in the calculation of U_T is that the elastic medium interacts with the needle shaft only when the needle deviates from the rupture trajectory it has previously established. Figure 5.31 provides a sketch of y_{c_i} and y_i, and the shaded area represents U_T at each step. Thus, for $i = 1$ and a needle segment of length l_1,

$$U_T = \frac{1}{2}\int_0^{l_1} K_T \left(y_1 - y_{c_1}\right)^2 dx, \tag{5.48}$$

where K_T is the previously defined needle-tissue interaction stiffness per unit length, given

in (5.28). In (5.48), y_{c_1} is a function of the bevel angle (α) and for simplicity is assumed to be

$$y_{c_1} = 0. \tag{5.49}$$

Similarly for the needle segment of length, l_2, U_T is calculated as the sum of energies for needle segments 0 to l_1 and l_1 to l_2

$$U_T = \frac{1}{2}\int_0^{l_1} K_T \left(y_2 - y_{c_1}\right)^2 dx + \frac{1}{2}\int_{l_1}^{l_2} K_T \left(y_2 - y_{c_2}\right)^2 dx, \tag{5.50}$$

where

$$y_{c_2} = y_1(l_1) \tag{5.51}$$

Thus, the general expression for U_T for a needle of length, l_n, is

$$U_T = \sum_{i=1}^{n} \frac{1}{2}\int_0^{l_i} K_T \left(y_n - y_{c_i}\right)^2 dx, \tag{5.52}$$

where

$$y_{c_i} = y_{i-1}(l_{i-1}). \tag{5.53}$$

The necessity of treating U_T step-wise can be understood through closer inspection of (5.52). The needle-tissue interaction energy is a function of the square of the deformation in the medium itself. If the needle was embedded in the tissue straight and then bent by tip loads, the deflection in the tissue would be y_i. However, since the needle tears a path

through the tissue, only the difference between the ruptured path and the current needle trajectory, $y_i - y_{c_i}$, interacts with the tissue. As insertion continues, the needle trajectory deviates from the original ruptured path it has taken, thus engaging the tissue. Prediction of this process is handled step-wise; the previous path of the needle and current predicted path of the needle are known for every i^{th} step. y_{c_i} is a linear discretization of the ruptured path employed to determine the tissue deformation. Note, the path predicted by y_{c_i} converges for smaller step sizes.

5.7.1.3 Work Done

In (5.40) the work done due to the transverse tip load, Q is

$$W_Q = Qy(l_i). \tag{5.54}$$

The work done by axial tip load, P, is

$$W_P = \int_0^{l_i} P\,du, \tag{5.55}$$

where $du = dl_i - dx$, shortening of the needle, as shown in Figure 5.30. Using the series expansion it is possible to express du in terms of dy_i and dx

$$du = dl_i - dx = \sqrt{(dx)^2 + (dy_i)^2} - dx \approx \frac{1}{2}\left(\frac{dy_i}{dx}\right)^2 dx. \tag{5.56}$$

Substituting (5.56) into (5.55) results in

$$W_P = \int_0^{l_i} \frac{P}{2} \left(\frac{dy_i}{dx} \right)^2 dx. \tag{5.57}$$

The work done to rupture the elastic medium, W_R, is a function of the effective rupture toughness, G_c, and the amount of tear or opening, a (crack length). G_c is defined as the work done per unit needle cross-section area to rupture and cut through tissue [30]. Thus,

$$W_R = aG_c l_i. \tag{5.58}$$

5.8 Results

We now present the needle deflection simulation results obtained using the model developed in the previous section. The Rayleigh-Ritz method, the functional form of the needle deflection is initially assumed. We chose

$$y_i = a_0 + a_1 x + a_2 x^2 + a_3 x^3, \tag{5.59}$$

where y_i satisfies the boundary conditions $y_i(0) = 0$ and $\frac{dy_i(0)}{dx} = 0$. Using the Rayleigh-Ritz method, the coefficients a_0, a_1, a_2, and a_3 are evaluated by minimizing the system potential, Λ (5.40). For each step of needle length segment, l_i, N_E, S_E, W_Q, W_P, and W_R are calculated using (5.44), (5.45), (5.54), (5.57), and (5.58), respectively. The deflection

equation coefficients, a_j (for $j = 0, 1, 2, 3$), are calculated by setting

$$\frac{\partial \Lambda}{\partial a_j} = 0. \tag{5.60}$$

The system parameters used for the simulation study are provided in Table 5.4 and are based on mean values calculated in Section 5.5.2.

Needle	Ø (mm)	I (m^4)	A (mm^2)	E (GPa)	a (mm)
	1.0	0.05	0.79	50.0	0.05
Tissue	K_T (kN/m)	ν	C_{10} (kPa)	G_c (N/m)	V (m^3)
	25.0	0.45	4.0	20.0	0.0045

Table 5.4: Simulation input parameters

Figure 5.32 depicts the simulated deflection of a needle of length 20 cm embedded in an elastic medium with P_{input}, P, and Q set to 2 N, 0.03 N, and 0.3 N, respectively. Figure 5.32 provides the deflection of needles for two additional cases with the same tip and insertion forces. In the first case, needle deflection is calculated in the absence of an elastic medium, i.e. $U_T = 0$. In the second case, needle deflection is computed when there is an elastic medium surrounding the needle but no rupture trajectory, i.e. $U_T = \frac{1}{2}\int_0^{l_i} K_T y_i^2 dx$. In both cases tip forces are applied to the needle. As seen, the deflection in the absence of a medium is greater than in the presence of the medium, while the absence of a rupture trajectory results in small deflection ($\sim$ 1 mm) of the needle. For the approximate material and needle properties, the final tip deflection of the needle was iteratively calculated to be 9.2 cm, which is in the same range as the observed deflection given in Figure 5.5. For this

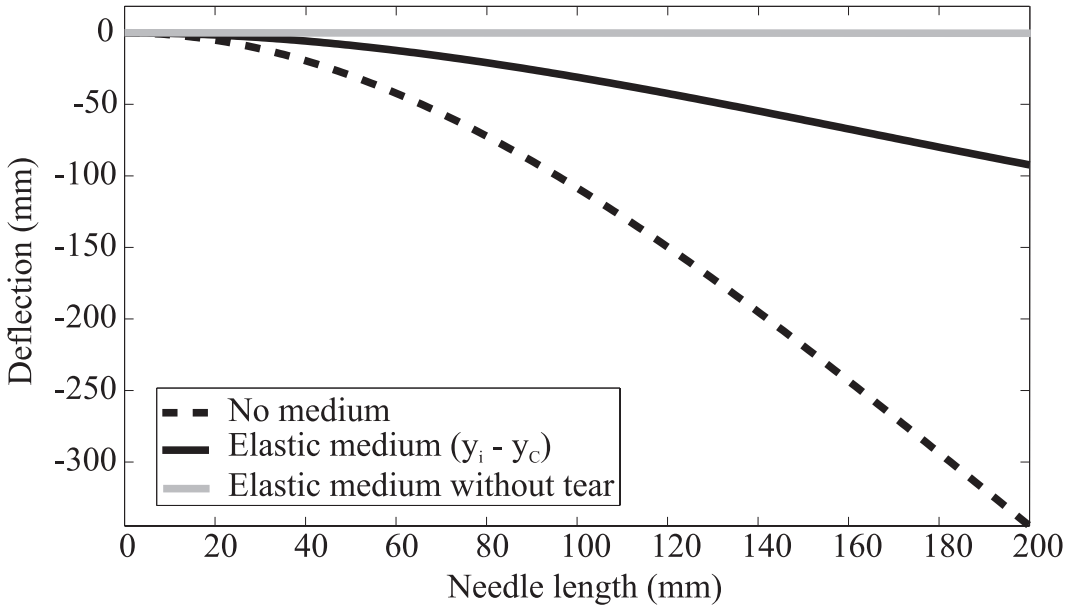

Figure 5.32: Simulation results for needle deflection versus insertion.

simulation case, the radius of curvature was also observed to be almost constant at 140 mm. The radius of curvature converges after approximately 18 iteration steps.

During the initial needle insertion phase, the needle-tissue interaction stiffness does not play a significant role in the needle bending process. But as the needle is further engaged in the elastic medium, the importance of the needle-tissue interaction stiffness increases. Figure 5.33 shows the contribution of the various energies in the system for a 20 cm insertion. As seen, U_T dominates the total energy contribution to the system. U_T and U_B contain 76.4% and 23.5% of total stored strain energy of the system. Simulation studies were also performed where the needle radius and tissue stiffness per unit length, K_T, were varied, and the changes in the radius of curvature, ρ, were observed. As seen in Figure 5.34, for a medium of fixed elasticity, as the radius of the needle increases, the radius of curvature

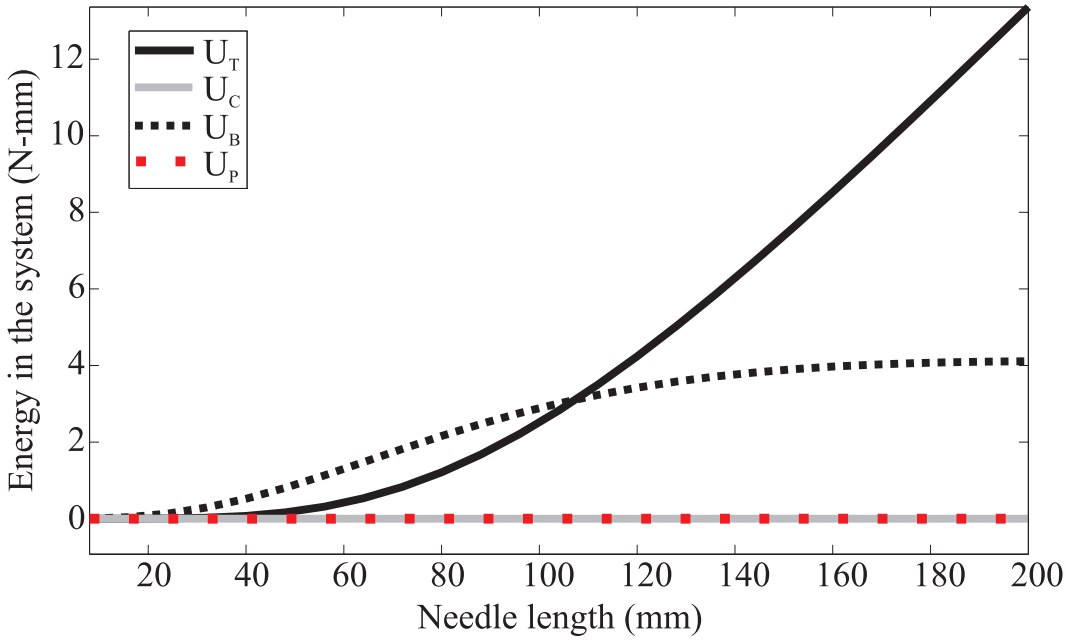

Figure 5.33: Contribution of various components of the system energy. U_T is the energy associated with the interaction of the elastic medium along the needle shaft, while U_C is the energy stored in the system due to compression of the elastic medium due to the needle. U_B and U_P are energies due pure needle bending and bending due to axial load, respectively. Both U_C and U_P are small (~ 5 mN-mm) compared to U_T and U_B.

also increases. The numbers for the radius of curvature observed in the simulation studies are in the same range as those seen in the experimental studies given in Table 5.1.

5.9 Summary

Our objective in this chapter was to understand of effects of surgical tool shape, specifically bevel-tipped flexible needles, for surgical simulation and planning. We conducted both microscopic and macroscopic experiments to observe the interactions at the needle tip with a soft elastic medium. We developed a macroscopic analytical model that pro-

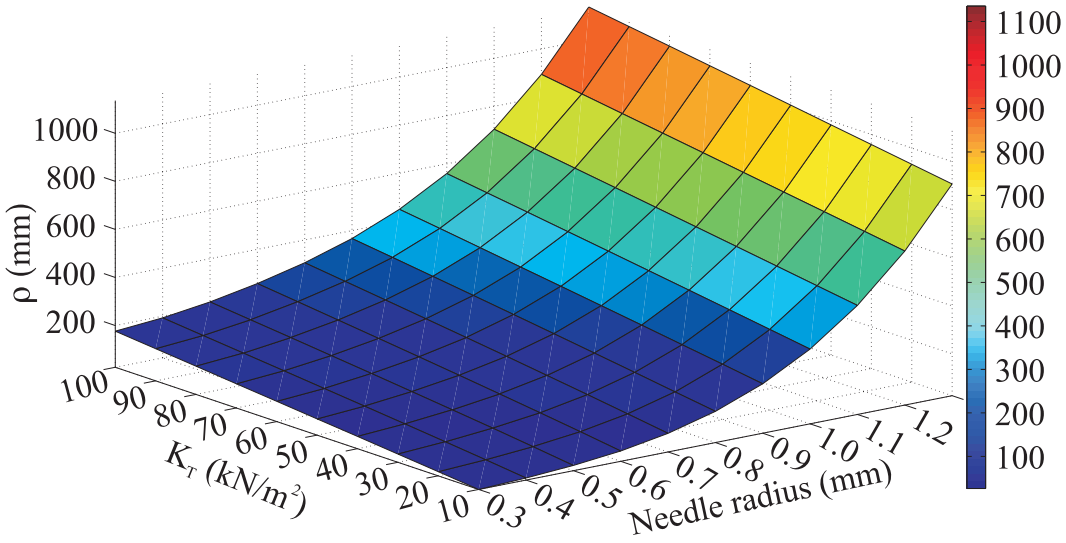

Figure 5.34: Variation of the radius of curvature (ρ) for changes in needle radius and tissue stiffness (K_T).

vided a relationship to calculate the tip loads. We also developed a FE-based model of the needle tip-tissue interaction using cohesive zone models. A mechanics-based model of a flexible bevel-tipped needle interacting with a soft elastic medium was developed using the Rayleigh-Ritz formulation. Elasticity and toughness experiments were used to populate our models. The deflection and radius of curvature predicted by the model was in the same as the those observed in the needle insertion studies. In this section, we summarize the results of this chapter.

This chapter presented a method to determine bevel-tip needle and tissue interaction forces using both an analytical model and FE simulations. Our analytical model relates the needle tip geometric and tissue material parameters to the needle-tissue interaction forces and moments at the bevel tip. The transverse tip load was compared to experimental data. The experiments used needle tips with a large diameter (Ø 1.5 cm) and varying bevel angle.

The experimental results and analytical models exhibit a similar trend for the transverse tip loads. Possible causes for discrepancies between the model and experiments are due to neglecting the effects of friction, and lack of accurate knowledge of the angle (γ) by which the needle tip cuts and displaces material in order to accommodate itself in the elastic medium. Experimental evidence has shown that needles with smaller bevel angles have larger curvature and hence, greater steerability [189]. Both our analytical model and experiments also show that smaller bevel angles result in larger transverse tip forces, which is an indication of greater needle bending and thus, larger curvature.

We demonstrated a technique to extract physically relevant tissue properties (tissue rupture toughness and nonlinear elasticity) and incorporated them into our FE simulation model in order to simulate the tissue cleavage process. Tissue properties for several materials were measured experimentally and the sensitivity of the needle tip forces to these parameters were shown using FE simulations. The needle tip forces were observed to be sensitive to the rupture toughness. A 38% variation in nonlinear material elasticity did not produce significant changes in tip forces. For most applications, in which the needle would be steered through soft tissue, large variations in tissue elasticity are not expected. Further, sensitivity of needle tip forces to changes in the bevel angle were also studied through FE simulations. In general, smaller bevel angles resulted in larger axial and transverse tip forces.

We also developed a mechanics-based model to determine the deflection of a robotically steered needle interacting with a soft elastic medium. The model was influenced by

observations made from microscopic images of the needle-gel interactions. Tissue properties such as rupture toughness and nonlinear elasticity were used in a mechanics-based needle-tissue interaction model. The simulation results concur with the trend observed in macroscopic observations of a needle inserted into a gel. The results indicated that the energy associated with the needle-tissue interaction stiffness dominates the total potential energy of the system, and energy due to compression and work done due to rupture and tip loads are less significant. The energy-based formulation used physically relevant tissue and needle properties, and computes the deflection of the needle by discretizing the needle length into segments. The simulation results for tip deflection was calculated to be 9.2 cm, which is in the same range as the observed deflection from needle insertion experiments. The simulation results for the radius of curvature also converge to a constant value. The method presented could be applied in general to a needle interacting with an elastic medium and is not specific to bevel-tipped needles.

Chapter 6

Conclusions and Future Work

Surgical tool-tissue interaction modeling and simulation are of interest for the development of physically-based virtual training, and for guidance systems aimed at reducing the incidence of complications, and improving planning of medical interventions. This thesis identified some of the factors that affect realism in the development of surgical simulators and planners. We specifically investigated factors that influence the deformation response of surgical tool-tissue interaction models. These factors include the soft tissue constitutive laws, organ anatomy and their surrounding connective tissue, and the geometry of the surgical instrument interacting with the tissue. The salient contributions of this thesis include:

- We used the Poynting effect to provide a concrete example of how tissue modeling techniques relate to haptic feedback in surgical simulators;
- For medical interventional planning procedures, which are essentially displacement-driven tasks, we quantitatively demonstrated that organ geometry and surrounding

connective tissue dominate the deformation response of the organ;

- Using robotically-steered bevel-tipped flexible needles, we provided a mechanics-based needle-tissue interaction model that calculates needle deflection during needle insertion.

In this chapter we summarize the work done in this thesis and also provide possible directions for future work.

6.1 Summary

Modeling and perception of nonlinear elastic tissues for surgical simulation:
Realistic modeling of the interaction between surgical instruments and human organs has been recognized as a key requirement in the development of high-fidelity surgical simulators. Primarily due to computational considerations, most previous real-time haptic simulation research has assumed linear elastic behavior for modeling tissues, even though human soft tissues generally possess nonlinear properties. For a nonlinear model, the well-known Poynting effect developed during shearing of the tissue results in normal forces not seen in a linear elastic model. In Chapter 3, constitutive equations of several nonlinear tissue models were derived in order to highlight the Poynting effect. Experimental studies using these models demonstrated that the difference in force magnitude for myocardial tissue was larger than the just noticeable difference for contact force discrimination thresholds published in the psychophysics literature. A MDS study was used to quantify the role of the

Poynting effect on material discrimination. For nonlinear elastic tissue models exhibiting the Poynting effect, MDS analysis indicated that both shear and normal forces affected user perception.

The importance of organ geometry and boundary constraints for surgical planning: Organ geometry, the soft-tissue constitutive laws, and boundary conditions imposed by the connective tissues surrounding the organ are some of the factors that govern the accuracy of medical intervention planning. In Chapter 4 we demonstrated that for needle path planning, the organ geometry and boundary constraints surrounding the organ are the most important factors influencing deformation. As an example, the procedure of needle insertion into the prostate (e.g. for biopsy or brachytherapy) was considered. Image segmentation was used to extract the anatomical details from magnetic resonance images, and object-oriented finite element analysis (OOF) software was used to generate FE meshes from the segmented images. 2D FE simulations that account for complex anatomical details along with relative motion between the prostate and its surrounding structure using cohesive zone models were compared with traditional simulation models having simple organ geometry and boundary constraints. Nodal displacements for these simpler models were observed to be up to 14 times larger than those obtained from the anatomically accurate models.

Effects of tool geometry and tissue properties for medical intervention planning: The asymmetry of a bevel-tip needle results in the needle naturally bending when it is inserted into soft tissue. In Chapter 5 we presented an analytical model for the loads developed at the bevel tip during needle-tissue interaction. The model calculated the loads based

on the geometry of the bevel edge and gel material properties. The modeled transverse force developed at the tip was compared to forces measured experimentally. The analytical model explained the trends observed in the experiments. We also developed an FE model to compute forces at the needle tip. In order to find the forces acting at the needle tip, we measured rupture toughness and nonlinear material elasticity parameters of several soft tissue simulant gels and chicken tissue. We incorporated these physical parameters into the FE model that included both contact and cohesive zone models to simulate tissue cleavage. We investigated the sensitivity of the tip forces to tissue rupture toughness, linear and nonlinear tissue elasticity, and needle tip bevel angle. The model showed that the tip forces are sensitive to the rupture toughness.

We also presented a mechanics-based model that calculated the deflection of the needle embedded in an elastic medium. Microscopic observations for several needle-gel interactions were used to characterize the interactions at the bevel tip and along the needle shaft. The model design was guided by microscopic observations of several needle-gel interactions. The energy-based model formulation incorporated tissue-specific parameters such as rupture toughness, nonlinear material elasticity, and interaction stiffness, and needle geometric and material properties. Simulation results followed similar trends (deflection and radius of curvature) to those observed in macroscopic experimental studies of a robot-driven needle interacting with different kinds of gels. The results from this chapter contribute to a mechanics-based model of robotic needle steering, extending previous work on kinematic models.

6.2 Future Work

A quantitative method to measure the fidelity of a surgical simulation system would help provide realistic organ deformation response to the user. This deformation response would be useful for surgical planning systems as well as simulators providing haptic feedback. In Chapter 1, we proposed an approach to quantify realism in simulators, by modeling the flow of information starting from acquiring data from real tissue to haptic and/or visual display to the user (Figure 1.1). The process of modeling tool-tissue interactions for surgical simulators and planners begins with choosing a specific clinical procedure and acquiring material properties of the organs involved. These tissue properties may be acquired either *ex vivo* or *in vivo*, depending on the fidelity of the required data and access to tissue samples. This acquired information flows into the development of complex tissue models, which include both anatomical and material properties of the organ. This complex organ model might need to be simplified so that it can rendered in real time. This is required so that force-position information is displayed to the human using a haptic device and/or other immersive virtual reality aids. The limiting factors during the rendering stage might be resolution of the haptic device or the graphics update rates of the virtual environment. This thesis specifically investigated the factors important in the development of the complex tissue models. One area of future work is to analyze each source of information loss in the surgical modeling and simulation procedure, and link them to metrics related to simulator realism, human perception, and clinical outcomes.

Chapter 3 provided a concrete example of how tissue modeling techniques relate to hap-

tic feedback in surgical simulators. The applicability of linear versus nonlinear elasticity-based constitutive models will depend on the surgical simulation application. This would require *in vivo* material parameter testing of the relevant organs and evaluation (experimental or FE simulation) of the Poynting effect. For both the force discrimination pre-study and the MDS study, participants had difficulty perceiving normal components for rendering with high force magnitudes (models 6 through 9). These problems were associated with limitations in rendering large forces by the device and normal forces being masked when shear components were large. To test large forces, the experimental setup should be re-designed in the future. This could be accomplished by using a real-time operating system coupled to the Delta haptic device and also increasing the sampling frequency to speed up force rendering. The addition of virtual or mechanical damping might also mitigate some of the observed instabilities.

The study design could also be changed so that participants perform smaller shearing motions, which in turn would prevent larger forces from being rendered. Also, instead of using a virtual model, the participants could interact with physical biological and artificial tissue samples. This would produce realistic shear and normal forces. An increase in the number of participants in the research study would improve statistical significance of the results. The long-term goal of this research is to quantify and understand how organ model fidelity affects realism in surgical simulators and planners. Considering physical phenomena such as the Poynting effect, which is significant for some organs but may not be for others, in combination with human perception studies, will allow researchers to

make justified simplifications to create realistic, real-time simulation of realistic tool-tissue interactions.

The objective of the research presented in Chapter 4 was to quantitatively demonstrate that anatomically valid organ geometry models and appropriate boundary constraints are essential for accurate simulation of organ deformation during invasive procedures such as needle insertion into the prostate. Each procedure brings to bear different tissue constitutive models, geometry, and boundary conditions. The extent to which our hypothesis is valid for any specific procedure needs to be examined, and only then can its general validity be considered. The current study considered 2D organ models and future work should include 3D geometry and boundary constraints. There exist several challenges in going from 2D to 3D models, which include acquiring 3D MR image data sets, generation of 3D elements, 3D mesh modification to simulate needle insertion, visualization of 3D mesh deformation, and significant increase in computational time. Also, there does not exist a standard validated method to generate 3D FE meshes. Further, with changes in boundary condition as the needle interacts with tissue, the simulation of 3D contact and 3D cohesive zone models is an ongoing research topic. For boundary value problems in which the input is an applied displacement, the induced stresses in the system are intrinsically linked to the material properties. Thus, for surgical simulation applications in which force is fed back to the user, the constitutive model of the organ and surrounding tissue should be studied in detail. In addition to accurate calculation of stresses developed, simulators with haptic feedback also require that the interaction forces be rendered in real time, which can be

computationally challenging. Further, for needle insertion procedures in which the needle is flexible and bends due to interactions with tissues, high-fidelity tissue models need to be considered. But for scenarios in which stiff needles are used, the boundary conditions govern the deformation of the organ.

To date, we have not compared the tissue deformation model to data from actual needle insertion tasks such as prostate biopsy or brachytherapy. Model validation will be addressed in future work, and could be accomplished by recording tissue deformation data from a sequence of ultrasound or MR images and comparing them to simulation data. The validation of the simulation model requires experiments in which a needle is inserted in a controlled manner (possibly by a robotic device) into a patient, and organ deformation is quantitatively recorded by soft tissue registration. During these *in vivo* needle insertion experiments, cutting forces would also need to be separated from the puncture and friction forces. Further, advanced simulation environments requiring accurate tissue deformation models might need to incorporate tissue rupture models using concepts from fracture mechanics.

In Chapter 5, preliminary validation showed that the model and experimental data followed similar trends for needle deflection and constant radius of curvature. The variations in experimental and simulation results could be attributed to: (1) gel properties (both elasticity and toughness) that were not measured accurately, (2) approximate value of the needle insertion force that was provided as input into the simulation model, and (3) medium-specific bevel tip loads that provided as input to the model. Thus, immediate extension

to this work includes detailed validation, which would cover obtaining tissue- and needle-specific material properties, and comparing the results of our model to experimental studies. Further, the model presented in this study introduces the needle-tissue interaction stiffness per unit length, K_T, which was assumed to be a constant. Future work could include considering tissue inhomogeneity and anisotropy by making $K_T(x,y)$ and $K_T(x) \neq K_T(y)$, respectively. Another possible extension to this work includes performing FE simulations with contact and cohesive zone models for various bevel angles. Also, including the needle shaft within the FE simulation model is essential to predict the needle curvature. Further, the validation of computational models with experimental data is integral for planning needle insertion procedures. These FE computational models would include the complete needle-tissue interaction, both along the needle shaft and also at the bevel tip.

One of the primary goals within the domain of robotically steered bevel-tip needles is to have an analytical and/or simulation model that would take inputs as the tissue and needle material properties, and needle geometry, and predict the interaction forces and deflection of the needle. This model could also be used to predict the needle path given an input history. Our present work investigated the interactions between a needle and an elastic medium as a 2D problem with a single curve. Future work could include extending this model to 3D needle-tissue interaction, or a needle insertion with multiple curves. The integration of the mechanics-based models into the current needle steering experimental setup for planning of needle insertion procedures is also deemed as future work. Other directions for future work include development of fast and optimized mechanics-based simulation algorithm for

interactive needle insertion, and to use the model to choose feasible clinical applications and optimize needle design. Futher, needles with pre-bent tips have been shown to have greater steerability than bevel-tipped needles. The formulation techniques and modeling could be extended to model the interaction of pre-bent needles with soft tissues.

In order to accomplish surgical training, and pre-and intra-operative planning using simulators that incorporate realistic tool-tissue interaction models, some significant challenges need to be overcome. The three main hurdles that need to be conquered are: first, the ability to obtain global responses of tool-tissue interactions *in vivo*; second, formulating a methodology to incorporate this experimental data in a continuum mechanics framework to simulate realistic deformations of organs; and finally, making simplifications to the computational model such that the simulation runs in real time but does not compromise the effective realism of the tissue response. In spite of scientific challenges, this thesis and trends over the past decade suggest that significant strides are being made by interdisciplinary research teams from the robotics, mechanics, graphics, and medicine communities to design surgical simulators. Such simulators hold great promise for surgical training, practice, and patient-specific pre-operative planning.

Appendix A

Environment Parameter Estimation during Bilateral Telemanipulation

Accurate models of remote environments generated during telemanipulation can be used to improve transparency, generate realistic simulations, and evaluate environment state. This appendix presents an architecture for environment parameter estimation during bilateral telemanipulation. Nonlinear stiffness and damping properties of the environment are estimated using an indirect adaptive control approach. The slave-environment contact force tracks the sum of the force applied by the human to the master and a persistent excitation force required for accurate environment parameter estimation. Since force feedback to the human operator should only reflect the environment properties, several methods for force feedback are considered. Simulations confirm the validity of the proposed telemanipulation architecture for obtaining reasonable estimates of nonlinear environment properties

and providing appropriate force feedback to the operator.

A.1 Introduction

A telemanipulator is an electro-mechanical system comprised of a master and a slave robot connected via a communication channel and controllers. The human operates a master device, while the slave robot directly interacts with the environment. To achieve reasonable performance in many telemanipulated tasks, the human operator needs information about the remote environment. Feedback can be provided in many different forms, including audio, visual, and haptic displays. The telemanipulated system is said to be bilateral if there is an exchange of energy between the master and slave robots through the feedback of force information [194].

This appendix provides a method for extracting environment properties, specifically the stiffness and damping properties of soft materials, during bilateral telemanipulation. Bilateral telemanipulation is typically performed without explicit environment modeling. However, accurate models of remote environments generated during telemanipulation can be used to improve transparency, generate realistic simulations, and evaluate environment state. We are particularly interested in surgical robotics applications, where soft tissue models obtained during surgery may improve operator performance, develop realistic training systems, and enable online diagnosis. It is envisioned that, during tissue palpation, estimation of environment properties would help surgeons quantitatively track variations in

stiffness and damping properties for diagnosis. Also, estimated environment properties would help in the development of realistic, patient-specific virtual environment models for surgical planning and training.

A.1.1 Previous Work

There are two main areas of prior work relevant to this research: soft tissue modeling and environment property estimation during telemanipulation.

Past research on soft tissue modeling has primarily focused on designing specialized surgical instruments and experimental apparatus for measuring tissue deformation and interaction forces, and using the resulting data to build finite element models, e.g. [13, 15, 17, 71, 85]. Most of this research uses phantom or *ex vivo* tissues, although *in vivo* tissues may have significantly different dynamics [119]. Researchers have also examined the theoretical and computational aspects of finite element modeling for soft tissues to be used in surgical simulators [146]. While the eventual goal of our work is to create similarly complex tissue models, in this appendix we are concerned with the identification of the effective environment stiffness and damping parameters at a single location.

Environment property estimation has been performed by both autonomous and telemanipulated robots. Dupont et al. [195] presented a high-level framework for property estimation during telemanipulation that considers three steps: task decomposition, data segmentation, and parameter estimation. Their algorithm directly computed the geometry, mass, and coefficient of friction of the environment, but did not generate sufficient excitation

for estimation of damping. Park et al. [196] presented a modified position-position telemanipulation architecture for online environment stiffness adaptation during force control of the slave robot. Hashtrudi-Zaad et al. [197] presented simulation studies that achieved transparency during telemanipulation using a composite adaptive controller to estimate the dynamic properties of high-stiffness environments. Duchemin et al. [129] used a hybrid force/position controller for robotic telesurgery in skin harvesting procedures. With appropriate choice of gains, their controller estimated skin stiffness, friction, and thickness. Diolaiti et al. [198] and Colton et al. [199], both used a least-squares method to estimate the stiffness of the environment. Alternatively, De Gersem et al. [130] used a Kalman filtering technique to estimate the stiffness of soft materials during telemanipulation.

A.1.2 Contributions

The goal of this work is to estimate and collect environment properties during a telemanipulated procedure, while simultaneously providing the user with a realistic feel of the environment dynamics. The new contributions of this work include: (1) a computationally efficient and easily implementable online parameter estimation algorithm for bilateral telemanipulation systems, (2) estimation of both nonlinear stiffness and damping during telemanipulation, and (3) methods to prevent the excitation signals from being fed directly back to the human operator.

Environment parameter estimation is achieved by using an indirect adaptive control scheme [200]. The indirect adaptation law is formulated to ensure that the interaction force

between the slave robot and its environment tracks the reference force provided from the master side. The indirect adaptive control approach has been considered because of its relative ease of implementation for real-time estimation of environment parameters [201].

This appendix also addresses higher level questions associated with persistent excitation of the environment, which is required for good parameter estimation [202]. We consider a closed-loop telemanipulation system architecture, which includes the slave-environment interaction force fed back to the operator. Since the required excitation is oscillatory, the contact force is also time varying. Various force feedback methods are explored to cancel the oscillations and to give the operator a more "transparent" telemanipulation experience during the parameter estimation process.

A.2 Integrating Telemanipulation and Parameter Estimation

In this section, we present a bilateral telemanipulation architecture that includes an environment parameter estimation algorithm. Online parameter estimation using indirect adaptive control requires a trajectory generator and a parameter adaptation law. The online trajectory generator and indirect adaptive law enable force tracking between a reference force and the sensed slave-environment contact force. Richness of the reference force is required for the estimated environment parameters to converge to the actual values [202]. In the proposed telemanipulation system, the reference force is generated as the sum of the

force applied by the human operator to the master robot and a high-frequency excitation force. The persistent excitation could possibly be accomplished by the operator's movements, but we ensure excitation by explicitly superimposing high-frequency vibrations.

A.2.1 System Architecture

Bilateral telemanipulation systems may have two-channel or four-channel controllers. Examples of two-channel control architectures are direct force feedback [194], position-position [203], force-force [204], and force-position [205] controllers. In contrast, four-channel controllers transmit both force and position information from the master to slave and vice versa [203]. The telemanipulation architecture we present uses a modified two-channel controller.

Figure A.1 provides an overview of the salient components of the proposed system required for parameter estimation during telemanipulation. f_h is the force applied by the human operator to the master robot and is measured by the force sensor on the master side. A position sensor measures the location of the master robot end-effector, x_m. f_r represents the reference force (which includes the excitation signal) provided from the master side. f_e is the interaction force between the slave robot end-effector and its environment, as measured by a force sensor located on the slave robot. x_s is the slave robot end-effector position measured by a position sensor. f_{fb} is the force fed back from the slave side to the master robot and subsequently to the operator.

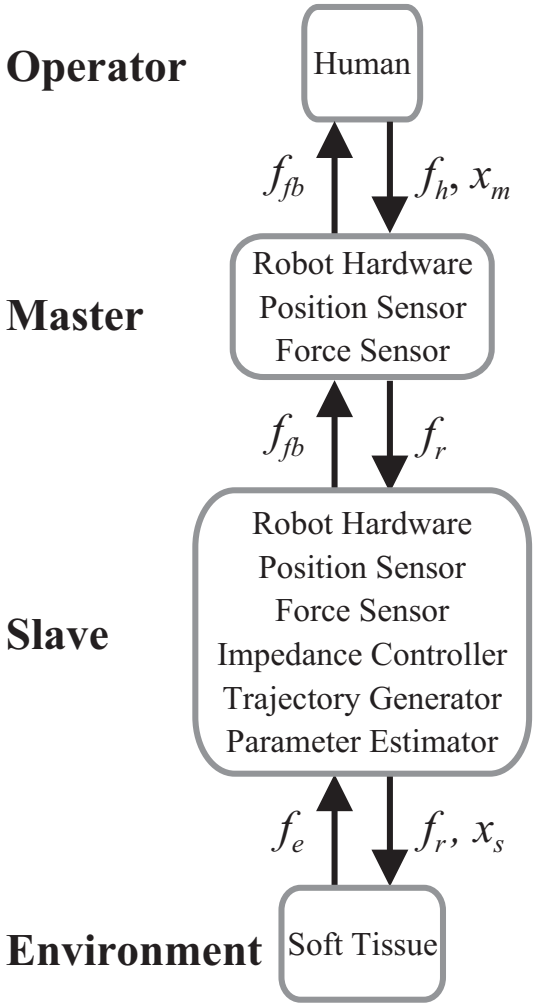

Figure A.1: Bilateral telemanipulation system components for environment parameter estimation.

Figure A.2 depicts the block diagram of the bilateral telemanipulation system. The elements corresponding to the *human + master robot* and *slave robot + controller + environment* have been grouped together for clarity. The dynamics and control model of the *human + master robot* is represented by the master robot $(Z_m(s))$ and human hand $(Z_h(s))$

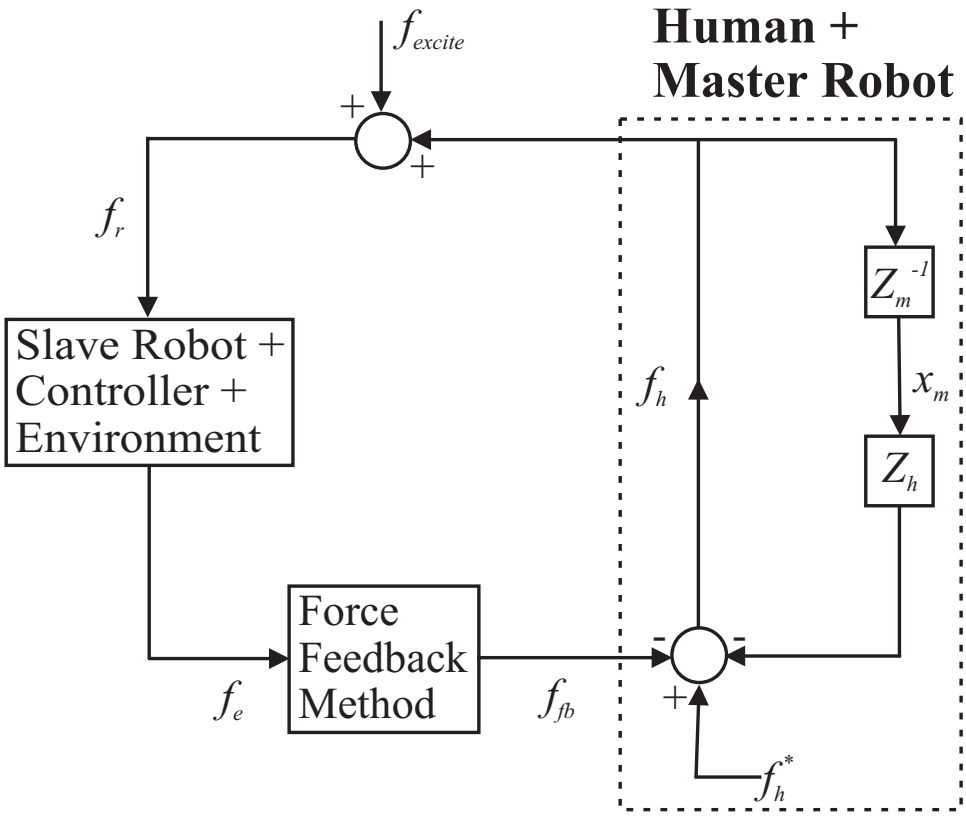

Figure A.2: Complete control scheme for the bilateral telemanipulation system used for environment parameter estimation.

impedances, which are given in (A.1) and (A.2), respectively.

$$Z_m(s) = M_m s^2 + B_m s + K_m \tag{A.1}$$

$$Z_h(s) = M_h s^2 + B_h s + K_h \tag{A.2}$$

In (A.1) and (A.2), M_m, B_m, and K_m, and M_h, B_h, and K_h, represent the effective mass, damping, and stiffness of the master robot and human hand, respectively. In Figure A.2, the input to the system is an exogenous force, f_h^*, that the operator intends to apply to the

master robot [203]. Since Figure A.2 represents a closed-loop telemanipulation system, f_h is the summation of f_h^*, f_{fb}, and the force due to the impedance of the human hand. As mentioned earlier, persistent excitation is essential for good parameter estimation [202], and this is represented by f_{excite}. Further, as seen in Figure A.2, $f_r = f_h + f_{excite}$.

The *slave robot + controller + environment* control block has been expanded in Figure A.3. The complete control architecture for the slave robot includes the *impedance controller* $Z_t^{-1}(s)$, *trajectory generator*, *parameter estimator*, and position controller C_s. The slave robot is essentially a position-controlled manipulator, and the input to C_s is the commanded position, $x_{s'}$, and the output is the measured position, x_s, of the slave robot end-effector. Further, x_e represents the initial deformation of the environment. Since x_s is the position of the end-effector of the slave robot, which is provided by the slave robot position sensor, the instantaneous deformation of the environment can be computed as $x_s - x_e$. Using the inverse kinematics, joint controllers, and robot dynamics, C_s computes the joint torques required to drive the slave robot.

In Figure A.3, x_p is the perturbed trajectory produced by the *impedance controller* and x_r is the reference trajectory generated by the *trajectory generator*. The perturbed trajectory alters the reference trajectory, resulting in the commanded slave robot trajectory, which is tracked by the the slave robot position controller. Further, $\widehat{K}_e$ and $\widehat{B}_e$ are the estimated environment stiffness and damping, respectively, which are computed by the *parameter estimator*. Details and formulation of the *impedance controller*, *trajectory generator*, and *parameter estimator* are provided in Section A.3.

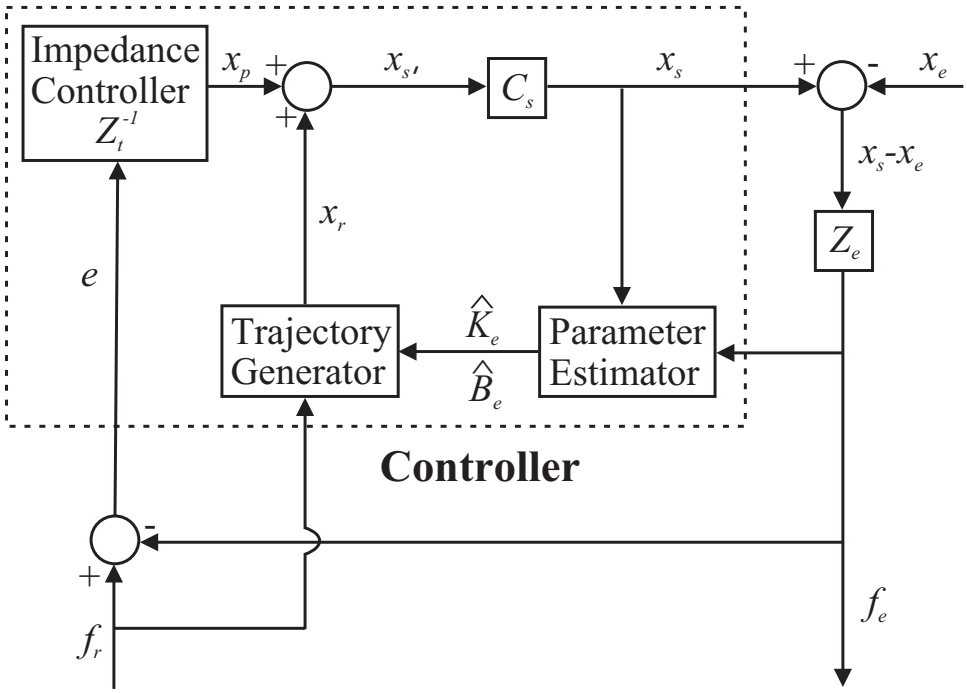

Figure A.3: Slave robot + Controller + Environment: Slave robot control system architecture for parameter estimation during bilateral telemanipulation.

The dynamics of the slave robot impedance controller and environment are:

$$Z_t(s) = M_t s^2 + B_t s + K_t \tag{A.3}$$

$$Z_e(s) = B_e s + K_e \tag{A.4}$$

In (A.3) and (A.4), M_t, B_t, and K_t, represent the impedance control gains for the slave robot, and K_e and B_e are the actual stiffness and damping of the soft environment, respectively. For the applications we are considering, the time delays are very small [206]. Hence, the delays caused by the communication channels are not shown in Figures A.2 and A.3.

A.2.2 Force Feedback Methods

As mentioned earlier, in Figure A.2, f_{excite} represents the persistent excitation required for good parameter estimation [202]. The proposed estimation algorithm is in essence part of a force tracking method, and since the reference force, f_r, is oscillatory, the sensed force between the slave robot end-effector and its environment is also oscillatory. Thus, it is practical to employ a vibration cancellation method prior to feeding back the contact force, f_e, to the human operator. This is represented by the *force feedback method* block in Figure A.2.

We consider three force feedback methods, which are depicted in Figure A.4 and described as follows:

(a) In Figure A.4(a), f_{fb} is based on the position and velocity of the master robot end-effector and the estimated environment parameters:

$$F_{fb}(s) = \widehat{Z}_e(s) X_m(s), \tag{A.5}$$

where $\widehat{Z}_e(s)$ represents the estimated environment impedance and $X_m(s)$ is the Laplace transform of the master robot end-effector motions. If good estimation of the environment parameters is achieved, then the operator would be able to feel the environment appropriately. As the user-applied force is constant, $X_m(s)$ is devoid of excitation signals, and thus, $F_{fb}(s)$ is not oscillatory.

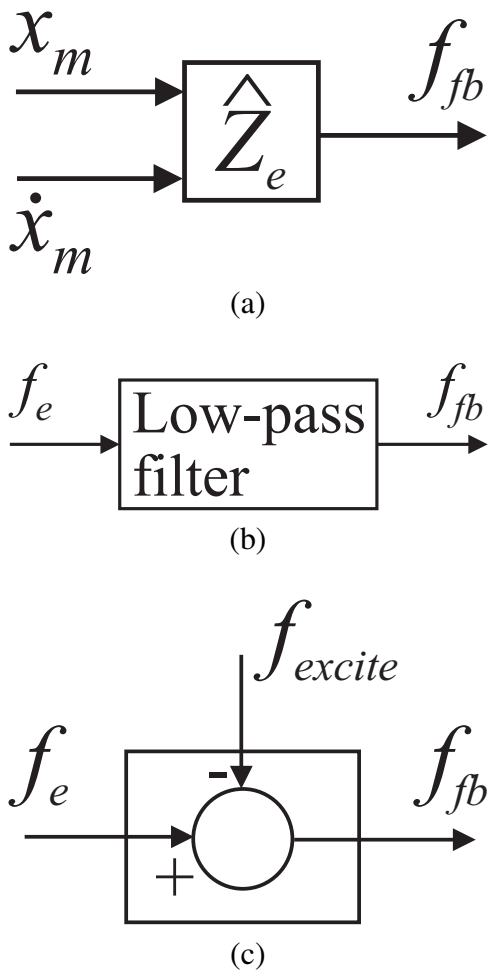

Figure A.4: Possible force feedback methods include (a) passing master robot motions through the estimated environment impedance, (b) low-pass filtering the environment contact force, and (c) subtracting the excitation force from the environment contact force.

(b) In Figure A.4(b), f_e is filtered to cancel out the high frequency vibrations. $5-10$ Hz is the maximum frequency beyond which the human finger cannot easily apply purposeful force or position commands [207]. So by adding a low-pass filter, the high frequencies (greater than 5 Hz) can be removed before sending them to the operator to ensure a "better feel" of the environment.

(c) As f_{excite} is provided by software, it is a known quantity. Thus, in Figure A.4(c), the

persistent excitation is explicitly subtracted from the contact force before being fed back to the operator.

The performance of the force feedback methods described in this section in conjunction with the complete bilateral telemanipulation system are examined by software simulations in Section A.4.

A.3 Environment Parameter Estimation

In Section A.2.1 an overview of the proposed bilateral telemanipulation system involving environment parameter estimation was presented. This section discusses in detail the adaptation law used for environment parameter estimation. As mentioned previously, the slave robot is considered to be position controlled, and the *impedance controller*, *trajectory generator*, and *parameter estimator* are provided as outer control loops. The estimation algorithm is based on force tracking; the goal is to have the contact force between the slave robot end-effector and its environment track the reference force. To achieve good force control, the position controller has to be accurate. In the method presented, force tracking is achieved by impedance control and an indirect adaptive control strategy for parameter estimation, introduced by Seraji et al. [200].

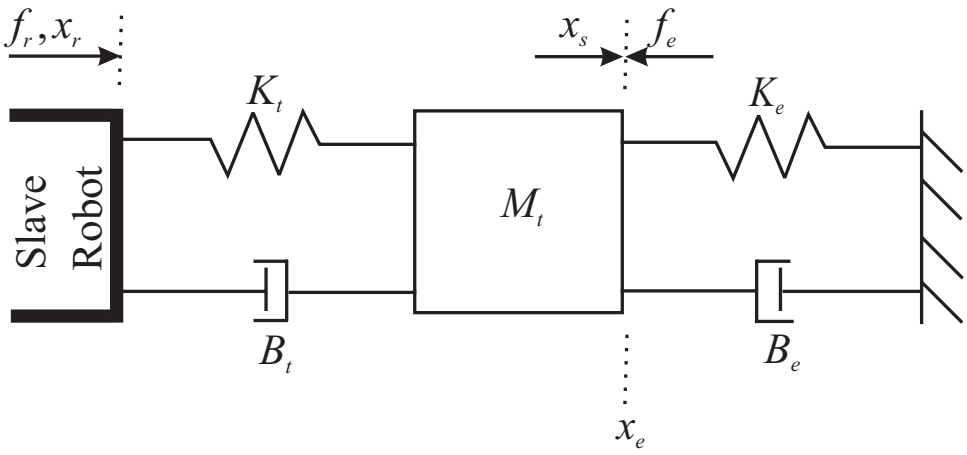

Figure A.5: Model of the slave robot impedance controller and soft environment.

A.3.1 Force Tracking

Impedance control aims to control the position and force by adjusting the mechanical impedance of the end-effector to external forces [208]. The external forces are generated due to contact between the slave robot end-effector and its environment. For the purposes of this study, we consider position-based impedance control. For clarity, we consider the master and slave robots as one degree-of-freedom linear time-invariant systems. The formulation presented can be extended to telerobotic systems with more than one degree of freedom. Figure A.5 shows the basic components of the slave robot under impedance control. In general, the impedance controller is chosen as a linear second-order system, where M_t, B_t, and K_t represent the controller gains [200]. Alternatively, M_t, B_t, and K_t could be interpreted as the target mass, damping, and stiffness of the impedance controller, respectively [201]. In Figure A.5, the slave robot is assumed to be probing a soft environment via a single point contact.

The variables used in Figure A.5 have been defined previously in Section A.2.1. As mentioned earlier, x_e is the initial deformation of the environment, so $\dot{x}_e = 0$ and is thus not included in the derivation presented. The force tracking error in terms of the user-applied reference force (including persistent excitations) and the sensed contact force is given as

$$e = f_r - f_e. \tag{A.6}$$

The impedance controller equation for the slave robot is given by the error dynamics of a second-order system as

$$e = M_t \left(\ddot{x}_{s'} - \ddot{x}_r\right) + B_t \left(\dot{x}_{s'} - \dot{x}_r\right) + K_t \left(x_{s'} - x_r\right), \tag{A.7}$$

where x_r and $x_{s'}$ are the reference and commanded positions of the slave robot end-effector, respectively. Also, the perturbed slave position is given by, $x_p = x_{s'} - x_r$. When the slave robot is not in contact with the environment, $f_e = f_r = 0$ and hence, $x_p = 0$. While the slave robot end-effector probes the environment, the force sensor measures f_e, resulting in perturbation of the reference trajectory. Thus, (A.7) is rewritten as

$$e = M_t \ddot{x}_p + B_t \dot{x}_p + K_t x_p, \tag{A.8}$$

which is analogous to a mass-spring-damper system, shown in Figure A.5. The perturbed trajectory is used to modify the reference trajectory to generate the commanded slave robot

trajectory ($x_{s'} = x_p + x_r$), which is tracked by slave robot position controller (C_s), as shown in Figure A.3. Further, for good slave robot position control, $x_{s'} \approx x_s$, which implies $x_s = x_p + x_r$. Taking the Laplace transform of (A.8) and using (A.4) results in

$$E(s) = Z_t(s) X_p(s). \tag{A.9}$$

The contact force depends on the actual nonlinear environment stiffness and damping, and can be expressed as

$$f_e = K_e(x_s - x_e) + B_e \dot{x}_s. \tag{A.10}$$

The mass of the environment is ignored in (A.10), since for medical robotics applications the environment tends to be quasi-static. Using (A.6), (A.10), and $x_s = x_p + x_r$, the error can be rewritten as

$$e = f_r + K_e(x_e - x_r) - B_e \dot{x}_r - K_e x_p - B_e \dot{x}_p. \tag{A.11}$$

Taking the Laplace transform of (A.11), and using (A.4) and (A.9) results in

$$E(s) = \frac{Z_t(s)\left[F_r(s) + Z_e(s)\left(X_e(s) - X_r(s)\right)\right]}{Z_t(s) + Z_e(s)}. \tag{A.12}$$

Thus, the steady-state force tracking error (e_{ss}) is obtained as

$$e_{ss} = \frac{K_t}{K_t + K_e}\left(f_r + K_e x_e - K_e x_r\right). \tag{A.13}$$

Further, $e_{ss} \rightarrow 0$ as

$$x_r = \frac{f_r}{K_e} + x_e, \tag{A.14}$$

and $E(s) \rightarrow 0$ as

$$\dot{x}_r = \frac{f_r + K_e (x_e - x_r)}{B_e}. \tag{A.15}$$

Also, substitution of (A.14) in (A.15) results in

$$\dot{x}_r = 0. \tag{A.16}$$

Thus, in order to have perfect force tracking, the slave robot end-effector must follow the reference position and velocity as defined in (A.14) and (A.16). In practice, we believe that reasonable environment parameter estimates can be achieved with good force tracking.

A.3.2 Indirect Adaptive Control

As seen in (A.14) and (A.15), accurate knowledge of the environment parameters is necessary for good force tracking. The indirect adaptive control strategy aims to adaptively compute the estimated environment stiffness ($\widehat{K}_e$) and damping ($\widehat{B}_e$) online during telemanipulation. The estimated parameters are then used to compute the reference trajectory. Hence, (A.14) and (A.16) are rewritten in terms of estimated environment parameters as:

$$x_r = \frac{f_r}{\widehat{K}_e} + x_e. \tag{A.17}$$

$$\dot{x}_r = 0. \tag{A.18}$$

The *trajectory generator*, shown in Figure A.3, is described by (A.17) and (A.18).

In order to develop the indirect adaptive control method for estimating environment parameters used in (A.17) and (A.18), consider the estimated contact force:

$$\widehat{f_e} = \widehat{K}_e \left(x_s - x_e\right) + \widehat{B}_e \dot{x}_s. \tag{A.19}$$

Subtracting (A.10) from (A.19) results in

$$\widehat{f_e} - f_e = \left(\widehat{K}_e - K_e\right)\left(x_s - x_e\right) + \left(\widehat{B}_e - B_e\right)\dot{x}_s. \tag{A.20}$$

Defining $\tilde{f}_e = \widehat{f_e} - f_e$, (A.20) can be rewritten as

$$\tilde{f}_e = \phi^T \tilde{\theta}, \tag{A.21}$$

where

$$\phi = \begin{bmatrix} x_s - x_e \\ \\ \dot{x}_s \end{bmatrix} \quad \text{and} \quad \tilde{\theta} = \begin{bmatrix} \widehat{K}_e - K_e \\ \\ \widehat{B}_e - B_e \end{bmatrix}. \tag{A.22}$$

Estimated parameters should be updated so that the predicted force error $(\tilde{f}_e)$ is reduced. In order to achieve this, we use a Lyapunov-based approach [200]. Consider the Lyapunov

function candidate

$$V = \tilde{\theta}^T \Gamma \tilde{\theta}, \tag{A.23}$$

where Γ is a positive definite and symmetric gain matrix. For successful parameter estimation, the estimated parameters, $\widehat{\theta} = [\widehat{K}_e \quad \widehat{B}_e]^T$ must be updated in the opposite direction of the gradient of the squared prediction error with respect to the estimated parameters [202], which results in

$$\dot{\widehat{\theta}} = -\Gamma^{-1} \frac{\partial}{\partial \widehat{\theta}} \left(\tilde{f}_e^T \tilde{f}_e \right). \tag{A.24}$$

Using (A.21) and (A.24) results in the following parameter adaptation law [201],

$$\dot{\tilde{\theta}} = -\Gamma^{-1} \phi \tilde{f}_e. \tag{A.25}$$

From (A.23) and using (A.25), the time derivative of the Lyapunov function is computed as

$$\begin{aligned} \dot{V} &= 2\tilde{\theta}^T \Gamma \dot{\tilde{\theta}} \\ &= -2\tilde{\theta}^T \phi \phi^T \tilde{\theta} \\ &< 0. \end{aligned} \tag{A.26}$$

Further, from (A.23) and (A.26), we infer that if $\tilde{\theta}$ is adjusted according to parameter estimation law given in (A.25), then $\tilde{\theta} \to 0$ as $t \to \infty$ i.e. $(\widehat{K}_e, \widehat{B}_e) \to (K_e, B_e)$ [200]. (A.25) represents the *parameter estimator*, shown in Figure A.3. Thus, we have demonstrated

Human hand (Z_h)	M_h	2.0 kg
	B_h	5.0 kg/s
	K_h	100.0 N/m
Master robot (Z_m)	M_m	2.5 kg
	B_m	50.0 kg/s
	K_m	250.0 N/m
Impedance controller (Z_t)	M_t	5.0 kg
	B_t	450.0 kg/s
	K_t	800.0 N/m
Position controlled slave robot	C_s	1.0

Table A.1: Values of system parameters used in numerical simulations.

that if the slave robot end-effector follows the prescribed reference trajectory, then force tracking is ensured by the impedance controller and accurate estimation of environment parameters is obtained.

A.4 Simulation Results and Discussion

Numerical simulations were performed to evaluate the proposed method for simultaneous bilateral telemanipulation and environment parameter estimation. The simulations were based on the system presented in Figure A.2. The system parameters for the human hand, master robot, and impedance controller used in the simulation studies are provided in Table A.1.

In the simulation, the slave robot was commanded to make contact with the soft environment, after which f_h^* was applied as a constant force of 15 N to the master robot. f_{excite} was provided as $4.5\sin(15t)$ N. The gain matrix (Γ) for the parameter adaptation law given

in (A.25) was

$$\Gamma = \begin{bmatrix} 1500 & 0 \\ 0 & 500 \end{bmatrix}. \tag{A.27}$$

For the system parameter and f_h^* values chosen, f_{excite} and Γ were selected manually in order to produce stable and accurate estimation of the environment parameters.

Simulations of the system for the three force feedback methods described in Section A.2.2 were performed. The schemes used to generate the feedback force were: (1) using the estimated environment impedance, (2) low-pass filtering the environment contact force, and (3) explicitly subtracting the excitation force from the environment contact force. Further, for the purposes of comparison, we also consider feeding back the "measured" contact force without modification.

Figure A.6 shows the performance of the environment estimation for the four force feedback methods described above. The solid lines represent the actual nonlinear environment stiffness and damping, and the dashed lines represent the estimation. The stiffness and damping of the soft environment varies nonlinearly with the deformation of the environment from 175 N/m to 230 N/m and 75 kg/s to 100 kg/s, respectively. In the simulations, initial conditions for the environment stiffness and damping estimates were set as 150 N/m and 65 kg/s, respectively. Also, the estimator is active only when the slave robot comes in contact with the environment and reset laws are used to ensure that the estimates do not go to zero. As seen in Figure A.6, the indirect adaptive algorithm was able to stably pre-

dict the nonlinear environment stiffness and damping for all force feedback methods. The convergence time for the damping estimate varied significantly, depending on the force feedback method. Also, persistent excitation in the reference force was only required for correct estimation and convergence of environment damping, not for stiffness. In order to compare the different force feedback methods, the system inputs and gains were the same for all the simulation cases considered. Thus, better environment damping estimates could be obtained for each method with a different choice of controller gains.

Figure A.7 shows the force fed back to the operator for each of the force feedback methods mentioned previously. Figure A.7(b), which uses the estimated environment parameters to generate the force feedback, shows the best results in terms of reducing the oscillatory behavior of f_e, and would likely create the most realistic environment sensations for the operator. As mentioned earlier, $5-10$ Hz is the maximum frequency range beyond which the human finger cannot apply meaningful position or force commands [207]. So for Figure A.7(c), a low-pass filter with cutoff frequency of 2 Hz was applied to remove the high-frequency oscillations from the environment contact force. For the purposes of this simulation study, a 2 Hz low-pass filter was used instead of a $5-10$ Hz low-pass filter because the frequency of the excitation signals was not greater than 5 Hz. Using persistent excitation of higher frequency did not produce better results for environment parameter estimation, and in some applications higher frequency excitation might not be advisable. Nonetheless, using low-pass filters to ensure a "better feel" of the environment is still a valid option. Since there is a phase difference between f_r and f_e, direct subtraction of

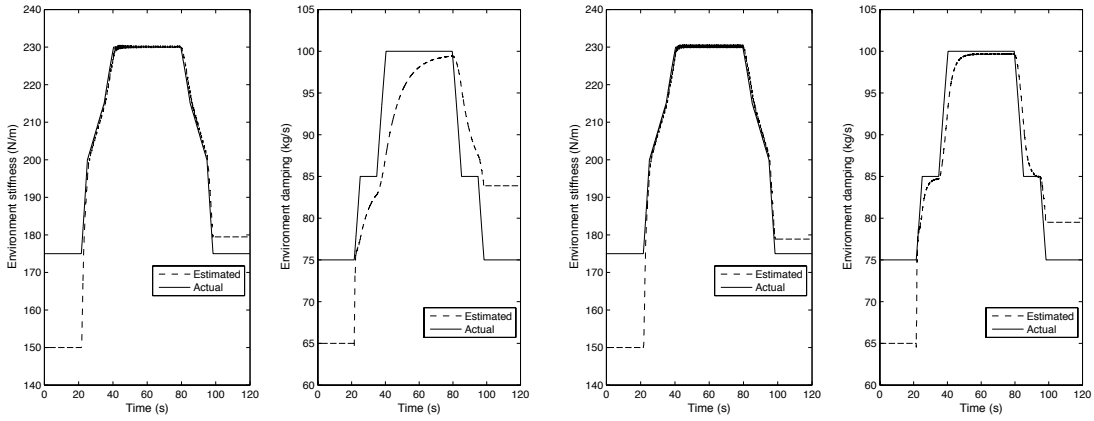

(a) $f_{fb} = f_e$ (b) $F_{fb}(s) = \widehat{Z}_e(s) X_m(s)$

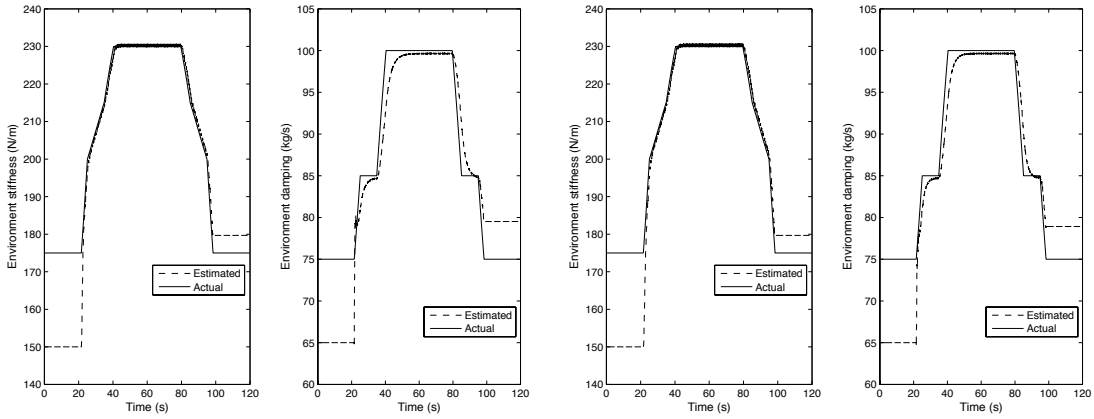

(c) $f_{fb} = \text{Low-pass filter}(f_e)$ (d) $f_{fb} = f_e - f_{excite}$

Figure A.6: Estimated versus actual environment parameters for various force feedback cases during bilateral telemanipulation.

f_{excite} from f_e did not reduce the oscillations substantially, as seen in Figure A.7(d).

A.5 Conclusion

We presented a bilateral telemanipulator system that used an indirect adaptive control algorithm to estimate soft environment parameters. The scheme was based on achieving

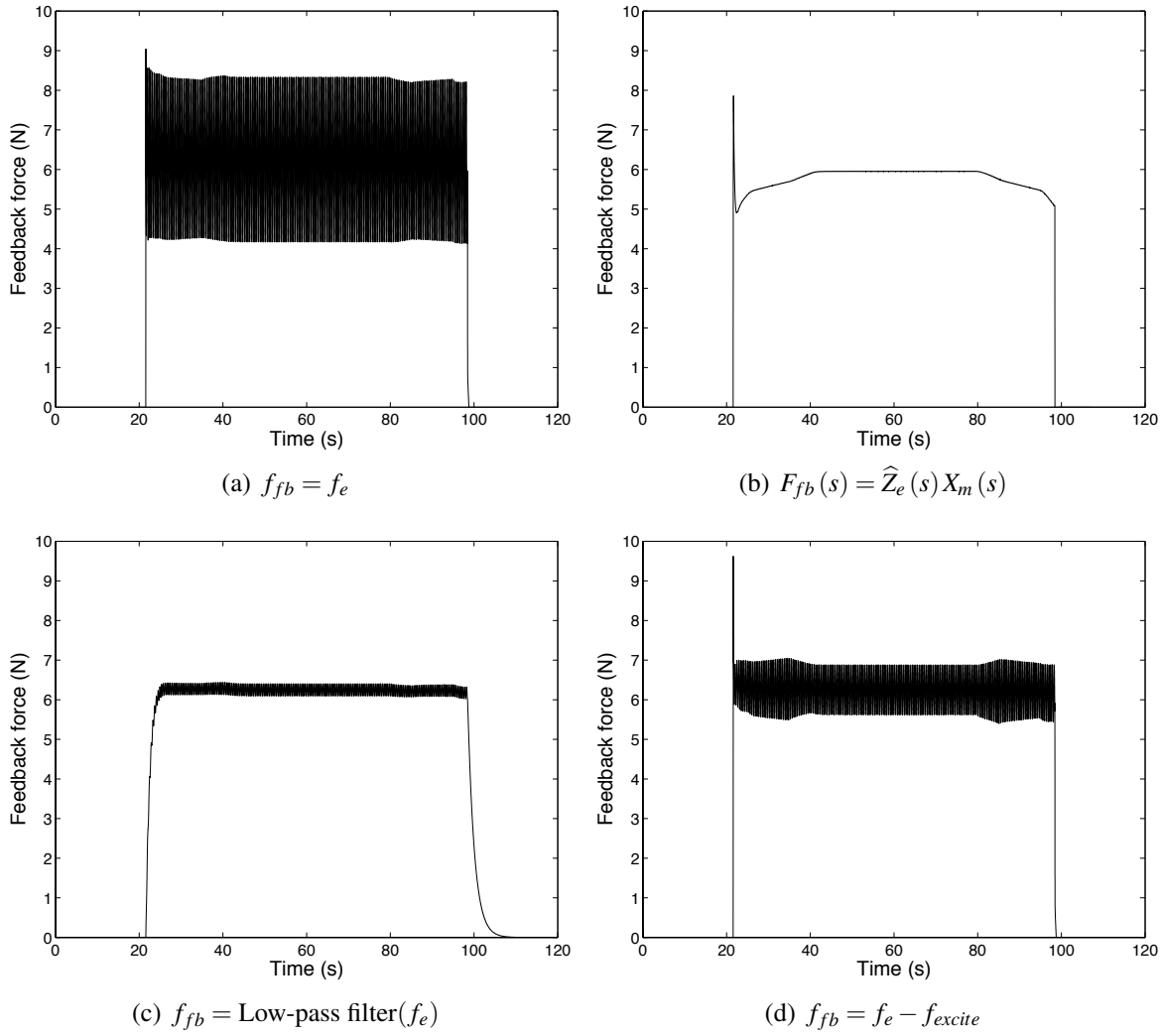

(a) $f_{fb} = f_e$

(b) $F_{fb}(s) = \widehat{Z}_e(s) X_m(s)$

(c) $f_{fb} = \text{Low-pass filter}(f_e)$

(d) $f_{fb} = f_e - f_{excite}$

Figure A.7: Feedback force during bilateral telemanipulation

force tracking between the reference (user-applied force superimposed with excitations) and environment contact forces. This was done using an online trajectory generator and an indirect adaptation law. The slave robot was a position-controlled manipulator and the estimator control architecture was provided as an outer control loop. This non-intrusive approach for parameter estimation enabled straightforward implementation of control algo-

rithms. Simulation studies showed that it was possible to get accurate and stable estimates for nonlinear environment properties.

Persistent excitation of the environment was required for robustness of the parameter estimator. Since our intended application is surgical robotics, the excitation signals are of small amplitude in order to prevent unwanted tissue motion during robot manipulation. Further, various methods were explored to eliminate the effects of persistent excitation in the force fed back to the human operator, so as to make the parameter estimation process seamless and transparent to the user. It was concluded that using the estimated environment impedance produces the least oscillatory force feedback. Hence, this would give the most realistic feel of environment to the operator during parameter estimation.

Possible extensions to this work will be to implement and test the environment parameter estimation algorithm first on a set of one degree-of-freedom haptic devices equipped with force and position sensors during telemanipulation of a phantom soft tissue environment. Further, we will obtain more complex environment models using telemanipulation systems with more degrees of freedom, such as the da Vinci Surgical System (Intuitive Surgical, Inc., Sunnyvale, CA) [209]. Efforts will also be made to theoretically quantify the stability of the proposed telemanipulation system. Sensitivity studies will be done in order to evaluate the effects of force sensor noise, choice of adaptation law gains, and larger variation in environment stiffness and damping values on the environment property estimation and force feedback to the human. We will also explore variations of the proposed algorithm that eliminate the use of force sensors. In the long-term, we would like to explore

the online development of large-scale virtual tissue models based on estimated soft tissue properties.

Bibliography

[1] Y. Chi, J. Liang, and D. Yan, "Material sensitivity study of deformable organ registration," *Medical Physics*, vol. 33, no. 2, pp. 421–433, 2006.

[2] H. Yamada, *Strength of biological materials*, 1st ed. Baltimore, USA: The Williams & Wilkins Company, 1970.

[3] J. C. Roberts, A. C. Merkle, P. J. Biermann, E. E. Ward, B. G. Carkhuff, R. P. Cain, and J. V. O'Connor, "Computational and experimental models of the human torso for non-penetrating ballistic impact," *J. Biomechanics*, vol. 40, no. 1, pp. 125–136, 2007.

[4] Eidgenössische Technische Hochschule, Institute of Mechanical Systems, CLA, Tannenstrasse 3, 8092 Zurich, Switzerland. http://www.zfm.ethz.ch/e/biomechanics/.

[5] Sacred Heart Medical Center, 1255 Hilyard Street, Eugene, OR 97401 USA. http://www.peacehealth.org/OHVI/CardiacSurgery.htm.

BIBLIOGRAPHY

[6] SensAble Technologies Inc., 15 Constitution Way, Woburn, MA 01801 USA. http://www.sensable.com/haptic-phantom-omni.htm.

[7] Institut National de Recherche en Informatique et en Automatique, Virtual Reality Platform, Rhône-Alpes, Inovallée, 655 avenue de l'Europe, Montbonnot, 38 334 Saint Ismier Cedex, France. http://www.inrialpes.fr/sed/PRV/.

[8] M. Harders, M. Bajka, U. Spaelter, S. Tuchschmid, H. Bleuler, and G. Székely, "Highly-realistic, immersive training environment for hysteroscopy," in *Medicine Meets Virtual Reality*, ser. Studies in Health Technology and Informatics. Amsterdam, Netherlands: IOS Press, 2006, vol. 119, pp. 176–181.

[9] L. Zhukov and A. H. Barr, "Heart-muscle fiber reconstruction from diffusion tensor mri," in *Proc. IEEE Visualization Conf.*, vol. 1, Seattle, USA, October 2003, pp. 597–602.

[10] Y. C. Fung, *Biomechanics: mechanical properties of living tissues*, 2nd ed. New York, USA: Springer-Verlag Inc., 1993.

[11] J. Kim and M. A. Srinivasan, "Characterization of visoelastic soft tissue properties from in vivo animal experiments and inverse fe parameter characterization," in *8th Int'l. Conf. Medical Image Computing and Computer Assisted Intervention (MICCAI)*, ser. Lecture Notes in Computer Science, vol. 3750. Berlin/Heidelberg: Springer, 2005, pp. 599–606.

[12] M. Mahvash, V. Hayward, and J. E. Lloyd, "Haptic rendering of tool contact," in *Proc. Eurohaptics*, vol. 1, Edinburgh, Scotland, August 2002, pp. 110–115.

[13] A. E. Kerdok, S. M. Cotin, M. P. Ottensmeyer, A. M. Galea, R. D. Howe, and S. L. Dawson, "Truth cube: Establishing physical standards for soft tissue simulation," *Medical Image Analysis*, vol. 7, no. 3, pp. 283–291, 2003.

[14] G. Székely, C. Brechbühler, J. Dual, R. Enzler, J. Hug, R. Hutter, N. Ironmonger, M. Kauer, V. Meier, P. Niederer, A. Rhomberg, P. Schmid, G. Schweitzer, M. Thaler, V. Vuskovic, G. Tröster, U. Haller, and M. Bajka, "Virtual reality-based simulation of endoscopic surgery," *Presence: Teleoperators and Virtual Environments*, vol. 9, no. 3, pp. 310–333, 2000.

[15] S. P. DiMaio and S. E. Salcudean, "Needle insertion modeling and simulation," *IEEE Trans. Robotics and Automation*, vol. 19, no. 5, pp. 864–875, 2003.

[16] G. Picinbono, H. Delingette, and N. Ayache, "Non-linear anisotropic elasticity for real-time surgery simulation," *Graphical Models*, vol. 65, no. 5, pp. 305–321, 2003.

[17] V. Vuskovic, M. Kauer, G. Székely, and M. Reidy, "Realistic force feedback for virtual reality based diagnostic surgery simulators," in *Proc. IEEE Int'l. Conf. Robotics and Automation*, vol. 2, San Francisco, USA, April 2000, pp. 1592–1598.

[18] M. P. Ottensmeyer, "Tempest I-D: an instrument for measuring solid organ soft tissue properties," *Experimental Techniques*, vol. 26, no. 3, pp. 48–50, 2002.

[19] M. Harders, D. Bachofen, M. Bajka, M. Grassi, B. Heidelberger, R. Sierra, U. Spaelter, D. Steinemann, M. Teschner, S. Tuchschmid, J. Zatonyi, and G. Szekely, "Virtual reality based simulation of hysteroscopic interventions," *Presence: Teleoperators and Virtual Environments*, vol. 17, no. 5, pp. 441–462, 2008.

[20] M. S. Sacks, "Biaxial mechanical evaluation of planar biological materials," *J. Elasticity*, vol. 61, no. 1–3, pp. 199–246, 2000.

[21] F. H. Netter, *Atlas of human anatomy*, 4th ed. Philadelphia, USA: W. B. Saunders Company, 2006.

[22] L. Grady, "Random walks for image segmentation," *IEEE Trans. Pattern Analysis and Machine Intelligence*, vol. 28, no. 11, pp. 1768–1783, 2006.

[23] P. Ström, L. Hedman, L. Särnå, A. Kjellin, T. Wredmark, and L. Felländer-Tsai, "Early exposure to haptic feedback enhances performance in surgical simulator training: a prospective randomized crossover study in surgical residents," *Surgical Endoscopy*, vol. 20, no. 9, pp. 1383–1388, 2006.

[24] E. M. McDougall, "Validation of surgical simulators," *J. Endourology*, vol. 21, no. 3, pp. 244–247, 2007.

[25] S. Misra, A. M. Okamura, and K. T. Ramesh, "Force feedback is noticeably different for linear versus nonlinear elastic tissue models," in *Proc. 2nd Joint Eurohaptics*

Conf. and Symp. Haptic Interfaces for Virtual Environment and Teleoperator Systems (World Haptics), Tsukuba, Japan, March 2007, pp. 519–524.

[26] S. Misra, K. T. Ramesh, and A. M. Okamura, "Physically valid surgical simulators: linear versus nonlinear tissue models," in *Proc. Medicine Meets Virtual Reality (MMVR)*, ser. Studies in Health Technology and Informatics. Amsterdam, Netherlands: IOS, 2008, vol. 132, pp. 293–295.

[27] S. Misra, P. Fuernstahl, K. T. Ramesh, A. M. Okamura, and M. Harders, "Quantifying perception of nonlinear elastic tissue models using multidimensional scaling," in *Proc. 3rd Joint Eurohaptics Conf. and Symp. Haptic Interfaces for Virtual Environment and Teleoperator Systems (World Haptics)*, Salt Lake City, USA, March 2009, pp. 570–575.

[28] S. Misra, M. Harders, K. T. Ramesh, and A. M. Okamura, "Modeling of nonlinear elastic tissues for surgical simulation: the poynting effect," *Computer Methods Biomechanics and Biomedical Engineering*, *Under Review*.

[29] S. Misra, K. J. Macura, K. T. Ramesh, and A. M. Okamura, "The importance of organ geometry and boundary constraints for planning of medical interventions," *Medical Engineering and Physics*, vol. 31, no. 2, pp. 195–206, 2009.

[30] S. Misra, K. B. Reed, A. S. Douglas, K. T. Ramesh, and A. M. Okamura, "Needle-tissue interaction forces for bevel-tip steerable needles," in *IEEE RAS/EMBS Int'l.*

Conf. on Biomedical Robotics and Biomechatronics, Scottsdale, USA, October 2008, pp. 224–231.

[31] S. Misra, K. B. Reed, B. W. Schafer, K. T. Ramesh, and A. M. Okamura, "Observations and models for needle-tissue interactions," in *Proc. IEEE Int'l. Conf. Robotics and Automation*, Kobe, Japan, May 2009, pp. 2687–2692.

[32] S. Misra, K. B. Reed, K. T. Ramesh, and A. M. Okamura, "Observations of needle-tissue interactions," in *Proc. Int'l. Conf. IEEE Engineering in Medicine and Biology*, Minneapolis, USA, September 2009, *Accepted*.

[33] S. Misra, K. B. Reed, B. W. Schafer, K. T. Ramesh, and A. M. Okamura, "Mechanics of flexible needles robotically steered through soft tissue," *Int'l. J. Robotics Research*, *Under Review*.

[34] J. C. Carpue, *An account of two successful operations for restoring a lost nose*, 1st ed. Birmingham, USA: The Classics of Medicine Library, 1981.

[35] A. B. Davis, "Louis Thomas Jerôme Auzoux and the papier mâché anatomical model," in *La Ceroplastica nella Scienza e nell'Arte: atti del I Congresso Internazionale Firenze*, Florence, Italy, June 1975, pp. 257–279.

[36] Y. C. Fung, "Biorheology of soft tissues," *Biorheology*, vol. 10, pp. 139–155, 1973.

[37] S. F. Gibson and B. Mirtich, "A survey of deformable modeling in computer graph-

ics," Mitsubishi Electric Research Laboratories, Tech. Rep. TR–97–19, November 1997, http://www.merl.com.

[38] U. Meier, O. López, C. Monserrat, M. C. Juan, and M. Alcañiz, "Real-time deformable models for surgery simulation: a survey," *Computer Methods and Programs in Biomedicine*, vol. 77, no. 3, pp. 183–197, 2005.

[39] A. Liu, F. Tendick, K. Cleary, and C. Kaufmann, "A survey of surgical simulation: applications, technology, and education," *Presence: Teleoperators and Virtual Environments*, vol. 12, no. 6, pp. 599–614, 2003.

[40] R. M. Satava, "Accomplishments and challenges of surgical simulation," *Surgical Endoscopy*, vol. 15, no. 3, pp. 232–241, 2001.

[41] C. Basdogan, C. H. Ho, and M. A. Srinivasan, "Virtual environments for medical training: Graphical and haptic simulation of laparoscopic common bile duct exploration," *IEEE/ASME Trans. Mechatronics*, vol. 6, no. 3, pp. 269–285, 2001.

[42] Y. Liu, A. E. Kerdok, and R. D. Howe, "A nonlinear finite element model of soft tissue indentation," in *Proc. Medical Simulation: Int'l Symposium, ISMS 2004*, ser. Lecture Notes in Computer Science, S. Cotin and D. N. Metaxas, Eds. Berlin/Heidelberg: Springer, 2004, vol. 3078, pp. 67–76.

[43] M. A. Puso and J. A. Weiss, "Finite element implementation of anisotropic quasi-

linear viscoelasticity using a discrete spectrum approximation," *J. Biomechanical Engineering*, vol. 120, no. 1, pp. 62–70, 1998.

[44] R. Balaniuk and K. Salisbury, "Dynamic simulation of deformable objects using the long elements method," in *Proc. 10th Symp. Haptic Interfaces Virtual Environments and Teleoperator Systems*, Orlando, USA, March 2002, pp. 58–65.

[45] K. Sundaraj, C. Mendoza, and C. Laugier, "A fast method to simulate virtual deformable objects with force feedback," in *7th Int'l. Conf. Automation, Robotics, Control, and Vision (ICARCV)*, vol. 1, Singapore, December 2002, pp. 413–418.

[46] M. Bro-Nielsen, "Finite element modeling in surgery simulation," *Proc. IEEE*, vol. 86, no. 3, pp. 490–503, 1998.

[47] X. Wu, M. S. Downes, T. Goktekin, and F. Tendick, "Adaptive nonlinear finite elements for deformable body simulation using dynamic progressive meshes," *Computer Graphics Forum*, vol. 20, no. 3, pp. 349–358, 2001.

[48] H. Delingette, G. Subsol, S. Cotin, and J. Pignon, "A craniofacial surgery simulation testbed," in *Proc. 3rd Int'l. Conf. on Visualization in Biomedical Computing (VBC)*, vol. 1, Rochester, USA, October 1994, pp. 607–618.

[49] E. Keeve, S. Girod, and B. Girod, "Craniofacial surgery simulation," in *Proc. 4th Int'l. Conf. on Visualization in Biomedical Computing (VBC)*, vol. 1, Hamburg, Germany, September 1996, pp. 541–546.

[50] R. M. Koch, M. H. Gross, F. R. Carls, D. F. von Buren, G. Fankhauser, and Y. I. H. Parish, "Simulating facial surgery using finite element models," in *Proc. ACM SIGGRAPH Conf. on Computer Graphics and Interactive Techniques*, vol. 1, New Orleans, USA, August 1996, pp. 421–428.

[51] S. Cotin, H. Delingette, and N. Ayache, "Real-time elastic deformations of soft tissues for surgery simulation," *IEEE Trans. Visualization and Computer Graphics*, vol. 5, no. 1, pp. 62–73, 1999.

[52] M. A. Padilla Castañeda and F. Arámbula Cosío, "Computer simulation of prostate resection for surgery training," in *Proc. Int'l. Conf. IEEE Engineering in Medicine and Biology*, vol. 1, Cancun, Mexico, September 2003, pp. 1152–1155.

[53] K. Waters, "Physical model of facial tissue and muscle articulation derived from computer tomography data," *Proc. SPIE-The International Society for Optical Engineering*, vol. 1808, pp. 574–583, 1992.

[54] A. O. Frank, I. A. Twombly, T. J. Barth, and J. D. Smith, "Finite element methods for real-time haptic feedback of soft-tissue models in virtual reality simulators," in *Proc. IEEE Virtual Reality Annual Int'l. Symposium (VRAIS)*, vol. 1, Yokohama, Japan, March 2001, pp. 257–263.

[55] D. d'Aulignac, R. Balaniuk, and C. Laugier, "A haptic interface for a virtual exam of the human thigh," in *Proc. IEEE Int'l. Conf. Robotics and Automation*, vol. 3, San Francisco, USA, April 2000, pp. 2452–2457.

[56] E. Gladilin, S. Zachow, P. Deuflhard, and H. C. Hege, "A biomechanical model for soft tissue simulation in craniofacial surgery," in *Proc. Int'l Workshop on Medical Imaging and Augmented Reality*, vol. 1, Hong Kong, June 2001, pp. 137–141.

[57] S. De and M. A. Srinivasan, "Thin walled models for haptic and graphical rendering of soft tissues in surgical simulators," in *Proc. Medicine Meets Virtual Reality (MMVR)*, ser. Studies in Health Technology and Informatics. Amsterdam, Netherlands: IOS, 1999, vol. 62, pp. 94–99.

[58] U. Kühnapfel, H. K. Çakmak, and H. Maaß, "Endoscopic surgery training using virtual reality and deformable tissue simulation," *Computers and Graphics*, vol. 24, no. 5, pp. 671–682, 2000.

[59] S. De, J. Kim, Y.-J. Lim, and M. A. Srinivasan, "The point collocation-based method of finite spheres (pcmfs) for real time surgery simulation," *Computers and Structures*, vol. 83, no. 17–18, pp. 1515–1525, 2005.

[60] S. De, Y.-J. Lim, M. Manivannan, and M. A. Srinivasan, "Physically realistic virtual surgery using the point-associated finite field (paff) approach," *Presence: Teleoperators and Virtual Environments*, vol. 15, no. 3, pp. 294–308, 2006.

[61] D. James and D. K. Pai, "A unified treatment of elastostatic contact simulation for real time haptics," *Haptics-e*, vol. 2, no. 1, pp. 1–13, September 2001.

[62] M. A. Sagar, D. Bullivant, G. D. Mallinson, P. J. Hunter, and I. W. Hunter, "A virtual

environment and model of the eye for surgical simulation," in *SIGGRAPH '94: Proc. 21st annual conf. on Computer graphics and interactive techniques*, vol. 1, Orlando, USA, July 1994, pp. 205–212.

[63] A. H. Gosline, S. E. Salcudean, and J. Yan, "Haptic simulation of linear elastic media with fluid pockets," in *Proc. 12th Symp. Haptic Interfaces Virtual Environments and Teleoperator Systems*, Chicago, USA, March 2004, pp. 266–271.

[64] F. J. Carter, T. G. Frank, P. J. Davies, D. McLean, and A. Cuschieri, "Measurements and modelling of the compliance of human and porcine organs," *Medical Image Analysis*, vol. 5, no. 4, pp. 213–236, 2001.

[65] T. Hu and J. P. Desai, "A biomechanical model of the liver for reality-based haptic feedback," in *6th Int'l. Conf. Medical Image Computing and Computer Assisted Intervention (MICCAI)*, ser. Lecture Notes in Computer Science. Berlin/Heidelberg: Springer, 2003, vol. 2878, pp. 75–82.

[66] C. Chui, E. Kobayashi, X. Chen, T. Hisada, and I. Sakuma, "Measuring forces in liver cutting: new equipment and experimental results," *Medical and Biological Engineering and Computing*, vol. 42, no. 6, pp. 787–798, 2004.

[67] J. Lang, D. K. Pai, and R. J. Woodham, "Acquisition of elastic models for interactive simulation," *Int'l. J. Robotics Research*, vol. 21, no. 8, pp. 713–734, 2002.

[68] M. Sedef, E. Samur, and C. Basdogan, "Visual and haptic simulation of linear vis-

coelastic tissue behaviour based on experimental data," in *Proc. 14th Symp. Haptic Interfaces Virtual Environments and Teleoperator Systems*, vol. 1, Alexandria, USA, March 2006, pp. 201 – 208.

[69] P. J. Davies, F. J. Carter, and A. Cuschieri, "Mathematical modelling for keyhole surgery simulations: A biomechanical model for spleen tissue," *IMA Journal of Applied Mathematics*, vol. 67, no. 1, pp. 41–67, 2002.

[70] K. Miller, "Biomechanics of soft tissues," *Medical Science Monitor*, vol. 6, no. 1, pp. 158–167, 2000.

[71] T. Hu and J. P. Desai, "Characterization of soft-tissue material properties: large deformation analysis," in *Proc. Medical Simulation: Int'l Symposium, ISMS 2004*, ser. Lecture Notes in Computer Science, S. Cotin and D. N. Metaxas, Eds. Berlin/Heidelberg: Springer, 2004, vol. 3078, pp. 28–37.

[72] A. Nava, E. Mazza, O. Haefner, and M. Bajka, "Experimental observation and modelling of preconditioning in soft biological tissues," in *2nd Int'l Symposium on Medical Simulation*, Cambridge, USA, June 2004, pp. 1–9, http://www.medicalsim.org/symposium2004/.

[73] E. Molinari, M. Fato, G. D. Leo, D. Riccardo, and F. Beltrame, "Simulation of the biomechanical behavior of the skin in virtual surgical applications by finite element method," *IEEE Trans. Biomedical Engineering*, vol. 52, no. 9, pp. 1514–1521, 2005.

[74] J. Kim, B. K. Tay, N. Stylopoulos, D. W. Rattner, and M. A. Srinivasan, "Characterization of intra-abdominal tissues from in vivo animal experiments for surgical simulation," in *6th Int'l. Conf. Medical Image Computing and Computer Assisted Intervention (MICCAI)*, ser. Lecture Notes in Computer Science. Berlin/Heidelberg: Springer, 2003, vol. 2879, pp. 206–213.

[75] R. Alterovitz, K. Goldberg, J. Pouliot, R. Taschereau, and C. I. Hsu, "Needle insertion and radioactive seed implantation in human tissues: simulation and sensitivity analysis," in *Proc. IEEE Int'l. Conf. Robotics and Automation*, vol. 2, Taipei, Taiwan, September 2003, pp. 1793–1799.

[76] H.-W. Nienhuys and F. A. van der Stappen, "A computational technique for interactive needle insertions in 3d nonlinear material," in *Proc. IEEE Int'l. Conf. Robotics and Automation*, vol. 2, New Orleans, USA, May 2004, pp. 2061–2067.

[77] D. Glozman and M. Shoham, "Flexible needle steering and optimal trajectory planning for percutaneous therapies," in *7th Int'l. Conf. Medical Image Computing and Computer Assisted Intervention (MICCAI)*, ser. Lecture Notes in Computer Science. Berlin/Heidelberg: Springer, 2004, vol. 3217, pp. 137–144.

[78] K.-K. Kyung, D.-S. Kwon, S.-M. Kwon, H.-S. Kang, and J. B. Ra, "Force feedback for a spine biopsy simulator with volume graphic model," in *Proc. IEEE/RSJ Int'l. Conf. Intelligent Robots and Systems*, vol. 3, Maui, USA, October-November 2001, pp. 1732–1737.

[79] X. Wang and A. Fenster, "A virtual reality based 3d real-time interactive brachytherapy simulation of needle insertion and seed implantation," in *IEEE Int'l. Symposium Biomedical Imaging: From Nano to Macro*, vol. 1, Arlington, USA, April 2004, pp. 280–283.

[80] J. R. Crouch, C. M. Schneider, J. Wainer, and A. M. Okamura, "A velocity-dependent model for needle insertion in soft tissue," in *8th Int'l. Conf. Medical Image Computing and Computer Assisted Intervention (MICCAI)*, ser. Lecture Notes in Computer Science, vol. 3750. Berlin/Heidelberg: Springer, 2005, pp. 624–632.

[81] P. N. Brett, T. J. Parker, A. J. Harrison, T. A. Thomas, and A. Carr, "Simulation of resistance forces acting on surgical needles," *Proc. Institution Mechanical Engineers, Part H: J. Engineering in Medicine*, vol. 211, no. 4, pp. 335–347, 1997.

[82] S. P. DiMaio and S. E. Salcudean, "Interactive simulation of needle insertion models," *IEEE Trans. Biomedical Engineering*, vol. 52, no. 7, pp. 1167–1179, 2005.

[83] P. N. Brett, A. J. Harrison, and T. A. Thomas, "Schemes for the identification of tissue types and boundaries at the tool point for surgical needles," *IEEE Trans. Information Technology in Biomedicine*, vol. 4, no. 1, pp. 30–36, 2000.

[84] J. T. Hing, A. D. Brooks, and J. P. Desai, "Reality-based needle insertion simulation for haptic feedback in prostate brachytherapy," in *Proc. IEEE Int'l. Conf. Robotics and Automation*, vol. 1, Orlando, USA, May 2006, pp. 619–624.

[85] I. Brouwer, J. Ustin, L. Bentley, A. Sherman, N. Dhruv, and F. Tendick, "Measuring in vivo animal soft tissue properties for haptic modeling in surgical simulation," in *Proc. Medicine Meets Virtual Reality (MMVR)*, ser. Studies in Health Technology and Informatics. Amsterdam, Netherlands: IOS, 2001, vol. 81, pp. 69–74.

[86] A. M. Okamura, C. Simone, and M. D. O'Leary, "Force modeling for needle insertion into soft tissue," *IEEE Trans. Biomedical Engineering*, vol. 51, no. 10, pp. 1707–1716, 2004.

[87] G. Picinbono, J.-C. Lombardo, H. Delingette, and N. Ayache, "Anisotropic elasticity and force extrapolation to improve realism of surgery simulation," in *Proc. IEEE Int'l. Conf. Robotics and Automation*, vol. 1, San Francisco, USA, April 2000, pp. 596–602.

[88] S. Cotin, H. Delingette, and N. Ayache, "A hybrid elastic model for real-time cutting, deformations, and force feedback for surgery training and simulation," *Visual Computer*, vol. 16, no. 8, pp. 437–452, 2000.

[89] W. Wu and P. A. Heng, "An improved scheme of an interactive finite element model for 3d soft-tissue cutting and deformation," *Visual Computer*, vol. 21, no. 8–10, pp. 707–716, 2005.

[90] T. Chanthasopeephan, J. P. Desai, and A. C. W. Lau, "Measuring forces in liver cutting: new equipment and experimental results," *Annals of Biomedical Engineering*, vol. 31, no. 11, pp. 1372–1382, 2003.

[91] M. Mahvash and V. Hayward, "Haptic rendering of cutting: a fracture mechanics approach," *Haptics-e*, vol. 2, no. 3, pp. 1–12, 2001.

[92] A. M. Okamura, R. J. Webster III, J. T. Nolin, K. W. Johnson, and H. Jafry, "The haptic scissors: cutting in virtual environments," in *Proc. IEEE Int'l. Conf. Robotics and Automation*, vol. 1, Taipei, Taiwan, September 2003, pp. 828–833.

[93] R. W. Ogden, *Non-linear elastic deformations*, 1st ed. Chichester, UK: Ellis Horwood Ltd., 1984.

[94] A. J. M. Spencer, *Deformations of Fibre-Reinforced Materials*, 1st ed. Oxford, UK: Clarendon Press, 1972.

[95] G. A. Holzapfel, *Nonlinear solid mechanics: a continuum approach for engineering*, 1st ed. Chichester, UK: John Wiley & Sons, Ltd., 2000.

[96] R. D. Cook, D. S. Malkus, and M. E. Plesha, *Concepts and applications of finite element analysis*, 3rd ed. New York, USA: John Wiley & Sons, 1989.

[97] Simulia, Rising Sun Mills, 166 Valley Street, Providence, RI 02909 USA. http://www.simulia.com/.

[98] ADINA R & D Inc., 71 Elton Avenue, Watertown, MA 02472 USA. http://www.adina.com/.

[99] ANSYS Inc., Southpointe, 275 Technology Drive, Canonsburg, PA 15317 USA. http://www.ansys.com/.

BIBLIOGRAPHY

[100] Lawrence Livermore National Laboratory, Methods Development Group, 7000 East Avenue, Livermore, CA 94550 USA. http://www.eng.llnl.gov/mdg/mdg_codes_dyna3d.html.

[101] COMSOL Inc., 1 New England Executive Park, Suite 350, Burlington, MA 01803 USA. http://www.femlab.com/.

[102] Georgia Tech-CASE Center, School of Civil & Environmental Engineering, Atlanta, GA 30332 USA. http://www.gtstrudl.gatech.edu/.

[103] Siemens PLM Software, 5800 Granite Parkway, Suite 600, Plano, TX 75024 USA. http://www.plm.automation.siemens.com/.

[104] MSC Software Corp., 2 MacArthur Place, Santa Ana, CA 92707 USA. http://www.mscsoftware.com/.

[105] C. S. Desai and J. F. Abel, *Introduction to the finite element method: a numerical method for engineering analysis*, 1st ed. Belmont, USA: Wadsworth Publishing Company, 1972.

[106] O. C. Zienkiewicz, R. L. Taylor, and J. Z. Zhu, *The finite element method: its basis and fundamentals*, 6th ed. Oxford, UK: Elsevier Butterworth-Heinemann, 2005.

[107] S. P. DiMaio and S. E. Salcudean, "Simulated interactive needle insertion," in *Proc. 10th Symp. Haptic Interfaces Virtual Environments and Teleoperator Systems*, vol. 1, Orlando, USA, March 2002, pp. 344–351.

[108] E. M. Arruda and M. C. Boyce, "Three-dimensional constitutive model for the large stretch behavior of rubber elastic materials," *Journal of the Mechanics and Physics of Solids*, vol. 41, no. 2, pp. 389–412, 1993.

[109] F. Tendick, M. Downes, T. Goktekin, M. C. Cavusoglu, D. Feygin, and X. Wu, "A virtual environment testbed for training laproscopic surgical skills," *Presence: Teleoperators and Virtual Environments*, vol. 9, no. 3, pp. 236–255, 2000.

[110] R. Hutter, K. U. Schmitt, and P. Niederer, "Mechanical modeling of soft biological tissues for application in virtual reality based laparoscopy simulators," *Technology and Health Care*, vol. 8, pp. 15–24, 2000.

[111] K. Miller and K. Chinzei, "Mechanical properties of brain tissue in tension," *J. Biomechanics*, vol. 35, no. 4, pp. 483–490, 2002.

[112] D. d'Aulignac, C. Laugier, and M. C. Cavusoglu, "Towards a realistic echographic simulator with force feedback," in *Proc. IEEE/RSJ Int'l. Conf. Intelligent Robots and Systems*, vol. 2, Kyongju, South Korea, October 1999, pp. 727–732.

[113] R. Alterovitz, K. Goldberg, J. Pouliot, R. Taschereau, and C. I. Hsu, "Sensorless planning for medical needle insertion procedures," in *Proc. IEEE/RSJ Int'l. Conf. Intelligent Robots and Systems*, vol. 4, Las Vegas, USA, October 2003, pp. 3337–3343.

[114] S. P. DiMaio and S. E. Salcudean, "Needle steering and model-based trajectory plan-

ning," in *6th Int'l. Conf. Medical Image Computing and Computer Assisted Intervention (MICCAI)*, ser. Lecture Notes in Computer Science. Berlin/Heidelberg: Springer, 2003, vol. 2879, pp. 33–40.

[115] O. Goksel, S. E. Salcudean, S. P. DiMaio, R. Rohling, and J. Morris, "3d needle-tissue interaction simulation for prostate brachytherapy," in *8th Int'l. Conf. Medical Image Computing and Computer Assisted Intervention (MICCAI)*, ser. Lecture Notes in Computer Science. Berlin / Heidelberg: Springer, 2005, vol. 3749, pp. 827–834.

[116] D. O. Popa and S. K. Singh, "Creating realistic force sensations in a virtual environment: experimental system, fundamental issues and results," in *Proc. IEEE Int'l. Conf. Robotics and Automation*, vol. 1, Leuven, Belgium, May 1998, pp. 59–64.

[117] M. Mahvash and A. M. Okamura, "A fracture mechanics approach to haptic synthesis of tissue cutting with scissors," in *Proc. 1st Joint Eurohaptics Conf. and Symp. Haptic Interfaces for Virtual Environment and Teleoperator Systems (World Haptics)*, vol. 1, Pisa, Italy, March 2005, pp. 356–362.

[118] M. Mahvash, L. Voo, D. Kim, K. Jeung, and A. M. Okamura, "Modeling the forces of cutting with scissors," *IEEE Trans. Biomedical Engineering*, vol. 55, no. 3, pp. 848–856, 2007.

[119] M. P. Ottensmeyer, A. E. Kerdok, R. D. Howe, and S. L. Dawson, "The effects of testing environment on the viscoelastic properties of soft tissues," in *Proc. Int'l.*

Symp. Medical Simulation (ISMS), ser. Lecture Notes in Computer Science, S. Cotin and D. N. Metaxas, Eds. Berlin/Heidelberg: Springer, 2004, vol. 3078, pp. 9–18.

[120] J. D. Brown, J. Rosen, M. N. Sinanan, and B. Hannaford, "In vivo and postmortem compressive properties of porcine abdominal organs," in *6th Int'l. Conf. Medical Image Computing and Computer Assisted Intervention (MICCAI)*, ser. Lecture Notes in Computer Science. Berlin/Heidelberg: Springer, 2003, vol. 2879, pp. 238–245.

[121] W. W. Lau, N. A. Ramey, J. J. Corso, N. V. Thakor, and G. D. Hager, "Stereo-based endoscopic tracking of cardiac surface deformation," in *7th Int'l. Conf. Medical Image Computing and Computer Assisted Intervention (MICCAI)*, ser. Lecture Notes in Computer Science. Berlin/Heidelberg: Springer, 2004, vol. 3217, pp. 494–501.

[122] J. Leven, D. Burschka, R. Kumar, G. Zhang, S. Blumenkranz, X. Dai, M. Awad, G. D. Hager, M. Marohn, M. Choti, C. Haser, and R. H. Taylor, "Davinci canvas: a telerobotic surgical system with integrated robot-assisted, laproscopic ultrasound capability," in *8th Int'l. Conf. Medical Image Computing and Computer Assisted Intervention (MICCAI)*, ser. Lecture Notes in Computer Science. Berlin/Heidelberg: Springer, 2005, vol. 3749, pp. 811–818.

[123] M. Kaneko, C. Toya, and M. Okajima, "Active strobe imager for visualizing dynamic behavior of tumors," in *Proc. IEEE Int'l. Conf. Robotics and Automation*, vol. 1, Rome, Italy, April 2007, pp. 3009–3014.

[124] J. Ophir, , S. K. Alam, B. S. Garra, F. Kallel, E. E. Konofagou, T. Krousko, C. R. B.

Merritt, R. Righett, R. Souchon, S. Srinivasan, and T. Varghese, "Elastography: imaging the elastic properties of soft tissues with ultrasound," *J. Medical Ultrasonics*, vol. 29, no. 4, pp. 155–171, 2000.

[125] L. Gao, K. J. Parker, R. M. Lerner, and S. F. Levinson, "Imaging of the elastic properties of tissue-a review," *Ultrasound in Medicine and Biology*, vol. 22, no. 8, pp. 959–977, 1996.

[126] E. Tönuk and B. Silver-Thorn, "Nonlinear elastic material property estimation of lower extremity residual limb tissues," *IEEE Trans. Neural Systems and Rehabilitation Engineering*, vol. 11, no. 1, pp. 43–53, 2003.

[127] M. Zhang, Y. P. Zheng, and A. F. Mak, "Estimating the effective young's modulus of soft tissues from indentation tests-nonlinear finite element analysis of effects of friction and large deformation," *Medical Engineering and Physics*, vol. 19, no. 6, pp. 512–517, 1997.

[128] E. Turgay, S. Salcudean, and R. Rohling, "Identifying the mechanical properties of tissue by ultrasound strain imaging," *Ultrasound in Medicine and Biology*, vol. 32, no. 2, pp. 221–235, 2006.

[129] G. Duchemin, P. Maillet, P. Poignet, E. Dombre, and F. Pierrot, "A hybrid position/force control approach for identification of deformation models of skin and underlying tissues," *IEEE Trans. Biomedical Engineering*, vol. 52, no. 2, pp. 160–170, 2005.

[130] G. De Gersem, H. Van Brussel, and J. Vander Sloten, "Enhanced haptic sensitivity for soft tissues using teleoperation with shaped impedance reflection," in *World Haptics Conf. (WHC)*, Pisa, Italy, March 2005.

[131] S. Misra and A. M. Okamura, "Environment parameter estimation during bilateral telemanipulation," in *Proc. 14th Symp. Haptic Interfaces Virtual Environments and Teleoperator Systems*, Alexandria, USA, March 2006, pp. 301–307.

[132] T. Yamamoto, B. Vagvolgyi, K. Balaji, L. L. Whitcomb, and A. M. Okamura, "Tissue property estimation and graphical display for teleoperated robot-assisted surgery," in *Proc. IEEE Int'l. Conf. Robotics and Automation*, Kobe, Japan, May 2009, pp. 4239–4245.

[133] Reachin Technologies AB, Årstaängsvägen 24, 117 43 Stockholm, Sweden. http://www.reachin.se/.

[134] Simbionix USA Corp., 11000 Cedar Ave., Suite 210, Cleveland, OH 44106 USA. http://www.simbionix.com/.

[135] Immersion Medical, 55 West Watkins Mill Road, Gaithersburg, MD 20878 USA. http://www.immersion.com/medical.

[136] Surgical Science Ltd., Haraldsgatan 5, SE 413 14 Göteborg, Sweden. http://www.surgical-science.com/.

BIBLIOGRAPHY

[137] Haptica Inc., 101 Federal Street, Suite 1900, Boston, MA 02110 USA. http://www.haptica.com/.

[138] Mimic Technologies Inc., 119 1st Ave South, Suite 360, Seattle 98104 USA. http://www.mimic.ws/.

[139] Mentice AB, Rosenlundsgatan 8, 411 20 Göteborg, Sweden. http://www.mentice.com/.

[140] Medical Educational Technologies Inc., 6000 Fruitville Road, Sarasota, FL 34232 USA. http://www.meti.com/.

[141] VRmagic GmbH, Augustaanlage 32, 68165 Mannheim, Germany. http://www.vrmagic.com/.

[142] Stanford University Medical Media and Information Technology, 251 Campus Drive, MSOB-2nd Floor, MC:5466, Stanford, CA 94305 USA http://summit.stanford.edu/.

[143] Center for Integration of Medicine and Innovative Technology, 165 Cambridge St., Suite 702, Boston, MA 02114 USA http://www.cimit.org/.

[144] National Capital Area Medical Simulation Center, Uniformed Services University, 4301 Jones Bridge Road, Bethesda, MD 20814 USA http://simcen.usuhs.mil/.

[145] T. F. Cox and M. A. Cox, *Multidimensional scaling*, 2nd ed. Boca Raton, USA: CRC Press LLC, 2001.

[146] S. Misra, K. T. Ramesh, and A. M. Okamura, "Modeling of tool-tissue interactions for computer-based surgical simulation: a literature review," *Presence: Teleoperators and Virtual Environments*, vol. 17, no. 5, pp. 463–491, 2008.

[147] E. Dehghan and S. E. Salcudean, "Comparison of linear and non-linear models in 2d needle insertion simulation," in *9th Int'l. Conf. Medical Image Computing and Computer Assisted Intervention (MICCAI)*, ser. Workshop Proc. Computational Biomechanics for Medicine, Copenhagen, Denmark, October 2006, pp. 117–124.

[148] N. Dhruv and F. Tendick, "Frequency dependence of complience contrast detection," *ASME J. Dynamic Systems, Measurement, and Control*, vol. 2, no. 1, pp. 1087–1093, 2000.

[149] B. Forsyth and K. E. MacLean, "Predictive haptic guidance: intelligent user assistance for the control of dynamic tasks," *IEEE Trans. Visualization and Computer Graphics*, vol. 12, no. 1, pp. 103–113, 2006.

[150] E. Ruffaldi, D. Morris, T. Edmunds, F. Barbagli, and D. K. Pai, "Standardized evaluation of haptic rendering systems," in *Proc. 14th Symp. Haptic Interfaces Virtual Environments and Teleoperator Systems*, vol. 1, Washington D.C., USA, March 2006, pp. 225–232.

[151] R. L. Klatzky, S. Lederman, and C. Reed, "Haptic integration of object properties: texture, hardness, and planar contour," *Journal of Experimental Psychology: Human Perception and Performance*, vol. 15, no. 1, pp. 45–57, 1989.

[152] S. J. Lederman, "The perception of surface roughness by active and passive touch," *Bulletin of the Psychonomic Soceity*, vol. 18, no. 5, pp. 253–255, 1981.

[153] H. Z. Tan, M. A. Srinivasan, B. Eberman, and B. Cheng, "Human factors for the design of force-reflecting haptic interfaces," in *Proc. 3rd Int'l. Symp. on Haptic Interfaces for Virtual Environment and Teleoperator Systems (ASME/ASME Dynamic Systems and Control Division)*, vol. 55, Chicago, USA, March 1994, pp. 353–359.

[154] J. Pasquero, J. Luk, S. Little, and K. MacLean, "Perception analysis of haptic icons: an investigation into the validity of cluster sorted mds," in *Proc. 14th Symp. Haptic Interfaces Virtual Environments and Teleoperator Systems*, vol. 1, Washington D.C., USA, March 2006, pp. 437–444.

[155] M. Yoshida, "Dimensions of tactual impressions (1)," *Japanese Psychological Research*, vol. 10, no. 3, pp. 123–137, 1968.

[156] ——, "Dimensions of tactual impressions (2)," *Japanese Psychological Research*, vol. 10, no. 4, pp. 157—-173, 1968.

[157] M. Hollins, R. Faldowski, S. Rao, and F. Young, "Individual differences in perceptual space for tactile textures: evidence from multidimensional scaling analysis," *Perception and Psychophysics*, vol. 54, no. 6, pp. 697–705, 1993.

[158] W. M. Bergmann Tiest and A. M. L. Kappers, "Analysis of haptic perception of

materials by multidimensional scaling and physical measurements of roughness and compressibility," *Acta Psychologica*, vol. 121, no. 1, pp. 1–20, 2006.

[159] K. MacLean and M. Enriquez, "Perceptual design of haptic icons," in *EuroHaptics Conference*, vol. 1, Dublin, UK, July 2003, pp. 1–13.

[160] P. Leskovsky, T. Cooke, M. Ernst, and M. Harders, "Using multidimensional scaling to quantify the fidelity of haptic rendering of deformable objects," in *Proc. Eurohaptics*, vol. 1, Paris, France, March 2006, pp. 289—-295.

[161] M. E. Gurtin, *An introduction to continuum mechanics*, 1st ed. London, UK: Academic Press, 2003.

[162] "Rheometerics Solids Analyzer RSAII Owner's Manual," Rheometrics Inc., Tech. Rep. 902–00013A, December 1991.

[163] L. A. Jones, "Perception and control of finger forces," in *Proc. ASME Dynamic Systems and Control Division*, vol. 64, Anaheim, USA, November 1998, pp. 133–137.

[164] Force Dimension, PSE-C, 1015 Lausanne, 1015 Switzerland http://www.forcedimension.com/.

[165] F. A. Wichmann and N. J. Hill, "The psychometric function: I. fitting, sampling and goodness-of-fit," *Perception and Psychophysics*, vol. 63, no. 8, pp. 1293–1313, 2001.

[166] SPSS Inc., 233 S. Wacker Drive, 11th floor, Chicago, IL 60606 USA http://www.spss.com/.

[167] J. B. Kruskal, "Multidimensional scaling by optimizing goodness of fit to a nonmetric hypothesis," *Psychometrika*, vol. 29, no. 1, pp. 1–27, March 1964.

[168] N. Abolhassani and R. V. Patel, "Deflection of a flexible needle during insertion into soft tissue," in *Proc. Int'l. Conf. IEEE Engineering in Medicine and Biology*, vol. 1, New York, USA, August/September 2006, pp. 3858–3861.

[169] A. Mohamed, C. Davatzikos, and R. Taylor, "A combined statistical and biomechanical model for estimation of intra–operative prostate deformation," in *5th Int'l. Conf. Medical Image Computing and Computer Assisted Intervention (MICCAI)*, ser. Lecture Notes in Computer Science, S. Cotin and D. N. Metaxas, Eds. Berlin/Heidelberg: Springer, 2002, vol. 2489, pp. 452–460.

[170] E. Samur, M. Sedef, C. Basdogan, L. Avtan, and O. Duzgun, "A robotic indenter for minimally invasive measurement and characterization of soft tissue response," *Medical Image Analysis*, vol. 11, no. 4, pp. 361–373, 2007.

[171] V. Daanen, J. Gastaldo, J. Y. Giraud, P. Fourneret, J. L. Descotes, M. Bolla, D. Collomb, and J. Troccaz, "MRI/TRUS data fusion for brachytherapy," *The International Journal of Medical Robotics and Computer Assisted Surgery*, vol. 2, no. 3, pp. 256–261, 2006.

[172] R. C. Susil, K. Camphausen, P. Choyke, E. R. McVeigh, G. S. Gustafson, H. Ning, R. W. Miller, E. Atalar, C. N. Coleman, and C. Ménard, "System for prostate brachytherapy and biopsy in a standard 1.5 t mri scanner," *Magnetic Resonance in Medicine*, vol. 52, no. 3, pp. 683–687, 2004.

[173] A. K. Sinop and L. Grady, "A seeded image segmentation framework unifying graph cuts and random walker which yields a new algorithm," in *Proc. IEEE Int'l. Conf. Computer Vision*, vol. 1, Rio de Janeiro, Brazil, October 2007, pp. 1–8.

[174] M. Ferrant, S. K. Warfield, C. R. G. Guttmann, R. V. Mulkern, F. A. Jolesz, and R. Kikinis, "3d image matching using a finite element based elastic deformation model," in *2nd Int'l. Conf. Medical Image Computing and Computer Assisted Intervention (MICCAI)*, ser. Lecture Notes in Computer Science, vol. 1679. Berlin/Heidelberg: Springer, 1999, pp. 202–209.

[175] J. M. Sullivan, G. Charron, and K. D. Paulsen, "A three-dimensional mesh generator for arbitrary multiple material domains," *Finite Elements in Analysis and Design*, vol. 25, no. 3, pp. 219–241, 2000.

[176] A. Bharatha, M. Hirose, N. Hata, S. K. Warfield, M. Ferrant, K. H. Zou, E. Suarez-Santana, J. Ruiz-Alzola, A. D'Amico, R. A. Cormack, R. Kikinis, F. A. Jolesz, and C. M. Tempany, "Evaluation of three-dimensional finite element-based deformable registration of pre- and intraoperative prostate imaging," *Medical Physics*, vol. 28, no. 12, pp. 2551–2560, 2001.

[177] J. R. Crouch, S. M. Pizer, E. L. Chaney, and M. Zaider, "Medially based meshing with finite element analysis of prostate deformation," in *6th Int'l. Conf. Medical Image Computing and Computer Assisted Intervention (MICCAI)*, ser. Lecture Notes in Computer Science, vol. 2878. Berlin/Heidelberg: Springer, 2003, pp. 108–115.

[178] National Institutes of Standards and Technology, 100 Bureau Drive, Stop 1070, Gaithersburg, MD 20899 USA. http://www.ctcms.nist.gov/oof/.

[179] H. Zhang, K. T. Ramesh, and E. S. C. Chin, "Effects of interfacial debonding on the rate-dependent response of metal matrix composites," *Acta Materialia*, vol. 53, no. 17, pp. 4687–4700, 2005.

[180] X.-P. Xu and A. Needleman, "Numerical simulations of fast crack growth in brittle solids," *J. Mechanics Physics Solids*, vol. 42, no. 9, pp. 1397–1434, 1994.

[181] J. A. Engh, G. Podnar, S. Khoo, and C. Riviere, "Flexible needle steering system for percutaneous access to deep zones of the brain," in *Proc. 32nd Annual IEEE Northeast Bioengineering Conf.*, vol. 1, Easton, USA, April 2006, pp. 103–104.

[182] D. Glozman and M. Shoham, "Image-guided robotic flexible needle steering," *IEEE Trans. Robotics*, vol. 23, no. 3, pp. 459–467, 2007.

[183] S. Okazawa, R. Ebrahimi, J. Chuang, S. E. Salcudean, and R. Rohling, "Hand-held steerable needle device," *IEEE/ASME Trans. Mechatronics*, vol. 10, no. 3, pp. 285–296, 2005.

[184] P. Sears and P. Dupont, "A steerable needle technology using curved concentric tubes," in *Proc. IEEE/RSJ Int'l. Conf. Intelligent Robots and Systems*, vol. 1, Beijing, China, October 2006, pp. 2850–2856.

[185] R. J. Webster III, J. S. Kim, N. J. Cowan, G. S. Chirikjian, and A. M. Okamura, "Nonholonomic modeling of needle steering," *Int'l. J. Robotics Research*, vol. 25, no. 5–6, pp. 509–525, 2006.

[186] N. Abolhassani, R. V. Patel, and M. Moallem, "Needle insertion into soft tissue: a survey," *Medical Engineering and Physics*, vol. 29, no. 4, pp. 413–431, 2007.

[187] M. Heverly, P. Dupont, and J. Triedman, "Trajectory optimization for dynamic needle insertion," in *Proc. IEEE Int'l. Conf. Robotics and Automation*, vol. 1, Barcelona, Spain, 2005, pp. 1646–1651.

[188] O. A. Shergold and N. A. Fleck, "Mechanisms of deep penetration of soft solids, with application to the injection and wounding of skin," *Proc. of the Royal Society of London A*, vol. 460, no. 2050, pp. 3037–3058, 2004.

[189] R. J. Webster III, J. Memisevic, and A. M. Okamura, "Design considerations for robotic needle steering," in *Proc. IEEE Int'l. Conf. Robotics and Automation*, vol. 1, Barcelona, Spain, April 2005, pp. 3588–3594.

[190] K. B. Reed, V. Kallem, R. Alterovitz, K. Goldberg, A. M. Okamura, and N. J. Cowan, "Integrated planning and image-guided control for planar needle steer-

ing," in *IEEE RAS/EMBS Int'l. Conf. on Biomedical Robotics and Biomechatronics*, Scottsdale, USA, October 2008, pp. 819–824.

[191] O. A. Shergold and N. A. Fleck, "Experimental investigation into the deep penetration of soft solids by sharp and blunt punches with application to the piercing of skin," *J. Biomechanical Engineering*, vol. 127, no. 5, pp. 838–848, 2005.

[192] G. I. Barenblatt, *Scaling, self-similarity, and intermediate asympotics*, 1st ed. Cambridge, UK: Cambridge University Press, 2002.

[193] S. P. Timoshenko and J. Gere, *Theory of elastic stability*, 2nd ed. Columbus, USA: McGraw-Hill Companies, 1961.

[194] B. Hannaford, "Design framework for teleoperators with kinesthetic feedback," *IEEE Trans. Robotics and Automation*, vol. 5, no. 4, pp. 426–434, 1989.

[195] P. E. Dupont, P. A. Millman, T. M. Schulteis, and R. D. Howe, "Automatic identification of environment haptic properties," *Presence: Teleoperators and Virtual Environments*, vol. 8, no. 4, pp. 392–409, 1999.

[196] J. Park, R. Cortesao, and O. Khatib, "Robust and adaptive teleoperation for compliant motion tasks," in *11th Int'l. Conf. on Advanced Robotics*, vol. 1, Coimbra, Portugal, June 2003, pp. 513–519.

[197] K. Hashtrudi-Zaad and S. E. Salcudean, "Adaptive transparent impedance reflecting

teleoperation," in *Proc. IEEE Int'l. Conf. Robotics and Automation*, vol. 2, Minneapolis, USA, April 1996, pp. 1369–1374.

[198] N. Diolaiti, C. Melchiorri, and S. Stramigioli, "Contact impedance estimation for robotic systems," in *Proc. IEEE/RSJ Int'l. Conf. Intelligent Robots and Systems*, vol. 3, Sendai, Japan, September 2004, pp. 2538–2543.

[199] M. B. Colton and J. M. Hollerbach, "Identification of nonlinear passive devices for haptic simulations," in *Proc. 1st Joint Eurohaptics Conf. and Symp. Haptic Interfaces for Virtual Environment and Teleoperator Systems (World Haptics)*, vol. 1, Pisa, Italy, March 2005, pp. 363–368.

[200] H. Seraji and R. Colbaugh, "Force tracking in impedance control," in *Proc. IEEE Int'l. Conf. Robotics and Automation*, vol. 2, Atlanta, USA, May 1993, pp. 499–506.

[201] D. Erickson, M. Weber, and I. Sharf, "Contact stiffness and damping estimation for robotic systems," *Int'l. J. Robotics Research*, vol. 22, no. 1, pp. 41–57, 2003.

[202] J.-J. E. Slotine and L. Weiping, *Applied Nonlinear Control*, 1st ed. Englewood Cliffs, NJ: Prentice-Hall Inc., 1991.

[203] D. A. Lawrence, "Designing teleoperator architectures for transparency," in *Proc. IEEE Int'l. Conf. Robotics and Automation*, vol. 2, Nice, France, May 1992, pp. 1406–1411.

[204] H. Kazerooni, T.-I. Tsay, and K. Hollerbach, "Controller design framework for telerobotic systems," *IEEE Trans. Control Systems Technology*, vol. 1, no. 1, pp. 50–62, 1993.

[205] H. Kobayashi and H. Nakamura, "A scaled teleoperation," in *IEEE Int'l. Workshop on Robot and Human Communication*, vol. 1, Tokyo, Japan, September 1992, pp. 269–274.

[206] A. Sherman, M. C. Cavusoglu, and F. Tendick, "Comparison of teleoperator control architectures for palpation task," in *Proc. 10th Symp. Haptic Interfaces Virtual Environments and Teleoperator Systems*, vol. 1, Orlando, USA, November 2000, pp. 1261–1268.

[207] K. B. Shimoga, "Survey of perceptual feedback issues in dexterous telemanipulation: Part i. finger force feedback," in *IEEE Annual Virtual Reality Int'l. Symposium*, vol. 1, Seattle, USA, September 1993, pp. 263–270.

[208] N. Hogan, "Impedance control: an approach to manipulation: part i-iii," *ASME J. Dynamic Systems, Measurement, and Control*, vol. 107, no. 1, pp. 1–24, 1985.

[209] Intuitive Surgical Inc., 1266 Kifer Road, Building 101, Sunnyvale, CA 94086 USA. http://www.intuitivesurgical.com/.

Vita

Sarthak Misra joined the doctoral program in the Department of Mechanical Engineering at Johns Hopkins University in 2005. Prior to commencing his studies at Johns Hopkins, Sarthak received his Bachelor of Technology degree at the National Institute of Technology, Warangal, India, and his Master of Engineering degree at the Center for Intelligent Machines, McGill University, Montreal, Canada. Both degrees were in Mechanical Engineering. After finishing his studies at McGill, Sarthak worked for three years as a dynamics and controls analyst at MacDonald Dettwiler and Associates on the International Space Station Program. Sarthak is the recipient of the McGill Major Fellowship and the Link Foundation Fellowship. Starting August 2009, Sarthak will begin working as an Assistant Professor at the University of Twente, Enschede, The Netherlands.